

**STUDYING THE MILKY WAY THROUGH ITS
EXTRAGALACTIC ANALOGS**

by

Timothy C. Licquia

B.A., University of Michigan, 2008

M.S., University of Pittsburgh, 2012

Submitted to the Graduate Faculty of
the Kenneth P. Dietrich School of Arts and Sciences in partial
fulfillment

of the requirements for the degree of

Doctor of Philosophy

University of Pittsburgh

2016

UNIVERSITY OF PITTSBURGH
KENNETH P. DIETRICH SCHOOL OF ARTS AND SCIENCES
DEPARTMENT OF PHYSICS AND ASTRONOMY

This dissertation was presented

by

Timothy C. Licquia

It was defended on

April 27th 2016

and approved by

Jeffrey A. Newman, Assoc. Prof., Physics & Astronomy, University of Pittsburgh

Carles Badenes, Asst. Prof., Physics & Astronomy, University of Pittsburgh

Anthony H. Duncan, Prof. Emeritus, Physics & Astronomy, University of Pittsburgh

Chad M. Schafer, Assoc. Prof., Statistics, Carnegie Mellon University

Andrew R. Zentner, Assoc. Prof., Physics & Astronomy, University of Pittsburgh

Dissertation Director: Jeffrey A. Newman, Assoc. Prof., Physics & Astronomy, University
of Pittsburgh

STUDYING THE MILKY WAY THROUGH ITS EXTRAGALACTIC ANALOGS

Timothy C. Licquia, PhD

University of Pittsburgh, 2016

The Universe is teeming with galaxies, which are complex structures with a broad range of colors, shapes, and sizes. We reside within the Milky Way (MW), just one example of this population, allowing us to study its stars and gas, and hence the physical mechanisms that shape galactic properties, in intimate detail. Unfortunately, our inside-out view prohibits us from measuring the MW's light as an integrated source, and perhaps more problematic is that dust in the interstellar medium shrouds most its light from view. Consequently, our knowledge of the global characteristics of the MW, and hence how it fits among the galaxy population, has remained very limited. This thesis is focused on employing modern statistical techniques as well as preexisting Galactic and extragalactic data to overcome these challenges. A key aspect of this work is the development of a hierarchical Bayesian meta-analysis technique for better constraining properties of our Galaxy that have been studied by many authors and for which there exist extensive observational data, but may be prone to large systematic uncertainties. Applying this machinery yields new estimates of the MW's mass properties, including its star formation rate and total stellar mass, as well as its exponential disk scale length measured from both visible and infrared starlight. Additionally, this thesis presents a new method for identifying a sample of MW analog galaxies from extragalactic data in order to determine properties of our Galaxy that are all but impossible to observe directly. Herein, this technique yields new estimates of the MW's photometric properties — i.e., its global color and luminosity at visible wavelengths, as measured from across cosmic distances. This work culminates with new, accurate investigations of how the

MW fits into a variety of extragalactic contexts, which quantitatively demonstrates that in several ways the MW is not the prototypical spiral galaxy it was recently thought to be. Notably, the MW most likely lies in the sparsely populated “green-valley” region of the galaxy color-magnitude diagram. Furthermore, comparing the MW to spiral galaxy scaling relations reveals that it is extraordinarily compact versus its peers.

TABLE OF CONTENTS

1.0 INTRODUCTION	1
1.1 THE UNIVERSE: A GALAXY ZOO	1
1.2 GALAXY FORMATION AND EVOLUTION	4
1.3 THE MILKY WAY: A UNIQUE LABORATORY FOR GALACTIC SCIENCE	6
1.4 THE GALACTIC-EXTRAGALACTIC DICHOTOMY	8
1.5 DISSERTATION OVERVIEW	10
2.0 IMPROVED ESTIMATES OF THE MILKY WAY'S STELLAR MASS AND STAR FORMATION RATE FROM HIERARCHICAL BAYESIAN META-ANALYSIS	14
2.1 INTRODUCTION	14
2.2 HIERARCHICAL BAYESIAN ANALYSIS	16
2.2.1 Defining the Problem	16
2.2.2 Relieving the Tension	17
2.2.3 The Formalism	19
2.2.3.1 The Likelihood	19
2.2.3.2 The Prior	21
2.2.3.3 The Marginalized Posterior	22
2.2.3.4 Choosing Amongst Models	23
2.3 THE MILKY WAY'S STAR FORMATION RATE	25
2.3.1 The SFR Data	25
2.3.2 Setting a Prior on \dot{M}_\star	25
2.3.3 SFR Results	26

2.4	THE MASS OF THE MILKY WAY'S STELLAR COMPONENTS	29
2.4.1	The Stellar Disk Model	29
2.4.2	Monte Carlo Techniques	33
2.4.3	A Uniform Sample of Bulge+Bar Mass Measurements	36
2.4.4	Setting a Prior on M_{\star}^B	41
2.4.5	Stellar Mass Results	42
2.5	SUMMARY & DISCUSSION	45
3.0	UNVEILING THE MILKY WAY: A NEW TECHNIQUE FOR DE- TERMINING THE OPTICAL COLOR AND LUMINOSITY OF THE GALAXY	61
3.1	INTRODUCTION	61
3.2	OBSERVATIONAL DATA	64
3.2.1	The Milky Way	65
3.2.2	SDSS Galaxies	66
3.2.2.1	Photometry	66
3.2.2.2	MPA-JHU Stellar Masses and SFRs	68
3.2.2.3	Initial Cuts	70
3.3	CONSTRUCTING USEFUL SDSS GALAXY SAMPLES	71
3.3.1	Selection of a Volume-Limited Sample	71
3.3.2	Identifying Milky Way Analogs	73
3.4	SYSTEMATICS	77
3.4.1	Eddington Bias	77
3.4.2	Inclination Reddening	79
3.5	RESULTS	83
3.6	SUMMARY & DISCUSSION	88
3.6.1	Comparisons to Earlier Color Measurements	89
3.6.2	Comparisons to Earlier Absolute Magnitude Measurements	91
3.6.3	Comparisons to Luminosity Function Measurements	92
3.6.4	Comparisons to Green-Valley Definitions	93
3.6.5	Comparisons to Earlier Mass-to-Light Ratio Measurements	94

3.6.6	Conclusions and Future Studies	95
4.0	SIZING UP THE MILKY WAY: A HIERARCHICAL BAYESIAN META-ANALYSIS OF PHOTOMETRIC SCALE LENGTH MEASURE- MENTS	111
4.1	INTRODUCTION	111
4.2	THE MILKY WAY SCALE LENGTH DATASET	114
4.2.1	Observational Data	120
4.2.2	Models of the Milky Way	121
4.2.3	Analysis Techniques Used for Scale Length Measurements	122
4.2.3.1	Integrated Light	122
4.2.3.2	Star Counts	123
4.2.3.3	Photometric Parallax	124
4.2.3.4	Two-Point Correlation Function	125
4.3	METHODS	126
4.3.1	Hierarchical Bayesian Technique	126
4.3.1.1	Posterior Results From Bayesian Model Averaging	129
4.3.1.2	Choosing Priors for L_d and Θ_k	130
4.3.1.3	Corrections Toward a Uniform Dataset	132
4.3.1.4	Monte Carlo Techniques	137
4.4	RESULTS	138
4.4.1	Parameters Describing the Consistency of the Data	141
4.4.2	Marginalized Posterior Results for L_d	145
4.4.3	Impact of R_0 Prior	147
4.4.4	Tests of Alternative Assumptions and Robustness	147
4.5	DISCUSSION	149
4.5.1	Comparisons to Dynamical Estimates	149
4.5.2	Comparisons to Multi-band Photometry for Extragalactic Disks	152
4.5.3	A Revised Estimate of the Milky Way’s Total Stellar Mass	153
4.5.3.1	Updating the Disk Model Assumptions	153
4.5.3.2	Correcting for Local Density Variations	155

4.5.3.3 Revised Stellar Mass Results	157
4.6 SUMMARY AND CONCLUSIONS	158
5.0 DOES THE MILKY WAY OBEY SPIRAL GALAXY SCALING RE-	
LATIONS?	161
5.1 INTRODUCTION	161
5.2 DATA	163
5.2.1 SDSS Spiral Galaxies	164
5.2.2 The Milky Way	166
5.3 INVESTIGATING TULLY-FISHER RELATIONS	169
5.3.1 Methods	169
5.3.2 Results	171
5.4 INVESTIGATING 3-DIMENSIONAL <i>LVR</i> RELATIONS	175
5.4.1 Methods	175
5.4.2 Results	177
5.5 DISCUSSION	178
5.5.1 Comparison to Prior Investigations of the Milky Way’s Consistency with the TFR	178
5.5.2 The Emergent Picture of a “Too-Small” Milky Way Galaxy	182
5.5.2.1 Potential Concerns	183
5.5.2.2 External Support	184
5.6 SUMMARY AND CONCLUSIONS	185
6.0 DISSERTATION CONCLUSION	187
6.1 SUMMARY OF PREVIOUS CHAPTERS	187
6.2 FUTURE WORK	190
APPENDIX A. ALTERNATIVE MODELS OF THE GALACTIC DISK	193
APPENDIX B. UPDATED ESTIMATES OF MILKY WAY PROPERTIES	197
BIBLIOGRAPHY	201

LIST OF TABLES

2.1	Combined SFR Results For Various Model Assumptions	52
2.2	Combined SFR Results For Various Data Assumptions	52
2.3	Disk Model Parameters	53
2.4	The Galactic Bulge+Bar Mass Dataset	53
2.5	Combined M_{\star}^B Results For Various Model Assumptions	58
2.6	Milky Way Properties and Derivatives	59
3.1	Photometric Properties for the Milky Way: Rest-frame $z=0$ SDSS Passbands	106
3.2	Photometric Properties for the Milky Way: Rest-frame $z=0.1$ SDSS Passbands	107
3.3	Photometric Properties for the Milky Way: Rest-frame $z=0$ Johnson-Cousins Passbands	108
3.4	Photometric Properties for the Milky Way: Rest-frame $z=0.1$ Johnson-Cousins Passbands	109
3.5	Photometric Properties for the Milky Way: Global Stellar Mass-to-Light Ratios	110
4.1	Milky Way Scale Length Measurements: Observational Data, Galactic Models, Analysis Techniques	117
2	Ranges for Flat Priors	131
4.2	Milky Way Radial Scale Length Measurements Renormalized For HB Analysis	136
4.3	HB Results for the Milky Way Radial Scale Length	140
5.1	Global Properties of the Milky Way	165
5.2	Consistency of the Milky Way with Tully-Fisher Relations	172
5.3	Consistency of the Milky Way with LVR Relations	180
B1	Updated Structural Properties of the Milky Way	198

B2	Updated Mass Properties of the Milky Way	198
B3	Updated Photometric Properties for the Milky Way: Rest-frame $z=0$ Passbands	199
B4	Updated Photometric Properties for the Milky Way: Rest-frame $z=0.1$ Passbands	199
B5	Updated Global Stellar Mass-to-light Ratios for the Milky Way	200

LIST OF FIGURES

1.1	The Hubble Ultra-Deep Field image	13
2.1	The joint posterior PDF, $P(f_{\text{good}}, n \mid \mathcal{D}_{\text{SFR}})$	49
2.2	The marginal posterior PDF, $P(f_{\text{good}} \mid \mathcal{D}_{\text{SFR}})$	50
2.3	The marginal posterior PDF, $P(\dot{M}_{\star} \mid \mathcal{D}_{\text{SFR}})$	51
2.4	The joint posterior PDF, $P(f_{\text{good}}, F \mid \mathcal{D}_{\text{M}})$	54
2.5	The marginal posterior PDF, $P(F \mid \mathcal{D}_{\text{M}})$	55
2.6	The marginal posterior PDF, $P(f_{\text{good}} \mid \mathcal{D}_{\text{M}})$	56
2.7	The marginal posterior PDF, $P(M_{\star}^{\text{B}} \mid \mathcal{D}_{\text{M}})$	57
2.8	The bulge-to-total mass ratio, B/T , of the Milky Way	60
3.1	Position of the Milky Way in \dot{M}_{\star} - M_{\star} space.	97
3.2	Flowchart outlining the steps and criteria we use to select different samples of SDSS galaxies.	98
3.3	Sample of $\sim 3,500$ Milky Way analog galaxies in \dot{M}_{\star} - M_{\star} space.	99
3.4	Sample of $\sim 3,500$ Milky Way analog galaxies in the SDSS ${}^0(g-r)$ vs. 0M_r color-magnitude diagram.	100
3.5	Modeling the Eddington bias in the Milky Way analog selection method.	101
3.6	Testing for inclination reddening in the Milky Way analog selection method.	102
3.7	The distribution of M_{\star} and \dot{M}_{\star} values for our Milky Way analog sample at different stages of our analysis overlaid upon the Galactic posterior PDFs used for selecting them.	103
3.8	The position of the Milky Way in SDSS ${}^0(g-r)$ vs. 0M_r color-magnitude space.	104
3.9	The position of the Milky Way in SDSS ${}^0(u-r)$ vs. M_{\star} space.	105

4.1	The evolution of Milky Way's L_d estimates.	116
4.2	The joint posterior PDF, $P(f_{\text{good}}, n \mid \mathcal{D}, \mathcal{M}_{\text{free-}n})$, for different subsets of the L_d data.	142
4.3	The marginal posterior PDF, $P(f_{\text{good}} \mid \mathcal{D}, \mathcal{M}_k)$, for different subsets of the L_d data.	144
4.4	The marginal posterior PDF, $P(L_d \mid \mathcal{D})$, for different subsets of the L_d data.	146
5.1	The Milky Way compared to Tully-Fisher relations.	171
5.2	The Milky Way compared to LVR relations.	179

1.0 INTRODUCTION

This dissertation provides a detailed investigation into the global characteristics of our home Galaxy¹, the Milky Way, with the overarching goal of better understanding how it fits in amongst the other galaxies in the Universe. Its chapters are designed as a series of steps toward this goal, and are relatively self-contained. This allows readers with various backgrounds to focus in on certain chapters or sections according to their level of interest or expertise. For instance, the remainder of Chapter 1 is geared toward those with a limited background in galactic astronomy, and provides a relatively non-technical introduction to the topics that follow. This sets the scene for Chapters 2–5, where I detail at a higher scientific level the methods and machinery that I use to derive my main results. Lastly, Chapter 6 is useful for readers who are looking for a short summary of this work, as well as their broader impact on Galactic and extragalactic astronomy.

1.1 THE UNIVERSE: A GALAXY ZOO

Over the past century, astronomy has delivered remarkable progress toward understanding the Universe that we live in. Only in this relatively short and recent period of time have we grasped the true immensity of the cosmos and our unexceptional place within it. We have surpassed the notion that the collection stars and gas surrounding Sun encompasses all celestial bodies — i.e., that our home Galaxy, the Milky Way, defines the totality of the Universe. Instead, with the aid of continual advancements in instrumentation, we have firmly established that the Milky Way is but one amongst hundreds of billions of other galaxies

¹I will use capitalization when distinctly referring to the Milky Way.

glowing ubiquitously amidst the otherwise dark and infinite expanse that is cosmic space². The Hubble Ultra-Deep Field image now represents an iconic visualization of this, included below as Figure 1.1, which also reveals the wide assortment of colors, shapes, and sizes that galaxies display. Today we understand that, invariably, these are aggregates of luminous stars, gas, and dust that are gravitationally bound together with reinforcement from a much more massive and spatially extended component of invisible *stuff*, which we have dubbed “dark matter” (Zwicky, 1933; Ostriker et al., 1974; Rubin et al., 1978, 1980).

If we are to disperse the light that we receive from any one of these objects (barring those nearest to us) in order to measure its spectrum, we find that the distinct atomic signatures that it contains are displaced to some degree toward longer wavelengths (i.e., *redshifted*) compared to rest-frame positions. Evidently, galaxies in general are traveling away from us. Furthermore, for those that we can independently measure a distance to, we find that the magnitude of this redshift (z) is on average proportional to distance of the object from us — this is known as Hubble’s Law (Hubble, 1929). From this basic result, we have since developed a remarkably successful model of cosmology³ (Weinberg, 1972; Peebles, 1993), where the Universe has a finite age and space itself is expanding over time, but comes with no discernible edge or center. Thanks to the fixed, cosmically-universal speed of light, the distance to (and hence z of) a particular galaxy maps directly to a distinct age of the Universe, and hence observing progressively more distant galaxies allows us to peer progressively further back in time. In this way, cosmology is inevitably linked to the study of galaxies and their evolution through cosmic history.

Progress in the field of extragalactic astronomy was relatively slow through the mid-twentieth century due to limited technology, as studies of galaxies were restricted to small sample sizes stemming from targeted observations. The situation has improved drastically over the past few decades, however, as a variety of large-scale galaxy surveys have been carried out at wavelengths from the ultraviolet (UV) to the radio. Most notably, this includes the Sloan Digital Sky Survey (SDSS; York et al., 2000), conducted at visible wavelengths to

²With this imagery in mind, it’s interesting to note that galaxies were, in fact, dubbed “island universes” when astronomers initially pondered the idea that they existed outside of the Milky Way system.

³Cosmology is the study of the structure and evolution of the Universe as whole and the physical laws that govern it.

produce both deep, multi-band CCD imaging and high-quality spectroscopic measurements for $\sim 10^6$ galaxies. The combination of these two techniques provides a wealth of information for each object, characterizing both its light and mass properties. In addition, a dataset of this scale is sufficient for studying the full dynamic range of properties that galaxies display, as well as their true underlying distributions (see, e.g., [Blanton et al., 2003a](#)).

A particularly important example is illustrated by the color-magnitude diagram (CMD), where one plots integrated color as a function of absolute magnitude. In this parameter space, the SDSS sample reveals that the vast majority of galaxies fall into two primary groups: a *red* population and a *blue* population, which are typically labeled the “red sequence” and “blue cloud”, respectively. Furthermore, it is found that this pattern closely parallels the two primary modes of morphological type: spirals and ellipticals, respectively. While hints of this trend were found from smaller galaxy samples previously, the SDSS dataset established the bimodality of galaxies to a high level of significance ([Strateva et al., 2001](#); [Buta, 2011](#)).

Myriad investigations into the SDSS data have since further characterized this dichotomy (e.g., [Blanton et al., 2005](#); [Schawinski et al., 2014](#)). The blue cloud predominantly consists of spiral galaxies that are still actively forming stars today. They contain hot (but short-lived) O- and B-stars that emit copious amounts of blue light, dominating the galaxy’s overall spectral energy distribution (SED), and hence leading to a bluer integrated color. Studies of both the light and velocity profiles for spiral galaxies indicate that their stars and gas are organized into a rotationally supported disk-like structure. Generically, they display a surface brightness profile that, to first order, dims exponentially with radius, but often display secondary or substructure features, e.g., rings, gaps, or breaks ([van der Kruit & Freeman, 2011](#)). As the moniker suggests, vivid spiral arms often appear superimposed upon the smoother underlying disk structure; these mark the sites of active star formation. Correspondingly, spiral arms become more prominent in observations made using bluer filter passbands. Secondary stellar components are often found at their central regions, such as a bar or bulge; these appear redder in color as they are composed of older stellar populations.

The red sequence is representative of elliptical galaxies, which display far less morphological features ([Graham, 2013](#)). They are spheroidal or ellipsoidal in shape and produce smooth, featureless surface brightness profiles that dim much more slowly at large radii than

those of spirals. They appear relatively devoid of gas and dust, and correspondingly show marginal, if any, star formation activity. Thus, elliptical galaxies are composed of ancient stellar populations; blue O- and B-stars have faded away long ago with the lack of stellar nurseries to replenish them. In turn, this renders ellipticals redder in color than their spiral counterparts, yet they can reach luminosities that are orders of magnitude brighter than the brightest spirals.

1.2 GALAXY FORMATION AND EVOLUTION

A major outstanding question in extragalactic astronomy is: what caused the bimodality of the galaxy population? This is puzzling especially since we expect that all galaxies formed under nearly identical initial conditions in the homogenous early Universe. More explicitly, our standard “Big Bang” model of cosmology postulates that tiny fluctuations were present in the distribution of cosmic matter density when the Universe sufficiently cooled to the point where neutral atoms initially formed ($z \sim 1,300$). Subsequently, these perturbations increasingly grew under gravitational instability, eventually producing clouds of gas that cooled, fragmented, and further collapsed into the first stars ($z \sim 10\text{--}100$), leading to the first galaxies ($z \sim 10$) that eventually built up to be the present-day ($z \sim 0$) colossal systems that we see. Given their uniform beginnings, it is unclear what has driven galaxies into two distinct classes of objects.

Another broad, yet fundamental question related to this is: how did galaxies form and evolve into the structures we observe today? These are systems that can change visibly only on timescales of hundreds of millions of years or more, and hence the answer cannot come from observing any one galaxy progress through time. Instead, we must take advantage of the constant speed of light, which renders measurements of progressively farther away objects into observations of the Universe at progressively early times. Hubble’s Law establishes that there is a tight relationship between a galaxy’s redshift (z)— i.e., the displacement of its spectral lines toward longer wavelengths compared to their rest-frame positions — and its distance, and hence implicitly the age of the Universe. Therefore, investigations into galactic

properties as a function of z constitute one of the primary ways to study galaxy evolution.

Another major approach is to study galaxy scaling relations. These were discovered empirically in the late 1970s through the combination of photometry and spectroscopy for small samples of galaxies, first revealing that a galaxy’s luminosity is tightly correlated with its internal kinematic properties. Spirals and ellipticals each obey their own version of this relationship since they are kinematically different systems. For example, ellipticals are supported by the random, unorganized or “thermal” motions of its stars, giving rise to an isotropic dispersion in their velocities. This velocity dispersion can be measured from the broadening of distinct stellar absorptions lines found in the integrated spectrum of the galaxy. The Faber-Jackson relation (Faber & Jackson, 1976) links an elliptical’s velocity dispersion to its luminosity, both technically measured within its effective radius, which contains half the surface brightness of the galaxy. Spiral galaxies, on the other hand, are supported by the ordered rotational motions of their stars and gas into roughly circular orbits about their centers. They rotate differentially, such that at large radii from their centers they typically approach a constant tangential velocity — i.e., their rotation curves (circular velocity vs. radius) become flat (Sofue & Rubin, 2001). Traditionally, this maximum circular velocity is measured from the Doppler width of a galaxy’s 21-cm spectral emission line, associated with the spin-flip transition of neutral hydrogen (HI) atoms, in the radio where interference due to dust is minimal. It can also be measured from HI and H α rotation curves developed from long-slit spectroscopy (Springob et al., 2007). One limitation here is that this signal is maximized for edge-on spirals, where one side of the disk is moving away from us and the other side toward us, whereas it cannot be measured for face-on systems. The Tully-Fisher relation (Tully & Fisher, 1977) links a spiral’s maximum rotational velocity to its luminosity. Note that these internal velocity measurements provide distance-independent quantities, and hence their intrinsic relationship to galaxy luminosities is important for studying not only galaxy formation, but also the Universe itself. The Tully-Fisher and Faber-Jackson relations are important tools for extending Hubble’s Law beyond the local Universe.

It is now well understood that galaxies obey scaling relations based not only on their luminosities and internal velocity measures, but also their sizes. Elliptical galaxies in particular appear to cluster most tightly (i.e., with minimal scatter) along a plane, commonly known

as the *fundamental plane* (FP), in the 3-dimensional space defined by luminosity, velocity dispersion, and radius (Dressler et al., 1987; Djorgovski & Davis, 1987). The Faber-Jackson relation represents just one projection of the FP, which can be theoretically accounted for almost entirely as a consequence of the virial theorem. The small observed deviation from the exact virial theorem prediction is referred to as the tilt in the FP; a major focus of research is to understand the variations in stellar populations amongst elliptical galaxies that can account for this tilt (e.g., Cappellari et al., 2013). Spiral galaxies appear to be more complicated. They too form a sequence or plane in the 3-dimensional space defined by luminosity, maximum rotational velocity, and radius, but with several surprising features (Courteau & Rix, 1999; Courteau et al., 2007). For instance, the inclusion of radius in any way is always seen to increase the dispersion, such that the Tully-Fisher relation appears to be the edge-on view of the analogous fundamental plane for spirals (Hall et al., 2012, and references therein). Studies of the Tully-Fisher relation using larger datasets over the past few decades have found it challenging to explain the observed scatter about the relation. For example, it is found that the scatter about the Tully-Fisher relation is uncorrelated with disk surface brightness, which supports that dark matter halos play an important part in this relation. However, studies have shown it to be extremely challenging to construct models that simultaneously reproduce all empirical disk galaxy scaling relations while also matching other statistical properties of the spiral galaxy population (Dutton et al., 2007, 2011). This has led to the question: is our standard model of cosmology consistent with our standard picture of galaxy formation?

1.3 THE MILKY WAY: A UNIQUE LABORATORY FOR GALACTIC SCIENCE

A major advantage we have in answering many of these questions is that we reside in the middle of our own massive and star-forming galaxy. More specifically, the Sun is located nearly at the mid-plane of the Milky Way's disk, roughly two-thirds of the way out from its center (Jurić et al., 2008). This in fact places us within our Galaxy's zone of vitality,

where new stars are being forged from the coalescence of gas and dust that permeates the disk (i.e., the interstellar medium, or ISM). Our internal vantage point therefore provides us with intimate views of stellar nurseries, such as the Orion nebula, and enables us to make detailed observations of the star formation process (Chomiuk & Povich, 2011).

Furthermore, the Milky Way is the only galaxy where we can measure the properties of large samples of individual stars. The SDSS again has served as a vital tool in this endeavor, as it has provided both photometric and spectroscopic measurements for $\sim 300,000$ stars in our Galaxy (Allende Prieto et al., 2008; Yanny et al., 2009). While it's not feasible to map the entirety of our Galaxy in this way, for those stars that are near enough, we can determine 3-dimensional position and velocity information, elemental abundances, as well as among many other properties to a high degree of accuracy. In turn, this has enabled us to study the structural and kinematic properties of stars as a function of their age (e.g., Bovy et al., 2012a; Bovy & Rix, 2013; Anders et al., 2014), which should directly point to how our Galaxy has built up its stellar mass over cosmic time.

The advent of this rich stellar dataset has also sparked a multitude of Milky Way-like galaxy simulations being developed in recent years. In short, these are computer programs designed to track the dynamical interaction and evolution of a mock galaxy's stars, gas, and dark matter starting from a set of initial conditions, governed by physical laws that are encoded. These are generally limited by their mass resolution — i.e., the number particles per unit volume, which in turn dictates the amount of stars or gas that is represented by a single particle — and hence their inability to account for small-scale (or *sub-grid*) physics. Nevertheless, simulations are an invaluable tool for interpreting the observational data in hand, allowing us to extrapolate our relatively local measurements of the Galaxy to its properties at earlier times or on more global scales (e.g., Loebman, 2013). Varying the model ingredients allows one to explore the evolutionary histories that can lead to a configuration that matches the true geometrical, dynamical, and chemical structure of stars from direct observations, while also exploring the roles that particular physical mechanisms play in shaping galactic properties (e.g., Martig et al., 2014; Taylor et al., 2015a).

1.4 THE GALACTIC-EXTRAGALACTIC DICHOTOMY

To be able to fairly extend what we have learned from studies of the Milky Way to extragalactic objects, we must first understand how our Galaxy fits in amongst the population of external galaxies. This has been a challenging task historically, and ironically this is fundamentally due, again, to our inside-out view of the Milky Way, which prohibits us from measuring it using the same methodologies as those that are viable for extragalactic objects. First, from our internal vantage point, starlight from the Milky Way is spread over the full 4π steradians of the night sky, making it practically impossible to measure as one integrated source. Second, and perhaps more troublesome, dust is ubiquitous in the Galactic disk (Cardelli et al., 1989; Schlegel et al., 1998), which is increasingly efficient at both absorbing and scattering light as a decreasing function of wavelength. As a result, the vast majority of the Milky Way's stars are either obscured from our view or appear dimmer and redder than they would otherwise. This makes it all but impossible to determine many of our Galaxy's basic global properties from direct measurement, such as its integrated luminosity and color. These, on the other hand, are some of the easiest measurements we can make for any other galaxy of known z , and hence play a fundamental role in their classification. As a result the Milky Way has remained poorly constrained in many of the standard diagrams that are used for studying galaxy evolution.

One important example, which will be the focus of Chapter 3, is that the present uncertainties in the global color of our Galaxy make it practically impossible to determine whether the Milky Way lies amongst the blue cloud, the red sequence, or anywhere between in the CMD; such a determination is critical for understanding how typical the star formation history of the Milky Way is compared to those of other spiral galaxies. The major challenge here is that we are inevitably constrained to measuring starlight in the local disk, nearby to the Sun, characterizing just a tiny fraction of the Milky Way's overall stellar population. To extrapolate such measurements to an estimate of the global color of the Galaxy, one must construct a model of its stellar structure and populations, requiring a long list of assumptions that each introduce compounding sources of uncertainty. On the other hand, with current instruments and our external vantage point, it is rather straightforward to measure

integrated colors for extragalactic objects to high accuracy. The same contrasts apply for measuring the integrated luminosity, particularly using optical filter passbands, of the Milky Way versus external galaxies.

Another important example, which will be the focus of Chapter 5, is that systematic differences in Galactic versus extragalactic measurements make it difficult to assess how the Milky Way compares to the Tully-Fisher relation and other scaling relations which include galaxy size. Our inside-out perspective of the Milky Way forces us to measure its global properties, such as its integrated luminosity, maximum rotation speed, and physical size, using methodologies that are infeasible for studying any other galaxy. Generically, determinations of such Galactic properties come from observing samples of resolved stars or gas in the local disk — a tiny fraction of its overall stellar or gaseous content — and extrapolating their properties to an estimate for the entire disk using Milky Way models (de Vaucouleurs & Pence, 1978; Bahcall & Soneira, 1980, 1984; Bahcall, 1986); this sometimes relies on obtaining 3-dimensional position and velocity information for each star in the sample (e.g., McMillan, 2011). Resolved stellar or gas measurements are unobtainable for essentially all other galaxies; instead, we must measure their integrated light either photometrically or spectroscopically to determine their properties. Hence, measurements of Galactic and extragalactic property each come with their own sets of model choices and assumptions that can lead to calibration issues.

Bridging the gap between Galactic and extragalactic science is paramount to understanding how galaxies form and evolve over cosmic time. Our ability to study the Milky Way in high resolution and interpret our observations through detailed modeling is a major advantage in decoding the distinct physical processes that govern galactic properties, and hence the origin of scaling relations. This is especially true with large-scale Galactic surveys that have recently or will soon see first light at both optical and infrared wavelengths, and will lead to drastically improved studies of our Galaxy. However, to broaden these results into statements about galaxies in general we must determine how representative our Galaxy is of extragalactic objects; this can be achieved by sharpening our picture of how the Milky Way fits amongst the galaxy population in key diagrams, such as the CMD or Tully-Fisher relation. Simultaneously, this additionally will provide us a better understanding of what

formation histories could give rise to the Milky Way we observe today.

1.5 DISSERTATION OVERVIEW

This dissertation is focused on employing advanced statistical techniques to overcome many of the challenges and systematic uncertainties that limit our understanding of Milky Way properties as well as our ability to relate our Galaxy to extragalactic contexts. A short synopsis of each chapter is as follows.

In Chapter 2 I present a novel method for determining improved constraints on Milky Way properties. This relies on the power of a hierarchical Bayesian (HB) statistical method which allows me to perform a meta-analysis of previous measurements in the literature, and hence combine the observational data that they individually contain, but also account for the possibility that any value may be incorrect or have underestimated errors. I apply this machinery to produce new estimates for several mass properties of the Milky Way, including the current star formation rate (SFR), the stellar mass contained in its disk and bulge+bar components, as well as its total stellar mass. I show that this method is robust to a wide variety of assumptions about the nature of problems in individual measurements or error estimates. I also demonstrate how Monte Carlo techniques can be applied to produce model-consistent realizations of the bulge and disk components of the Galaxy, as well as to force these estimates to reflect our current knowledge (most importantly, the uncertainties) in the parameters describing the structure of the disk.

In Chapter 3 I demonstrate a new statistical method of determining the global photometric properties of the Milky Way to an unprecedented degree of accuracy, allowing our Galaxy to be compared directly to objects measured in extragalactic surveys. Capitalizing on the high-quality imaging and spectroscopy dataset from the Sloan Digital Sky Survey (SDSS), I exploit the inherent dependence of galaxies' luminosities and colors on their total stellar mass, M_* , and star formation rate, \dot{M}_* , by selecting a sample of *Milky Way analog galaxies* designed to reproduce the best Galactic M_* and \dot{M}_* measurements, including all measurement uncertainties. Making the Copernican assumption that the Milky Way is not

extraordinary amongst galaxies of similar stellar mass and star formation rate, I then analyze the photometric properties of this matched sample, constraining the characteristics of our Galaxy without suffering interference from interstellar dust. I explore a variety of potential systematic errors that could affect this method, and find that they are subdominant to random uncertainties. In this chapter I present absolute magnitudes, color indexes, and mass-to-light ratios for the Milky Way in both SDSS *ugriz* and Johnson-Cousins *UBVRI* passbands and in both $z=0$ and $z=0.1$ rest frames; these are in agreement with previous estimates but can have up to $\sim 3\times$ lower errors. This demonstrates that our Galaxy may belong to the green-valley region in color-magnitude space and ranks it amongst the brightest and reddest of spiral galaxies.

In Chapter 4 I focus on the exponential scale length (L_d) of the Milky Way's (MW's) disk. This is a critical parameter for describing the global physical size of our Galaxy, important both for interpreting other Galactic measurements and helping us to understand how our Galaxy fits into extragalactic contexts, as we will see in Chapter 5. Dozens of attempts have been made to determine L_d over the past few decades, making it one of the most studied characteristics of our Galaxy. Discouragingly, current estimates span a wide range of values ($\sim 1\text{--}6$ kpc) and often are statistically incompatible with one another — a strong indication that some must be contaminated by systematic or underestimated errors. Here, I set out to determine an improved, consensus estimate for L_d by again utilizing the hierarchical Bayesian (HB) meta-analysis technique that is laid out in Chapter 2. Within this machinery I explore a variety of ways of modeling the nature of problematic measurements, and then use a Bayesian model averaging technique to derive net posterior distributions that account for the probability of each model being correct. This meta-analysis combines 29 different (15 visible and 14 infrared) photometric measurements of L_d available in the literature; these correspond to a vast assortment of observational datasets, MW models and assumptions, and methodologies, all of which are tabulated herein. I analyze various subsets of this data in order to determine a photometric estimate using either visible or IR starlight, or combining both. I show that these results are highly consistent with the available dynamical estimates, and that the ratio between the visible and infrared scale lengths determined here is very similar to that measured in external spiral galaxies. Finally, within this chapter I

develop an updated model of the Galactic disk using the photometric scale length determined here in order to update the mass property estimates from Chapter 2 and subsequently the photometric properties from Chapter 3.

In Chapter 5, with all of the Milky Way properties determined in the previous chapters finally in hand, I investigate how the Milky Way compares to a variety of scaling relations for other spiral galaxies. To generalize what has been learned about galaxy formation and evolution from studies of the Milky Way (MW), we must understand how it compares to other galaxies. A key example is the Tully-Fisher relation (TFR), the tight relationship observed between a spiral galaxy’s luminosity (L) and its rotational velocity (V_{rot}), which links the properties of dark matter halos to those of the luminous matter that they host. Using our new estimates of MW properties, which are robust to many of the systematic uncertainties that have been a problem in the past, we find that our Galaxy’s properties are in excellent agreement with the TFR, in contrast to previous studies that found 1–1.5 σ tension. I provide an in-depth look at how previous comparisons of the Milky Way with the TFR were impacted by systematic errors. I next extend this investigation to 3-dimensional scaling relations that include galaxy size in the form of the disk scale length. I conclude that the MW must be extraordinarily compact compared to other spiral galaxies of similar L and V_{rot} . I elaborate on this with an extensive discussion on the fidelity of this result, and discuss how similar peculiarities have been found by comparing the Milky Way satellite properties to predictions from Λ CDM cosmological simulations.

Lastly, in Chapter 6, I summarize the many insights that this dissertation has yielded about our home Galaxy. I describe for the reader the more comprehensive picture of the Milky Way that has been developed — one that is not simply the prototypical blue, star-forming spiral system that people believed just a decade or two ago. This is illuminated by examining the various ways that the Milky Way falls into the galaxy population in varying contexts. I conclude by discussing ways that this work can be expanded upon in the future, especially through the further study of Milky Way analog galaxies.

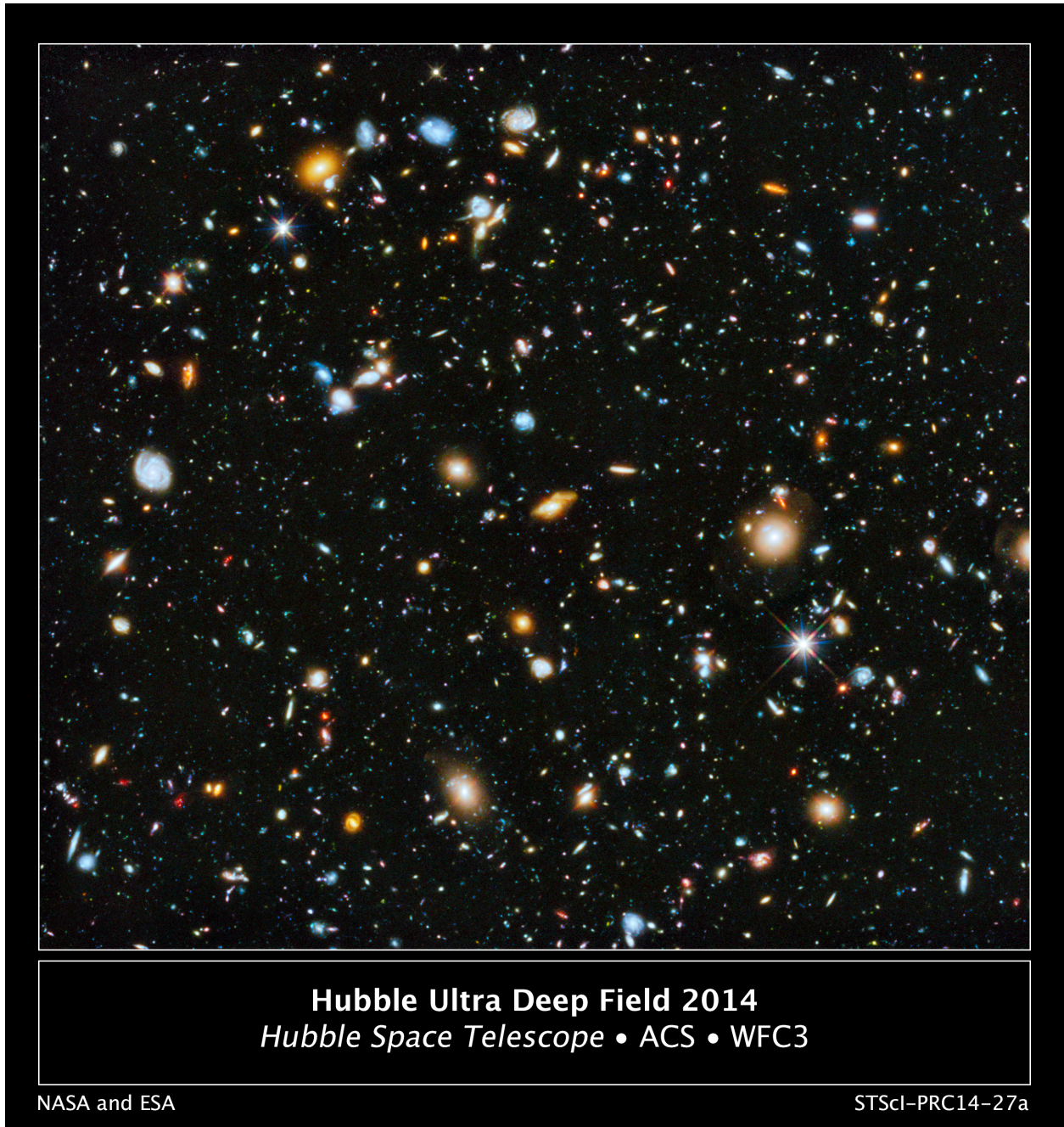


Figure 1.1: The Hubble Ultra-Deep Field image. (Credit: NASA; ESA; G. Illingworth, D. Magee, and P. Oesch, University of California, Santa Cruz; R. Bouwens, Leiden University; and the HUDF09 Team.)

2.0 IMPROVED ESTIMATES OF THE MILKY WAY'S STELLAR MASS AND STAR FORMATION RATE FROM HIERARCHICAL BAYESIAN META-ANALYSIS

2.1 INTRODUCTION

Determining the global properties of the Milky Way inherently poses unique challenges. Unlike any other galaxy in the universe, we lack the ability to study the Milky Way from an outside perspective. This disadvantage is greatly amplified by our location within the disk, forcing us to peer through the dusty interstellar medium (ISM) when looking toward other stars. The Galactic ISM inhibits our view of more distant regions of the disk, particularly in the optical and near-UV wavelengths (cf. [Herschel, 1785](#); [Schlegel et al., 1998](#)). For these reasons, there are a limited number of studies in the literature that aim to produce a global picture of our Galaxy.

Here, we aim to improve our understanding both of the total star formation rate (SFR) and the total stellar mass of the Milky Way. We do this, *not* by analyzing any new observational data, but by statistically combining the prior measurements of these properties in the literature using the power of a hierarchical Bayesian (HB) method ([Press, 1997](#)). Such methods are not new to astronomy, though still rare in the literature; they can be a robust and versatile tool for both data and model analysis, and subsequently their prevalence in the literature has grown greatly in the past few decades ([Loredo, 2012a](#)). For instance, [Newman et al. \(1999\)](#) applied this technique (in a maximum likelihood framework) to combine the observed properties of 43 ± 7 real and similar number of imposter Cepheid variables found in the Centaurus cluster, handling the possibility of false positive detections, in order to determine a period-luminosity-relation based distance modulus to NGC 4603. [Lang & Hogg](#)

(2012) were able to produce tight constraints on the orbit of Comet 17P/Holmes by applying this method to the diverse set of image query results for “Comet Holmes” obtained from the *Yahoo!* internet search engine. March et al. (2014) present an HB model to improve constraints on cosmological parameters by combining information from supernovae (SN) Ia lightcurves. Shetty et al. (2013, 2014) use the HB method to reveal the Kennicutt-Schmidt relation, i.e., the relationship between star formation rate, \dot{M}_* , and molecular gas surface density, Σ_{mol} , to be non-universal and in many cases sub-linear, indicating that Σ_{mol} alone is insufficient to predict a galaxy’s SFR. Most recently, Mandel et al. (2014) applied this method in order to disentangle the effect of systematic reddening due to host galaxy dust from the expansion-velocity-dependent variation in intrinsic SN Ia colors.

Adopting a Bayesian perspective, our major goal in this chapter is to answer the question: Given the previous measurements of a given parameter of the Milky Way, what conclusions can we draw about its true value? We first apply this analysis method to estimate the Milky Way’s SFR. We next consider the bulge and overall mass of the Milky Way. This introduces additional complications due to variations in the Galactocentric radius of the Sun, R_0 , assumed in different measurements. To deal with this, we combine our HB analysis with Monte Carlo (MC) simulations which incorporate the current uncertainties in R_0 . The MC method allows us to simultaneously produce new estimates for the stellar mass contained in the bulge+bar, M_*^{B} , the stellar disk mass, M_*^{D} , and the total stellar mass, M_* , of the Milky Way, assuming the single-exponential disk model from Bovy & Rix (2013) and incorporating uncertainties in R_0 , the exponential scale length of the disk, L_d , and the local surface density of stellar material, $\Sigma_*(R_0)$.

We structure this chapter as follows. In §2.2 we describe the hierarchical Bayesian formalism we use in order to construct aggregate results incorporating the information from a variety of independent measurements. In §2.3 we apply this technique to the prior estimates of the Milky Way’s star formation rate. The results of the SFR analysis are discussed in §2.3.3. Next, we take on a more complex example, ultimately constraining the total stellar mass in the Milky Way. §2.4.1 details the stellar disk model we assume for this study. In §2.4.2, we explain how we use Monte Carlo simulations to produce a new estimate of the disk mass, to supplement the HB analysis used to determine the bulge+bar mass, and we

combine these two results to yield the total stellar mass in the Galaxy. The results for these three measurements are discussed in §2.4.5. We summarize and discuss the main results of this study in §2.5. Lastly, in Appendix A we explore how plausible it is that Galactic disk deviates from a pure exponential profile, and investigate how this would affect our results.

2.2 HIERARCHICAL BAYESIAN ANALYSIS

In this section, we describe the analysis methods we use to combine a set of measurements for some observable (e.g., \dot{M}_\star or M_\star^B), along with their attendant uncertainties, into one aggregate result using a hierarchical Bayesian (HB) formalism. Ultimately, this process provides a new probability distribution function (PDF), referred to in Bayesian terms as the *posterior*, for the observable of interest by combining the PDFs yielded from multiple individual estimates, enabling us to incorporate the information gained from a variety of independent observations and analyses. This method allows us to account for the possibility that any of the measurements may be incorrect, or affected by systematic errors that have been overlooked. This is a key advantage over calculating simpler statistics, such as the standard inverse-variance weighted mean, which are more easily skewed by outliers and are also contingent on the assumptions that the individual PDFs are Gaussian in form and statistically compatible.

2.2.1 Defining the Problem

We begin by collecting a set of N independent measurements of observable \mathcal{O} from the literature, and denote this dataset as \mathcal{D} . In a Bayesian framework, each study can be considered to provide a PDF for the true value of \mathcal{O} , μ_0 , given the data obtained; if the probability distribution is Gaussian in form, it can be described by its mean value μ_i and standard deviation σ_i . Under the assumption of normality, we know there should be a $\sim 68\%$ chance of μ_0 being in the range $\mu_i \pm \sigma_i$ and $\sim 95\%$ chance of it being within $\mu_i \pm 2\sigma_i$, assuming all errors (statistical and systematic) are accounted for in σ_i . Of course, this is not always a

safe assumption; often we may find that two separate measurements of \mathcal{O} are in tension with each other, producing results with 1σ or even 2σ confidence regions that do not overlap. If this tension is sufficiently great, we can conclude that *at least* one of the estimates of μ_0 must be affected by a bias or systematic error that has not been incorporated in σ_i ; this is not sufficient to determine which of the two estimates is problematic.

2.2.2 Relieving the Tension

Practically speaking, the measurements included in our dataset, given their nominal errors, must always be in tension with each other at some level of significance. In order to resolve this tension we can hypothesize that some of these studies have overestimated their ability to measure \mathcal{O} . Suppose that f_{good} denotes the fraction of “good” measurements; i.e., the probability that any single measurement within \mathcal{D} is accurately described by μ_i and σ_i . Thus, $1 - f_{\text{good}}$ is the global fraction of measurements that are “bad” – i.e., inaccurate – generally due to underestimated error bars (e.g., ones that omit the possibility of significant systematic errors). With no *a priori* knowledge of which estimates are not “good”, we must find a way to remedy their effect when obtaining combined constraints on μ_0 . In this study we explore a number of ways to do this. For instance, perhaps the “bad” estimates simply require their error bars to be scaled by a constant factor; we will denote the resulting degraded uncertainty estimate by $\sigma_{n,i} = n\sigma_i$. We refer to this as the “free- n ” model below.

More likely, problematic measurements may have overlooked systematic uncertainties in their methods which should be added in quadrature to the nominal error estimates. Let μ_i^{MED} denote the median of all the μ_i values. We investigate what happens when adding a fractional amount Q of μ_i^{MED} in quadrature to the nominal error bars, such that the error for a “bad” estimate is given by $\sigma_{Q,i}^2 = \sigma_i^2 + (Q\mu_i^{\text{MED}})^2$. We use $Q\mu_i^{\text{MED}}$ here, instead of $Q\mu_i$, to avoid a slight bias toward assigning lower errors to lower valued estimates of μ_0 . We refer to this as the “free- Q ” model below. Instead, we could consider a case where there is a floor value of fractional error which the the nominal error bars should not dip below. In such a case we would use $\sigma_{F,i} = F\mu_i^{\text{MED}}$ if $\sigma_i < F\mu_i^{\text{MED}}$, or otherwise $\sigma_{F,i} = \sigma_i$. We refer to this as the “free- F ” model below.

Furthermore, it is possible that some of the included estimates are entirely wrong, and thus should effectively be excluded from \mathcal{D} . In this scenario we would handle this by replacing the nominal Gaussian PDF with μ_i and σ_i by a uniform probability distribution over the full potential parameter range. We label this as the “ P_{bad} -flat” model below. We also examine the results of assuming we have included no “bad” measurements in our analysis by forcing $f_{\text{good}} = 1$ instead of allowing it as a free parameter (i.e., to assume that all of the μ_i and σ_i are correct). All of these ways of dealing with the inclusion of “bad” measurements in our dataset have different advantages and address the problem from a slightly different approach. A hierarchical model allows us to quantify the affect of the “bad” measurements on the combined results by simultaneously fitting parameters that describe the data (e.g., f_{good} , n , Q , F), while also fitting for those that describe the physical model (e.g., μ_0). It is important to note that, in all cases, the constraints on the physical parameter of interest yielded by this technique will only be improved if the systematics affecting the individual measurements are different, as systematic errors that are common across a set of measurements do not improve by adding more data. In the following section, we describe the HB formalism we use to analyze each scenario and the criteria we use to distinguish which of these models best fits the data.

We note that while we have labeled our technique as “hierarchical,” this should not be confused with methods that recently have been labeled as “Bayesian hierarchical modeling” or “Hierarchical Bayes” (e.g., [Loredo, 2012b](#); [Gelman et al., 2013](#); [Martinez, 2015](#)), which are defined by having several layers of parameters, typically such that priors on model parameters are themselves dependent on additional free parameters (i.e., hyperparameters), and hence require their own priors (i.e., hyperpriors). Here, we use the terminology “hierarchical” in the sense that our method relies on fitting for free parameters that characterize only a subset of the data that we analyze simultaneous to the physical parameter of interest (e.g., L_d). One could alternatively refer to our method as a “Bayesian mixture model” approach to meta-analysis ([Hogg et al., 2010](#)).

2.2.3 The Formalism

We closely follow the prescription laid forth by Press (1997) and refer the reader to this work for a more in-depth derivation. Bayes' theorem provides the framework in which we can calculate the probability of a particular model given data \mathcal{D} :

$$P(\Theta | \mathcal{D}) = \frac{P(\mathcal{D} | \Theta)P(\Theta)}{P(\mathcal{D})}, \quad (2.1)$$

where Θ is a vector containing the free parameters of the model. Here, the *posterior* probability $P(\Theta | \mathcal{D})$ is equal to the product of the *likelihood* $P(\mathcal{D} | \Theta)$ and the *prior* $P(\Theta)$, divided by the *evidence* $P(\mathcal{D})$. The likelihood is the probability of obtaining the actual measurements \mathcal{D} , given that the parameters Θ specify the correct model of the data. The prior reflects our previous knowledge of what the parameters of the true model are, before the data \mathcal{D} are considered. In general, this must be subjectively chosen. The evidence represents the overall probability of finding the data in hand, and when considered on its own it provides a useful means of comparing different models, as we will discuss in §2.2.3.4. This is obtained by integrating the likelihood weighted by the prior (i.e., the numerator of Equation (2.1)) over all possible values of Θ ; hence it is also sometimes called the *marginal likelihood*. As written here, the posterior yields a properly normalized PDF representing the degree of belief of the model parameters Θ being in a given range.

2.2.3.1 The Likelihood We begin with the assumption that all measurements may be represented by the combination of two probability distributions, representing the possibility that it is “good” or “bad”. The PDF for μ_0 given a measurement will be $P(\mu_0) = P(\mu_0 | \text{“good”})P(\text{“good”}) + P(\mu_0 | \text{“bad”})(1 - P(\text{“good”}))$; the probability that a given measurement is “good” is simply f_{good} . We assume that each measurement in \mathcal{D} is statistically independent from all the others; in that case we may write the overall likelihood for \mathcal{D} as the product of the likelihoods for each measurement we include. For each of the scenarios described above in §2.2.2, the appropriate likelihood is given by:

For the free- n model (i.e., where “bad” measurements are assumed to be underestimating errors by a constant factor), the likelihood is

$$P(\mathcal{D} \mid \mu_0, f_{\text{good}}, n) = \prod_{i=1}^N \left(\frac{f_{\text{good}}}{\sqrt{2\pi\sigma_i^2}} \exp \left[\frac{-(\mu_i - \mu_0)^2}{2\sigma_i^2} \right] + \frac{1 - f_{\text{good}}}{\sqrt{2\pi(n\sigma_i)^2}} \exp \left[\frac{-(\mu_i - \mu_0)^2}{2(n\sigma_i)^2} \right] \right). \quad (2.2)$$

For the free- Q model (i.e., where “bad”-measurement errors are assumed to require extra uncertainty added in quadrature), the likelihood is

$$P(\mathcal{D} \mid \mu_0, f_{\text{good}}, Q) = \prod_{i=1}^N \left(\frac{f_{\text{good}}}{\sqrt{2\pi\sigma_i^2}} \exp \left[\frac{-(\mu_i - \mu_0)^2}{2\sigma_i^2} \right] + \frac{1 - f_{\text{good}}}{\sqrt{2\pi((\sigma_i)^2 + (Q\mu_i^{\text{MED}})^2)}} \exp \left[\frac{-(\mu_i - \mu_0)^2}{2((\sigma_i)^2 + (Q\mu_i^{\text{MED}})^2)} \right] \right). \quad (2.3)$$

For the free- F model (i.e., where “bad” measurements are assumed to be underestimating errors only if they are below a minimum threshold), the likelihood is

$$P(\mathcal{D} \mid \mu_0, f_{\text{good}}, F) = \prod_{i=1}^N \begin{cases} \frac{f_{\text{good}}}{\sqrt{2\pi\sigma_i^2}} \exp \left[\frac{-(\mu_i - \mu_0)^2}{2\sigma_i^2} \right] + \frac{1 - f_{\text{good}}}{\sqrt{2\pi(F\mu_i^{\text{MED}})^2}} \exp \left[\frac{-(\mu_i - \mu_0)^2}{2(F\mu_i^{\text{MED}})^2} \right], & \text{if } \sigma_i < F\mu_i^{\text{MED}} \\ \frac{1}{\sqrt{2\pi\sigma_i^2}} \exp \left[\frac{-(\mu_i - \mu_0)^2}{2\sigma_i^2} \right], & \text{otherwise.} \end{cases} \quad (2.4)$$

In this model, f_{good} is the fraction of “good” measurements assuming the given value of F ; i.e., it is the fraction of accurate measurements amongst those with $\sigma_i < F\mu_i^{\text{MED}}$. This is subtly different from the former two models, where f_{good} characterizes the entire dataset at any given value of n or Q .

For each of the above 3 models, we also explore the results of assuming that *all* measurements included in \mathcal{D} have misestimated errors to some extent by *not* treating f_{good} as a free parameter, but rather setting it to zero.

For the P_{bad} -flat model (i.e., where “bad” measurements are assumed to be entirely wrong and discardable, and so we replace their PDFs with a flat distribution), the likelihood is

$$P(\mathcal{D} \mid \mu_0, f_{\text{good}}) = \prod_{i=1}^N \left(\frac{f_{\text{good}}}{\sqrt{2\pi\sigma_i^2}} \exp \left[\frac{-(\mu_i - \mu_0)^2}{2\sigma_i^2} \right] + (1 - f_{\text{good}}) \times \text{const.} \right). \quad (2.5)$$

The constant here is chosen such that the integral of $P(\mu_0 \mid \text{“bad”})$ is equal to 1.

Lastly, there is the possibility that all of the measurements included in our analysis are “good” and have accounted for all uncertainties in their analyses. We can determine μ_0 for this scenario by setting f_{good} to unity; in this case, the results of the HB analysis method become equivalent to the inverse-variance weighted mean of the individual measurements. Effectively, this model serves as the null hypothesis of our study, and we denote this as the all-“good” model when comparing our results.

In total, this yields 8 different ways of modeling “bad” measurements that could influence our aggregate estimate of μ_0 . In §2.2.3.4 we will describe which of these options is best to follow.

2.2.3.2 The Prior If we assume that our prior knowledge of the parameters of our model are unrelated to each other, the overall prior for Θ is separable into the product of the priors for each parameter. For example, in the context of this study, we would not expect that the probability of an astronomer quoting accurate error bars on his/her result should be different if the Milky Way is truly producing 3 solar masses worth of new stars each year as opposed to 2. This means we can write the joint prior $P(\mu_0, f_{\text{good}})$ as $P(\mu_0)P(f_{\text{good}} \mid \mu_0) = P(\mu_0)P(f_{\text{good}})$. Likewise, in the absence of data, we would not expect a parameter that describes how inaccurate a study’s error bars are to be dependent on the probability of any one measurement being “bad” or the mass of new stars being formed in the Galaxy per year.

For all 4 free parameters we use to characterize “good” and “bad” estimates we choose flat priors, meaning that we believe there is a 100% chance of the true value being within a given range, and any single value within that range has equal probability to any other. We note that these assumptions are somewhat arbitrary; for instance, a flat prior in a given quantity corresponds to a non-flat prior for the log of that quantity. Flat priors in log space are generally preferred for quantities with no relevant scales/order of magnitude; however, that does not apply here. Effectively, our choice causes all posterior distributions we calculate to be determined only by the likelihood of the observed data. For the free- n model we assume 100% probability that n is in the range [1,4]; i.e., that the errors for “bad” measurements

will be underestimated by a factor no less than 1 and no greater than 4. In turn, for the free- Q model we assume 100% probability that Q is in the range $[0,1]$; i.e., the extra error needed to be added in quadrature to correct the nominal error bars of a “bad” measurement is no less than 0 and no more than 100% of μ_i^{MED} . Lastly, for the free- F model we assume 100% probability that F is in the range $[\sigma_i^{\text{MIN}}/\mu_i^{\text{MED}},1]$, where σ_i^{MIN} is the minimum error estimate of all measurements included in \mathcal{D} ; i.e., the minimum error estimate for any “bad” measurement should be no less than σ_i^{MIN} and no larger than μ_i^{MED} . The priors can then be expressed as piece-wise functions,

$$P(f_{\text{good}}) = \begin{cases} 1, & \text{if } 0 \leq f_{\text{good}} \leq 1 \\ 0, & \text{otherwise;} \end{cases} \quad (2.6)$$

$$P(n) = \begin{cases} \frac{1}{3}, & \text{if } 1 \leq n \leq 4 \\ 0, & \text{otherwise;} \end{cases} \quad (2.7)$$

$$P(Q) = \begin{cases} 1, & \text{if } 0 \leq Q \leq 1 \\ 0, & \text{otherwise;} \end{cases} \quad (2.8)$$

$$P(F) = \begin{cases} \frac{1}{1-\sigma_i^{\text{MIN}}/\mu_i^{\text{MED}}}, & \text{if } \sigma_i^{\text{MIN}}/\mu_i^{\text{MED}} \leq F \leq 1 \\ 0, & \text{otherwise.} \end{cases} \quad (2.9)$$

2.2.3.3 The Marginalized Posterior In this subsection, we detail how the posterior PDF for a single parameter of our model is produced from the joint posterior from the HB analysis, using the free- n model as an example. Returning to Equation (2.1), the posterior PDF for the parameters of our model will be

$$P(\mu_0, f_{\text{good}}, n \mid \mathcal{D}) \propto P(\mu_0)P(f_{\text{good}})P(n) \prod_{i=1}^N \left(\frac{f_{\text{good}}}{\sqrt{2\pi\sigma_i^2}} \exp \left[\frac{-(\mu_i - \mu_0)^2}{2\sigma_i^2} \right] + \frac{1 - f_{\text{good}}}{\sqrt{2\pi(n\sigma_i)^2}} \exp \left[\frac{-(\mu_i - \mu_0)^2}{2(n\sigma_i)^2} \right] \right). \quad (2.10)$$

It is often more informative to consider the posterior for an individual parameter; we can simply obtain this by *marginalizing*: i.e., integrating the PDF over all other parameters of the model. For instance, in our example, if we are interested in the marginalized posterior for μ_0 , then we calculate

$$P(\mu_0 | \mathcal{D}) = \int \int P(\mu_0, f_{\text{good}}, n | \mathcal{D}) df_{\text{good}} dn. \quad (2.11)$$

Note that this result averages over all possible values of f_{good} and n . Lastly, we normalize the posterior to be a true PDF by dividing by the evidence, which is obtained by integrating Equation (2.11) over all μ_0 .

2.2.3.4 Choosing Amongst Models In this study, we consider a variety of ways to model the inclusion of “bad” measurements in our dataset. Generally speaking, a model with more free parameters will be able to produce a better fit to the data; however, the constraints on the model will be weaker, as there are more degeneracies introduced between parameters. In order to compare the utility of the models to each other, we calculate the *evidence* for each model. If \mathcal{M}_k labels a particular model which is specified by parameters Θ , then the evidence for model \mathcal{M}_k is

$$P(\mathcal{D} | \mathcal{M}_k) = \int P(\mathcal{D}, \Theta | \mathcal{M}_k) d\Theta = \int P(\mathcal{D} | \Theta)P(\Theta | \mathcal{M}_k) d\Theta; \quad (2.12)$$

this is simply the likelihood integrated over all possible parameter values of the model, weighted by their priors. This provides a natural, Bayesian method of incorporating the principle of Ockham’s razor into our model comparison. Essentially, the evidence will be maximized by a model’s ability to better fit the data; however, this will be compromised if excessive parameter space is required to achieve such a fit. As the all-“good” model represents the null hypothesis for our HB analysis, for each model we report the *Bayes Factor* defined as

$$\mathcal{B}_k = \frac{P(\mathcal{D} | \mathcal{M}_k)}{P(\mathcal{D} | M_{\text{all-“good”}})}. \quad (2.13)$$

Effectively, \mathcal{B}_k represents the ratio of the posterior odds to the prior odds of \mathcal{M}_k the being the correct model over $M_{\text{all-“good”}}$ (Kass & Raftery, 1995, and references therein). As defined this way, we choose the best model of the data to be the one with largest \mathcal{B}_k . In our tables

we list for each model the difference in $\log_{10} \mathcal{B}_k$ compared to our fiducial model; a difference of 2 is commonly used to indicate statistically significant differences in model utility.

As alternatives to the Bayes Factor, we also report the Akaike information criterion (Akaike, 1974, hereafter AIC), defined as

$$\text{AIC} = -2 \ln \mathcal{L} + 2k, \quad (2.14)$$

and the Bayesian information criterion (Schwarz, 1978, hereafter BIC), defined as

$$\text{BIC} = -2 \ln \mathcal{L} + k \ln N, \quad (2.15)$$

where N is the number independent measurements included in our analysis, k is the number of free parameters of the model, and \mathcal{L} is the maximum likelihood value. These provide a secondary and less sophisticated way of weighing the goodness of fit against the number of free parameters included in each model, and whose comparison can serve as a rough (and less computationally intensive) approximation to comparing $\log_{10} \mathcal{B}_k$ values. However, in contrast to the \mathcal{B}_k values, the best model of the data would be the one that *minimizes* the information criteria. Thus, for each model we report ΔAIC (or ΔBIC) measured from the *lowest* AIC (or BIC) value amongst all models; similar to the $\Delta \log_{10} \mathcal{B}_k$ values, a change of ~ 2 is indicative of statistically significant differences in model utility (Burnham & Anderson, 2002). Note that, as AIC and BIC values are calculated on a natural logarithm scale, this constraint is a bit less conservative than the one used for $\Delta \log_{10} \mathcal{B}_k$ values (i.e., bigger differences in $\Delta \ln \mathcal{B}_k$ are required to indicate a significant difference).

The remainder of this chapter focuses on two application of the HB method. First, we use this technique to constrain the star formation rate of the Milky Way. In our second and more complex example, we produce an hierarchical estimate of the stellar mass contained in the combined bulge & bar components of the Milky Way, where we must incorporate Monte Carlo simulations into our technique to reflect uncertainties in the Sun’s Galactocentric radius. Simultaneously, we produce PDFs for the stellar mass of the disk component of the Galaxy, as well as its total stellar mass. As mentioned earlier, we are effectively assuming that if there are systematic errors in measurements of the Milky Way properties, they will generally not be in common amongst all the techniques, but rather, given the multitude of

methods applied, many methods should have different systematics (of differing signs). If that is not the case, errors will not be reduced when combining information from multiple results.

2.3 THE MILKY WAY’S STAR FORMATION RATE

2.3.1 The SFR Data

Recent work by [Chomiuk & Povich \(2011\)](#) provides a thorough review and renormalization of Galactic star formation rate (SFR), \dot{M}_* , estimates made in the last three decades. Examining these original works reveals a discouraging scatter in the derived results, spanning the range of 1 to 10 $M_\odot \text{ yr}^{-1}$. This proves to be predominantly due to a heterogeneous mixture of initial mass functions (IMFs) and stellar population synthesis (SPS) models used. The authors translate these results all to a uniform choice of the Kroupa broken-power-law IMF ([Kroupa & Weidner, 2003](#)) as well as the Starburst99 v5.1 SPS model ([Vázquez & Leitherer, 2005](#)). As a result, these studies, which encompass many different methods and observational surveys, all collectively are in general agreement with each other after being placed on an equal footing, converging to a SFR of $\dot{M}_* = 1.9 \pm 0.4 M_\odot \text{ yr}^{-1}$. We refer the reader to Table 1 of [Chomiuk & Povich \(2011\)](#) for the data we use to estimate the Milky Way SFR, as well as to their §3 for a detailed discussion of the measurements. We do not utilize the first two entries in that table, the measurements from Smith et al. (1978) and Güsten & Mezger (1982), as these were both updated by the Mezger (1987) radio free-free result. Additionally, the error estimate on the Misiriotis et al. (2006) dust-heating measurement has been increased to 0.95 M_\odot ; i.e., due to the lack of error estimates we assign 50% uncertainty to it. This particular dataset is denoted \mathcal{D}_{SFR} hereafter.

2.3.2 Setting a Prior on \dot{M}_*

To place a prior on its SFR, we utilize the fact that the Milky Way is confidently known to be a spiral galaxy. In addition, it appears that the Galaxy has experienced a relatively quiet

merger history, undergoing predominantly secular evolution with no significant interactions to spark a large burst of new stars (e.g., Unavane et al., 1996; Mutch et al., 2011). Therefore, we agnostically assume that the Galactic SFR could be anywhere from 0 to 6 solar masses per year (before considering the data in §2.3.1). This is represented using a uniform probability distribution, such that

$$P(\dot{M}_\star) = \begin{cases} \frac{1}{6}, & \text{if } 0 \leq \dot{M}_\star \leq 6 \text{ M}_\odot \text{yr}^{-1} \\ 0, & \text{otherwise.} \end{cases} \quad (2.16)$$

2.3.3 SFR Results

Table 2.1 shows the hierarchical Bayesian constraints on \dot{M}_\star from each model that we consider. The overwhelming similarity between the posterior results from these different models to a simple weighted average (corresponding to the last line in the table) suggests that nominal errors on each measurement in the SFR dataset are likely very accurate, if not overestimated. In Figure 2.1, we show the joint posterior PDF for f_{good} and n (normalized to a peak value of 1); the posterior obtained by marginalizing over \dot{M}_\star is maximized where f_{good} and n each approach unity. Figure 2.2 shows the marginalized posterior probability for f_{good} for each model which allows it to be a free parameter. It is clear from the plot that modifying the error bars of "bad" measurements in any way yields little preference for a particular value of f_{good} , whereas throwing out "bad" estimates favors values near one. This occurs because for values of n near 1 (or Q or F near 0), f_{good} has very little effect, so a broad range of f_{good} values yield similar results.

Similar analyses to that in Fig. 2.1 for each of the models of "bad" measurements yields the same overall message: the measurements are sufficiently consistent with each other that little, if any, adjustment of the nominal errors is demanded. In fact, we find that for any model for how to remedy "bad" estimates within the HB formalism, the data always drives towards a point in k -dimensional parameter space with few points treated as discrepant; i.e., $f_{\text{good}} \approx 1$, and $\dot{M}_\star \approx 1.66 \text{ M}_\odot \text{ yr}^{-1}$; or, alternatively, $f_{\text{good}} < 1$ but $n = 1$ or Q or $F = 0$, which has equivalent effect. The best model of the data (i.e., the one with largest Bayes Factor, \mathcal{B}_k) turns out to be where we set $f_{\text{good}} = 1$, uniformly treating every estimate as

“good” and hence requiring the fewest free parameters in the fit (only \dot{M}_\star itself). This yields an aggregate SFR for the Milky Way of $\dot{M}_\star = 1.65 \pm 0.19 M_\odot \text{ yr}^{-1}$, which we choose as our fiducial result. For comparison, we overlay the individual measurements in the SFR dataset on our fiducial hierarchical result in Figure 2.3. We note that, as we are using flat priors, this scenario gives the same result as the inverse-variance weighted mean (IVWM). The finding that the data are sufficiently compatible that a simple model is sufficient matches well with what we would conclude using the chi-squared statistic to judge goodness-of-fit. Specifically, the IVWM for our sample of SFR measurements yields $\chi^2 = 3.83$, and we would expect a 95% chance of this statistic falling in the range [2.18, 17.53].

Chomiuk & Povich present arguments suggesting that the Robitaille & Whitney (2010) measurement may more accurately be treated as a lower limit rather than a best-fit value for the SFR. Given that uncertainty, we investigate the effect of doubling the nominal errors in that measurement within our calculation. Making this change yields a $< 1\sigma$ shift in the mean of the posterior distribution. With this deweighting, the inclusion or exclusion of this measurement has little impact on our results (changing the consensus Milky Way SFR by no more than $0.17 M_\odot \text{ yr}^{-1}$). A second concern arises from that fact that equations (2.2)-(2.5) are contingent on the individual measurements being independent of one another. We note that, even though Bennett et al. (1994) and McKee & Williams (1997) utilize the same *COBE* data, the errors in their SFR estimates appear to be dominated by the differences between the assumptions made by the authors, and so we expect that we can treat them as independent measurements. We show how our aggregate SFR estimate varies under these different treatments of the Robitaille & Whitney (2010) measurement, as well as when excluding the Bennett et al. (1994) measurement, in Table 2.2.

If all of the star formation rate estimates employed suffer from a common systematic error, this would not be reflected in the hierarchical Bayesian result. For instance, if the Kroupa IMF is unlike the actual initial mass function in the Milky Way, our SFR estimates could all be systematically off from the true value in a similar way. However, this error would cancel out when the Galaxy is compared to extragalactic objects, for which SFRs and stellar masses are generally calculated assuming Kroupa-like IMFs. Similarly, Chomiuk & Povich have recalibrated each of the Milky Way \dot{M}_\star estimates to the Kennicutt (1998a) assumption

that a SFR of $1 M_{\odot} \text{ yr}^{-1}$ produces a Lyman continuum photon rate of 9.26×10^{52} photon s^{-1} for a Salpeter IMF (this relationship is then reduced by a factor of 1.44 to convert it to the Kroupa IMF). If this assumption is in error, then all the SFRs in our dataset would be affected. However, once more, extragalactic SFRs would be off by the same factor, so that this systematic will drop out when comparing the Milky Way to other galaxies.

Apart from the IMF and the Lyman continuum rate to SFR relationship, common-mode systematics amongst all the SFR measurements appear to be unlikely. This is due to both the diversity of techniques used to estimate the Galactic star formation rate and the wide range of assumptions made by the different studies that utilize the same basic techniques. However, one might still worry that there are common underlying assumptions that may systematically offset SFR results from one method in comparison to all the others. For instance, two of the nine studies we use estimate the Galactic SFR by modeling the population of young stellar objects (YSOs) found from infrared (IR) surveys of the Galaxy. While these studies employ entirely different IR data, they are both contingent on assumptions about the properties of YSOs, which do not affect the other measurements, and in turn can systematically shift these results in unison with respect to the measurements utilizing different methods. Our HB analysis assumes that the errors from each study are random compared to each other and hence does not address this type of common-mode effect (much as the inverse-variance weighted mean would not).

To test whether method-to-method variations are significant, we have performed bootstrap resampling of the SFR data by randomly drawing only one measurement out of those utilizing each measurement technique (e.g., all those based on the measured ionization rate or YSO counts). Hence, each resampled dataset comprises four SFR estimates, each obtained from a unique measurement method, which we then use to calculate the HB posterior using the all-“good” model (allowing no extra compensation for systematic errors). We repeat this process 1,000 times, each time measuring the mean from the posterior distribution. We then do a similar analysis, but where we instead draw four measurements at random from the entire dataset each time. We find the standard deviation of the mean to be 0.22 if we use four measurements from different methods and 0.25 if we select four measurements completely at random. This indicates that inter-method variations are negligible compared

to intra-method random variations – if anything, SFR measurements from *different* methods are more similar to each other than those which utilize the *same* technique. We therefore can safely conclude that common-mode systematics do not have a large impact.

2.4 THE MASS OF THE MILKY WAY’S STELLAR COMPONENTS

In this section we describe the methods we use to produce improved estimates of the total stellar mass, M_\star , in the Milky Way and its components. To do so, we first make independent estimates of the stellar mass contained in the disk and bulge+bar components, M_\star^D and M_\star^B respectively. For M_\star^D , we assume the single-exponential model of the Galactic disk from [Bovy & Rix \(2013\)](#), and use Monte Carlo (MC) simulations to incorporate updated estimates of the Sun’s Galactocentric radius, R_0 . We constrain M_\star^B using our HB formalism, similar to the analysis done in §2.3 for \dot{M}_\star , but now using the MC simulations to propagate uncertainties in the value of R_0 into the bulge mass posterior. Lastly, we combine self-consistent realizations of M_\star^B and M_\star^D to yield a probability distribution describing the total stellar mass.

2.4.1 The Stellar Disk Model

To model the structure of the Milky Way, we assume the stellar material of the disk is distributed in a single-exponential surface density profile. Integrating this profile over all radii yields the total stellar mass,

$$M_\star^D = 2\pi\Sigma_\star(R_0)L_d^2 \exp(R_0/L_d), \quad (2.17)$$

where $\Sigma_\star(R_0)$ is the surface density of stellar mass in the local neighborhood and L_d is the exponential scale length of the disk. Specifically, we constrain these parameters to be consistent with the measurements made by [Bovy & Rix \(2013\)](#), (see Appendix A for a discussion of alternative disk models).

Using SDSS/SEGUE spectroscopic measurements, these authors have segregated a uniform sample of $\sim 16,000$ G-type dwarf stars into 43 mono-abundance populations (MAPs)

based on their position in $[\alpha/\text{Fe}]-[\text{Fe}/\text{H}]$ space. G-type dwarfs were considered to be the optimal tracers of the structure of the disk as they are most luminous stars whose main-sequence lifetimes are larger than the age of the disk at practically all metallicities. Separated in this way, the spatial distribution of each MAP is well fit by a single-exponential profile both radially from the Galactic center and perpendicularly from the plane of the disk, indicating that the disk is likely composed of a more continuous distribution of populations rather than just the classical separation into thin and thick disk components (see also [Bovy et al., 2012a](#); [Rix & Bovy, 2013](#)).

By independently fitting an action-based distribution function and Galactic potential to each MAP in position-velocity phase-space, the authors are able to measure the vertical force at $|Z| \approx 1$ kpc as a function of Galactocentric radius in the region $4 \lesssim R \lesssim 9$ kpc; this quantity is directly proportional to the surface density of stellar mass, Σ_\star . Including the contribution from all MAPs, the authors are able to make the first dynamical determination of the total stellar surface-mass density at the Galactocentric radius of the Sun, $\Sigma_\star(R_0) = 38 \pm 4 M_\odot \text{ pc}^{-2}$; this is measured directly from the mass distribution of substellar objects, main-sequence stars, and stellar remnants, as opposed to inferring it from their luminosity (cf. [Jurić et al., 2008](#)). Similarly, the mass-weighted scale length determined from all MAPs is $L_d = 2.15 \pm 0.14$ kpc.

Assuming $R_0 = 8$ kpc and accounting for the uncertainty and covariance in L_d and $\Sigma_\star(R_0)$, [Bovy & Rix \(2013\)](#) find $M_\star^D = 4.6 \pm 0.3 \times 10^{10} M_\odot$. They also find that increasing R_0 to 8.5 kpc in their model produces a $1.5 \times 10^{10} M_\odot$ increase in M_\star ; this effect approximately scales linearly for intermediate radii. The scale length and local surface density of the disk are independent of R_0 . For our purposes, it is important to include the current uncertainties in R_0 into our model of the Milky Way, and so we employ the following process for this study:

- I) We model the covariance between the local surface density and scale length in this model by calculating $\Sigma_\star(R_0)$ as a function of L_d . To do so, we first fit for a linear mapping between these two parameters based on the 2D joint-posterior PDF that describes them (provided by [Bovy, 2013](#), priv. comm.). This relation gives the appropriate value of $\Sigma_\star(R_0)$ for a given value of L_d . We then determine what uncertainty in $\Sigma_\star(R_0)$ would

yield the [Bovy & Rix \(2013\)](#) error of $0.3 \times 10^{10} M_{\odot}$ in M_{\star}^D using Equation (2.17) after this covariance and the errors in L_d are accounted for.

- II)** We assume $R_0 = 8.33 \pm 0.35$ kpc from [Gillessen et al. \(2009\)](#), which is estimated by fitting the orbital parameters of 28 stars in near-orbit of the Galaxy’s central massive black hole, building upon 16 years of observations, and taking into account both random and systematic errors. This result is in excellent agreement with other recent measurements of R_0 (e.g., [Ghez et al., 2008](#); [Vanhollebeke et al., 2009](#); [Sato et al., 2010](#); [Chatzopoulos et al., 2015](#)), with a large enough error to encompass the variation in results amongst different methods.
- III)** Given dM_{\star}^D/dR_0 from [Bovy & Rix](#), we can then predict both the mass that would have been measured by [Bovy & Rix](#) for different R_0 and the uncertainty in that estimate due to measurement errors in L_d and $\Sigma_{\star}(R_0)$ alone.

The overall goal of this study is to produce updated and accurate estimates of the total stellar mass and star formation rate of the Milky Way that may be directly compared with those properties measured for any external galaxy. In particular, we aim to be consistent with the definition of M_{\star} and \dot{M}_{\star} as measured for external galaxies in the MPA-JHU catalogs ([Brinchmann et al., 2004](#)), which assume the Kroupa IMF and that M_{\star} includes the contribution from both main-sequence stars and remnants, but not brown dwarfs (BDs), in accordance with the assumptions made for the stellar spectral evolution models of [Bruzual & Charlot \(2003\)](#). The dynamical estimate of $\Sigma_{\star}(R_0)$ from [Bovy & Rix \(2013\)](#) effectively includes BDs, so one way to get the density we want is to subtract them off.

The BD mass function (i.e., $\xi(M) \propto M^{-\alpha}$ where $0.005 < M/M_{\odot} < 0.1$) appears to have power-law index in the range $-0.5 \lesssim \alpha \lesssim 0.5$ ([Cruz et al., 2007](#); [Kirkpatrick et al., 2012](#); [Day-Jones et al., 2013](#); [Burningham et al., 2013](#)). We normalize the mass function so that the portion corresponding to L0–L3 BDs, i.e., objects with masses in the range $0.03 < M/M_{\odot} < 0.05$ (following the models of [D’Antona & Mazzitelli, 1997](#), updated 1998), integrates to a total number density of $1.7 \times 10^{-3} \text{ pc}^{-3}$ (matching [Cruz et al., 2007](#)). Accounting for the range of possible α values, we then integrate $\xi(M) \times M$ over the entire BD mass range to find a mass density of $\sim 2.5\text{--}3 \times 10^{-4} M_{\odot} \text{ pc}^{-3}$. Lastly, as required for a single-exponential disk profile, we multiply this by 2 times a scale height of the disk of $h_z = 400$ pc ([Bovy &](#)

Rix, 2013), yielding predicted BD surface densities of $\sim 5\text{--}6 M_{\odot} \text{ pc}^{-2}$. Earlier measurements, however, have yielded lower surface densities at $\sim 0.5\text{--}2 M_{\odot} \text{ pc}^{-2}$ (Fuchs et al., 1998; Flynn et al., 2006, and references therein). Based on these analyses, we conservatively assume that the local surface density of BDs is in the range $0.5 \lesssim \Sigma_{\text{BD}}(R_0) \lesssim 6 M_{\odot} \text{ pc}^{-2}$; assuming a uniform distribution over this range, we find $\Sigma_{\text{BD}}(R_0) = 3.25 \pm 1.59 M_{\odot} \text{ pc}^{-2}$. Subtracting this from Bovy & Rix’s dynamical estimate, we find $\Sigma_{\star}(R_0) = 34.75 \pm 4.30 M_{\odot} \text{ pc}^{-2}$.

Alternatively, we could compare to the stellar surface density estimate from Bovy et al. (2012a), which omits BDs but also white dwarfs (WDs) that we want to include. To remedy this, we collect a number of literature estimates of the spatial density of local white dwarfs: Oswalt et al. (1996) find 0.0076 pc^{-3} ; Leggett et al. (1998) find 0.0034 pc^{-3} ; Jahreiß & Wielen (1997) find 0.005 pc^{-3} ; Knox et al. (1999) find 0.00416 pc^{-3} ; Holberg et al. (2008) find 0.0048 pc^{-3} ; and Sion et al. (2009) find 0.0049 pc^{-3} . Using the mean and standard deviation of this sample, we assume the local volume density of WDs is $\rho_{\text{WD}} = 5.0 \pm 1.4 \times 10^{-3} \text{ pc}^{-3}$. Following our disk model, we multiply this by 2 times a scale height of $h_z = 400 \text{ pc}$ (Bovy & Rix, 2013, and ascribing 10% error) and an average WD mass of $\langle M \rangle_{\text{WD}} = 0.65 \pm 0.01 M_{\odot}$ (Falcon et al., 2010) to find the local surface density of white dwarfs $\Sigma_{\text{WD}}(R_0) = \rho_{\text{WD}} \times 2h_z \times \langle M \rangle_{\text{WD}} = 2.6 \pm 0.8 M_{\odot} \text{ pc}^{-2}$. As a consistency check, we add this to the Bovy et al. (2012a) photometric estimate of $32.0 \pm 3.2 M_{\odot} \text{ pc}^{-2}$ (due to main-sequence stars, assuming the Kroupa (2003) IMF and 10% uncertainty), yielding $\Sigma_{\star}(R_0) = 34.6 \pm 3.3 M_{\odot} \text{ pc}^{-2}$; this is in excellent agreement with the corrected dynamical estimate, which we adopt for the remainder of this study, given its more conservative error estimate. For convenience, we tabulate all parameters of our disk model, and their interdependencies, in Table 2.3. Plugging these expressions into Equation (2.17), any realization of the total stellar disk mass from our Monte Carlo simulations is a function of the Galactocentric radius of the Sun and the scale length (independently drawn from their attendant probability distributions):

$$M_{\star}^{\text{D}}(R_0, L_d) = 2\pi(31.75L_d/\text{kpc} - 33.5125 \pm 2.89)(L_d/\text{kpc})^2 \exp(8 \text{kpc}/L_d) + 3(R_0/\text{kpc} - 8) \times 10^{10} M_{\odot}. \quad (2.18)$$

2.4.2 Monte Carlo Techniques

As we shall see in §2.4.3, many estimates included in our Galactic bulge+bar mass dataset are dependent on assumptions made about the values of R_0 and/or M_\star^D , and hence depend upon all of our disk model parameters. However, as denoted in Table 2.3, the true value of these parameters are not perfectly known; we can describe our prior knowledge of each one by a probability density function. In order to propagate the uncertainties in these parameters’ values into the resulting posteriors describing the stellar mass of the disk and bulge, as well as their combination for the total stellar mass of the Galaxy, we perform a series of Monte Carlo (MC) simulations.

Unlike the parameters describing our “bad”-measurement models (Θ), we are uninterested in producing new results for our disk model parameters. We have much greater confidence in the priors we have chosen for R_0 , L_d , and $\Sigma_\star(R_0)$ based on the more direct observations described in the previous section than anything we would infer about those quantities from the set of bulge mass measurements. Therefore, in this application we want to ensure that the results of our HB formalism will reflect the information contained in the priors in Table 2.3. We will collectively denote the set of disk parameters as \mathcal{N} , as we are uninterested in allowing the M_\star^B data to modify any conclusions about what the values of those “nuisance” parameters may be. Formally, we are making the assumption that $P(\mathcal{N} | \mathcal{D}) = P(\mathcal{N})$ – i.e., that our state of knowledge of the nuisance parameters is not affected by the bulge dataset – and we refer to this as the “strict-prior” method below. In this framework, our procedure is as follows:

- I) We independently and randomly generate a sample of 10^3 values of R_0 and L_d , which collectively reproduce the respective mean and standard deviation given in Table 2.3. Then for each realization of the scale length of the disk, $L_{d,i}$, we randomly draw a corresponding value of $\Sigma_\star(R_0)_i$ based on the relationship listed in Table 2.3.
- II) For each of the 10^3 sets of randomly drawn parameters, $\mathcal{N}_i = \{R_0, L_d, \Sigma_\star(R_0)\}_i$, we calculate the corresponding disk mass, $M_{\star,i}^D$, using Equation (2.18). The result is a distribution of possible Galactic disk masses, which we normalize to produce $P(M_\star^D | \mathcal{D})$. Note that this is consistent with our strict-prior assumption that $P(\mathcal{N} | \mathcal{D}) = P(\mathcal{N})$, and

so the fraction of times that $M_{\star,i}^D$ calculated from the \mathcal{N}_i occurs in the Monte Carlo will be proportional to $P(\mathcal{N})$.

- III)** We determine the value of each literature M_{\star}^B measurement (listed in Table 2.4) that would have been obtained assuming these parameters are correct. This ensures that all measurements make consistent assumptions about the structure of the Galaxy, allowing them to be combined fairly. We refer the reader to the following section for these details.
- IV)** For each iteration of **III**, along with the prior chosen for M_{\star}^B , which we will detail in §2.4.4, we calculate the joint k -dimensional posterior $P(\Theta | \mathcal{D}, \mathcal{N}_i)$ via an HB analysis, as described in §2.2. After marginalizing out the other parameters in Θ , each realization of the bulge mass posterior can be written

$$P(M_{\star}^B | \mathcal{D}, \mathcal{N}_i) = \frac{P(\mathcal{D} | M_{\star}^B, \mathcal{N}_i)P(M_{\star}^B)}{P(\mathcal{D} | \mathcal{N}_i)}, \quad (2.19)$$

applying Bayes theorem as usual. By the definition of marginalization, $P(M_{\star}^B | \mathcal{D}) = \int P(M_{\star}^B, \mathcal{N} | \mathcal{D}) d\mathcal{N}$; and applying the definition of joint probability and our strict-prior assumption, this is equal to $\int P(M_{\star}^B | \mathcal{D}, \mathcal{N})P(\mathcal{N}) d\mathcal{N}$. If we draw values \mathcal{N}_i from our prior distribution $P(\mathcal{N})$, this integral will be equal to

$$\lim_{n \rightarrow \infty} \frac{1}{n} \sum_{i=1}^n P(M_{\star}^B | \mathcal{D}, \mathcal{N}_i), \quad (2.20)$$

since the fraction of times that \mathcal{N}_i occurs in the Monte Carlo will be proportional to $P(\mathcal{N})$. Note also that Bayes' theorem allows us to rewrite the denominator in Equation (2.19) as $P(\mathcal{D} | \mathcal{N}_i) = P(\mathcal{N}_i | \mathcal{D})P(\mathcal{D})/P(\mathcal{N}_i)$, and by applying our strict-prior assumption this reduces to simply $P(\mathcal{D})$. Thus, in order to construct the combined M_{\star}^B result for a given model of “bad” measurements, we are able to simply average the individual posteriors from the Monte Carlo realizations:

$$P(M_{\star}^B | \mathcal{D}) = \frac{1}{1000} \sum_{i=1}^{1000} \frac{P(\mathcal{D} | M_{\star}^B, \mathcal{N}_i)P(M_{\star}^B)}{P(\mathcal{D})}. \quad (2.21)$$

The posterior PDF for each of the other parameters of the “bad”-measurement model are calculated in the same way. In addition, we record the AIC, BIC, and \mathcal{B}_k for each iteration, yielding a distribution of values. In practice, we find that 10^3 realizations produces a standard error in the median $\Delta \log_{10} \mathcal{B}_k/\text{AIC}/\text{BIC}$ values much smaller than

0.5, which is sufficient to assess differences in the utility of different models securely (compared to our $\Delta = 2$ criterion for significance).

V) We also produce a posterior for the total stellar mass from each iteration, $P(M_\star | \mathcal{D}, \mathcal{N}_i)$, in a model-consistent manner by simply defining $M_{\star,i} = M_\star^B + M_{\star,i}^D$. Again, we can average the individual posteriors, $P(M_\star | \mathcal{D}, \mathcal{N}_i)$, to obtain $P(M_\star | \mathcal{D})$, similar to Equation (2.21). Lastly, we also calculate the model-consistent posterior describing the bulge-to-total mass ratio by normalizing the distribution of values $(B/T)_i = \langle P(M_\star^B | \mathcal{D}, \mathcal{N}_i) \rangle / \langle P(M_\star | \mathcal{D}, \mathcal{N}_i) \rangle$ to integrate to unity, where angled brackets denote the mean of the enclosed posterior distribution.

One way of thinking about the strict-prior method is in terms of the Bayesian definition of probability as a degree of belief: $P(M_\star^B | \mathcal{D}, \mathcal{N}_i)$ represents what we would conclude about M_\star^B based on living in a Galaxy with parameters \mathcal{N}_i . The prior $P(\mathcal{N})$ represents our belief of how likely the parameter values \mathcal{N}_i are to be correct compared to other possible values, and hence is the correct weighting to determine what we would believe about $P(M_\star^B | \mathcal{D})$, taking into account all possible values of \mathcal{N} and how probable we believe each of those values are. This assumption is appropriate here, given that the bulge mass determinations depend only very indirectly on disk parameters, so we would place little faith in constraints on disk properties that came from the bulge mass dataset as opposed to the much more direct methods now available.

An alternative method would be to sum the *likelihoods*, $P(\mathcal{D} | M_\star^B, \mathcal{N}_i)$, and normalize that result to unity (which we will refer to as the “weak-prior” method). This is equivalent to calculating the evidence-weighted average of the posteriors calculated in the course of the strict-prior method. In this case, the posterior we calculate incorporates the assumption that $P(\mathcal{N} | \mathcal{D}) \neq P(\mathcal{N})$: i.e., that our state of knowledge of the nuisance (disk) parameters should be influenced by the set of bulge mass measurements. Hence, all the parameters in Table 2.3 would be treated in the same way as those contained in Θ , differing only in the informativeness and nature of the priors applied. Effectively, the weak-prior method assumes that values of the parameters \mathcal{N} under which the data were most likely to have been observed should be given greatest weight, even if they are disfavored by our priors.

We have much greater confidence, however, in the priors we have chosen for R_0 , L_d ,

and $\Sigma_*(R_0)$ based on more direct observations than anything we would infer from the set of bulge mass measurements, and so the weak-prior method appears to be inappropriate here. In practice, the posteriors for the disk mass, $P(M_*^D | \mathcal{D})$, and hence also for the total mass, $P(M_* | \mathcal{D})$, differ significantly (with a mean differing by $\sim 1\sigma$) between the two methods; however, the bulge mass estimate differs little between the strict- and weak-prior methods (with a mean differing by $\sim 0.1\sigma$).

2.4.3 A Uniform Sample of Bulge+Bar Mass Measurements

In this study, we define M_*^B as the excess mass over a single-exponential disk in the total stellar mass budget for the Galaxy. We begin by searching the literature for measurements of the combined stellar mass of the bulge, pseudo-bulge, and/or bar components of the Milky Way, which collectively fall into the category of M_*^B . A diverse set of methods, models, and observations have been used to make these estimates. For instance, [Dwek et al. \(1995\)](#) photometrically determined the Galactic bulge morphology, luminosity, and mass using triaxial bar-like models constrained by the *COBE/DIRBE* observations, measuring $M_*^B = 1.3 \pm 0.5 \times 10^{10} M_\odot$. In contrast, [Klypin et al. \(2002\)](#) consider Λ CDM-based models for the Milky Way, accounting for the mass and angular momentum of the DM halo, constrained by a variety of kinematic measurements, to estimate that $M_*^B \approx 1 \times 10^{10} M_\odot$. Alternatively, [Picaud & Robin \(2004\)](#) use Monte Carlo techniques to fit the Besançon model of stellar population synthesis to the observed near-IR luminosity of the bulge using observations from the DENIS survey, finding $M_*^B = 2.4 \pm 0.6 \times 10^{10} M_\odot$. These are only a few of the alternatives; we provide the entire list of studies included in our Galactic bulge+bar mass dataset, hereafter denoted as \mathcal{D}_M , in [Table 2.4](#) for reference.

The incorporated studies use a heterogeneous mixture of assumptions and models for the Galaxy; we follow the basic model of [Chomiuk & Povich \(2011\)](#) and attempt to place them on a uniform basis here. One of the most common sources of variation is the adopted value of the Galactocentric radius of the Sun’s orbit, R_0 . For instance, using the virial theorem one can demonstrate that kinematic estimates of the Galactic bulge+bar mass will be directly proportional to R_0 . On the other hand, photometric estimates of the luminosity of the bulge,

based on the flux measured from our location, should scale as R_0^2 .

A bulge mass inferred from the microlensing event rate observed toward the Galactic center, however, has a more complex dependence on R_0 . The measured rate of microlensing events can be directly converted into an optical depth, $\tau = \tau_{\text{bulge}} + \tau_{\text{disk}}$, which is the sum of the contribution from the stars in the bulge and the intervening part of the disk. [Hamadache et al. \(2006\)](#) show that $M_\star^{\text{B}} \propto \tau_{\text{bulge}} \times R_{\text{bulge}}$, where R_{bulge} is the radius of the bulge, which itself should be proportional to R_0 based on geometric arguments (i.e., $R_{\text{bulge}} = R_0 \tan \theta/2$, where θ is the angular diameter of the bulge). Unfortunately, the typical contribution from disk stars, which we would need to subtract in order to obtain τ_{bulge} , is $\sim \tau/3$ ([Sumi et al., 2003](#); [Hamadache et al., 2006](#), and references therein) and turns out to be highly sensitive to the chosen value of R_0 . As an example, if we are to assume that τ_{disk} is proportional to the mass of disk stars between us and the bulge, which in turn depends on the total mass of the disk, the disk model described above yields $d \ln M_\star^{\text{B}} / d \ln R_0 \approx 5.7$; i.e. τ_{disk} should scale roughly as R_0^6 . Based on this complexity, we assume for the purposes of this study that estimates of M_\star^{B} based on measurements of τ do not scale with R_0 .

In order to combine the M_\star^{B} estimates in our dataset into one aggregate result, after choosing a value of R_0 from our [Gillessen et al. \(2009\)](#) prior, we renormalize each result to that R_0 value using the appropriate scaling relation. Unless otherwise noted, the central value and error bar are scaled by the same factor in order to ensure the fractional error remains unchanged (this is equivalent to holding the error bars constant in log space), as essentially none of the literature estimates include the uncertainty in R_0 in their error estimates (a problem that our Monte Carlo technique will fix). For reference, we list the type of observational constraint and appropriate R_0 power-law index used to scale to each M_\star^{B} estimate in [Table 2.4](#). We note that if we assume that microlensing-rate based measurements of M_\star^{B} scale as R_0^1 (as bulge stars are the dominant contribution to τ), rather than treating them as independent of R_0 , the change in our results proves to be negligible.

As discussed in [§2.4.1](#), our definition of stellar mass includes the contribution from remnants, but not that from substellar objects. Kinematically derived measurements of the bulge mass in our dataset will not reflect this distinction. Therefore, we multiply the results from dynamical measurements by a normalization factor of 0.94 ± 0.02 to exclude the contri-

bution from brown dwarfs. We derive this scale factor by varying the power-law index of the IMF in the brown dwarf mass range ($0.005 < M/M_{\odot} < 0.01$) from -0.5 to 0.5 (Cruz et al., 2007; Kirkpatrick et al., 2012; Day-Jones et al., 2013; Burningham et al., 2013) and including their contribution within the Bruzual & Charlot (2003) model using solar metallicity and the Kroupa (2003) IMF over the main-sequence mass range.

Unlike dynamically constrained models of the Milky Way, which are indifferent to the mass distribution of the stellar populations, those which rely on photometric constraints (and thus mass-to-light ratios) to estimate M_{\star}^{B} will depend strongly on the IMF of choice. It is important then to set all measurements of this type on the same footing before applying the HB analysis by converting them to the same IMF. As previously discussed, we choose that to be the Kroupa IMF in accordance with the MPA-JHU spectrum measurements (Brinchmann et al., 2004).

The HB analysis we apply to estimate M_{\star}^{B} requires an error estimate for each independent measurement. Many of the studies in the literature, however, do not provide error estimates. We therefore must estimate the uncertainty in each measurement lacking an error bar in a uniform and unbiased manner; we do this in either one of two ways. First, for any study that lists a single M_{\star}^{B} result sans an error bar, we conservatively choose the error to be 50% of the value. However, if the authors instead provide a list of results corresponding to a variety of models or parameters explored, we then find the standard deviation of these listed values and add this in quadrature to 25% of their favored value to produce an error estimate.

Lastly, as we will detail below, the central value of many of the M_{\star}^{B} estimates in our dataset will vary with the disk parameters that we draw for each MC simulation. In such a case, it becomes problematic to use the median estimated value (which will vary) as a reference value that multiplies Q or F in those models of unreliable data. Consequentially, for the stellar mass portion of this study we always multiply Q and F by $10^{10} M_{\odot}$ when augmenting the errors estimates of “bad” measurements. For example, this means that $Q = 0.5$ corresponds to adding $0.5 \times 10^{10} M_{\odot}$ in quadrature to the nominal error bars when accounting for the possibility that a measurement is inaccurate (compare to Equation (2.3)).

In the following list, we detail any studies included in our analysis of M_{\star}^{B} that require further special treatment to be comparable to the others in Table 2.4:

Picaud & Robin (2004): This work uses the Besançon model of stellar population synthesis (see also Robin et al., 2003) to simultaneously constrain the mass of the bulge and thin disk through direct comparison with near-infrared star counts in ~ 100 windows of low extinction in the Galaxy. The thin disk is divided into 7 distinct age components with a two-slope IMF, while the bulge is modeled as a single older population with a Salpeter IMF; all of these populations are converted to follow the Kroupa (2003) IMF as the first step in our renormalization process. Additionally, the Besançon model features a double-exponential profile for the thin disk. This disk model has a hole at the center, so the same amount of mass at the center of the Galaxy would correspond to a greater bulge mass than in a non-holed model. For consistency, we integrate the holed density profile to determine the mass of the Besançon thin disk within the bulge radius of 3.71 kpc, and subtract this value from the single-exponential disk mass within the same radius for each realization of our disk model. The difference we calculate corresponds to the portion of the Picaud & Robin bulge mass estimate ($2.4 \pm 0.6 \times 10^{10} M_{\odot}$) that has already been included in the Bovy disk, so we subtract it off. Given that this correction is uncertain, we also add in quadrature to the nominal errors an amount equal to 50% of the holed-disk correction when assuming $R_0 = 8.33$ kpc; i.e., 50% of $1.86 \times 10^{10} M_{\odot}$. Picaud & Robin find that changes in the model mass when R_0 is changed are comparable in impact to the other variations amongst the models studied, and so we do not apply any R_0 scaling beyond this correction. Changes in R_0 affect their models in multiple ways, rendering any simple scaling of their M_{\star}^B value unsuitable. In the end, the results of Picaud & Robin (2004) are included in our dataset as a value of $M_{\star}^B = 0.54 \pm 1.11 \times 10^{10} M_{\odot}$ for $R_0 = 8.33$ kpc and best-fit Bovy disk parameters; for simplicity of analysis, this error estimate is used regardless of disk parameters.

Zhao (1996): This work models the disk with the Miyamoto & Nagai (1975, hereafter NM) potential, whose profile roughly resembles that of the double-exponential disk. Ideally, we would make the same correction using our disk model as we have done with Picaud & Robin (2004). However, the authors have normalized the NM profile to produce a total disk mass $M_{\star}^D = 8M_{\star}^B$, chosen so as to incorporate the dynamical effects of the dark halo

and produce a flat rotation curve at $1 < R < 3$ kpc from the Galactic center. We find, however, that this produces an extremely high surface density at nearly all radii within the disk, and indeed the authors note that this model does not fit the *COBE* map data except near the center. Since we cannot disentangle the dark mass from the stellar mass in this model, we do not attempt to do a correction as for [Picaud & Robin \(2004\)](#), since we would not have confidence in its accuracy. To account for that inability to correct, we increase the errors on this estimate to 50% of the derived bar mass. Lastly, as this is a dynamical measurement, we remove the contribution of brown dwarfs to the bulge mass budget by multiplying by a factor of 0.94 ± 0.02 . It is therefore included in our dataset as a value of $M_{\star}^{\text{B}} = 2.07 \pm 1.03 \times 10^{10} M_{\odot}$. We note that changes in the treatment of this measurement yield a much smaller difference in our combined results than our final estimated errors.

[Dwek et al. \(1995\)](#): As mentioned above, this work constrains the mass of the Galactic bulge using photometry taken from the *COBE/DIRBE* observations, measuring $M_{\star}^{\text{B}} = 1.3 \pm 0.5 \times 10^{10} M_{\odot}$, where a Salpeter IMF has been assumed. We convert this measurement to the Kroupa IMF by multiplying it by 1.62, derived using our definition of stellar mass and the assumptions made for the stellar models of [Bruzual & Charlot \(2003\)](#). Hence, we include this measurement in our dataset as a value of $M_{\star}^{\text{B}} = 2.11 \pm 0.81 \times 10^{10} M_{\odot}$.

[Freudenreich \(1998\)](#): This work favors a bar-to-disk (B/D) luminosity ratio of 0.33 based upon matching their Galactic model to infrared observations of the Milky Way from *COBE*. This model again includes a holed stellar disk. We integrate this profile both with and without the hole implemented, under the assumption that the mass gained by the disk when excluding the hole was previously incorporated into the bar, in order to calculate a hole-less B/D value. We note that the results of this study are published as a function of R_0 in their Table 4, allowing us to interpolate from this table to obtain B/D at a given R_0 , instead of assuming a scaling relation. Thus, for each MC simulation we include within our dataset a value of $M_{\star}^{\text{B}} = M_{\star,i}^{\text{D}} \times (B/D)$, where (B/D) represents

the hole-less model bar-to-disk ratio corresponding to $R_{0,i}$. We ascribe a 50% error bar to this value, accounting for uncertainty in the mass-to-light ratios of the bar and disk. Similarly to the [Picaud & Robin \(2004\)](#) estimate, we conservatively add in quadrature to this error estimate a value of 50% of the holed-disk correction at $R_0 = 8.33$ kpc. As a nominal value, we list $M_\star^B = 0.47 \pm 0.65 \times 10^{10} M_\odot$ in [Table 2.4](#), the result from assuming our standard disk model values. This overall error estimate is held constant for other values for the disk parameters.

Dehnen & Binney (1998): This study provides a parameterized model of the mass distribution in the Galaxy fitted to several observational constraints. They assume a single-exponential profile for the stellar disk, much like [Bovy & Rix \(2013\)](#). [Tables 3 & 4](#) of their paper list the resulting bulge mass when varying a large number of parameters in the model. Comparing models 2, 2a, and 2b we find that M_\star^B in their model approximately scales as $\sim (R_0/8\text{kpc})^{1/2}$. To provide the central value of this estimate we interpolate amongst M_\star^B results from their models 1–4 using the value $L_d/R_0 = 0.26$ from our standard disk model detailed in [§2.4.1](#). We estimate the random uncertainty in this value via propagation of errors: $\sigma(M_\star^B)^2 \simeq \frac{1}{4} [M_\star^B(L_d + \sigma(L_d)) - M_\star^B(L_d - \sigma(L_d))]^2$. In addition, we estimate the systematic error to be the standard deviation of the results from [Dehnen & Binney’s](#) models 2c–i, which we add in quadrature to the random error. Lastly, as this is a dynamical measurement, we remove the contribution of brown dwarfs to the bulge mass budget by multiplying by a factor of 0.94 ± 0.02 . Overall, this is included in our dataset a value of $M_\star^B = 0.65 \pm 0.38 \times 10^{10} M_\odot$.

2.4.4 Setting a Prior on M_\star^B

To place a prior on the mass of the Galactic bulge, we again consider the properties of spiral galaxies previously observed in the local universe. Some spirals appear to have no bulge component, whereas in extreme cases the bulge-to-total ratio can be as large as $B/T \sim 0.8$ (e.g., [Simien & de Vaucouleurs, 1986](#); [Gadotti, 2009](#)). Given our prior understanding of the

total mass of the Milky Way to be of order $\sim 5 \times 10^{10} M_\odot$ (e.g. [McMillan, 2011](#), and references therein) we assume the mass of the Galactic bulge can be anywhere in the range $0-4 \times 10^{10} M_\odot$ with equal weighting. This is represented by a flat distribution, such that

$$P(M_\star^{\text{B}}) = \begin{cases} \frac{1}{4} \times 10^{-10}, & \text{if } 0 \leq M_\star^{\text{B}} \leq 4 \times 10^{10} M_\odot \\ 0, & \text{otherwise.} \end{cases} \quad (2.22)$$

2.4.5 Stellar Mass Results

Table 2.5 shows the results for each model of “bad” measurements from our HB analysis. We list the optimal value of n , Q , or F , as appropriate for each model, which we take to be the value corresponding to the peak of the marginalized posterior PDF for these parameters. In Figure 2.4, we marginalize out M_\star^{B} and show the resulting joint posterior for f_{good} and F normalized to a peak value of 1. We can see in this case that the likelihood is maximized near $f_{\text{good}} \approx 1$ and $F \approx 0$, in similarity to the SFR results in §2.3.3 which favored $f_{\text{good}} \approx 1$ and minimally adjusted error bars. If we are to then marginalize out f_{good} from the joint posterior, this yields the result $P(F | \mathcal{D})$ shown in Figure 2.5 as a solid green curve. Assuming that $f_{\text{good}} = 0$ (i.e., that all included measurements are inaccurate to some extent) produces the the dashed green curve in Fig. 2.5; this is equivalent to the curve produced by cutting through the $f_{\text{good}} = 0$ plane in Fig. 2.4.

All model-comparison criteria listed in Table 2.5 result from comparing values with the all-“good” model for each realization. For example, $\Delta \log_{10} \mathcal{B}_k$ for the free- n model reflects the mean and standard error of the set $\{\log_{10}(\mathcal{B}_{\text{free-}n}/\mathcal{B}_{\text{all-“good”}})_i\}$, and similarly for ΔAIC & ΔBIC . In accordance with the likelihood peaking on the $f_{\text{good}} \approx 1$ plane, as seen in Fig. 2.4 and 2.6, all criteria values indicate that the best fit of the data results when the fewest free parameters are employed in the HB analysis. That said, several of the other models listed in Table 2.5 have criteria values that do not differ enough to be statistically significant (i.e., their differences in $\Delta \log_{10} \mathcal{B}_k$, ΔAIC , or ΔBIC are less than 2). Again, similar to the SFR results, the model with highest \mathcal{B}_k is the one where all measurements are treated as accurate, indicating that once differences in the assumed Galactic model, IMF, and definition of M_\star are accounted for, no correction for systematic effects is needed in order to relieve any

tension in these measurements. This is supported by the AIC & BIC values as well. Taking the all-“good” model as our fiducial measurement, we therefore find the stellar mass of the Galactic bulge+bar to be $M_{\star}^{\text{B}} = 0.91 \pm 0.07 \times 10^{10} M_{\odot}$; a comparison with the other values in Table 2.5 shows that this estimate is quite robust to any way we account for “bad” estimates in the HB analysis. We have also tested the impact that the Bissantz & Gerhard (2002) and Widrow et al. (2008) M_{\star}^{B} estimates make on our final results, as these two measurements are more strongly peaked than the other estimates and are centered at similar bulge mass values (see Figure 2.7). We find that doubling the nominal errors on both of these estimates produces only a 25% increase in the error of our aggregate result and a negligible change to the mean value, indicating that these two estimates are not dominating our final estimate.

Lastly, we show in Table 2.5 the inverse-variance weighted mean (IVWM) of the nominal values from our M_{\star}^{B} dataset (Table 2.4) with no corrections to uniform R_0 and M_{\star}^{D} . We can see that the IVWM is more strongly pulled by lower-valued outliers in comparison to the HB results. This is likely in large part the result of the heterogeneous mixture of R_0 values in the sample, as the all-“good” model is equivalent to 10^3 MC simulations of the IVWM, but rescaling all measurements to reflect $R_0 = 8.33 \pm 0.35$ kpc (Gillessen et al., 2009); in this case, the all-“good” model corresponds to the average of the IVWM from our 10^3 MC simulations, rather than the IVWM of the set of original measurements. With 18 M_{\star}^{B} estimates in our dataset, and thus 17 degrees of freedom, we expect 68% chance of finding χ^2 in the range [11.31, 22.68] and a 95% chance of it being in the range [7.56, 30.19]. Hence, the observed $\chi^2 = 14.03$ indicates only modest tension amongst the measurements; $\sim 2/3$ of the time one would observe a χ^2 this large or larger.

Similarly to our SFR analysis, we have tested whether common-mode systematics have a large impact on our bulge mass estimate, an effect our HB method is unable to account for as we assume that errors from each study are random compared to each other. As initially discussed in §2.3.3, this involves applying the HB method using the all-“good” model to a bootstrap resampling of the M_{\star}^{B} dataset in two different ways. In the first case, we draw only one measurement at random from all those which use a common measurement technique (i.e., one of the four categorizations listed in Table 2.4 under the column labeled “Constraint type”), yielding four estimates from a unique measurement method. In the second case,

we draw four measurements at random from the entire list of estimates in Table 2.4. For each case, we perform this process 1,000 times and measure the mean from the posterior distribution $P(M_\star^B | \mathcal{D})$ for each set of measurements. We find the standard deviation of the mean to be 0.19 when resampling with only one measurement of each type from the M_\star^B dataset and 0.23 when resampling at random from the entire dataset. Again, there is greater scatter between measurements of the same type than between random measurements in the dataset. Hence, similarly to our SFR results, we can safely conclude that common-mode systematics make a negligible impact on our bulge mass results.

The results from our HB analysis and MC simulations for $P(M_\star^D | \mathcal{D})$ and $P(M_\star | \mathcal{D})$ are well-described by Gaussian distributions. These correspond to $M_\star^D = 5.17 \pm 1.11 \times 10^{10} M_\odot$ and $M_\star = 6.08 \pm 1.14 \times 10^{10} M_\odot$. We note that the mass of the stellar halo component of the Galaxy ($\sim 10^9 M_\odot$) is negligible compared to the uncertainties in our estimate (Bell et al., 2008a; Bullock & Johnston, 2005), and thus we can disregard its contribution. The uncertainty in M_\star is dominated by that in M_\star^D , making our M_\star result highly insensitive to the choice of model used in the HB analysis of the Galactic bulge+bar mass estimates. The largest sources of uncertainty in M_\star^D and M_\star thus come from the values of R_0 and L_d that we adopt (Table 2.3). The constraints on these parameters are likely to improve with upcoming Galactic surveys, such as *Gaia*, and so we also calculate derivatives of our mass estimates with respect to each so that they may be easily adjusted to reflect any improved information. To do so, we simply redo our analysis after independently offsetting either parameter by one-half of its error estimate above and below the central value. The derivative is calculated from the curve yielded from Lagrangian interpolation of the resulting 3 data points. For convenience, we tabulate our stellar mass results for each component and their derivatives in Table 2.6.

Lastly, we display the PDF for the bulge-to-total mass ratio of our model in Figure 2.8 as a solid black curve, which indicates a median with 1σ error estimate of $B/T = 0.150_{-0.019}^{+0.028}$. This is obtained from the distribution of values, $(B/T)_i = M_{\star,i}^B / (M_{\star,i}^B + M_{\star,i}^D)$, resulting from each self-consistent realization of the Galaxy. Calculating $P(B/T)$ in a model-consistent way (i.e. accounting for covariances within our model) yields measurably tighter constraints than when doing so by combining independent estimates of M_\star^B and M_\star . For example, the blue dashed curve in Figure 2.8 is the result of combining randomly drawn pairs of M_\star^B

and M_{\star}^D values drawn from the PDFs for each mass component in this study and assuming $M_{\star} = M_{\star}^B + M_{\star}^D$. The red dash-dotted curve in Figure 2.8 shows the distribution of bulge-to-total luminosity ratios for a sample of 212 Sbc-Sc galaxies measured from SDSS by Oohama et al. (2009). The mass-to-light ratio of the older stellar population in the bulge is higher than that of the younger stellar disk and so converting this to a bulge-to-total mass ratio would shift the distribution toward slightly higher values; however, we can safely assess that Milky Way lies well within the range of B/T values. Graham & Worley (2008) find the average bulge-to-disk K -band flux ratio for a sample of 79 Sbc galaxies to be $\log(B/D) = -0.82$, which converts to an average B/T of 0.13; this compares well with our Milky Way value.

2.5 SUMMARY & DISCUSSION

In this chapter we have developed improved constraints on several of the Milky Way’s global properties. We build upon the prior measurements found in the literature, joining them into consensus results using the power of the hierarchical Bayesian (HB) method. This method (Press, 1997; Lang & Hogg, 2012) takes into account the possibility of inaccurate measurements being included in our datasets, and has proven to be quite robust when varying how we dealing with such “bad” measurements. By incorporating all the information contained in the individual measurements, we have obtained significantly improved constraints on the Milky Way properties we investigate. At the same time, given the expectation that there could be systematics affecting the Milky Way data, the HB method has given us confidence in the robustness of our results, even though Occam’s razor favored the simplest model (i.e., the inverse-variance weighted mean) in the end. For convenience, we tabulate the main results from this study in Table 2.6, as well as their derivatives with respect to the Galactocentric radius of the Sun, R_0 , and the exponential scale length of the disk, L_d , allowing for our results to be updated if constraints on these parameters improve.

In our first application, we capitalize on the work of Chomiuk & Povich (2011), who provide a tabulation of the star formation rate (SFR) estimates in the literature over the last several decades. The authors make huge strides in placing each measurement on equal

footing by renormalizing them all to the same choice of initial mass function and stellar population synthesis model. Using these updated estimates as our dataset, we find the SFR of the Milky Way to be $\dot{M}_\star = 1.65 \pm 0.19 \text{ M}_\odot \text{ yr}^{-1}$ (assuming a Kroupa IMF and Kroupa-normalized Kennicutt ionizing photon rate).

Next we investigate the stellar mass contained in each of the major components of the Milky Way. In Table 2.4, we have compiled an extensive list of Galactic bulge, pseudo-bulge, and/or bar mass estimates from the literature. We assume the single-exponential density profile for the disk laid forth by Bovy & Rix (2013); we tabulate the adopted probability distributions for all relevant parameters in Table 2.3. We then combine our HB analysis with Monte Carlo (MC) simulations that uniformly scale each estimate to the same value of R_0 , ensuring propagation of R_0 errors into the hierarchical M_\star^{B} result. The MC calculations also yield estimates of the stellar mass of the bulge+bar, the stellar mass of the disk, and the total stellar mass in the Milky Way.

Our combined estimate of the bulge+bar mass is $M_\star^{\text{B}} = 0.91 \pm 0.07 \times 10^{10} \text{ M}_\odot$. This estimate has substantially smaller errors than the individual estimates used to derive it. We note that the error given not only reflects the random and systematic uncertainties in each individual estimate, but also current uncertainties in R_0 . Our results show that once we have renormalized each estimate to reflect the same choice of IMF, stellar distribution profile for the disk, and definition of stellar mass that likely there are minimal systematics to further correct for. We adopt the Kroupa (2003) IMF in this study and include the contributions of main-sequence stars and remnants, but not substellar material, in our definition of stellar mass in accord with the MPA-JHU measurements of SFR and M_\star for external galaxies found in SDSS.

Under consistent assumptions, we find the disk mass of the Milky Way is $M_\star^{\text{D}} = 5.17 \pm 1.11 \times 10^{10} \text{ M}_\odot$. Our model of the Galactic stellar disk is based on that of Bovy & Rix (2013), but we directly incorporate current uncertainties in the Galactocentric radius of the Sun. Our disk mass estimate is in broad agreement with other measurements found in the literature. One of the earliest models of the Milky Way by Bahcall & Soneira (1980), primarily constrained by star counts from photometric observations of the Galaxy, yields a stellar disk mass of $5.6 \times 10^{10} \text{ M}_\odot$. The Λ CDM-based Milky Way models by Klypin et al.

(2002) favor a range of $4\text{--}5 \times 10^{10} M_{\odot}$. Similarly, the kinematically constrained models from [Dehnen & Binney \(1998\)](#) find the mass of the disk to lie in the range of $4.2\text{--}5.1 \times 10^{10} M_{\odot}$.

We find that total stellar mass in the Milky Way is $M_{\star} = 6.08 \pm 1.14 \times 10^{10} M_{\odot}$ by statistically combining the stellar disk and bulge+bar mass estimates through model-consistent MC simulations (the mass of the stellar halo component ($\sim 10^9 M_{\odot}$) is negligible compared to our uncertainty). The overall error in our M_{\star} estimate is dominated by that contributed from the disk component, rendering our final result highly insensitive to any assumptions involved with combining bulge mass estimates to determine $P(M_{\star}^{\text{B}} | \mathcal{D})$. In comparison, [McMillan \(2011\)](#) find a total baryonic mass of $6.43 \pm 0.63 \times 10^{10} M_{\odot}$, from which we can subtract the atomic and molecular phase gas mass of $9.5 \pm 3.0 \times 10^9 M_{\odot}$ ([Dame \(1993a\)](#)), corrected for helium contributions by [Flynn et al. \(2006\)](#)), giving $M_{\star} = 5.48 \pm 0.70 \times 10^{10} M_{\odot}$. In addition, [Flynn et al. \(2006\)](#) give a back-of-the-envelope calculation for M_{\star} , finding it to be in the range $4.85\text{--}5.5 \times 10^{10} M_{\odot}$. Our estimate for the total stellar mass compares well with the results of these two recent studies, but takes advantage of a large sample of bulge mass measurements found in the literature and is founded on improved knowledge of several of the properties of the Galactic disk from SDSS. Again, we stress that all of our mass results assume a Kroupa IMF and an exponential profile for the Galactic disk, to match the assumptions used in studies of extragalactic objects.

Ultimately, the constraints we are able to place on the stellar mass of the disk component as well as the total stellar mass of the Galaxy depend strongly on the value we assume for R_0 . For our main results, we have chosen the [Gillessen et al. \(2009\)](#) estimate of 8.33 ± 0.35 kpc for its direct determination of the distance to Sgr A* (i.e., the center of the Milky Way) based on the orbits of nearby stars, its thorough treatment of systematic errors, and (thanks in part to the breadth of its errors) its consistency with a large variety of other R_0 measurements (both direct and indirect) in the literature, which range as low as $\lesssim 8$ kpc or as high as $\gtrsim 8.5$ kpc. It is likely, however, that constraints on R_0 will tighten as geometric methods are continually improving, while indirect methods that are plagued by systematic errors become obsolete ([Genzel et al., 2010](#)). For instance, the most recent measurement by [Chatzopoulos et al. \(2015\)](#) finds $R_0 = 8.30 \pm 0.09|_{\text{stat}} \pm 0.10|_{\text{syst}}$ kpc by dynamically modeling the nuclear star cluster dynamics. The constraints from that analysis in the distance vs. mass of the

black hole plane are in modest tension with those from monitoring stellar orbits by [Gillessen et al. \(2009\)](#); a joint analysis of the two ignoring this tension yields $R_0 = 8.36 \pm 0.11$ kpc. If we are to use this result for our study, the uncertainty in both the disk mass and the total mass are reduced to $0.5 \times 10^{10} M_\odot$, and our bulge mass error is reduced to $0.06 \times 10^{10} M_\odot$, while the central values are changed only slightly.

From the distribution of model-consistent realizations of M_\star^B and M_\star^D , accounting for covariance between the two, we find that the Milky Way has a bulge-to-total mass ratio of $B/T = 0.150_{-0.019}^{+0.028}$. As seen in [Fig. 2.8](#), this result makes our Galaxy typical amongst galaxies of similar morphological type in the local universe. Finally, combining our results for \dot{M}_\star and M_\star , we find that the specific star formation rate of the Milky Way is $\dot{M}_\star/M_\star = 2.71 \pm 0.59 \times 10^{-11} \text{ yr}^{-1}$.

In the following chapter, we will continue towards our goal of producing a better global picture of the Milky Way. With the improved constraints placed on M_\star and \dot{M}_\star in this work, we will next show that we can convert this information into accurate predictions for the integrated photometric properties of the Milky Way; i.e., the brightness and color of our Galaxy as they would be observed by alien astronomers from across cosmological distances. All of this work will culminate in a newfound ability to accurately place the Milky Way in context — i.e., we now have tight constraints on where our Galaxy falls compared to observational trends we find for other galaxies.

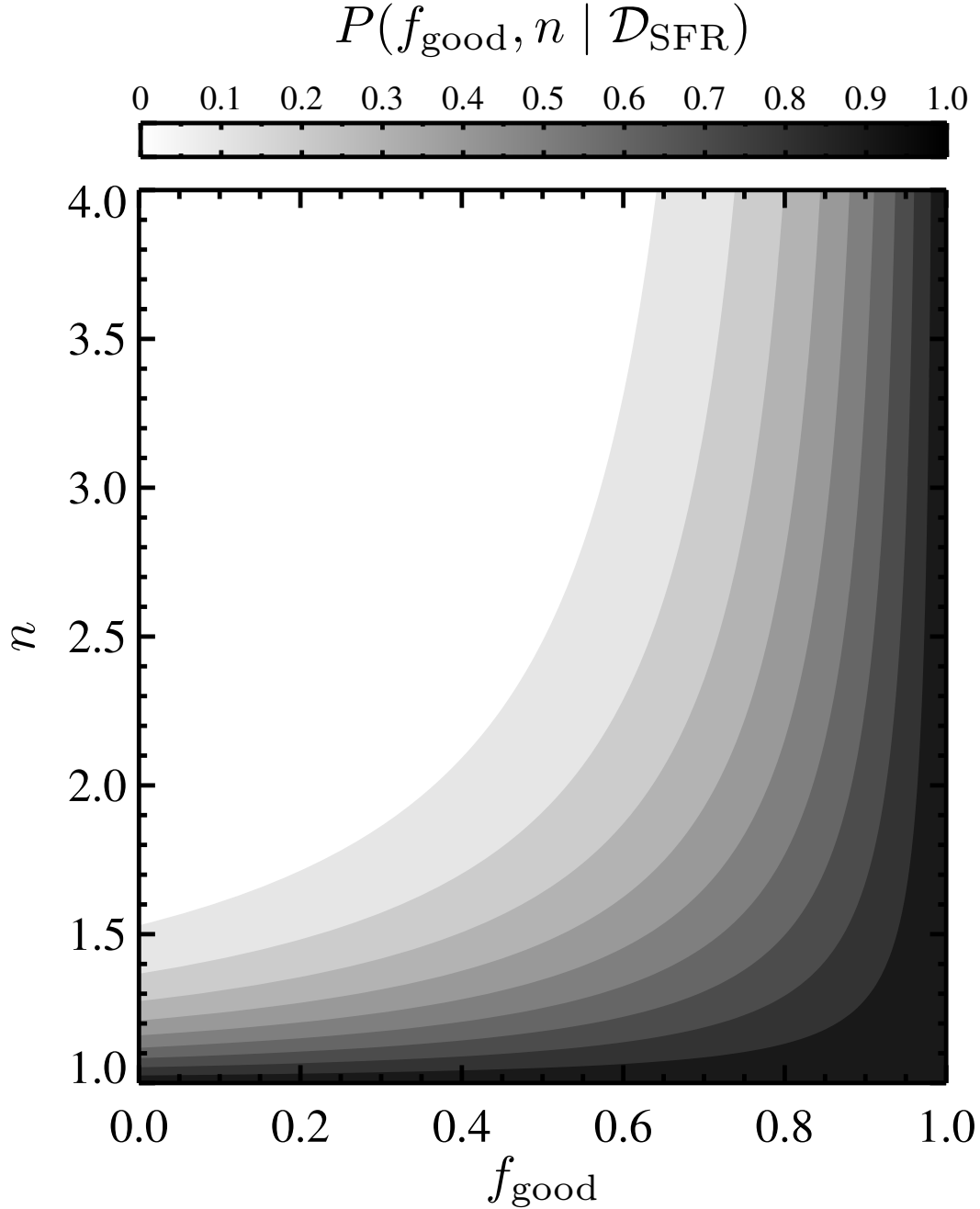


Figure 2.1: The joint posterior probability distribution function (PDF), $P(f_{\text{good}}, n \mid \mathcal{D}_{\text{SFR}})$, describing the probability of each possible value of the fraction of “good” estimates, f_{good} , (i.e., ones with accurate error bars) included in our Milky Way star formation rate (SFR) dataset, \mathcal{D}_{SFR} , and the scale factor n needed to expand the error bars for any measurement treated as not “good”. This 2-dimensional probability distribution is produced from a hierarchical Bayesian (HB) analysis, where we have marginalized over all possible true values for the Milky Way’s SFR. For ease of reading, we have normalized the peak value to 1. This plot clearly shows how strongly the HB analysis favors a model with minimally adjusted error bars on the individual estimates included in our analysis: the probability given the observed dataset is maximized if either n is ~ 1 , and/or f_{good} is ~ 1 .

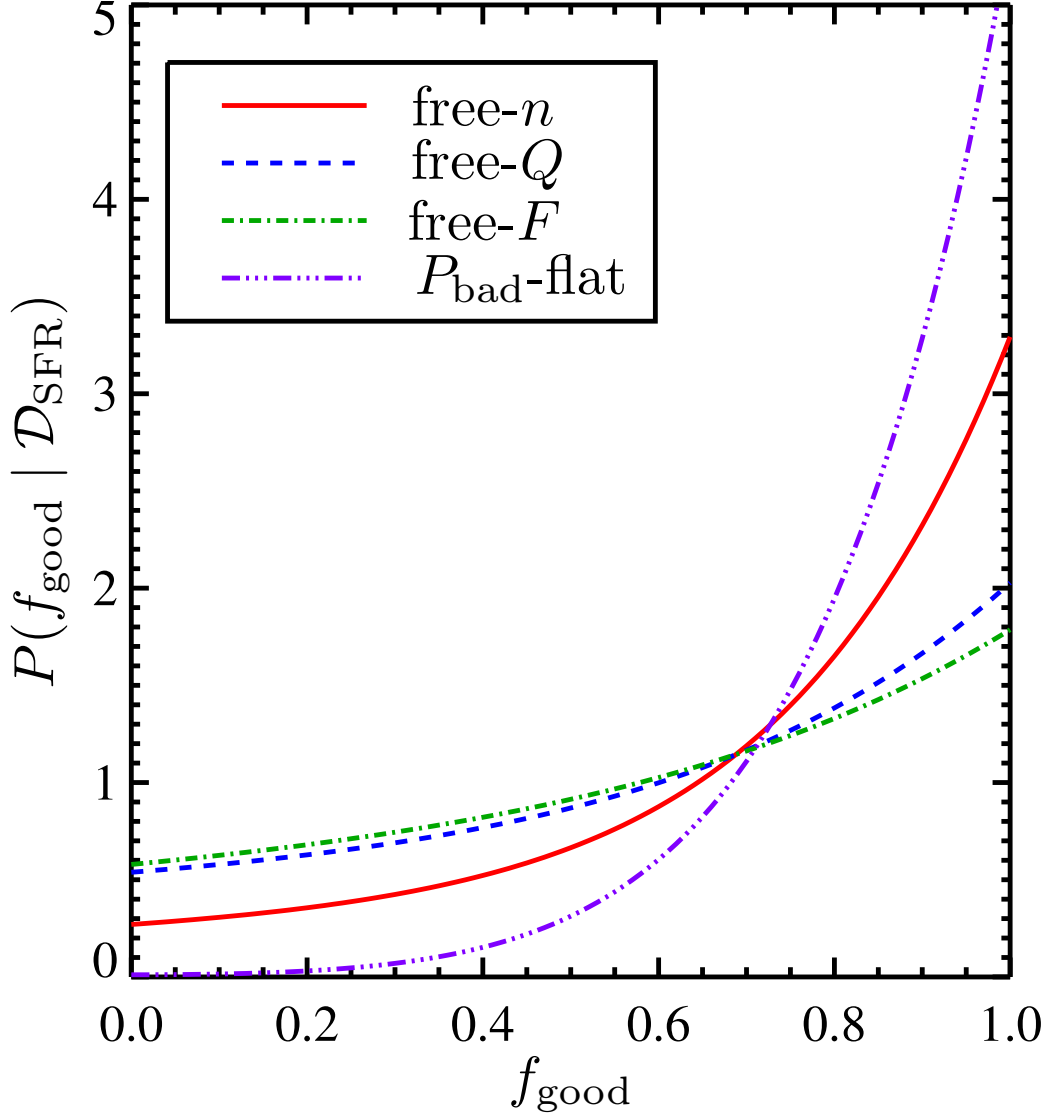


Figure 2.2: The marginal posterior PDF, $P(f_{\text{good}} | \mathcal{D}_{\text{SFR}})$, for the fraction of “good” estimates (i.e., ones with accurate error bars), f_{good} , included in our Milky Way star formation rate (SFR) dataset, \mathcal{D}_{SFR} , for each model of “bad” measurements we consider. Each curve is produced from a hierarchical Bayesian analysis, where we have marginalized over all other free parameters in the model. Each corresponds to a different model of how to remedy the inclusion of “bad” measurements included in \mathcal{D}_{SFR} : the solid red curve corresponds to a case where we must multiply the error bars for “bad” measurements by a free parameter n ; the dashed blue curve is produced by adding a fractional amount (given by the free parameter Q) of the median value of all estimates included in \mathcal{D}_{SFR} in quadrature to their nominal error bars; the green dash-dotted curve results from imposing a floor on “bad” measurements’ nominal error bars equal to a fraction amount (given by the free parameter F) of the median estimated SFR; and the purple triple-dot-dashed curve corresponds to a case where we model “bad” measurements as entirely wrong, and replace them with uniform probability distributions over the entire parameter space. We see that all models peak at $f_{\text{good}} = 1$, indicating that there is minimal tension between the measurements included in \mathcal{D}_{SFR} . Smaller values of f_{good} can be consistent with the data for most models, but only if Q or F is ~ 0 or $n \sim 1$, corresponding to no difference between “good” and “bad” measurements.

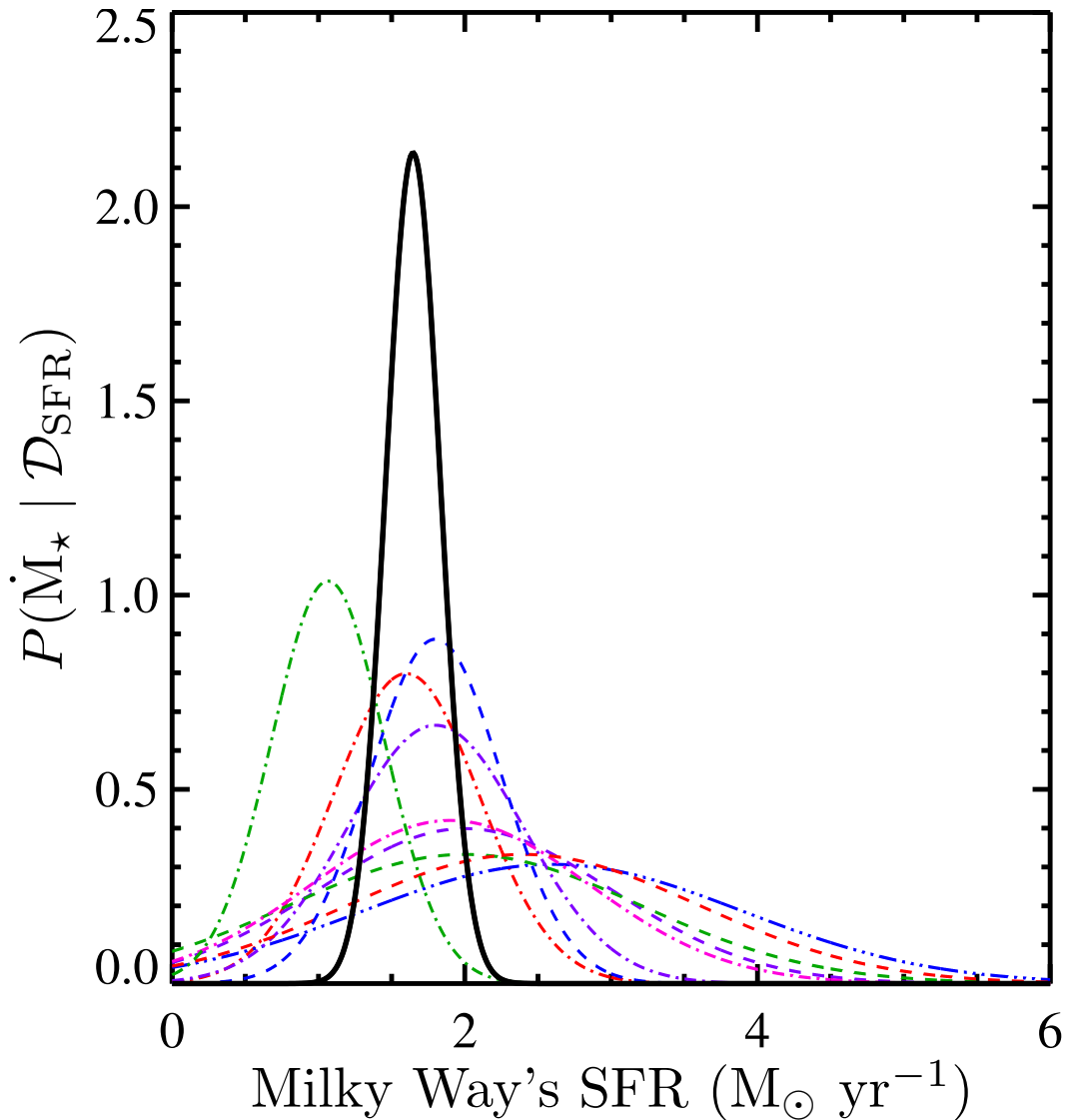


Figure 2.3: The marginal posterior PDF, $P(\dot{M}_\star | \mathcal{D}_{\text{SFR}})$, for the Milky Way's star formation rate (SFR) is shown as a solid black line. This result is produced from the hierarchical Bayesian (HB) analysis where we assume all measurements have accurately estimated error bars; since we have assume flat priors over the entire parameter space, this is equivalent to the inverse-variance weighted mean. This model is the simplest one which provides a good fit to the data, and hence is favored by both the Bayesian evidence and information criteria. For comparison, we overlay the individual estimates from our SFR dataset as dashed/dotted colored lines. We see that our methods yield a more tightly constrained estimate of the SFR of the Milky Way, while also being consistent with each individual estimate incorporated into the combined result.

Table 2.1. Combined SFR Results For Various Model Assumptions

Model	Optimal Value ^a	Combined $\dot{M}_* \pm 1\sigma$ ($M_\odot \text{ yr}^{-1}$)	k^b	ΔAIC	ΔBIC	$\Delta \log_{10} \mathcal{B}_k$
f_{good} free – Some of the measurements have inaccurate error bars.						
free- n	1.00	1.65 ± 0.20	3	4.0	4.4	-0.73
free- Q	0.00	1.66 ± 0.21	3	4.0	4.4	-0.31
free- F	0.26	1.67 ± 0.22	3	4.0	4.4	-0.25
P_{bad} -flat	N/A	1.65 ± 0.20	2	2.0	2.2	-0.73
$f_{\text{good}} = 0$ – All of the measurements have inaccurate error bars.						
free- n	1.00	1.65 ± 0.22	2	2.0	2.2	-1.59
free- Q	0.00	1.67 ± 0.23	2	2.0	2.2	-0.58
free- F	0.16 ^c	1.69 ± 0.26	2	2.0	2.2	-0.49
$f_{\text{good}} = 1$ – None of the measurements have inaccurate error bars.						
all-“good” ^d	N/A	1.65 ± 0.19	1	—	—	—

^aThe value of n , Q , or F marking the peak of marginalize posterior PDF for these quantities in each model.

^bThe number of free parameters in the model. See §2.2.3.4.

^cThis corresponds to the lowest allowed value of F in the model, F^{MIN} , where the smallest allowed error on any estimate in \mathcal{D}_{SFR} is just the minimum error estimate; that is, $\sigma_{F,i} = F^{\text{MIN}} \mu_i^{\text{MED}} = \sigma_i^{\text{MIN}}$. Since F^{MIN} affects no estimates in \mathcal{D}_{SFR} , this is equivalent to setting f_{good} to unity (see Equation 2.4). In fact, the HB analysis most strongly supports making no adjustment to the nominal error bars (i.e., the all-“good” model where we always set $f_{\text{good}} = 1$).

^dSince we use flat priors that are much broader than the likelihood PDF, this is equivalent to the inverse-variance weighted mean.

Table 2.2. Combined SFR Results For Various Data Assumptions

Model	Treatment of Data	Combined $\dot{M}_* \pm 1\sigma$ ($M_\odot \text{ yr}^{-1}$)
all-“good”	Including RW10 ^a with nominal errors (Fiducial)	1.65 ± 0.19
all-“good”	Including RW10 with errors doubled	1.77 ± 0.21
all-“good”	Excluding RW10 from the calculation	1.82 ± 0.21
all-“good”	Excluding B94 ^b from the calculation	1.63 ± 0.19

^aRobitaille & Whitney (2010).

^bBennett et al. (1994).

Table 2.3. Disk Model Parameters

Parameter	Value	Units	Description	Reference
R_0	8.33 ± 0.35	kpc	Galactocentric radius of the Sun	Gillessen et al. (2009)
L_d	2.15 ± 0.14	kpc	Scale length of exponential disk	Bovy & Rix (2013)
$\Sigma_\star(R_0)$	$31.75L_d/\text{kpc} - 33.5125 \pm 2.89$	$M_\odot \text{ pc}^{-2}$	Local surface mass density of MS stars and remnants for a given L_d^a	Bovy (2013, priv. comm.)
M_\star^D	See Equation (2.18)	M_\odot	The total stellar disk mass from Equation (2.17), given R_0 and L_d	Bovy & Rix (2013)

^aSee §2.4.1. This relationship accounts for the covariance between the dynamical estimates of L_d and $\Sigma_\star(R_0)$ from [Bovy & Rix \(2013\)](#), while also subtracting the contribution from brown dwarfs, $\Sigma_{\text{BD}}(R_0)$.

Table 2.4. The Galactic Bulge+Bar Mass Dataset

Reference	$M_\star^B \pm 1\sigma$ ($10^{10} M_\odot$)	R_0 assumed (kpc)	Constraint type	β^a	$M_\star^B \pm 1\sigma(R_0 = 8.33\text{kpc})$ ($10^{10} M_\odot$)
Kent (1992)	1.69 ± 0.85	8.0	Dynamical	1	1.76 ± 0.88
Dwek et al. (1995)	2.11 ± 0.81	8.5	Photometric	2	2.02 ± 0.78
Han & Gould (1995)	1.69 ± 0.85	8.0	Dynamical	1	1.76 ± 0.88
Blum (1995)	2.63 ± 1.32	8.0	Dynamical	1	2.74 ± 1.37
Zhao (1996)	2.07 ± 1.03	8.0	Dynamical	1	2.15 ± 1.08
Bissantz et al. (1997)	0.81 ± 0.22	8.0	Microlensing	0	0.81 ± 0.22
Freudenreich (1998)^b	0.48 ± 0.65	...	Photometric	...	0.48 ± 0.65
Dehnen & Binney (1998)	0.61 ± 0.38	8.0	Dynamical	1/2	0.62 ± 0.38
Sevenster et al. (1999)	1.60 ± 0.80	8.0	Dynamical	1	1.66 ± 0.83
Klypin et al. (2002)	0.94 ± 0.29	8.0	Dynamical	1	0.98 ± 0.31
Bissantz & Gerhard (2002)^c	0.84 ± 0.09	8.0	Dynamical	1	0.87 ± 0.09
Han & Gould (2003)	1.20 ± 0.60	8.0	Microlensing	0	1.20 ± 0.60
Picaud & Robin (2004)	0.54 ± 1.11	8.5	Photometric	0	0.54 ± 1.11
Hamadache et al. (2006)	0.62 ± 0.31	None	Microlensing	0	0.62 ± 0.31
Wyse (2006)	1.00 ± 0.50	None	Historical review	0	1.00 ± 0.50
López-Corredoira et al. (2007)	0.60 ± 0.30	8.0	Photometric	2	0.65 ± 0.33
Calchi Novati et al. (2008)	1.50 ± 0.38	8.0	Microlensing	0	1.50 ± 0.38
Widrow et al. (2008)	0.90 ± 0.11	7.94	Dynamical	1	0.95 ± 0.12

Note. — Bulge mass estimates, M_\star^B , listed in this table have been converted to the Kroupa IMF. See §2.4.3 for further notes on individual estimates.

^a β denotes the assumed relationship between each M_\star^B estimate, based on the constraint type, and the R_0 assumed; i.e. $M_\star^B \propto R_0^\beta$.

^bValue (in both cases) calculated assuming $M_\star^D = 5.17 \times 10^{10} M_\odot$ and $R_0 = 8.33$ kpc. *B/D* results are published as a function of R_0 , so no scaling relation needs to be assumed.

^cValues provided by [McMillan \(2011\)](#).

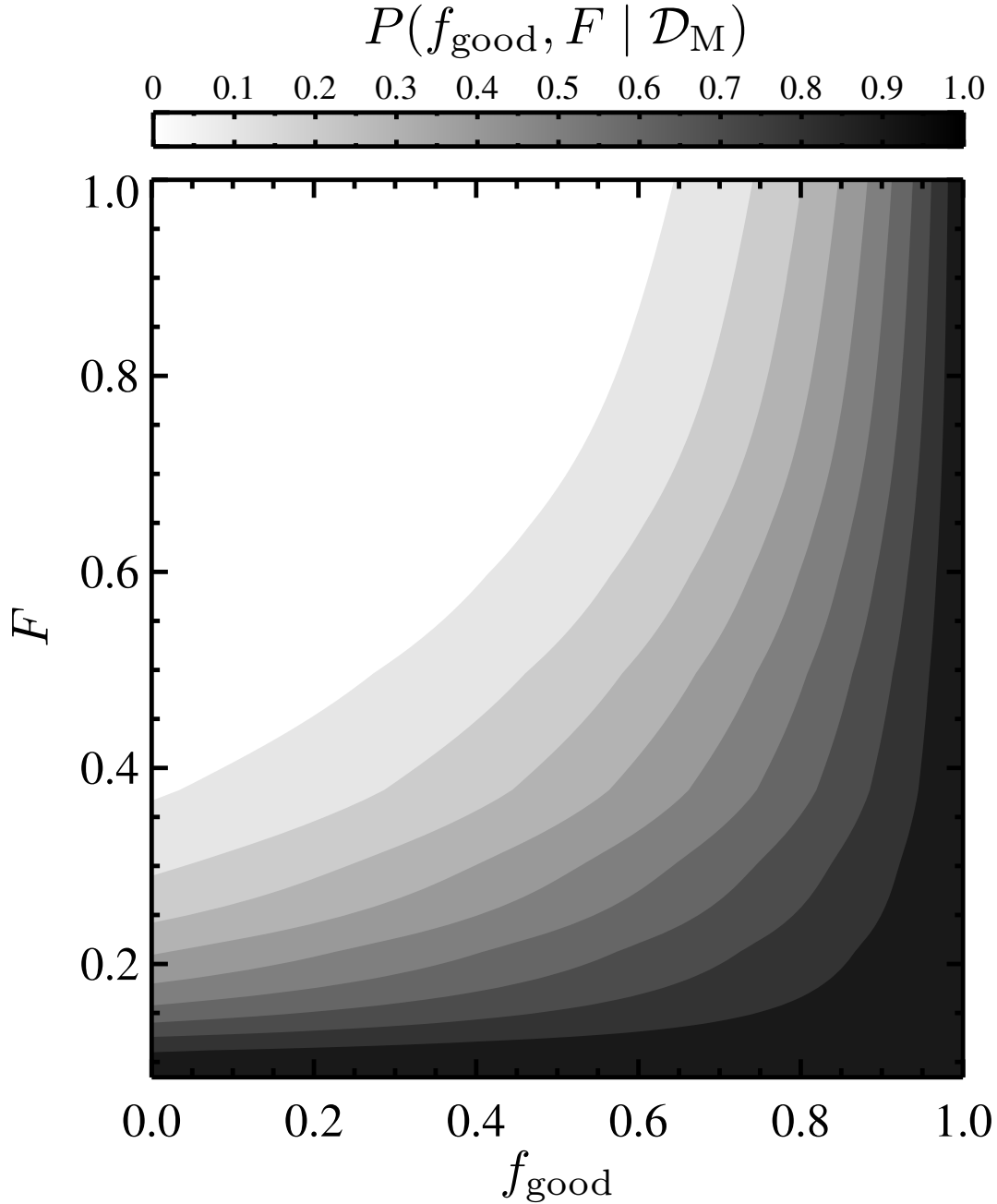


Figure 2.4: The joint posterior PDF, $P(f_{\text{good}}, F \mid \mathcal{D}_M)$, for the free parameters describing the Milky Way bulge+bar mass dataset, \mathcal{D}_M , when applying a hierarchical Bayesian analysis. The parameter f_{good} quantifies the probability that any one measurement included in \mathcal{D}_M is “good” (i.e., has accurately estimated error bars), and F denotes the fraction of $10^{10} M_{\odot}$ used as a floor on each individual error estimate when treated as not “good” in the model. For ease of comparison, we have normalized the peak of this distribution to 1. We see, similar to the results for the Milky Way SFR, that the likelihood, and thus the posterior, peaks near $f_{\text{good}} \approx 1$ and $F \approx 0$, indicating little tension amongst the Milky Way bulge+bar mass estimates.

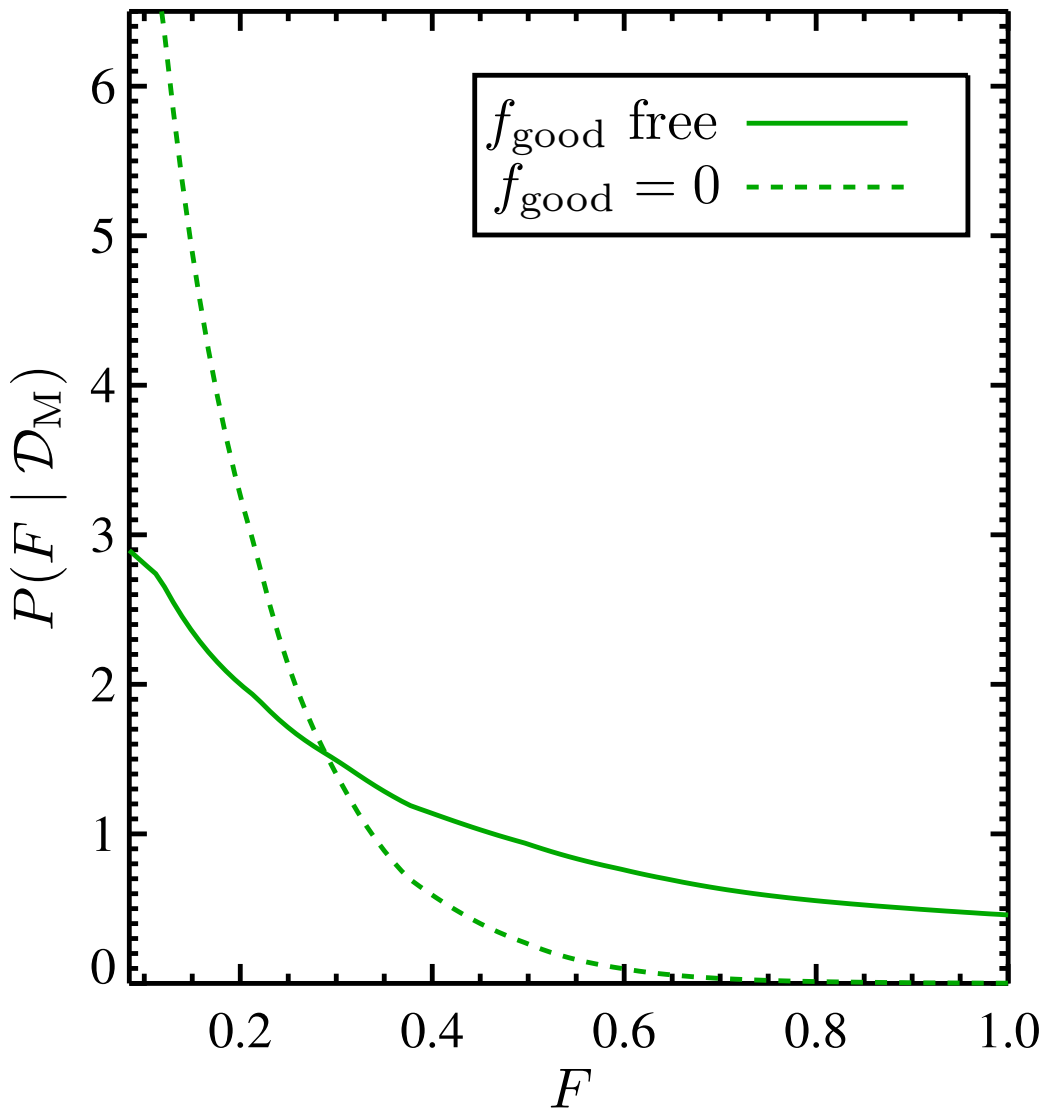


Figure 2.5: The marginal posterior PDF, $P(F | \mathcal{D}_M)$, for the floor value, F , defined as a fraction of $10^{10} M_\odot$ imposed as a minimum error estimate for “bad” measurements in our Milky Way bulge+bar mass dataset, \mathcal{D}_M . These results are obtained by marginalizing over all possible values of f_{good} (solid curve) or else by setting $f_{\text{good}} = 0$ (dashed curve). Here we see the competition between multiple possible solutions within the HB analysis. We note that both curves are marginalized over all possible values of the stellar mass contained in the bulge+bar component of the Galaxy, M_\star^B .

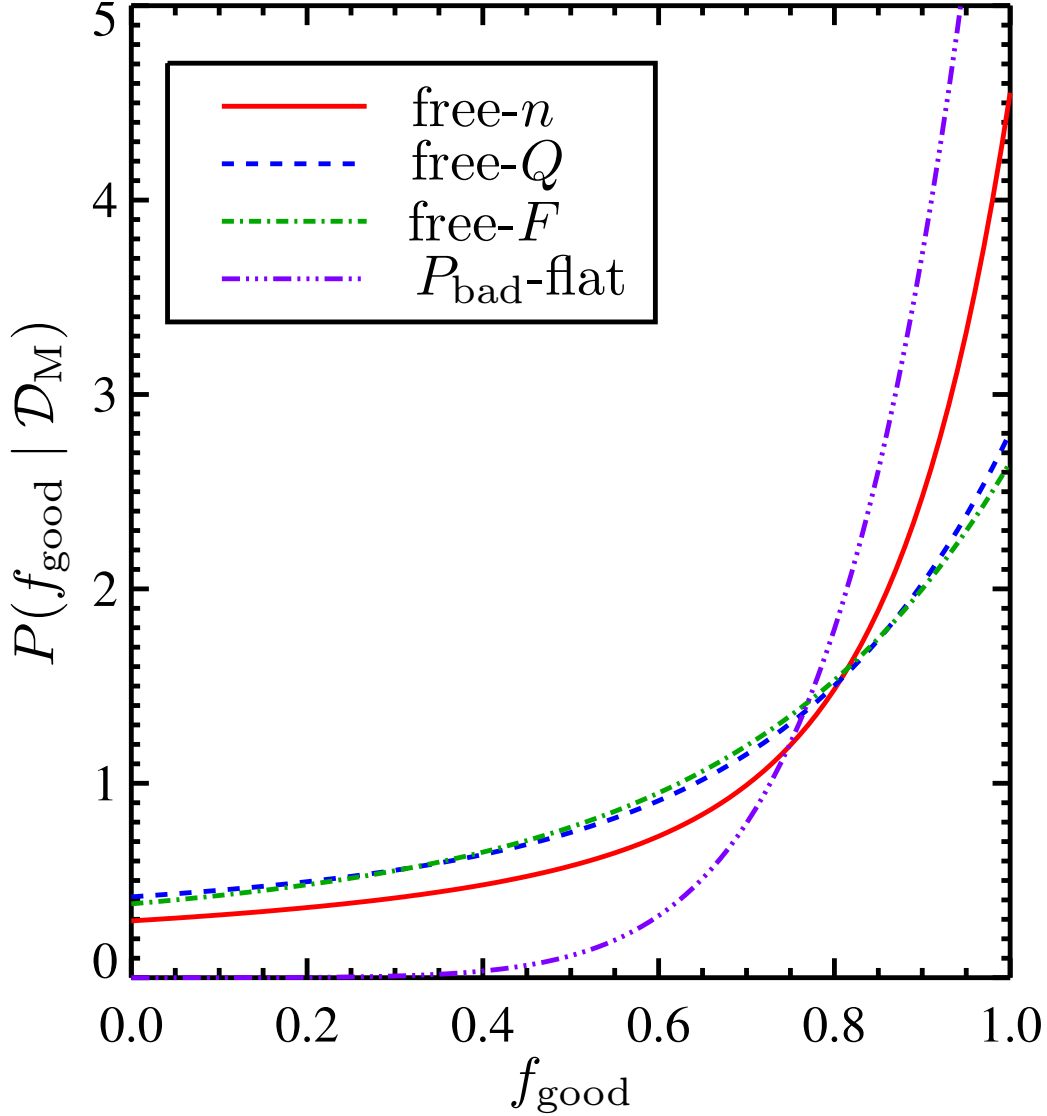


Figure 2.6: The marginal posterior PDF, $P(f_{\text{good}} | \mathcal{D}_M)$, for the fraction of “good” M_*^B measurements, f_{good} , (i.e., ones having accurately estimated errors) in our bulge+bar mass dataset, \mathcal{D}_M . Each model shown accounts for the inclusion of “bad” measurements in a different way: the free- n model (solid red) remedies underestimated errors by multiplying them by a scaling factor of n ; the free- Q model (dashed blue) adds extra error in quadrature to the errors on a measurement when treated as “bad”; the free- F model (dash-dotted green) places a floor on the errors of “bad” measurements; while the P_{bad} -flat model (triple-dot-dashed purple) works to completely disregard a measurement from \mathcal{D}_M when considering it “bad”. Similar to the SFR results, the PDF for all “bad”-measurement models are peaked around $f_{\text{good}} = 1$, more strongly so for the free- n and P_{bad} -flat scenarios than the free- Q and free- F scenarios. Regardless, it turns out that the best model of \mathcal{D}_M , i.e., the one favored by the Bayesian evidence and information criteria, is one where f_{good} is assumed to be 1, instead of allowing it as a free parameter – i.e. an all-“good” model.

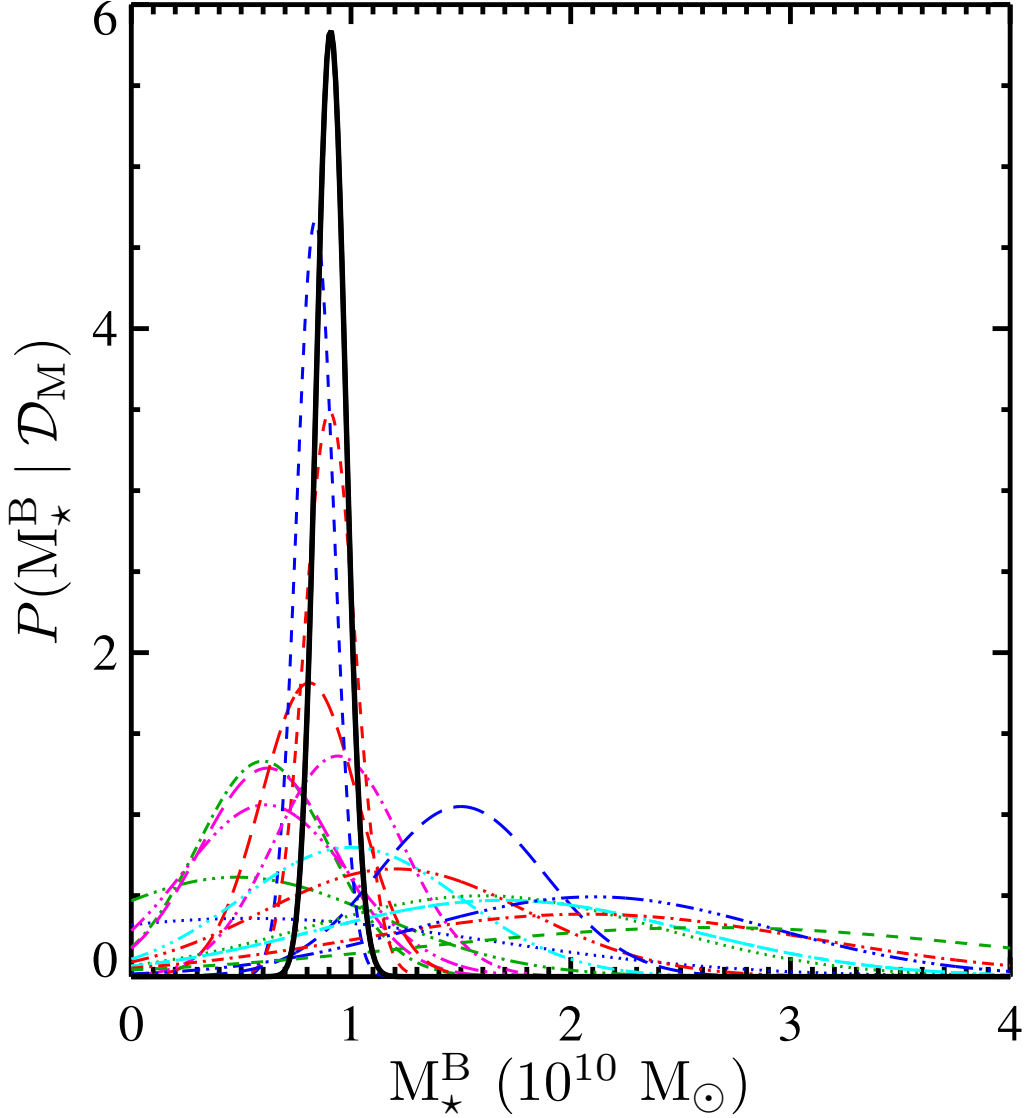


Figure 2.7: The marginal posterior PDF, $P(M_{\star}^{\text{B}} | \mathcal{D}_{\text{M}})$. The solid black curve shows the aggregate M_{\star}^{B} result as determined from our HB analysis when using an all-“good” model and Monte Carlo simulations to incorporate up-to-date information for the Galactocentric radius of the Sun, R_0 , the scale length of the single-exponential disk, L_d . Here, we have assumed $R_0 = 8.33 \pm 0.35$ kpc from the work of [Gillessen et al. \(2009\)](#) and $L_d = 2.15 \pm 0.14$ kpc based on the measurements by [Bovy & Rix \(2013\)](#). For comparison, we overlay the individual estimates from our Galactic bulge+bar mass dataset as dashed/dotted colored lines. Some of these measurements are in tension with others; the HB methods allows us to account for that tension in obtaining consensus results. Doubling the error bars on the [Bissantz & Gerhard \(2002\)](#) and [Widrow et al. \(2008\)](#) M_{\star}^{B} estimates (the relatively strongly-peaked dashed red and blue curves) yields only a 25% increase in the error in our aggregate result, indicating that these estimates are not dominating in our final estimate.

Table 2.5. Combined M_{\star}^{B} Results For Various Model Assumptions

Model	Optimal Value ^a	$M_{\star}^{\text{B}} \pm 1\sigma$ ($10^{10} M_{\odot}$)	k^{b}	$\Delta\text{AIC}^{\text{c}}$	ΔBIC	$\Delta \log_{10} \mathcal{B}_k$
<u>$f_{\text{good}} = \text{free}$ – Some of the measurements have inaccurate error bars.</u>						
free- n	1.00	0.91 ± 0.07	3	4.00 ± 0.00	5.78 ± 0.00	-0.66 ± 0.00
free- Q	0.00	0.91 ± 0.08	3	4.00 ± 0.00	5.78 ± 0.00	-0.45 ± 0.00
free- F	0.08	0.92 ± 0.08	3	4.00 ± 0.00	5.78 ± 0.00	-0.42 ± 0.00
P_{bad} flat	N/A	0.91 ± 0.07	2	2.00 ± 0.00	2.89 ± 0.00	-0.86 ± 0.00
<u>$f_{\text{good}}=0$ – All of the measurements have inaccurate error bars.</u>						
free- n	1.00	0.91 ± 0.08	2	2.00 ± 0.00	2.89 ± 0.00	-1.20 ± 0.00
free- Q	0.00	0.93 ± 0.09	2	2.00 ± 0.00	2.89 ± 0.00	-0.83 ± 0.00
free- F	0.08	0.94 ± 0.10	2	2.00 ± 0.00	2.89 ± 0.00	-0.85 ± 0.00
<u>$f_{\text{good}}=1$ – None of the measurements have inaccurate error bars.</u>						
all-“good” ^d	N/A	0.91 ± 0.07	1	—	—	—
<u>Non-hierarchical combinations of the data.</u>						
IVWM ^e		0.88 ± 0.06	$\chi^2 = 14.03$			
IVWM($R_0 = 8.33\text{kpc}$)		0.91 ± 0.06	$\chi^2 = 13.69$			

Note. — The M_{\star}^{B} results are well described by Gaussian distributions, and the values listed in this column represent the mean and 1σ parameter of fits to these distributions. The distributions we find for ΔAIC , ΔBIC , and $\Delta \log_{10} \mathcal{B}_k$ from the MC simulations are strongly peaked but also highly asymmetric, and so in these columns we quote the median and standard deviation of the median obtained by bootstrapping these sets of values. Errors of 0.00 indicate that the standard deviation of the median is $\ll 0.01$.

^aThe value of n , Q , or F corresponding to the peak of marginalize posterior PDF for these quantities in each model.

^bThe number of free parameters in the model. See §2.2.3.4.

^cFor each iteration of the HB analysis, we record the AIC and BIC. We then calculate the mean and standard error from the distribution of AIC and BIC values produced from all 10^3 iterations for each model. ΔAIC and ΔBIC reflects the difference in the mean AIC and BIC value measured from the model which has the lowest AIC/BIC (here, this is the all-“good” model). We see 10^3 iterations yields sufficiently small standard errors (i.e., less than 0.5) in order to securely assess differences of 2, which would indicate a statistically significant difference between models.

^dEquivalent to the combined inverse-variance weighted mean (IVWM) from 10^3 MC simulations, uniformly scaling each estimate to the same R_0 value from our Galactic model (see Table 2.3).

^eThe IVWM obtained from the nominal estimate values listed in Column 2 of Table 2.4. Essentially, since we have used flat priors, these are the same values we would find in the all-“good” scenario if we did not use MC simulations to renormalize each estimate to the same choice of R_0 . IVWM($R_0 = 8.33\text{kpc}$) shows the results from the same calculation for the M_{\star}^{B} estimates after scaling each to $R_0 = 8.33$ kpc, as in the last column of Table 2.4.

Table 2.6. Milky Way Properties and Derivatives

Property	Fiducial Result	$\partial/\partial R_0$	$\partial/\partial L_d$
M_\star^B	$0.91 \pm 0.07 \times 10^{10} M_\odot$	$0.093 \times 10^{10} M_\odot \text{ kpc}^{-1}$	$0.004 \times 10^{10} M_\odot \text{ kpc}^{-1}$
M_\star^D	$5.17 \pm 1.11 \times 10^{10} M_\odot$	$3.000 \times 10^{10} M_\odot \text{ kpc}^{-1}$	$0.469 \times 10^{10} M_\odot \text{ kpc}^{-1}$
M_\star	$6.08 \pm 1.14 \times 10^{10} M_\odot$	$3.093 \times 10^{10} M_\odot \text{ kpc}^{-1}$	$0.473 \times 10^{10} M_\odot \text{ kpc}^{-1}$
B/T	$0.150^{+0.028}_{-0.019}$	-0.061 kpc^{-1}	-0.011 kpc^{-1}
SFR	$1.65 \pm 0.19 M_\odot \text{ yr}^{-1}$	$0 M_\odot \text{ yr}^{-1} \text{ kpc}^{-1}$	$0 M_\odot \text{ yr}^{-1} \text{ kpc}^{-1}$
sSFR	$2.71 \pm 0.59 \times 10^{-11} \text{ yr}^{-1}$	$-1.381 \times 10^{-11} \text{ yr}^{-1} \text{ kpc}^{-1}$	$-2.111 \times 10^{-12} \text{ yr}^{-1} \text{ kpc}^{-1}$

Note. — Derivatives of M_\star are not simply the sum of the derivatives for M_\star^B and M_\star^D due to covariances between the parameters in our model. Derivatives of B/T represent the change in the median bulge-to-total mass ratio with respect to the appropriate parameter, measured independently from any other quantity in this table. The sSFR and its derivatives, however, are calculated directly from the \dot{M}_\star and M_\star results; e.g., here $\partial(\dot{M}_\star/M_\star)/\partial R_0 = -\dot{M}_\star M_\star^{-2} \times \partial M_\star/\partial R_0$ since $\partial \dot{M}_\star/\partial R_0 = 0$.

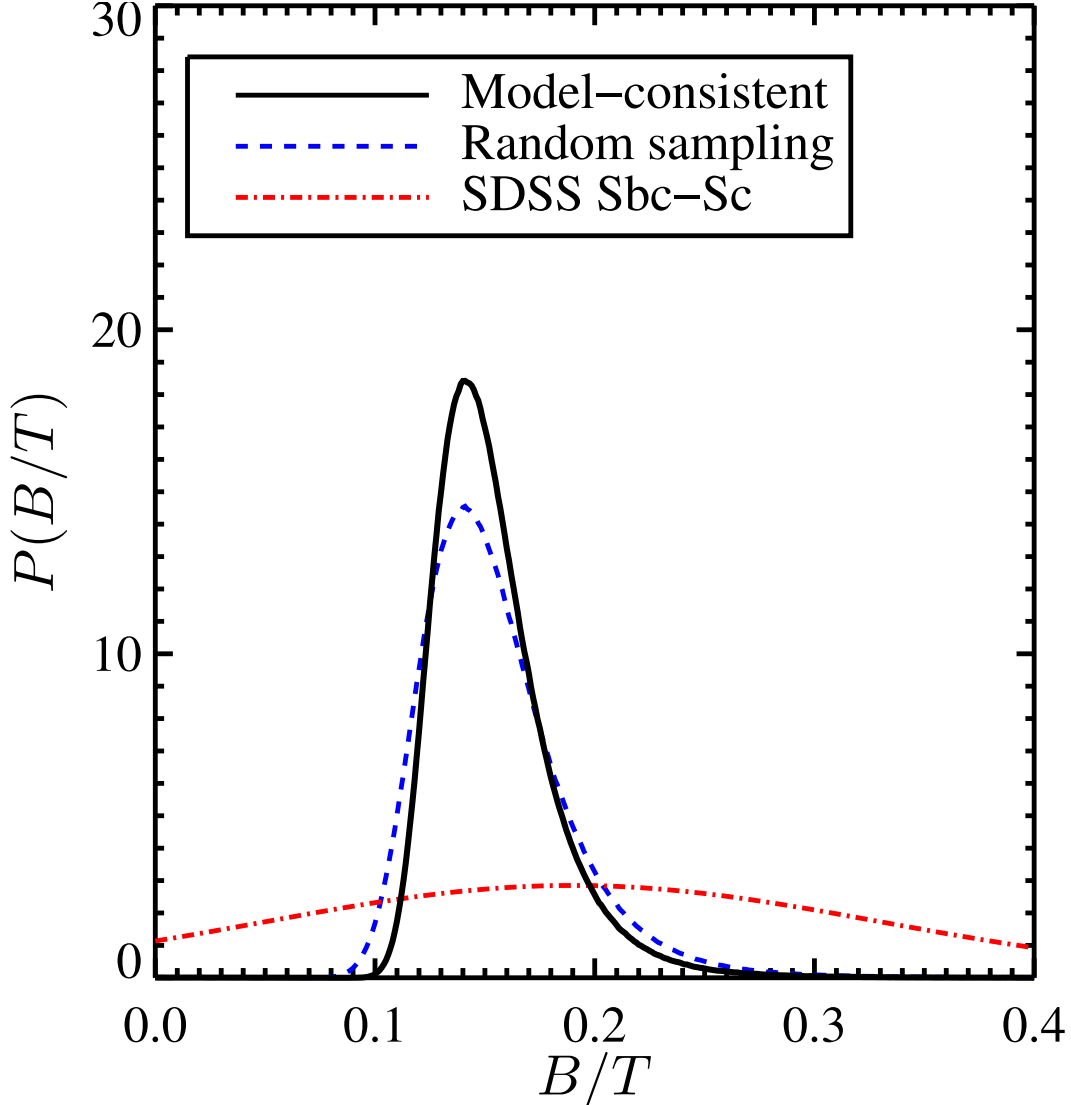


Figure 2.8: The bulge-to-total mass ratio, B/T , of the Milky Way as determined by our HB analysis (solid black curve). This is produced through Monte Carlo simulations where each realization of the bulge+bar mass ($M_{\star,i}^B$) and disk mass ($M_{\star,i}^D$) are determined using the same values for structural parameters for the disk, $\{R_0, L_d, \Sigma_{\star}(R_0)\}_i$, randomly drawn from their respective distributions listed in Table 2.3. The histogram of values $(B/T)_i = M_{\star,i}^B / (M_{\star,i}^B + M_{\star,i}^D)$ is then normalized to integrate to unity. The dashed blue curve shows the result of simply drawing from the fiducial estimates of $P(M_{\star}^B | \mathcal{D})$ and $P(M_{\star}^D | \mathcal{D})$ from our model independently. Calculating B/T in a model-consistent manner yields a noticeably tighter constraint than when not accounting for covariances between M_{\star}^B and M_{\star}^D . Lastly, we overlay the distribution of B/T luminosity ratios for a sample of 212 Sbc-Sc galaxies measured from SDSS by Oohama et al. (2009). Although converting to B/T mass ratios would produce a slight shift toward higher values, we see the B/T ratio for the Milky Way is not unusual for galaxies of its Hubble type.

3.0 UNVEILING THE MILKY WAY: A NEW TECHNIQUE FOR DETERMINING THE OPTICAL COLOR AND LUMINOSITY OF THE GALAXY

3.1 INTRODUCTION

Galaxy evolution studies primarily rely on observational comparisons between objects in the local universe (e.g., the Milky Way) and those at higher redshift, z (e.g., [Faber et al., 2007](#); [Ilbert et al., 2010](#); [Leauthaud et al., 2012](#)). For most galaxies of known z , rest-frame colors and absolute magnitudes are some of the easiest global properties to measure, regardless of their distance from us. Consequentially, color-magnitude diagrams (CMDs) provide a fundamental tool for interpreting galaxy evolution, especially at large z where morphological information is difficult to obtain. Yet to this day, the Milky Way's position on such a diagram has remained poorly determined, despite being the galaxy we can study in the most detail. Due to our location embedded within the disk of the Galaxy, interstellar dust obscures stars and hides most of the Milky Way from our view (cf. [Herschel, 1785](#)). Furthermore, because bluer light is absorbed and scattered more efficiently by the dust, the optical colors of distant stars are altered (e.g., [Cardelli et al., 1989](#); [Schlegel et al., 1998](#)). Thus, determining the global optical properties of the Milky Way from direct photometric observations has proven extremely difficult, requiring uncertain corrections and assumptions that are vulnerable to error.

For this reason, the history of measurements of the Galaxy's global photometric properties is sparse. P.C. [van der Kruit \(1986, hereafter vdK86\)](#) made the most recent significant measurement, utilizing a novel technique. The Zodiacal cloud, a thick disk-shaped concentration of dust lying in the ecliptic plane (or zodiac), produces a glow of diffuse optical light

throughout the night sky via the reflection of sunlight (Reach et al., 1996). This diffuse glow, known as the Zodiacal light, introduces a significant amount of contamination to attempts to estimate the amount of starlight from the Galaxy. The Pioneer 10 spacecraft, launched in 1972 on a mission to Jupiter, became the first space probe to travel beyond the asteroid belt, to distances where the effect of the Zodiacal light becomes negligible. Van der Kruit used photometric measurements of the Galactic background light in broad optical blue (3950-4850Å) and red (5900-6900Å) bands taken by Pioneer 10, corrected for diffuse Galactic light and extinction, and compared to stellar distribution models in order to find $M_B = -20.3 \pm 0.2$ and $B - V = 0.83 \pm 0.15$ in the Johnson magnitude system.

Two earlier studies used a model of the Galaxy that consisted of a disk and spheroid component, but utilizing different data and assumptions, in order to infer the luminosity and color of the Galaxy; both of these yielded significantly bluer color estimates for the Milky Way. First, de Vaucouleurs & Pence (1978, hereafter dV&P) had used a two-component model constrained to match the observed distribution of globular clusters in the Galactic bulge and the star counts near the Galactic poles of the disk in the solar neighborhood in order to infer $B - V = 0.53 \pm 0.05$. This work also yielded $M_B = -20.08$ (varying the shape of the bulge within this model yielded values ranging from -20.04 to -20.12); however, this estimate was updated to $M_B = -20.2 \pm 0.15$ in de Vaucouleurs (1983, hereafter dV83) assuming the Galactocentric radius of the Sun to be $R_0 = 8.5 \pm 0.5$ kpc. Second, Bahcall & Soneira (1980, hereafter B&S) constructed a similar model that combined a disk and spheroid component in order to match observed star counts as a function of magnitude, latitude, and longitude (rather than only the distribution of light across the sky). This work yielded global values of $M_B = -20.1$, $M_V = -20.5$ and $B - V = 0.45$ (assuming no reddening due to dust obscuration; no error estimates were provided). dV&P also summarized a series of earlier determinations of the Galaxy’s total absolute magnitude made before its morphology and gross stellar structure were well understood. These yielded estimates in the range of $M_B \simeq -19.5$ to -19.9 , or $M_V \simeq -20.2$ to -20.5 (Kreiken, 1950; de Vaucouleurs, 1970; Schmidt-Kaler & Schlosser, 1973), corresponding to an integrated $B - V$ color somewhere between 0.3 and 1.0 mag. Additionally, dV83 averaged the colors from a set of galaxies believed to have nearly the same morphological type as the Milky Way (assumed to be

Sb/c) in order to infer $B - V = 0.53 \pm 0.04$.

In the last decade, there has been a growing movement to quantify how typical the Milky Way is amongst galaxies of its type (e.g., Flynn et al., 2006; Hammer et al., 2007; Yin et al., 2009); most of this work has used the measurements of vdK86. We focus specifically on the recent work done by Mutch et al. (2011, hereafter M11) which investigates whether the Milky Way is located in the so-called “green valley” (cf. Mendez et al., 2011; Jin et al., 2014, and references therein); i.e., the sparsely populated region between the bimodal distribution of red and blue galaxies in the color-magnitude diagram (Strateva et al., 2001; Blanton et al., 2003a). After converting van der Kruit’s measurement of Johnson $B - V$ to SDSS AB model $u - r$ and placing the Milky Way on a color-stellar mass diagram, M11 found that no secure conclusions as to the Galaxy’s color could be drawn.

To help resolve this question, we present in this chapter a new method of determining our Galaxy’s global photometric properties with dramatically smaller uncertainties. Our technique resembles the “sosies” method utilized by Bottinelli et al. (1985) and de Vaucouleurs & Corwin (1986). The underlying idea behind that technique was that if two galaxies match well in several calibrated properties, it can be assumed that they share the same luminosity, and hence differences in their apparent brightness can be used to determine their relative distances. Here, we also look for sosies (i.e., analogs) of the Milky Way; however, our goal is different, and we take advantage of larger datasets and more sophisticated statistical treatments in order to take into account uncertainties properly. We derive our results using a method similar to that producing the dV83 value; i.e., we average the observed properties of galaxies selected as Milky Way analogs, though here we carefully account for the systematic biases that can affect such an approach.

Essentially, we make the Copernican assumption that the Milky Way should not be extraordinary for a galaxy of its stellar mass, M_* , and star formation rate, \dot{M}_* . As these two properties are very strongly correlated with galaxies’ global photometric properties, we first obtain a sample of Milky Way analog objects which collectively match the stellar mass and star formation rate of our own Galaxy (taking into account the relevant uncertainties). The range of observed photometric properties of galaxies in this sample provides tight constraints on our Galaxy’s color and absolute magnitude. With these values determined we are then

able to accurately determine the Milky Way’s position in color-magnitude space.

Throughout this chapter, all SDSS *ugriz* magnitudes are reported on the AB system, whereas all Johnson-Cousins *UBVRI* magnitudes are reported on the Vega system. We use a standard Λ CDM cosmology with $\Omega_M = 0.3$ and $\Omega_\Lambda = 0.7$. All absolute magnitudes are derived using a Hubble constant of $H_0 = 100h \text{ km s}^{-1} \text{ Mpc}^{-1}$, therefore making them measurements of $M - 5 \log h$. However, in order to compare measurements of the Galactic SFR and stellar mass, which are measured on an absolute distance scale, to those for extragalactic objects measured on the cosmic distance scale directly, we assume a Hubble parameter of $h = 0.7$, following [Brinchmann et al. \(2004\)](#). Consequentially, the $\log M_\star$ and $\log \dot{M}_\star$ values we use for external galaxies can be adjusted to different choices of H_0 by subtracting $2 \log(h/0.7)$. For clarity, in what follows we will explicitly display the h -dependence of all quantities we use, as well as explain how our results for Milky Way properties change with respect to h .

We structure this chapter as follows. In §3.2 we describe our observational data; this includes discussion of our total stellar mass and star formation rate estimates for the Milky Way in §3.2.1, as well as discussion of the sample of externally measured galaxies we employ in §3.2.2. In §3.3, we describe the criteria used in order to select the subsamples of SDSS galaxies used in this study. In particular, we describe the selection of a sample of Milky Way analog galaxies in §3.3.2, which we use to produce tight constraints on the integrated optical-wavelength properties of the Galaxy in §3.5. In §3.4 we investigate the principle sources of systematic error which may arise from our analog-sample selection methods. We present our final results in §3.5, including tables of useful photometric properties for the Milky Way. Lastly, we summarize this work and discuss its implications in §3.6.

3.2 OBSERVATIONAL DATA

In this section, we present a summary of the observational data we use for this study. We begin by focusing on the total stellar mass, M_\star , and star formation rate (SFR), \dot{M}_\star , of the Milky Way. With these parameters in hand, we then describe the uniform parent sample

of galaxies used, including the methods used to measure their stellar masses, SFRs, and rest-frame magnitudes. The overarching goal of this study is to use this uniformly measured set of galaxies to convert our knowledge of the stellar mass and star formation rate of the Milky Way into constraints on its global photometric properties. The following section will detail how we construct a set of Milky Way analog galaxies for that purpose.

3.2.1 The Milky Way

In Chapter 2, we present updated constraints on the total stellar mass and SFR of the Milky Way, incorporating the wide variety of measurements in the literature. For many of the same reasons that measuring the photometric properties of the Milky Way is difficult (cf. §3.1), there are a limited number of estimates of both Galactic parameters in the literature. In order to extract as much information as we can from these measurements, which encompass a variety of different observational data and methods, we employed a hierarchical Bayesian (HB) analysis method to combine all the measurements of a quantity into one aggregate result. The HB method allows us to account for the possibility that any one of the included Milky Way measurements is incorrect or has inaccurately estimated errors (e.g., due to neglected systematics). The probability of erroneous measurements being incorporated into our meta-analysis is quantified by the inclusion of hyper-parameters in the Bayesian likelihood that characterize the data itself, and which we can simultaneously fit for along with the physical parameters of interest (e.g., M_\star or \dot{M}_\star). The results of this study show that the conclusions from an HB analysis are robust to many different ways of modeling erroneous measurements.

With the present work in mind, the final results from Chapter 2 are normalized so that they can be directly compared to the stellar masses and star formation rates of external galaxies in the MPA-JHU catalog. For the SFR of the Milky Way, we capitalize on the work of Chomiuk & Povich (2011), which tabulated \dot{M}_\star measurements made in the last three decades, renormalizing each to a uniform choice of the Kroupa (2003) initial mass function (IMF) as well as stellar population synthesis code. Applying the HB analysis method to these updated measurements yields a global star formation rate for the Milky

Way of $\dot{M}_\star = 1.65 \pm 0.19 M_\odot \text{ yr}^{-1}$.

For the total stellar mass of the Milky Way, in Chapter 2 we apply the HB analysis method to nearly 20 independent measurements of the stellar mass of the bulge component (including the contribution from the bar) from the literature, including results from photometric, kinematic, and microlensing techniques. For the disk component of the Galaxy, we assume the single-exponential model from [Bovy & Rix \(2013\)](#); this is developed from the dynamical analysis of $\sim 16,000$ G-type dwarf stars segregated into 43 mono-abundance populations based on their position in $[\alpha/\text{Fe}]$ - $[\text{Fe}/\text{H}]$ space, as measured by the SDSS/SEGUE spectroscopic survey. Through Monte Carlo techniques we are able to simultaneously produce model-consistent realizations of the bulge and disk masses; we sum these two components to yield the total stellar mass of the Galaxy, M_\star (the contribution of the stellar halo is negligible). The Monte Carlo techniques allow us to both ensure that each bulge mass estimate is placed on equal footing and to incorporate the current uncertainties in the Galactocentric radius of the Sun, R_0 . In particular, we assume the constraints of $R_0 = 8.33 \pm 0.35$ from [Gillessen et al. \(2009\)](#). We show that once the bulge mass estimates are renormalized to the same definition of stellar mass (including main-sequence stars and compact remnants, but not brown dwarfs), scaled to the same R_0 appropriate to the measurement technique, and normalized to reflect consistent assumptions about the structure and demographics of the stellar populations (Kroupa IMF and single-exponential profile disk) that the results from our HB analysis are insensitive to models of potential systematics affecting the data. All of this work culminates in a total stellar mass for the Milky Way of $M_\star = 6.08 \pm 1.14 \times 10^{10} M_\odot$.

3.2.2 SDSS Galaxies

3.2.2.1 Photometry To select a comparison sample of externally measured galaxies, we make use of data from the Eighth Data Release (DR8; [Aihara et al., 2011](#)) of the Sloan Digital Sky Survey III (SDSS-III; [York et al., 2000](#)). DR8 provides both imaging and spectroscopic data for almost 10^6 galaxies in the local universe, spanning over a third of the night sky. Its five broad optical passbands, labeled u , g , r , i , and z in order of increasing effective

wavelength, fully encompass of the CCD-wavelength window. We make use of DR8, made available in early 2011, due to its best-to-date calibration and reduction of the imaging data. All subsequent data releases from SDSS-III have provided no further refinements for low- z galaxies as studied here. The *Photo* pipeline processing yields a variety of magnitude measurements based on fitting both a pure de Vaucouleurs and a pure exponential profile to the surface brightness distribution of each object. Those quantities labeled `model` reflect the magnitude derived from the better of the two model profile fits in the best-measured band (generally r), which is then convolved with the object’s point spread function (PSF) in each passband to obtain a template for measuring its flux. DR8 also provides the magnitude derived from the optimal linear combination of the two model profiles that best fit the 2D image of any object in each passband, again convolved with the object’s PSF; these are labeled “composite model magnitudes” or `cmodel`¹. The `model` magnitudes are designed to produce the best, unbiased estimate of galaxy colors and so we use these to evaluate any color properties we discuss below. However, while the `cmodel` magnitudes are not recommended for producing galaxy colors, they do reflect the best estimate of the “total” flux of a galaxy in each passband. Therefore, all absolute magnitudes described below are derived from the `cmodel` measurements.

We have obtained K -corrections on all magnitudes in the DR8 catalog to rest-frame $z=0$ and $z=0.1$ SDSS passbands using the `kcorrect v4.2` software package (Blanton & Roweis, 2007). This entails fitting spectral energy distribution (SED) models to the observed *ugriz* extinction- and AB-corrected magnitudes, given the observed redshift, and then using this fit to determine offsets between observed quantities and magnitudes measured in rest-frame bands (e.g., Hogg et al., 2002). The observed z also provides a luminosity distance (given the cosmology we assume) and hence the distance modulus, $m - M$; we use the `kcorrect v4.2` software to obtain rest-frame absolute magnitudes that are derived by subtracting this distance modulus along with the K -correction from the extinction- and AB-corrected apparent `cmodel` magnitude in each band. We obtain galaxy colors by taking the difference of two rest-frame absolute magnitudes, but using `model` magnitudes in place of `cmodel` as

¹See <http://www.sdss3.org/dr8/algorithms/magnitudes.php> for further detail, as well as discussions in Dawson et al. (2013).

described above. We choose to adopt the notation from [Blanton & Roweis \(2007\)](#) when presenting our results: we denote an absolute magnitude for passband x as observed at redshift z by ${}^z M_x$.

At this point, we also use the `kcorrect` package to convert each galaxy’s set of SDSS *ugriz* (AB) magnitudes to an equivalent set of Johnson-Cousins *UBVRI* (Vega) magnitudes, as well as their respective K -corrections. This allows us to calculate *UBVRI* extinction- and K -corrected (`cmodel`-based) absolute magnitudes and (`model`-based) colors, which we can then analyze in parallel to *ugriz* measurements in order to yield our results transformed to the Johnson-Cousin system. As we will see in §3.6, this will be useful for comparing our results to the literature, and should be more robust than using any transformation equations available that are averaged over all galaxy types.

3.2.2.2 MPA-JHU Stellar Masses and SFRs For a large sample ($\sim 10^6$) of galaxies with spectroscopic redshifts from SDSS below 0.7, the MPA-JHU galaxy property catalog provides estimates of total stellar masses and star formation rates. These are currently publicly-available at <http://www.mpa-garching.mpg.de/SDSS/DR7/>, and are based on SDSS Data Release 7 photometry. However, to ensure the greatest possible accuracy in our results, for this study we have produced an upgraded version of this catalog by recalculating each galaxy’s M_\star and \dot{M}_\star using the same algorithms, but applied to the photometric measurements released in DR8. Hence, our initial dataset consists of the subset of galaxies in the MPA-JHU catalog that also have photometric measurements reduced through the DR8 pipeline. All results presented herein are based on our DR8-based M_\star and \dot{M}_\star measurements, which assume a Kroupa IMF. In the following, we briefly summarize the Bayesian methodology used to produce them.

Total stellar masses are determined following the same philosophy as [Kauffmann et al. \(2003\)](#) and [Gallazzi et al. \(2005\)](#), but by fitting models of stellar population synthesis (SPS) to each galaxy’s photometry instead of using any spectral features. Here, we first construct a large grid of galaxy models from [Bruzual & Charlot \(2003, BC03\)](#), encompassing a wide range of possible star formation histories. Each model produces a synthetic spectrum which we convolve with *ugriz* passbands to produce model photometry. For each galaxy, we then

determine the likelihood for each model by calculating the χ^2 from differences between fluxes corresponding to the model photometry and the observed model magnitudes. Adopting flat priors on all model parameters, we then calculate the posterior probability for each model given the observations. This is most similar to the methods of [Salim et al. \(2007\)](#), differing in that the latter generated sets of input parameters by randomly drawing them from their priors instead of employing a grid. Lastly, we integrate our grid of posteriors along all but the stellar mass axis in order to produce the marginalize posterior PDF for M_\star .

Star formation rates are determined from the technique described in [Brinchmann et al. \(2004\)](#), but with several improvements. For star-forming galaxies this entails fitting the emission line models from [Charlot & Longhetti \(2001, CL01\)](#) to their $H\alpha$, O II, $H\beta$, O III, N II, and S II emission fluxes measured from their SDSS spectra, after subtracting the continuum and absorption features using the SPS spectra from the latest updates to the BC03 libraries. In this case, a grid of $\sim 2 \times 10^5$ CL01 models are investigated, which make up a 4-dimensional grid of metallicities, ionization parameters, total dust attenuations, and dust-to-metal ratios. Similarly as described above, the resulting grid of posteriors for all models can then be integrated over the other three axes to produce the marginalized posterior PDF for dust attenuation. This is then used to estimate an unattenuated $H\alpha$ -luminosity, which is then converted to a SFR using the [Kennicutt \(1998b\)](#) conversion factor.

This yields a measurement of the SFR of each galaxy inside the SDSS 3'' fiber. To overcome aperture bias, and hence produce an estimate of \dot{M}_\star for the entire galaxy, we now follow in the footsteps of [Salim et al. \(2007\)](#). This requires calculating photometry for the light that falls outside of the fiber and fitting stochastic SPS models to it; for each galaxy we combine the SFR measured from inside and outside of the fiber to determine its total \dot{M}_\star . As a result, the SFRs employed herein should match well with the ‘‘UV’’ estimates by [Salim et al. \(2007\)](#) for all classes of galaxies over the entire dynamic range of \dot{M}_\star values. For a more in-depth discussion, the reader should see B04 and the MPA-JHU catalog website (listed above).

Ultimately, our methods produce DR8-based posterior PDFs for the log stellar mass and log star formation rate of each galaxy in our SDSS sample. In our discussions to follow, when referring to a galaxy’s log M_\star or log \dot{M}_\star we are truly referring to the mean value measured

from the posterior. We could equally have used median values for this study, as using them instead yields no differences in our results. We also calculate the cumulative distribution functions (CDFs) measured from each galaxy’s posteriors, and we use \mathcal{P}_x to denote the value corresponding to the x -th percentile in the CDF. We then calculate an effective standard deviation for both quantities as $(\mathcal{P}_{84} - \mathcal{P}_{16})/2$. We label these as $\sigma_{\log M_\star}$ and $\sigma_{\log \dot{M}_\star}$ hereafter. We note that these effective error estimates are used only to screen galaxies with highly uncertain measurements in §3.2.2.3 and for investigating the impact of Eddington bias on our results in §3.4.1, and hence are sufficient for our purposes.

3.2.2.3 Initial Cuts From the sample of galaxies we have described so far, we next restrict to a subset of those that make up the SDSS main galaxy spectroscopic sample (whose overall selection is described in [Strauss et al., 2002](#)), which includes only objects with good-quality, clean measurements. To do so, we take advantage of the *Photo* pipeline processing flags and image bitmasks to eliminate problematic objects from the full DR8 sample. We first restrict to objects that were targeted as main sample galaxies by enforcing that the `primTarget` flag is set to “galaxy.” We then reduce to galaxies with good-quality observations taken from the *Legacy* target plates by requiring the SDSS plate information tags `survey`, `programName`, and `plateQuality` are set to “sdss,” “legacy,” and “good,” respectively. We ensure a good-quality detection by requiring that the `BINNED1`, `BINNED2`, or `BINNED4` flag is set for the r -band image. We exclude objects with any of the following r -band image flags² set: `SATUR`, `BRIGHT`, `BLENDED`, `NODEBLEND`, `DEBLEND_NOPEAK`, `DEBLENDED_TOO_MANY_PEAKS`, `PEAKCENTER`, `NOTCHECKED`, `CR`, `NOPROFILE`, `MANYPETRO`, `NOPETRO`, `PSF_FLUX_INTERP`, `BAD_COUNTS_ERROR`, `INTERP_CENTER`, `BAD_MOVING_FIT`, or `DEBLENDED_AT_EDGE`. At this point, we also exclude any galaxy whose inverse variance ($= 1/\sigma^2$) in absolute g - or r -band magnitude is calculated to be 4 mag or smaller after K -corrections, or that has $\sigma_{\log M_\star} > 1$ or $\sigma_{\log \dot{M}_\star} > 0.5$, in order to exclude any object with highly uncertain luminosity, color, SFR, or stellar mass (these restrictions on property errors exclude only the most extreme outliers in the data, comprising $\ll 1\%$ of the sample). As a result of these cuts, the DR8 sample is

²See http://www.sdss3.org/dr8/algorithms/photo_flags.php and sources therein for explanations of these flags.

reduced to 337,331 galaxies from $\sim 10^6$ with no restrictions applied.

3.3 CONSTRUCTING USEFUL SDSS GALAXY SAMPLES

We next trim our set of cleanly measured galaxies from the main galaxy sample to produce a uniform subset suitable for statistical analyses. In this section we discuss the cuts employed to produce two important subsamples used in deriving our final results. First, we describe the selection of a volume-limited sample, which consists of all galaxies lying in a redshift range such that any object with both SFR and total stellar mass values similar to those of the Milky Way will be included in the SDSS sample. Next, we discuss our method of identifying a set of Milky Way analog galaxies from this volume-limited sample. These galaxies, chosen based upon their M_\star and \dot{M}_\star values, can then be used to estimate the global photometric properties of the Milky Way, while the volume-limited sample provides the context for discussing the Milky Way’s location in color-magnitude space.

3.3.1 Selection of a Volume-Limited Sample

The SDSS main galaxy sample (Strauss et al., 2002) is bounded by a limiting Petrosian magnitude of $r \leq 17.77$ after correction for Galactic extinction. Of course, this introduces a radial selection effect, known as Malmquist bias (Teerikorpi, 1997), whereby only the intrinsically-brightest galaxies are present in the data at large z , whereas less luminous galaxies at the same redshift will not be targeted for spectroscopy. We therefore restrict ourselves to a volume-limited sample, ensuring that all galaxies in the Milky Way SFR and M_\star ranges are detected and available for selection, regardless of their luminosities.

To do this, we first select a sample of Milky Way analog galaxies via the process described in the following section from the clean main galaxy sample (i.e., ones with good-quality measurements, as described in §3.2.2), but with no restriction in redshift. Next, we overlay this sample of analogs upon the clean main galaxy sample with $z > z_{\min}$ in ${}^0(g-r)$ vs. 0M_r color-magnitude space; we then increase z_{\min} until, by eye, the included objects fall as faint

as the faintest Milky Way analogs, but no more so. The corresponding value of z_{\min} will then serve as the *maximum* redshift for our volume-limited sample. This is true since we expect that the least-luminous galaxies in a sample must be at the smallest available redshift to be seen at all; or, we can conclude that at any redshift below z_{\min} such faint galaxies would be included in a sample, but at any greater redshift they would not. Therefore, z_{\min} corresponds to the upper bound on the range of redshifts allowed for a volume-limited sample of Milky Way analogs.

We note that this method is an extension of the standard procedure generally used to identify volume-limited samples of objects (see, e.g., [Tago et al., 2010](#); [Tempel et al., 2014](#)). Whereas one typically investigates the luminosity completeness level as a function of redshift, we have extended this analysis to the CMD. In this way, we have ensured that all the results we present below (i.e., the luminosities and colors we infer for the Milky Way) are guarded against Malmquist bias. We also note that this process of choosing a z_{\min} contributes a negligible amount of uncertainty to our final results presented below. For example, changing z_{\min} by ± 0.005 yields a shift in all of our results by $< 0.05\sigma$.

Based on investigation of Milky Way analog color-magnitude diagrams for different limiting redshifts, we find that a cut of $0.03 < z < 0.09$ ensures that all analogs have $r < 17.77$, so that the SDSS magnitude limit has no effect on our results. The lower bound on z is used to limit the impact of aperture effects on the properties measured for these galaxies; again, a ± 0.005 shift in this value yields a $< 0.05\sigma$ change in our results. In addition to applying this redshift cut, we simultaneously enforce that all galaxy redshifts are measured at high confidence by ensuring that no redshift warning flags are set within the SDSS catalog (i.e., each has a value `z_warning` = 0). The resulting volume-limited sample includes 124,232 galaxies from the clean main galaxy sample.

In [Figure 3.1](#), we show the position of the Milky Way with 1σ constraints as determined in [Chapter 2](#) in $\dot{M}_\star - M_\star$ space, overlaid upon log-spaced contours depicting the density of the volume-limited sample. We have highlighted the approximate locations of the “main-sequence” of star-forming SDSS galaxies in blue and the region of quiescent galaxies in red. We also do this in our color-magnitude plots below; note that the relative positions of the regions corresponding to these two populations are flipped in magnitude space. In

the following section, we explain how we apply the Galactic constraints discussed in §3.2.1 to the volume-limited sample in order to construct a sample of Milky Way analogs, which in total should exhibit the same properties as the Milky Way. We can then examine where these analogs lie in color-magnitude space, ultimately converting our knowledge of where the Milky Way lies in the \dot{M}_\star - M_\star plane into similar constraints on its photometric properties.

3.3.2 Identifying Milky Way Analogs

We now collect a set of galaxies that, as an ensemble, can be used to constrain the overall photometric properties of our Galaxy; i.e., a sample of *Milky Way analog galaxies*. By our definition, these analogs are selected in such a way that the distributions of their measured M_\star and \dot{M}_\star values match the posterior probability distributions describing the Galactic M_\star and \dot{M}_\star found in Chapter 2 using a hierarchical Bayesian (HB) analysis (these results are detailed in §3.2.1). To do so, we apply a randomized selection procedure to the galaxies in the volume-limited sample, as follows.

We begin by randomly drawing a single value from each of the adopted PDFs describing the Milky Way’s M_\star and \dot{M}_\star , independently of each other. Ideally, we would like to then select a single galaxy from the volume-limited sample whose measured properties match these values exactly; we could then trivially build a sample of Milky Way analogs by repeating this process a large number of times. However, in general there will be no galaxies with properties that match these values perfectly. Therefore, we use our pair of values drawn from the Galactic distributions as a point of reference in the \dot{M}_\star - M_\star plane and identify all galaxies from the volume-limited sample that lie within a small tolerance window centered on this point. We choose this window to be the rectangular box that encompasses all values to within $x\%$ of the M_\star & \dot{M}_\star values drawn. To ensure that the distributions of analog properties will still match the fiducial Galactic posteriors, we require that $x\%$ is much smaller than the error in either of the Milky Way M_\star and \dot{M}_\star results presented in Chapter 2. Finally, from the galaxies that lie within our tolerance window we randomly select one as a Milky Way analog. We repeat this process 5,000 times as the first step in building our sample, providing us with a set of 5,000 Milky Way analog galaxies.

We have employed a tolerance window in our method, as opposed to simply selecting the object in the volume-limited sample nearest each (M_\star, \dot{M}_\star) pair drawn, to maximize the number of unique Milky Way analogs that make up our sample. In practice, we find that when using a 1% tolerance our window encompasses at least one galaxy from the volume-limited sample $\sim 75\%$ of the time, and typically contains up to 8 candidate objects. The remaining $\sim 25\%$ of the time we can expand our window to a 3% tolerance from the drawn M_\star and \dot{M}_\star values in order to encompass a set of at least one galaxy, from which we randomly draw one analog. Given that the fractional error in the adopted M_\star and \dot{M}_\star for the Milky Way is $\sim 19\%$ and $\sim 12\%$, respectively, we find that the exact size of the 1%/3% acceptance window is inconsequential to this study. We have tested for the impact of using broader parameter space window sizes, though still small compared to the Milky Way measurement errors, and always recover the same results (to well within the quoted errors). We have also tested for any changes in our results when selecting analogs by their total specific star formation rate (SSFR) and M_\star in place of SFR and M_\star ; again, the differences are well within the uncertainties. In light of this, we have chosen to present the results of using the SFR measurements only, as using SSFR introduces substantial covariance (i.e., SSFR correlates strongly with M_\star), whereas the SFR and total stellar mass of the Milky Way are determined independently in Chapter 2.

Just as it is a problem for observing the Milky Way, dust alters the observed colors and magnitudes of star-forming galaxies observed with high inclination angles. We therefore exclude objects likely to be edge-on spiral galaxies from our Milky Way analog sample. Accordingly, from the 5,000 galaxies selected initially, we exclude all those which have both a best-fit axis ratio $b/a < 0.6$ measured from a purely exponential profile fit to the surface brightness density in the r -band, as well as a value $f_{\text{deV}} < 0.5$, where f_{deV} effectively denotes the fraction of light in the galaxy's image that is contributed from a bulge-like component vs. a disk-like component, again generally measured from the 2D r -band image. In effect, we are excluding all galaxies we have selected that are both edge-on and disk-dominated. It is important to note that, because we have applied no morphological constraints on Milky Way analogs, excluding disks in this way will introduce a morphological bias into our sample to some extent (i.e., the ratio of bulge-dominated and elliptical galaxies to disk-dominated

galaxies will increase), an effect we will need to correct for. Therefore, it is important to apply this cut *only later* in our Milky Way analog selection process so that we are able to track the fraction of disk galaxies that make it into the sample before and after its implementation; knowing these numbers will allow us to make the proper correction. In §3.4.2 we will provide a more in-depth discussion of this, including how this inclination cut was chosen and its impact on our results. Ultimately, after removing edge-on disks we are typically left with a clean sample of $\sim 3,500$ galaxies.

For the particular realization we use in this study, our process more precisely yields 3,402 galaxies that we will use to derive our results below, and which we henceforth call the Milky Way analog sample (MWAS). We note that, of the analog galaxies selected, only 935 (or $\sim 27\%$) are unique objects. It is important to keep duplicate objects so that the distribution of property values for the MWAS accurately matches the posterior distributions for the Milky Way properties we have found in Chapter 2 (see §3.2.1). In practice, we find that if we only keep the set of unique objects, the mean M_\star of our sample has a significant bias ($\sim 2\times$ the standard error) compared to when we eliminate duplicates. The SFR distribution is affected less. These biases are avoided altogether by allowing objects to be selected multiple times as a Milky Way analog.

For convenience, we show a flowchart in Fig. 3.2 that summarizes sections 3.2.2–3.3.2 into a step-by-step procedure that yields all of the different samples of galaxies that we employ in this study. Figure 3.3 shows the positions of the MWAS in \dot{M}_\star – M_\star space as red dots, overlaid upon the same contours for the volume-limited sample as Figure 3.1. The spread of these dots appears broader than the Galactic constraints in Fig. 3.1 due to both the saturation of color where there are many objects and the substantial number of $>3\sigma$ events to be expected in any sample of 3,500 numbers; as mentioned above, the size of the search box is small in comparison to the spread in Milky Way values.

Figure 3.4 shows our sample of Milky Way analogs (red dots) overlaid on the volume-limited sample (greyscale contours), similar to Fig. 3.3, but now plotted in the ${}^0(g-r)$ vs. 0M_r color-magnitude diagram. Mapping these galaxies from one parameter space to the other noticeably increases their scatter compared to the underlying population from which they were drawn. However, their tight correlation in \dot{M}_\star – M_\star space, as expected, produces

significant constraints in the color-magnitude diagram, providing us with information on what locations could feasibly be occupied by the Milky Way. We display a division line between the red sequence and blue cloud regions obtained by taking a line parallel to the slope of the red sequence, but offset to the point where contributions from red sequence and blue cloud galaxies are equal, determined based upon the assumption that the spread in red sequence colors about the center line is Gaussian (Graves, priv. comm.; cf. Taylor et al., 2015b). The peak density of the Milky Way analogs lies near the division line, though many lie far above or below it.

With the MWAS in hand, we are now ready to calculate new constraints on the photometric properties of the Milky Way. For instance, simply calculating the mean and standard deviation of the $^0(g - r)$ colors of our sample yields $\sim 0.72 \pm 0.07$, and similarly we find $\sim -20.75 \pm 0.37$ for 0M_r . However, as mentioned above, before presenting our final results we must first account for any major potential sources of systematic error in our method (e.g., the morphological bias introduced from removing any edge-on disks from the MWAS), and make the proper corrections. We will next discuss these systematics and the corrections that they require in the following section.

We note that for any *mean* quantity described hereafter, including those provided in our tables of results, we are actually using the Hodges-Lehmann (H-L) estimator (Hodges & Lehmann, 1963). The H-L estimator is a robust measure of the median of the data, which is calculated by determining the median value of the set $\{(x_i + x_j)/2\}$ for all pairs i, j . For N Gaussian-distributed data points with a standard deviation σ , the mean has standard error σ/\sqrt{N} , while the median has uncertainty $\sim\sigma/\sqrt{0.64N}$. The H-L estimator has an error of $\sim\sigma/\sqrt{0.955N}$, comparable to the mean, but shares the robustness to outliers of the median, making it a superior choice in most cases. Hence, using the H-L estimator should reduce the impact of significant outliers in our sample, in contrast to the ordinary mean, but will have smaller errors than the median.

Instead of calculating for all possible pairs, which requires excessive computation time, we bootstrap this estimate by choosing a set of random i, j pairs equal to ten times our effective sample size (reducing from $\sim 6 \times 10^6$ total pairs down to a much more manageable 34,020 for our typical calculations). This introduces a small amount of extra uncertainty (=

$\sigma/\sqrt{2}/\sqrt{0.64 \times 34,020} = 0.27\sigma$) which must be added in quadrature to the nominal standard error in the H-L estimator. The net result is that our estimator yields uncertainties 3% larger than the true H-L mean would. This additional uncertainty is negligible compared to our overall errors; hence this technique does not introduce any measurable amount of potential bias, and the bootstrapped H-L estimator in our application will still have significantly smaller uncertainty than the median value.

3.4 SYSTEMATICS

In this section we discuss the principle systematic errors and biases that could affect the methods applied in this study, other than systematic errors in either of Milky Way or extragalactic M_\star & \dot{M}_\star measurements, which we defer discussion of to §3.5. First, we investigate the impact of Eddington bias, i.e., the bias resulting from selecting objects using quantities that are affected by measurement errors. We provide details on how we can estimate its overall effect, which we then subtract from our final results. In addition, we analyze the impact of reddening associated with observing disk galaxies at an inclination on the optical properties of our Milky Way analog sample. We discuss how we identify inclined objects in the SDSS measurements, as well as our methodology for mitigating reddening or extinction effects that otherwise, when neglected amongst the Milky Way analog sample, could distort the inferred photometric properties of our Galaxy. We will demonstrate that, after corrections for these effects, the remaining systematic uncertainties from these effects are well below statistical uncertainties.

3.4.1 Eddington Bias

It is important to address how the uncertainties in our stellar mass and SFR estimates affect our results. Specifically, we are drawing each Milky Way analog from a small bin in SFR- M_\star space. For any parameter whose intrinsic probability distribution function has significant higher derivatives (second or beyond), scatter due to errors will move more objects from bins

with more objects to those with fewer as opposed to the converse. This causes the observed distribution of values with errors to be biased compared to the true, underlying distribution. This phenomenon is known as Eddington bias and is very common in astronomy; it is the generalized form of the Malmquist bias which affects luminosity distributions. For instance, since massive galaxies are rare, a galaxy with a large M_\star estimate is more likely to have an actual stellar mass below that value than above, since there are many more objects that could up-scatter than down-scatter. As a result, in aggregate the M_\star values of our Milky Way analogs should be biased high. Similar effects could affect SFR, luminosity, or color estimates.

To quantify this bias, we consider a statistical exercise of perturbing each galaxy’s M_\star and \dot{M}_\star value by Gaussian noise sampled from their estimated errors, and then reselecting a set of Milky Way analog galaxies utilizing the perturbed measurements. To be specific, we offset the mean $\log M_\star$ and $\log \dot{M}_\star$ values individually for each galaxy by a value randomly drawn from a Gaussian distribution centered at zero with a standard deviation of that object’s $\sigma_{\log M_\star}$ or $\sigma_{\log \dot{M}_\star}$ value. We perform $N = 100$ realizations of this perturbation process, each time selecting a new set of Milky Way analog galaxies in the same manner described in §3.3.2. Calculating the H-L mean for each *ugriz* property for each realization yields a distribution characterizing our nominal results with the effects of Eddington bias applied two times, instead of the single impact that should affect our standard sample. We bootstrap this distribution of doubly-biased values to measure the mean H-L mean and its standard error (Efron, 1979). We then repeat this exercise but applying the noise 2, 3, or 4 times consecutively before selecting a sample. This yields distributions of the mean property of interest after repeatedly applying the bias in our method n times; the mean of this distribution we denote μ_n . For clarity, note that we consider the actual Eddington bias in our standard MWAS as the first ($n = 1$) application, and thus distributions of *ugriz* properties yielded from p successive perturbations of the M_\star and \dot{M}_\star values by their errors are labeled $n = p + 1$ in our plots and discussion below. Fig. 3.5 displays examples of this analysis for 0M_r .

To estimate the Eddington bias in each property we then plot the difference between the means of the n and $n - 1$ values of a given parameter as a function of n ; i.e., $\mu_n - \mu_{n-1}$ versus

n . We then perform a least-squares quadratic fit to these four data points, incorporating the error estimates from our bootstrap analysis. We use the resulting curve to extrapolate to $n = 1$, whose ordinate corresponds to the offset in the “mean” of a given property between when Eddington bias affects our sample of Milky Way analog galaxies and when it does not. This value is then subtracted from the observed mean for that property of the MWAS. In Fig. 3.5 we show what the results of this exercise typically look like, again adopting 0M_r as an example.

In order to calculate the uncertainty in our estimate of the Eddington bias, we construct the covariance matrix for the coefficients of a least-squares quadratic fit, $A + Bn + Cn^2$. We are interested in the σ of the point at $n = 1$; this simply reduces to the square root of the sum of all elements of the covariance matrix. We note that if the uncertainties in our stellar mass estimates were primarily due to photometric errors, this treatment would be incorrect, as if an object had (say) a higher-than-actual estimated M_\star value, it would also have a too-bright M_r . However, this does not appear to be the case; we find that stellar mass errors are $> 5\times$ larger than would be expected from SDSS photometric errors, so other sources of uncertainty clearly dominate, and we can safely treat absolute magnitudes and stellar masses as statistically independent.

3.4.2 Inclination Reddening

As mentioned in §3.3.2, we have removed any edge-on disk galaxies that originally were included in the MWAS. This is because, just as reddening and extinction affect observations through the disk of the Milky Way, they also alter measurements of external spiral galaxies with their disks aligned along our line of sight. The spectral energy distribution (SED) measured for such an edge-on disk galaxy will be significantly distorted; we will receive a much smaller fraction of blue light than when observing face-on, while the flux of redder optical light detected will be much less affected. This means that the more edge-on a disk galaxy in the SDSS sample is, the less representative our observations will be of its intrinsic photometric properties (see, e.g., Unterborn & Ryden, 2008; Maller et al., 2009; Salim et al., 2009). It is important, therefore, to ensure the properties of the MWAS are not skewed by

this effect. In this section we discuss quantitatively our method of choosing the appropriate inclination threshold for the MWAS, as well as the unwanted side effect that it creates, namely morphological bias, which we will also need to correct for.

DR8 provides measurements of each galaxy’s semi-minor-to-semi-major-axis ratio, b/a , as determined from the exponential profile best fit to its 2D image (labeled `abExp` in the DR8 catalog). Low values of b/a indicate that the galaxy’s image has high eccentricity. Additionally, when calculating `cmodel` magnitudes (see §3.2.2), the weight of the de Vaucouleurs profile in the best-fit linear combination with the exponential profile matched to the object’s image is recorded as f_{deV} (or alternatively `fracDeV`). Essentially, this quantifies the fraction of the total light in the 2D image of the galaxy that is well fit by a Sérsic index of 4 as opposed to 1. For our purposes, we classify any object with $f_{\text{deV}} > 0.5$ as a bulge-dominated or elliptical galaxy, and any with $f_{\text{deV}} < 0.5$ as a disk-dominated galaxy. Our objective is then to use these two parameters to effectively eliminate edge-on disk-dominated objects (i.e., ones well fit by an exponential profile and that appear to have a high inclination angle) from being selected as part of the MWAS to prevent any systematic offsets in our results due to reddening. We are not concerned about including early-type galaxies with low b/a in the sample, as they contain little cold gas and dust, so extinction effects are comparatively minor for them.

We have tested the impact of this cut by varying the minimum-allowed axis ratio for disk-dominated galaxies in our sample and measuring how the mean ${}^0(g - r)$ color is affected. To do so, we again employ a process of selecting a set of 5,000 Milky Way analog galaxies identical to that explained in §3.3.2, but unlike before, we do not yet apply any constraints on the b/a or f_{deV} values in the sample. In Figure 3.6, we display how the integrated color of this set changes as we impose constraints on b/a and f_{deV} in three different ways.

First, the upper (red dashed) curve shows the effect of removing only disk galaxies (i.e., ones having $f_{\text{deV}} < 0.5$) as we systematically increase the minimum allowed axis ratio. Initially, as we increasingly remove the lowest b/a (most-inclined) disks we see the mean ${}^0(g - r)$ color shifts blue-ward, as expected. However, once we increase our threshold to remove disks with $b/a \lesssim 0.35$, we find an unwanted side effect: increasingly removing the disk population gives increasing weight to bulge-dominated and elliptical populations, yielding a

trend toward net redder color.

Second, we investigate a scenario that attempts to avoid this problem. The lower (dash-dotted blue) curve shows the effect of removing *any* object regardless of its type (i.e., its f_{dev} value) as we systematically increase the minimum allowed axis ratio. We note that at $b/a \gtrsim 0.35$ bulge-dominated and elliptical galaxies outnumber disk-dominated galaxies at a ratio of $\sim 3:2$; this is the case for the entire volume-limited sample, as well as Milky Way analogs. Hence, we find that in this case the mean color of the sample becomes increasingly bluer as we increase our minimum allowed b/a threshold above 0.35. However, since this trend does not stabilize as we push our threshold higher, it is likely that we are increasingly oversampling disk-dominated objects due to preferentially discarding the more prevalent elliptical and bulge-dominated galaxies in this regime.

Lastly, we present an alternative treatment shown by the middle (solid black) curve. Here, we remove the same disk galaxies that we do in the first scenario, leaving all bulge-dominated and elliptical types initially selected in the sample. However, we now calculate a *weighted* mean quantity, where we ensure that the contribution of disk galaxies remaining, after applying any minimum threshold on b/a , is equal to that from the disks present in the sample before any cut. In other words, we calculate the mean property of our filtered sample of galaxies by multiplying the contribution from the remaining disk types after selection by a weighting factor $W = N_{\text{disks}}^{\text{before}}/N_{\text{disks}}^{\text{after}}$, where $N_{\text{disks}}^{\text{before}}$ and $N_{\text{disks}}^{\text{after}}$ represent the number disk galaxies in the sample before and after applying this cut, respectively. For instance, for ${}^0(g-r)$ color our estimator reduces to

$$\langle {}^0(g-r) \rangle = \frac{N_{\text{disks}}^{\text{before}} \langle {}^0(g-r)_{\text{disks}}^{\text{after}} \rangle_{\text{H-L}} + N_{\text{ellipticals}} \langle {}^0(g-r)_{\text{ellipticals}} \rangle_{\text{H-L}}}{N_{\text{disks}}^{\text{before}} + N_{\text{ellipticals}}}, \quad (3.1)$$

where $N_{\text{ellipticals}}$ is the number of ellipticals in the MWAS, $\langle {}^0(g-r)_{\text{disks}}^{\text{after}} \rangle_{\text{H-L}}$ is the mean ${}^0(g-r)$ color of disk galaxies after the b/a and f_{dev} cuts are applied, and $\langle {}^0(g-r)_{\text{ellipticals}} \rangle_{\text{H-L}}$ is the mean ${}^0(g-r)$ color of ellipticals in the MWAS. The H-L subscript here denotes that we are truly using the Hodges-Lehmann estimator of the mean.

By comparing the different curves in Figure 3.6, it is clear that the weighted mean is favorable over the other scenarios for two reasons. First, the slope of the weighted-mean curve is shallow enough that moving from a cut of $b/a > 0.4$ to $b/a > 0.8$ makes a $\lesssim 0.01$

magnitude difference in integrated ${}^0(g-r)$ color. Hence, compared to the other scenarios, this prescription results in more stable values of mean ${}^0(g-r)$ over basically all reasonable threshold values of b/a . Second, the position of this curve is between the other two, indicating that we are avoiding giving too much weight to either of the red or blue populations, and hence limiting the impact of any morphological bias. We note that simply cutting out whole classes of galaxies based on their axis ratios, as in the first two scenarios, provides a more extreme way of dealing with inclination reddening. The difference measured, however, between the curve for our weighted-mean scenario and either of the other two scenarios is $\lesssim 0.02$ mag; all of these differences are significantly less than the statistical errors in ${}^0(g-r)$ color of the sample (~ 0.06 mag). Based on the results of this exercise, we eliminate any of the original 5,000 galaxies selected for the Milky Way analog sample having both $b/a < 0.6$ and $f_{\text{dev}} < 0.5$, and we report the reweighted mean property to minimize the impact of any reddening of the sample due to inclination. As noted above, this cut typically removes $\sim 30\%$ of a MWAS realization.

We note that if we were to avoid edge-on disks entirely during our selection of Milky Way analogs (they have been selected based only on their M_{\star} and \dot{M}_{\star} values), then our results would suffer from the same morphological bias that is evident from the red dashed curve in Fig. 3.6, but with no way of knowing to what quantitative extent. Therefore it is important to make a correction only at this stage in the analysis – i.e., calculating our results via a weighted mean after removing edge-on disks – so that we may correct for both systematic effects, namely inclination reddening and morphological bias. Fortunately, we have found that the variations due to such effects are far below the random uncertainties.

One other option would be to correct for inclination-related reddening on an object-by-object basis, rather than trimming and reweighting the sample as was done here. For instance, [Maller et al. \(2009\)](#) provide formulae for converting inclination-dependent observed quantities into intrinsic ones. When applied to the color-magnitude relationship their methods transform the SDSS blue-to-red galaxy ratio from 1:1 to 2:1 in the absolute magnitude range of $-22.75 \leq M_K \leq -17.75$. Converting to intrinsic properties could eliminate the need for inclination cuts altogether and allow us to utilize a larger subset of the SDSS main galaxy sample, though at the cost of adopting a particular model for extinction corrections.

In any case, we point out that the difference between our choice of correction and the extreme limits displayed in Fig. 3.6 is a ~ 0.02 mag shift, which turns out to be a factor of 3 times smaller than the uncertainties in our final results. In addition, the slope of this curve becomes very shallow beyond a minimum axis ratio of 0.4, so any reasonably chosen cut would yield negligible change to our results. Similar analyses have demonstrated that this same method works well for all colors considered as well as for correcting extinction in absolute magnitudes. Overall, we expect that any alternative prescription for inclination would have inconsequential impact on the results of this study.

Lastly, in Figure 3.7 we show the distribution of M_\star and \dot{M}_\star values for Milky Way analogs compared to the posterior distributions used for selecting them. This includes distributions for the original sample of 5,000 before any cuts, the 3,402 galaxies remaining after removing those with $b/a < 0.6$ and $f_{\text{dev}} < 0.5$, and the reweighted distribution of those 3,402 objects in congruence with Equation (3.1). Where necessary, we have renormalized each distribution to reflect a total sample size of 5,000 objects. In all cases, we find the mean and standard deviation of our sample match those of the posterior distribution and have confirmed that they are Gaussian distributed via a Q-Q plot analysis (Wilk & Gnanadesikan, 1968). Hence, we find that our treatment of inclination reddening and morphological bias does not compromise the fundamental design of our Milky Way analog sample in M_\star - \dot{M}_\star space.

3.5 RESULTS

With the Milky Way analog sample (MWAS) assembled and major systematic errors accounted for, we are now able to produce a comprehensive outside-in portrait of our Galaxy. Table 3.1 presents the inferred photometric properties we determine for the Milky Way in rest-frame $z=0$ SDSS passbands, and likewise Table 3.2 presents rest-frame $z=0.1$ SDSS passband results. The values shown are calculated as the weighted (Hodges-Lehmann estimator of the) mean as described in §3.4.2 and have been corrected for Eddington bias as detailed in §3.4.1. Each row is calculated independently of any other table entry; for instance, we utilize the full distribution of ${}^0(g-r)$ amongst the Milky Way analogs, rather than deriving

this value by subtracting 0M_r from 0M_g (this is also due to our colors being derived from `model` magnitudes, whereas absolute magnitudes are based upon `cmodel`). For reference we list the inherent Eddington bias that has been subtracted in juxtaposition to each corrected value.

In addition, we tabulate the derivative of each property with respect to total stellar mass and star formation rate. This is accomplished by offsetting the distributions we assume for the Galactic M_\star and \dot{M}_\star by ± 0.1 times their respective errors and redoing our analyses. Along with our fiducial results, this provides 3 data points to which we fit a quadratic Lagrangian-interpolation polynomial, and then calculate its derivative at the central data point. We choose an offset of $\pm 0.1\sigma$ so that the resulting Galactic range in \dot{M}_\star - M_\star space does not require selecting a new volume-limited sample of objects.

As discussed in §3.1, all extragalactic measurements of $\log M_\star$ and $\log \dot{M}_\star$, measured on the cosmic distance scale, can be converted to reflect different values of the Hubble constant by subtracting from them $2 \log(h/0.7)$, effectively shifting them relative to the Milky Way’s position in this parameter space. If we were to instead add this quantity to the Galactic $\log M_\star$ and $\log \dot{M}_\star$ values, the change in our results would be identical; this allows one to calculate how the absolute magnitudes and colors we calculate for the Milky Way change for different h using quantities given in Tables 3.1 & 3.2. For example,

$$\frac{d({}^0M_r - 5 \log h)}{dh} = \frac{\partial({}^0M_r - 5 \log h)}{\partial M_\star} \frac{dM_\star}{dh} + \frac{\partial({}^0M_r - 5 \log h)}{\partial \dot{M}_\star} \frac{d\dot{M}_\star}{dh}. \quad (3.2)$$

To be explicit, this means that calculating absolute magnitudes using a different value of h (where $h = H_0/(100 \text{ km s}^{-1} \text{ Mpc}^{-1})$ has been used) would shift both the positions of the Milky Way and the volume-limited sample together in unison along the absolute-magnitude axis of any color-magnitude diagram (CMD) we show. However, calculating M_\star and \dot{M}_\star values using a different value of h (where $h = 0.7$ has been used) would shift the position of the volume-limited sample relative to the Milky Way’s position in the CMD; the size of this effect can be estimated using Equation (3.2). For instance, for the Milky Way M_\star and \dot{M}_\star values we have used along with the values in Table 3.1, we find a ± 0.05 shift in h corresponds to a $\sim \pm 0.05$ magnitude shift in ${}^0M_r - 5 \log h$ and no shift in ${}^0(g - r)$. Therefore, we would expect any reasonable difference between the true value of h and 0.7 will yield negligible

changes in our results (well below the measurement uncertainties) and the conclusions we draw from them.

Similarly, the results for the total stellar mass of the Milky Way found in Chapter 2 would be changed if any adjustments are made to the absolute distance scale (see Table 2.6). Predominantly this manifests in changes to the Galactocentric radius of the Sun, R_0 ; in Chapter 2 we conservatively used 8.33 ± 0.35 kpc based on the work of Gillessen et al. (2009). Firstly, since we found $\partial M_\star / \partial R_0 = 3.09 \times 10^{10} M_\odot \text{ kpc}^{-1}$ for the Milky Way, the impact of a change in R_0 can be obtained by replacing h with R_0 in Equation (3.2) (note $\partial \dot{M}_\star / \partial R_0 = 0$).

Uncertainties in R_0 dominate the error budget in our M_\star model. We find that if we were to instead adopt $R_0 = 8.36 \pm 0.11$ kpc based on Chatzopoulos et al. (2015), yielding a $\sim 69\%$ decrease in uncertainty in R_0 , then the total stellar mass from Chapter 2 becomes $M_\star = 6.18 \pm 0.50 \times 10^{10} M_\odot$, corresponding to a net $\sim 57\%$ decrease in M_\star uncertainty. This ultimately yields a $\sim 20\%$ decrease in M_r uncertainty, while also causing the Milky Way analogs to lie along a tighter trend in color-magnitude space. Ultimately, as our knowledge of the structure of our Galaxy improves (e.g., by measurements from Gaia), our methods should be able to more strongly constrain the Milky Way’s location in CMDs. In contrast, the current uncertainties in the Galactic SFR have a negligible effect on the constraints on the photometric properties derived in this chapter. This is because the uncertainty in the Milky Way stellar mass is a significant fraction of the range of stellar masses amongst galaxies of comparable SFR, while the SFR uncertainty is a $\sim 7\times$ smaller fraction of the range of SFRs at fixed mass. We note also that the evolution of galaxies since $z \sim 0.1$ appears to have negligible effect on our results; e.g., limiting our analysis instead to objects at $0.045 < z < 0.075$ yields differences in our results that are much smaller than the errors.

Fig. 3.8 now shows the position of the Milky Way corrected for Eddington & inclination bias, as listed in Table 3.1, as a red dot in rest-frame SDSS ${}^0(g-r)$ vs. 0M_r space; it is overlaid upon log-spaced density contours for the volume-limited sample. The purple ellipse displays our 1σ confidence region, accounting for the covariance between color and absolute magnitude; this yields a vast improvement in constraining how our Galaxy fits amongst the extragalactic population compared to the previously best 1σ constraints from van der

Kruit (1986, grey dash-dotted lines). For convenience, we have highlighted the red-sequence and blue-cloud regions of this diagram (flipped in position compared to \dot{M}_\star - M_\star space, since higher-SFR galaxies are bluer). We see that Milky Way’s position straddles the boundary between these two populations, with a chance that it lies in the core of the red sequence or redder. In addition, given that the blue cloud includes the vast majority of the spiral galaxy population (S14; Wong et al., 2012; Strateva et al., 2001; Blanton et al., 2003a), we see that our value of ${}^0M_r - 5 \log h = -21.00_{-0.37}^{+0.38}$ establishes the Milky Way amongst the brightest spiral galaxies in the local universe, while its integrated color of ${}^0(g - r) = 0.682_{-0.056}^{+0.066}$ ranks it amongst the reddest as well.

Lastly, we produce an updated plot equivalent to Figure 1 of Mutch et al. (2011, M11) by showing our constraints on the Milky Way’s position in ${}^0(u - r)$ vs. M_\star space, where the green valley becomes stretched out and more distinguishable. Here, we have highlighted the green-valley region based on two different definitions. First, the dark green region shows the division line empirically derived for SDSS galaxies by Baldry et al. (2006) with an offset of ± 0.1 mag in the vertical direction (the definition of the green valley employed by M11), which matches well with the density contours for our volume-limited sample. Second, the light green region shows a definition based upon correcting all SDSS galaxies for dust effects, as defined by Schawinski et al. (2014, hereafter S14). In the second case, many of the intermediate-color objects are blue galaxies that are both dusty and viewed edge-on, and so switching to intrinsic (face-on) properties moves this population blue-ward in the plot, effectively thinning out and expanding the green-valley region more. Given that our measurement of the Milky Way’s position in this space is effectively face-on, the green-valley definition from S14 provides a suitable comparison.

Compared to the prior constraints (grey dash-dotted lines), we are in a much better position to now identify where the Milky Way lies relative to other galaxies. In particular, our Galaxy appears to be entering, if not already a part of, the green-valley region where objects are expected to be in a transitional phase; here star formation is quenching by some mechanism(s); consequentially, green-valley galaxies are moving on a trajectory towards the red sequence (for more detail see, e.g., Gonçalves et al. 2012; Fang et al. 2012; and S14).

In Tables 3.3 & 3.4 we present our results for Milky Way properties transformed to the

Johnson-Cousins passband system. As a reminder, these values have been calculated in an identical fashion to those listed in Tables 3.1 & 3.2, but after transforming each Milky Way analog’s set of SDSS *ugriz* magnitudes to an equivalent set of Johnson-Cousins *UBVRI* measurements using the `kcorrect` software package (Blanton & Roweis, 2007). This entails calculating magnitudes in *UBVRI* passbands from the linear combination of template galaxy SEDs from BC03 that best fits the observed SDSS *ugriz* photometry on an object-by-object basis, and hence should provide the most accurate transformations. A viable alternative would be to apply the empirical color transformations provided by Cook et al. (2014) directly to our results in Tables 3.1 & 3.2, though these equations represent the mean transformations between the two passband systems averaged over galaxies with a range of morphologies, star formation rates, etc. Nevertheless, we find that applying the Cook et al. 2014 transformation equations to our SDSS results produces estimates on the Johnson-Cousins system that are quite similar to our nominal values determined using `kcorrect`. The differences are almost always at the $0.1\text{--}0.3\sigma$ level (including for mass-to-light ratios, which we discuss next), the one exception being $^0(U - B)$, where the two methods agree at the 0.75σ level. Note that we have used the Cook et al. equations to transform the van der Kruit (1986) result in Fig. 3.8.

In addition to the photometric properties presented in Tables 3.1–3.4, we also provide in Table 3.5 new estimates of global stellar mass-to-light ratios, Υ^* , for the Milky Way for all SDSS and Johnson-Cousins passbands in the $z=0$ and $z=0.1$ rest-frames. These are calculated from the full distribution of Υ^* values for the MWAS, in the same manner as we calculate photometric properties. To do so, we first calculate the stellar mass-to-light ratio for each Milky Way analog in passband x in the rest-frame of redshift z as

$${}^z\Upsilon_x^* = M_\star \times 10^{0.4(({}^zM_x + 5 \log(0.7/h)) - {}^zM_{\odot,x})} L_\odot^{-1}, \quad (3.3)$$

where ${}^zM_{\odot,x}$ and L_\odot represent the absolute magnitude and luminosity, respectively, of the Sun, which we calculate using the `k_solar_magnitudes` routine from the `kcorrect` package. We note that Equation (3.3) is written to make it clear that we have converted absolute magnitudes to reflect $h = 0.7$ and hence be on the same scale as our M_\star values; however, it should be noted that Υ^* is intrinsically a cosmology-independent quantity. For instance, if

we now chose to rescale quantities from $h = 0.7$ to 0.8 , the right-hand side of Equation (3.3) would gain a factor of $(0.7/0.8)^2$ for the change in stellar mass and a factor of $10^{0.4(5\log(0.8/0.7))}$ for the change in luminosity, which cancel. Next, we use Equation (3.1), replacing ${}^0(g - r)$ with ${}^z\Upsilon_x^*$, in order to produce our weighted-mean estimate. Lastly, we multiply this by a factor of $10^{-0.4B}$, where B is the Eddington bias correction, which is listed in Tables 3.1–3.4. In this way, our results are corrected for Eddington bias, inclination effects and morphological bias (all subdominant to the random errors), consistent with all other properties presented here.

3.6 SUMMARY & DISCUSSION

This chapter has focused on determining the global photometric properties of the Milky Way (MW) to facilitate comparisons to observations of other galaxies. In Chapter 2 we have derived a new, highly constrained stellar mass and SFR for the MW using a multitude of independent results from the literature, which encompass many different methods and datasets. We then identified a set of SDSS galaxies analogous to the MW, whose distribution of SFR and total stellar mass values match the probability distributions for these quantities (given uncertainties) of the Milky Way. These two quantities are strongly correlated with a galaxy’s luminosity and color (see, e.g., Bell & de Jong, 2001), so a galaxy which matches our Galaxy in stellar mass and star formation rate would also be expected to have a similar overall spectral energy distribution. We then determine the range of photometric properties of these galaxies, allowing us to constrain MW properties in a manner that is largely robust to the effects of Galactic extinction (unless the Milky Way is so unusual that it has no true analogs amongst the set of galaxies matching its M_\star and \dot{M}_\star). We have accounted for the Eddington bias involved with selecting galaxies based on their SFR and stellar mass, and tested the impact of reddening effects on this sample. In §3.5 we have provided a full tabulation of useful Milky Way photometric properties.

3.6.1 Comparisons to Earlier Color Measurements

Overall, the results from our Milky Way analog-based analysis method compare well with literature estimates of the properties of the MW. Since many of those estimates are made using the Johnson-Cousins passband system, we will often rely on our results transformed to this system in order to make direct comparisons; these are available in Tables 3.3–3.5. First and foremost, our transformed estimate of ${}^0(B - V) = 0.744_{-0.054}^{+0.068}$ is in excellent agreement with the widely used [van der Kruit \(1986, vdK86\)](#) measurement of 0.83 ± 0.15 , consistent at the $\sim 0.5\sigma$ level. Our result indicates a slightly bluer color for the Milky Way with a smaller uncertainty by a factor of ~ 3 .

As mentioned in §3.1, earlier measurements yielded much bluer color estimates for the MW than vdK86, and hence also much bluer than the estimate we have presented here. The [de Vaucouleurs & Pence \(1978, dV&P\)](#) two-component model produced a color estimate of $B - V = 0.53 \pm 0.05$, which is inconsistent at nearly the 3σ level with our estimate. The [Bahcall & Soneira \(1980, B&S\)](#) two-component model yields $B - V = 0.45$; given the lack of any error estimates, this is difficult to compare to our value, though again significantly bluer. [Bahcall \(1986\)](#) advised using a ± 0.2 magnitude margin of error when comparing colors to the model, given the wide variety of systematic uncertainties existing in the data at that time. If we use this as the error estimate for the B&S model value, we find that our result is redder by 0.29 ± 0.21 magnitudes, making these estimates inconsistent at the $\sim 1.4\sigma$ significance level. It is possible that the tension between the dV&P and B&S color estimates and the one presented here would be reduced if the two-component models employed were updated to more current constraints on the Galaxy’s stellar populations.

In [de Vaucouleurs \(1983, dV83\)](#), an estimated color of $B - V = 0.53 \pm 0.04$ is quoted for the Milky Way, obtained by averaging the observed colors of nearby Sb/c types. This value appears to originate from data Table 4 of [de Vaucouleurs \(1977, hereafter dV77\)](#), which indicates that the distribution of corrected colors for a sample of 70 Sbc galaxies is described by $B - V = 0.564 \pm 0.066$. The measurements for each object are tabulated in the *Second Reference Catalogue of Bright Galaxies* (RC2; [de Vaucouleurs et al., 1976](#)), which collected extragalactic data published since the 1930s. Each $B - V$ color measurement in RC2 is

corrected to the asymptotical total light from each galaxy using a Laplace-Gauss integral technique, as a function of its morphological type (T) and the effective aperture diameter (A_e) containing 50% of its total light (in some cases, the $B - V$ color is transformed from measurements in different passbands). Each “total” $B - V$ color is then corrected to zero Galactic extinction via a model of the Galactic dust as a function of coordinates (l, b), to zero internal extinction based on a model of inclination reddening as a function of T and isophotal axis ratio, and to the $z = 0$ rest-frame via a K -correction modeled as a function of T and z .

Given the difficulties of these corrections, as well as the challenges of properly intercalibrating photographic and photoelectric measurements from a wide variety of sources, it is likely that there could be significant systematic errors in this mean $B - V$ estimate. Furthermore, dV83 assumes $T = 4$ for the Milky Way (no less than 2.5 and no more than 5.5) and quotes the rate of change of the mean corrected color along the T sequence near $T = 4$ to be -0.10. While $T = 4$ (or equivalently Sb/c) fits well with the Galactic bulge-to-total ratio of 0.15 we have found in Chapter 2, the uncertainty in the Milky Way’s morphological type will still represent an additional source of uncertainty which appears not to have been included in the error estimate from dV83. We can therefore only treat the uncertainties quoted in the dV83 measurement as a lower limit. If we instead consider the value of $B - V = 0.564 \pm 0.066$ from dV77, this is bluer than our nominal result by 0.18 mag and inconsistent at the $\sim 2\sigma$ significance level. We believe the tension between our color measurement (or that of vdK86) and the estimates from dV77 and dV83 would be relieved if the sources of uncertainty described above were included in this estimate.

For comparison, Fukugita et al. (1995) performed a similar analysis for galaxy types across the Hubble sequence by comparing synthetic colors measured from galaxy SEDs to broadband photometry taken from the *Third Reference Catalogue of Bright Galaxies* (de Vaucouleurs et al., 1991). Listed in their Table 2, the authors found the average $B - V$ color for 676 Sb/c types (using only objects with $|b| > 30^\circ$, but applying no reddening correction) is 0.68 ± 0.14 , which is in excellent agreement with our MW result. More recently, Fernández Lorenzo et al. (2012) investigated the colors of isolated galaxies in the AMIGA sample that are also found in SDSS-DR8. This sample included 466 galaxies, two-thirds

of which were classified as Sb/c. Similarly to the methods we employ, the authors used model magnitudes that were corrected for Galactic dust extinction and K -corrected to $z=0$ rest-frame passbands. Listed in their Table 3, they found the median ${}^0(g-r)$ color for Sb/c types is 0.65 ± 0.09 , which compares well with our MW ${}^0(g-r)$ estimate of $0.682_{-0.056}^{+0.066}$. That table also provides colors for a variety of Sb/c galaxy samples; these subsets vary in local environment and redshift range, but all yield color estimates that agree with our Milky Way value at or below the $\sim 1\sigma$ significance threshold.

3.6.2 Comparisons to Earlier Absolute Magnitude Measurements

Comparisons of absolute magnitudes require more care, as they require additional assumptions that are prone to systematic error, particularly the value of $h = H_0/(100\text{km s}^{-1}\text{Mpc}^{-1})$ used to bring extragalactic distance estimates (determined from z) and measurements based on absolute distances (in parsecs) onto a common scale. For the following discussion we adopt $h = 0.7$. The vdK86 study yielded estimates of $M_B = -20.3 \pm 0.2$ and (when combined with his $B - V$ estimate) $M_V = -21.1 \pm 0.3$; these compare well with our slightly brighter estimates of ${}^0M_B = -20.84_{-0.44}^{+0.40}$ and ${}^0M_V = -21.51_{-0.39}^{+0.37}$, which are consistent at the $\sim 1\sigma$ level. The B&S two-component model yields $M_B = -20.1$ and $M_V = -20.5$, measurably dimmer than the results we have found, though again hard to compare to with no error estimates given. The dV&P two-component model, on the other hand, produced $M_B = -20.2 \pm 0.15$ (dV83) and $B - V = 0.53 \pm 0.05$, leading to $M_V = -20.7 \pm 0.16$; these values are inconsistent with our 0M_B and 0M_V results at the $\sim 1.5\sigma$ and $\sim 2\sigma$ level, respectively.

More recently, [Flynn et al. \(2006\)](#) analyzed Hipparcos and Tycho data for the local disk and extrapolated using an exponential disk model (in combination with earlier bulge luminosity estimates) to determine $M_I = -22.3 \pm 0.17$. This compares well with our brighter value of $-22.61_{-0.39}^{+0.36}$, and is consistent with it at the $\sim 0.8\sigma$ level. Also, [Liu et al. \(2011\)](#) converted the best-to-date Vega-calibrated M_V measurement for the Milky Way ([van den Bergh, 2000](#)) into an AB-calibrated absolute ${}^{0.1}r$ -band magnitude of -21.97 (with no error estimate given); this is within $\sim 1\sigma$ our estimate of ${}^{0.1}M_r = -21.55_{-0.39}^{+0.37}$, but brighter, rather than fainter.

3.6.3 Comparisons to Luminosity Function Measurements

Blanton et al. (2003b) determined luminosity functions for galaxies in all SDSS passbands using the SDSS Early Data Release. These were determined as the Schechter function that fits best to the distribution of Petrosian absolute magnitudes of galaxies, converted to the AB system, K -corrected to $z = 0.1$ rest-frame $ugriz$ passbands, and corrected for galaxy luminosity evolution; this should compare well with the `cmodel` absolute magnitudes used in this work after correcting them for the luminosity evolution since $z = 0.1$. The Schechter function is parametrized by the characteristic absolute magnitude, M_* (not to be confused with the total stellar mass which we have denoted as M_*), which provides a measure of where the luminosity function transitions from being well-fit by a power law into an exponential drop-off. Thus, galaxies with increasing absolute magnitude beyond M_* rapidly become more rare. To compare our results, we add $0.1Q$ to the results listed in Table 3.2 of this chapter, where Q is the appropriate correction in units of magnitude per unit redshift for each band as listed in Table 3 of Blanton et al. (2003b), and then subtract from this quantity the appropriate M_* value for each band as listed in their Table 2. Based on this work, we find the Milky Way is brighter than their M_* by 0.50 ± 0.64 , 0.48 ± 0.48 , 0.18 ± 0.37 , 0.18 ± 0.38 , and 0.15 ± 0.39 magnitudes in the $^{0.1}ugriz$ bands, respectively, essentially showing the MW to be consistent with M_* in all bands at the $\lesssim 1\sigma$ significance level. Similarly, Montero-Dorta & Prada (2009) reproduced the analysis of Blanton et al. (2003b) using SDSS Data Release 6, which provides larger redshift-complete samples of galaxies and incorporates improved reductions of SDSS imaging data. However, the luminosity functions that result from this work neglect any correction for the evolution of galaxies, as its impact is estimated to be very small for the redshift ranges used (i.e., $z \lesssim 0.2$). To compare our results with this work, we subtract M_* listed for the appropriate band in their Table 2 from our values in Table 3.2 of this chapter. Based on this work, we find the Milky Way is brighter than M_* by 1.13 ± 0.63 , 0.54 ± 0.48 , 0.07 ± 0.37 , 0.23 ± 0.38 , and 0.01 ± 0.39 magnitudes in the $^{0.1}ugriz$ bands, respectively. Again, we find the MW to be consistent with their M_* in nearly all bands at the $\sim 1\sigma$ confidence level, and hence is comparable in luminosity to L_* galaxies in the nearby universe.

3.6.4 Comparisons to Green-Valley Definitions

In Figure 3.8, we have presented the Milky Way’s location in the ${}^0(g - r)$ vs. 0M_r plane, demonstrating that it falls in the intermediate region between the blue cloud and red sequence populations. Our results are consistent with the hypothesis posed by Mutch et al. (2011, M11) that the Milky Way could be a member of the “green-valley” population. In Figure 3.9, we have produced an updated ${}^0(u - r)$ vs. $\log M_\star$ diagram modeled on of Fig. 1 of M11, showing the vast improvement in our constraints compared to those from prior measurements. Here, the Milky Way lies bluer than their definition of the green valley, i.e., the region within 0.1 mag of the SDSS color-division line determined by Baldry et al. (2006).

However, more recent work by S14, using K -corrected and dust-corrected DR7 magnitudes for galaxies at $0.02 < z < 0.05$ (comparable to our sample at $0.03 < z < 0.09$), defines the green valley to be $-0.75 < {}^0(u - r) - 0.25 \log(M_\star/M_\odot) < -0.24$; this definition would indicate that the Milky Way is in fact a green-valley galaxy in this diagram. Jin et al. (2014) present a definition of the green valley that avoids dust-reddening effects by using face-on nearby galaxies with DR7 magnitudes K -corrected to $z = 0.1$. They define the center of the valley to be ${}^{0.1}(u - r) = -0.121({}^{0.1}M_r - 5 \log h) - 0.061$ (with no range given). Given the uncertainties in our measurements, we find the Milky Way is bluer than this line by 0.25 ± 0.21 mag, consistent with it at the $\sim 1.2\sigma$ confidence level.

Mendez et al. (2011) define the green-valley region of the ${}^0(U - B)$ vs. 0M_B plane for AEGIS galaxies to be within a ± 0.1 mag vertical offset of the line ${}^0(U - B) = -0.0189({}^0M_B - 5 \log h) - 0.32$ (where we have converted from AB to Vega magnitudes). We find that our results place the MW redder than this line by 0.089 ± 0.070 mag; hence the MW might be considered a green-valley galaxy by this definition. Willmer et al. (2006) present a similar CMD division line for red and blue galaxies measured in the DEEP2 Redshift Survey. They define this line as ${}^0(U - B) = -0.032({}^0M_B - 5 \log(h/0.7)) - 0.585$, where we have included small corrections to reflect the AB-to-Vega magnitude conversions from `kcorrect` that have been employed in this study. We find that our results place the MW redder than this line by 0.067 ± 0.071 mag.

It is interesting to note that in the color-magnitude plane shown in Figure 3.4, none of

the Milky Way analogs appear in the peak of the blue-cloud region where prototypical blue, star-forming spirals reside, which would hint that our Galaxy, too, very likely does not fit that mold. This is contrary, however, to what one finds in the SFR– M_* plane shown in Figure 3.3; the vast majority of the MWAS lie in the blue cloud or just below. Based on its color, if seen from outside, the MW would likely be defined as a member of the green valley. In $^0(g-r)$, in fact, it is likely very close to the minimum-density region of color space. However, based on its M_* & \dot{M}_* , it appears to fall just off the blue cloud, if it is not actually a member of it. It thus provides a cautionary example: objects may fall in the green-valley region of parameter space for a variety of reasons, especially when only optical (and not UV) color is considered.

3.6.5 Comparisons to Earlier Mass-to-Light Ratio Measurements

In Table 3.5 we have presented new estimates of the global stellar mass-to-light ratio, Υ^* , of the Milky Way in SDSS *ugriz* passbands in the $z=0$ and 0.1 rest-frames, as well as these results transformed to Johnson-Cousins *UBVRI* passbands. The most relevant study we can compare these to is Flynn et al. (2006), which presented direct estimates of Υ^* for the local Galactic disk by accounting for the mass and luminosity budget in the “Solar cylinder” (i.e., the column of stellar material at R_0). This work primarily relied on fitting their *Tuorla* Galactic model to data taken in the Hipparcos and Tycho surveys (reaching out to ~ 200 pc), which was shown to match well with the *Heidelberg* model-independent analysis of the much more shallow (<25 – 50 pc) Catalogue of Nearby Stars. They found $\Upsilon_V^* = 1.5 \pm 0.2 M_\odot/L_\odot$, and then used color conversion derived from Hipparcos/Tycho data to obtain $\Upsilon_B^* = 1.4 \pm 0.2 M_\odot/L_\odot$ and $\Upsilon_I^* = 1.2 \pm 0.2 M_\odot/L_\odot$. We note that if we were to update these to reflect the Solar absolute magnitudes and colors we have employed herein (~ 0.03 mag differences), they would increase by $\sim 3\%$, well below the 1σ uncertainties. Regardless, we find that these values compare well with our global Milky Way results of $\Upsilon_B^* = 1.89_{-0.65}^{+0.78} M_\odot/L_\odot$, $\Upsilon_V^* = 1.86_{-0.58}^{+0.69} M_\odot/L_\odot$, and $\Upsilon_I^* = 1.29_{-0.37}^{+0.43} M_\odot/L_\odot$, which are larger than but consistent with the corresponding Flynn et al. estimates at the $\sim 0.7\sigma$, 0.6σ , and 0.2σ level, respectively.

One should keep in mind that, whereas the Flynn et al. estimates describe the disk

itself, our results represent the global (disk+bulge) values and hence are expected to be larger to some extent, especially in the B- and V-band, as they include the contribution from older stars in the Galactic nucleus. We can illustrate this further, and hence make a more apples-to-apples comparison, by making the following back-of-the-envelope calculation. First, for the subset of our volume-limited sample that has $f_{\text{deV}} > 0.95$, which constitutes $\sim 33,000$ highly bulge-dominated or elliptical galaxies, we find a distribution of Υ_B^* values that is well-approximated as a Gaussian described by $4.1 \pm 0.9 M_\odot/L_\odot$ (after multiplying by a factor of 1.5 to convert from Kroupa to Salpeter IMF; cf. Fukugita et al., 1998). Second, in Chapter 2 we have determined the bulge-to-total ratio of stellar mass in the Milky Way to be $B/T = 0.15 \pm 0.02$. By combining our Υ_B^* estimate for spheroidal components with the Flynn et al. Υ_B^* estimate for the Galactic disk, using the estimate of B/T to calculate a mass-weighted average for both components from Chapter 2, we find a global mass-to-light ratio of $\Upsilon_V^* = 1.81 \pm 0.19 M_\odot/L_\odot$. This is in excellent agreement with our result and is consistent with it at the $\sim 0.1\sigma$ level. Doing the analogous calculations in the V- and I-band, the remaining Flynn et al. disk values correspond to global values of $\Upsilon_V^* = 1.80 \pm 0.20 M_\odot/L_\odot$ and $\Upsilon_I^* = 1.39 \pm 0.18 M_\odot/L_\odot$, which are again in excellent agreement with our results, consistent with them at the 0.1σ and 0.2σ levels, respectively.

3.6.6 Conclusions and Future Studies

Overall, since the vast majority of spiral galaxies populate the blue cloud (S14; Strateva et al., 2001; Blanton et al., 2003a), our results imply that the Milky Way ranks amongst the most luminous, yet reddest of spirals in the local universe. Based on a variety of empirical definitions in the literature, our results show that it is likely that the Milky Way would be classified as a green-valley galaxy if viewed from the outside, generally taken to indicate that it would be in a transitional evolutionary stage. Again, this is contrary to what we find in the SFR– M_* plane shown in Figure 3.3, where we find the Milky Way lies very near, if not on, the main sequence of star-forming galaxies. Apparently, even when the impact of dust effect are accounted for, the green valley can be misleading when using it to generally characterize the galaxies it contains (cf. S14). It is safe to say that our Galaxy’s SFR is in a

state of decline; the Milky Way produces only ~ 1.65 solar masses of new stars per year, even though it is amongst the brightest and most massive of late-types. Our findings support the emerging consensus view of the Milky Way; one in which it is not the prototypical, blue spiral it was commonly thought to be just a decade ago; but is instead similar to the passive, red spiral population investigated in [Cortese \(2012\)](#). In fact, based on the demographics of late-types presented by S14, if our Galaxy truly lies in the green valley then its photometric properties would be representative of only $\sim 19\%$ of the spiral galaxies in the nearby universe. It is beyond the scope of this study to discuss what evolutionary histories may produce an optically-red, yet still star-forming Milky Way (or equivalently late-types that appear in the green valley), but we refer the reader to [Hammer et al. \(2007\)](#), [Yin et al. \(2009\)](#), [M11](#), [Mendez et al. \(2011\)](#), [Jin et al. \(2014\)](#), and S14 for insightful discussions.

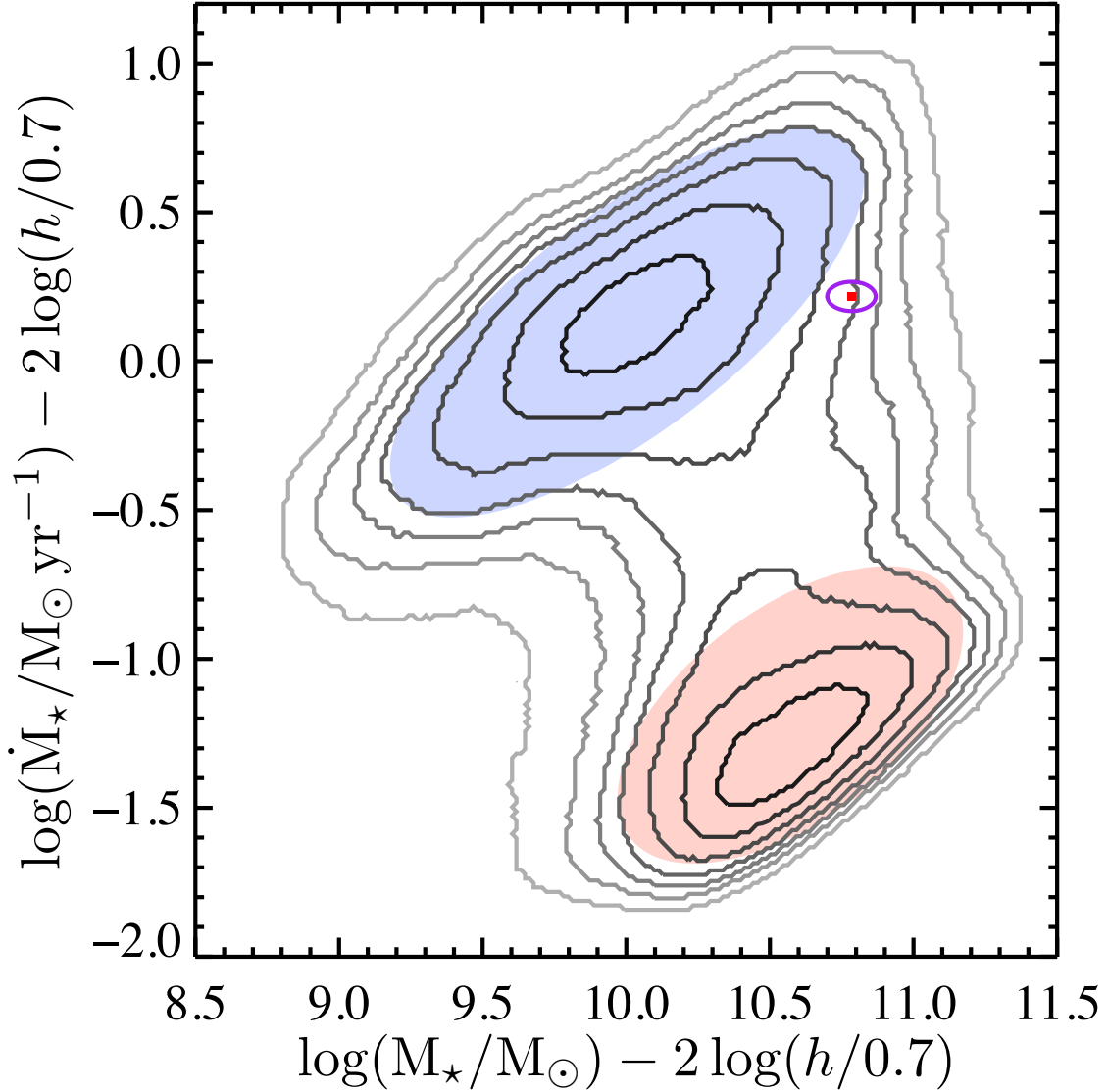


Figure 3.1: Position of the Milky Way in star formation rate (\dot{M}_*) vs. total stellar mass (M_*) space. Log-spaced contours depict the density of a volume-limited sample of SDSS galaxies in the range $0.03 < z < 0.09$. The most-likely position (red dot) and 1σ constraints (purple) for the Milky Way shown here are determined from a hierarchical Bayesian meta-analysis of the literature estimates in Chapter 2. The properties for both the Milky Way and the extragalactic sample displayed here reflect consistent assumptions about their stellar populations, including a Kroupa IMF, and hence should be well guarded from any substantial systematics relative to one another. We can see the Galaxy is offset from the main sequence of star-forming galaxies, hinting that it may be in a transitional evolutionary phase.

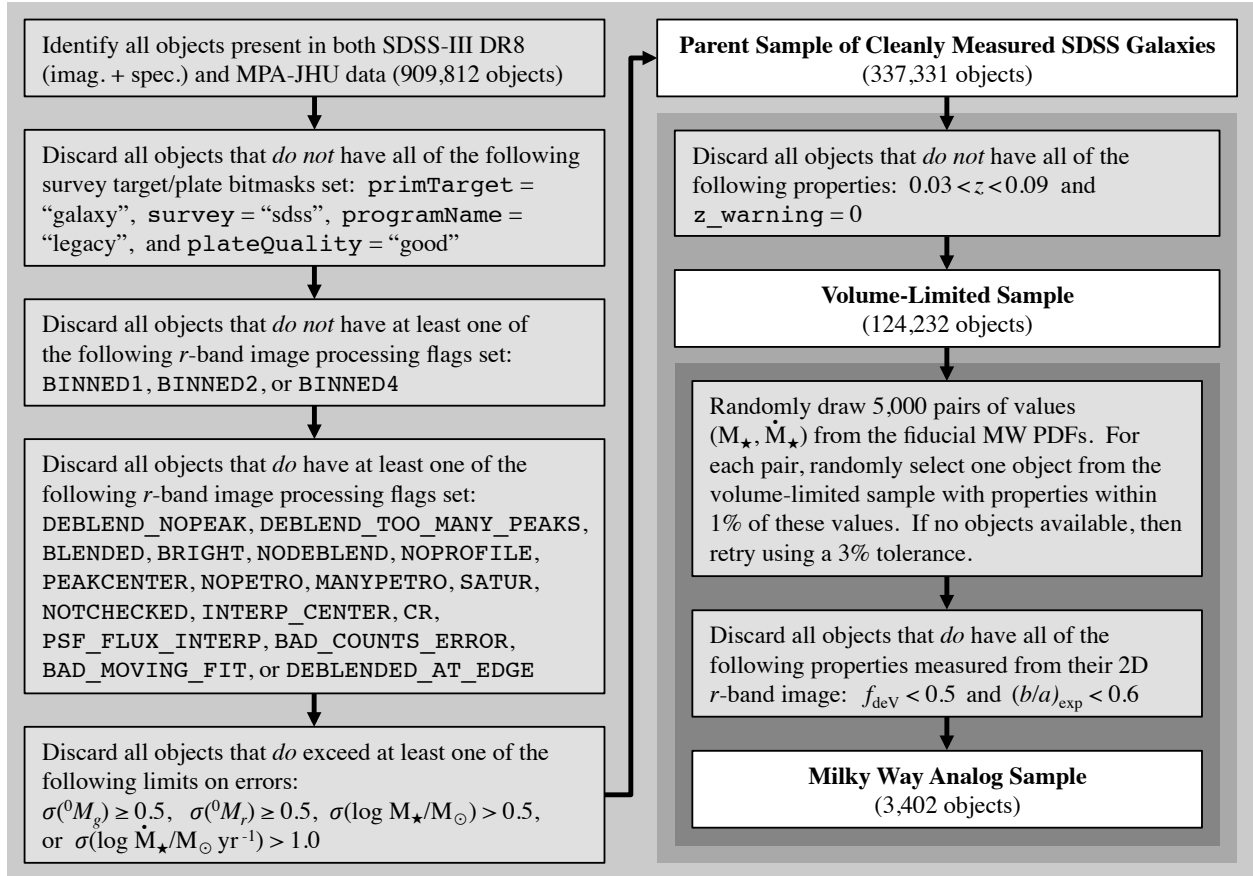


Figure 3.2: A flowchart outlining the steps and criteria we use to select different samples of SDSS galaxies that we employ in this study. This chart summarizes the processes described in sections 3.2.2–3.3.2, where more details may be found, including where we obtain or how we produce different property measurements for each object. Note that here we denote the error in galaxies’ stellar mass and SFR as $\sigma(\log M_\star/M_\odot)$ and $\sigma(\log \dot{M}_\star/M_\odot \text{ yr}^{-1})$, respectively. As mentioned in §3.3.2, $(b/a)_{\text{exp}}$ is the minor-to-major axis ratio obtained from the pure-exponential profile best fit to an object’s 2D image.

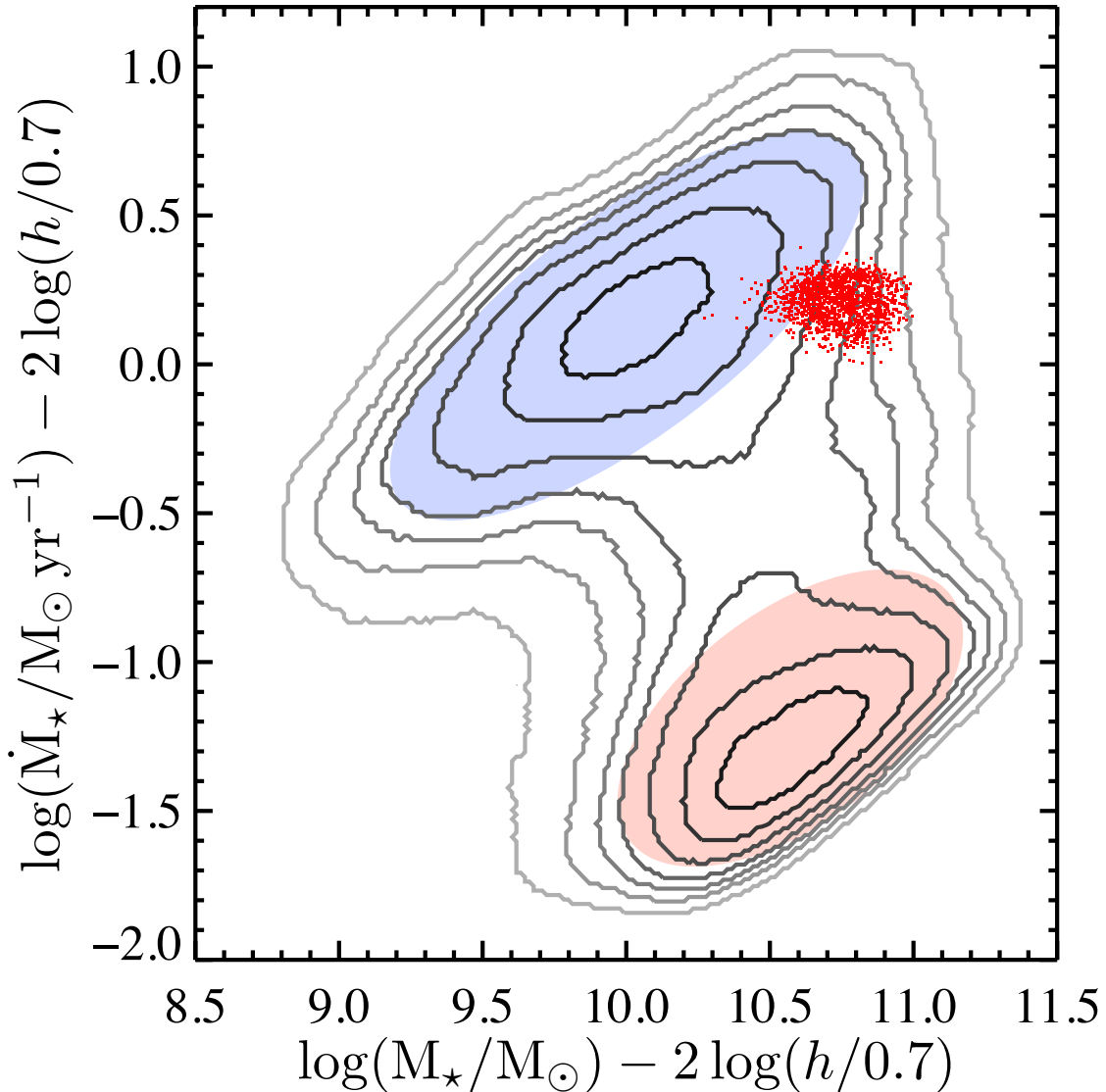


Figure 3.3: Sample of $\sim 3,500$ Milky Way analog galaxies (red dots), chosen through a random selection process such that they collectively match the same distribution in SFR– M_* space as the Milky Way (compare to Figure 3.1 and 3.7). The greyscale, log-spaced contour lines depict the density of a volume-limited sample of SDSS galaxies ($0.03 < z < 0.09$) that encompasses the Milky Way SFR and M_* ranges throughout this redshift range, but are not affected by any limiting magnitude. This is the same sample from which the Milky Way analogs are drawn (see §3.2.2 for the details). Fundamentally, we make the Copernican assumption that the Milky Way should not be extraordinary amongst the set of galaxies of similar stellar mass and star formation rate, and hence *some* galaxy in that set must have closely matching photometric properties; in this study we focus on integrated optical-wavelength properties which are all but impossible to directly measure.

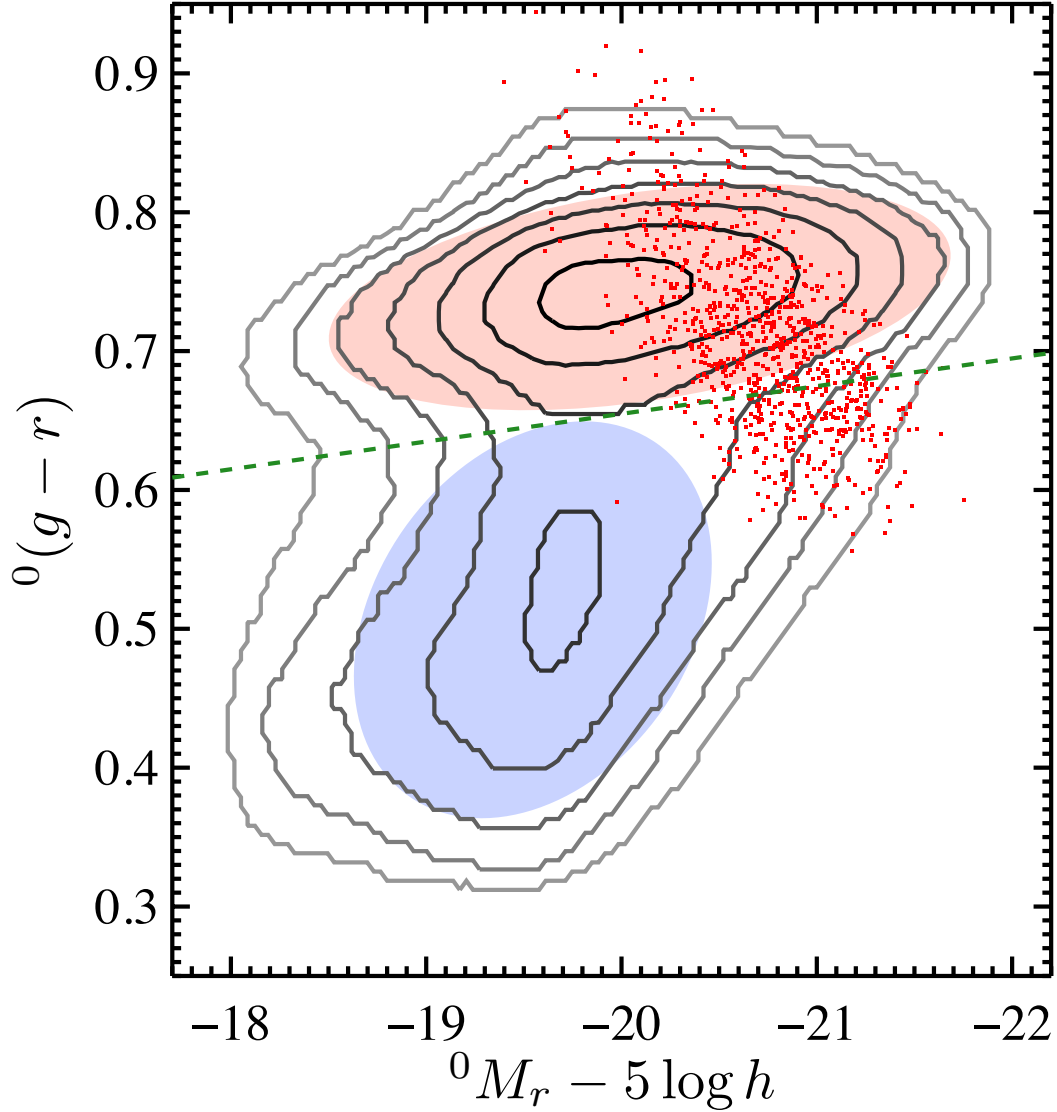


Figure 3.4: Sample of $\sim 3,500$ Milky Way analog galaxies (red dots) plotted in SDSS $^0(g-r)$ vs. 0M_r space. These are the same sample of objects shown in Figure 3.3; i.e., they are selected to produce a distribution of star formation rate and total stellar mass values matching the probability distribution describing those properties for our Galaxy. Again, the greyscale, log-spaced contours depict the density of a volume-limited sample of SDSS galaxies in the range $0.03 < z < 0.09$ (see §3.3.1). For reference, the dashed green line shows a simple SDSS color cut dividing the red sequence and blue cloud regions (Graves, priv. comm.; see §3.3.2 for more details).

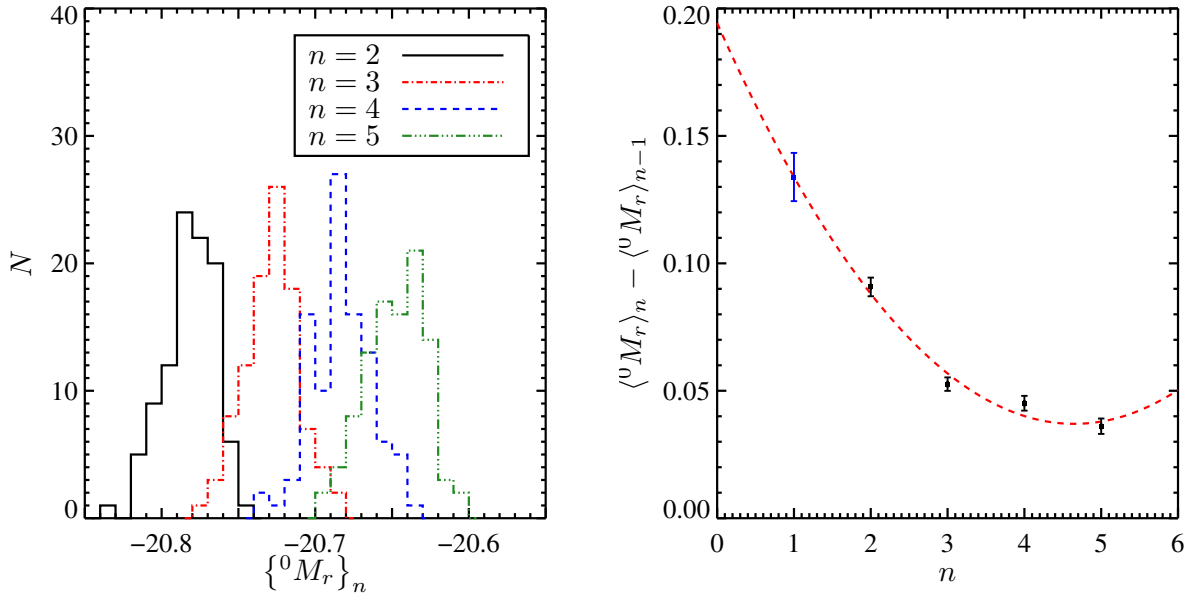


Figure 3.5: Modeling the Eddington bias in the Milky Way analog selection method. *Left Panel:* Histograms of the mean absolute 0r -band magnitudes produced from Monte Carlo (MC) simulations of selecting a new sample of Milky Way analog galaxies as increasing amounts of noise are added to galaxies’ total stellar mass (M_\star) and star formation rate (\dot{M}_\star) values. This noise is drawn from a normal distribution, with mean of zero and standard deviation determined by the errors in a galaxy’s estimated M_\star and \dot{M}_\star , and is applied p times successively before analogs are selected. Since nominal values are all affected by noise, we denote them as the $n = 1$ case, and so any further degradation is marked $n = p + 1$. *Right Panel:* A least-squares quadratic fit to the 4 points yielded from subtracting the mean of $\{{}^0M_r\}_{n-1}$ from that of $\{{}^0M_r\}_n$, using the distributions from the left panel, as a function of n . $\langle {}^0M_r \rangle_1$ is measured from the mean 0M_r of our MWAS to produce the point at $n = 2$. We then use this fit to extrapolate the blue datapoint at $n = 1$, the ordinate of which should reflect the difference between the actual measurements, which are affected by Eddington bias, and what would be measured with zero errors, i.e., the quantity we desire; this value is subtracted from the observed absolute r -band magnitude of the sample. This same process is applied to each absolute magnitude or color considered in this study, and the bias subtracted is listed in Tables 3.1 & 3.2. Almost always this offset is completely subdominant to the statistical errors of our method; the exception is u -band based color measurements, for which the bias is of the same order as, but still smaller than, statistical uncertainties. Even then, the uncertainty in the bias correction is much smaller than other sources of error.

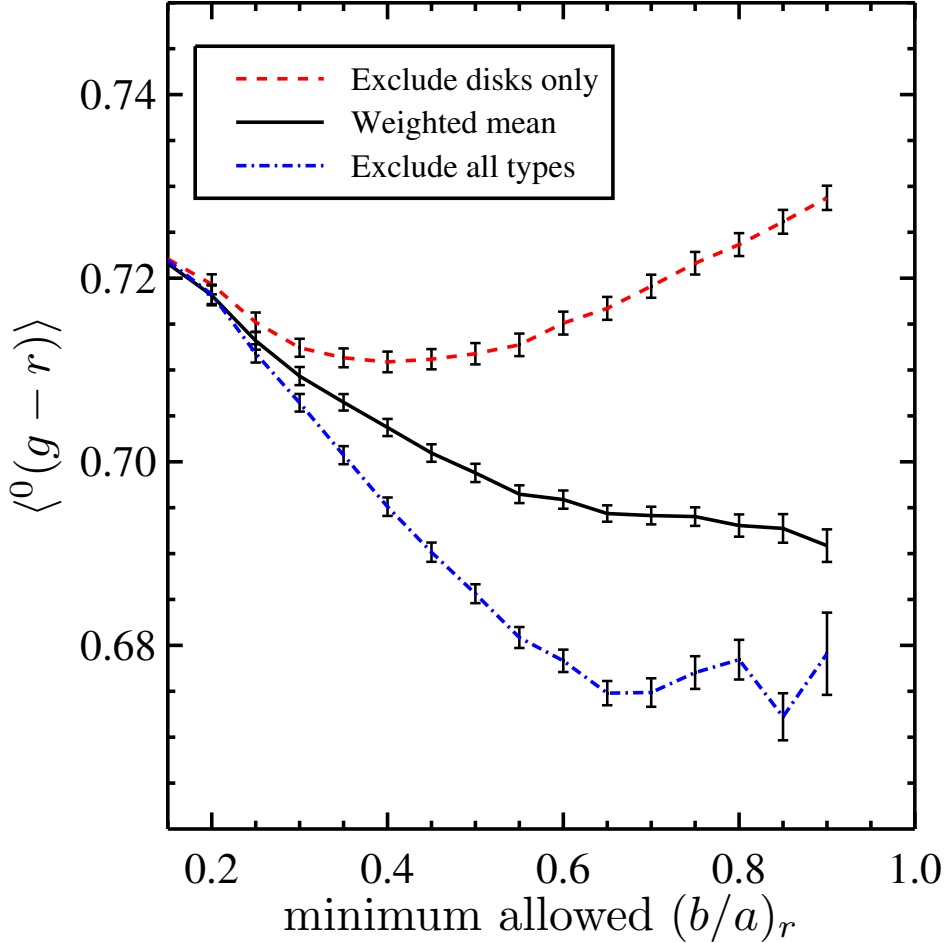


Figure 3.6: The mean ${}^0(g-r)$ color of our Milky Way analog sample as a function of the minimum allowed axis ratio of the objects included in 3 different scenarios. The red dashed curve is the result of removing only disk galaxies (i.e., objects having $f_{\text{dev}} < 0.5$) based on the axis ratio cut given on the x -axis. The blue dash-dotted curve is the result of removing any galaxy, regardless of type, based on the minimum ratio cut. The solid black line reflects the result of removing only disk galaxies again, but in this scenario we add extra weight to the contribution from disk galaxies remaining after the cut to the overall mean ${}^0(g-r)$ color to correct for the objects removed. Excluding only disk galaxies initially causes a trend toward net bluer color as edge-on systems are removed, but eventually this trend reverses toward redder average color due to increasingly oversampling the elliptical population. However, in the second case, since spheroids outnumber disks at $b/a \gtrsim 0.35$, throwing away any galaxy above this minimum-allowed threshold means discarding more spheroids than disks, giving extra weight to the blue population. Therefore, we chose the last scenario (a weighted mean) as our fiducial method, as it provides a stable behavior over a large range of reasonable choice of cutoff for b/a , and hence appears robust to such morphological bias. That is, the slope of the black curve is shallow enough that moving from a minimum allowed b/a of 0.4 to 0.8 would cause a $\lesssim 0.01$ magnitude change; $b/a > 0.6$ is our fiducial cut. The other scenarios provide a much more crude and extreme way of removing inclination reddening from our sample; we note the offset of the other curves from the black curve at $x = 0.6$ is still $\lesssim 0.02$ mag, which is subdominant to the statistical error (~ 0.06 mag). The analogous plot for 0r -band absolute magnitude yields a similar conclusion, and so we adopt the weighted-mean scenario as standard for all quantities.

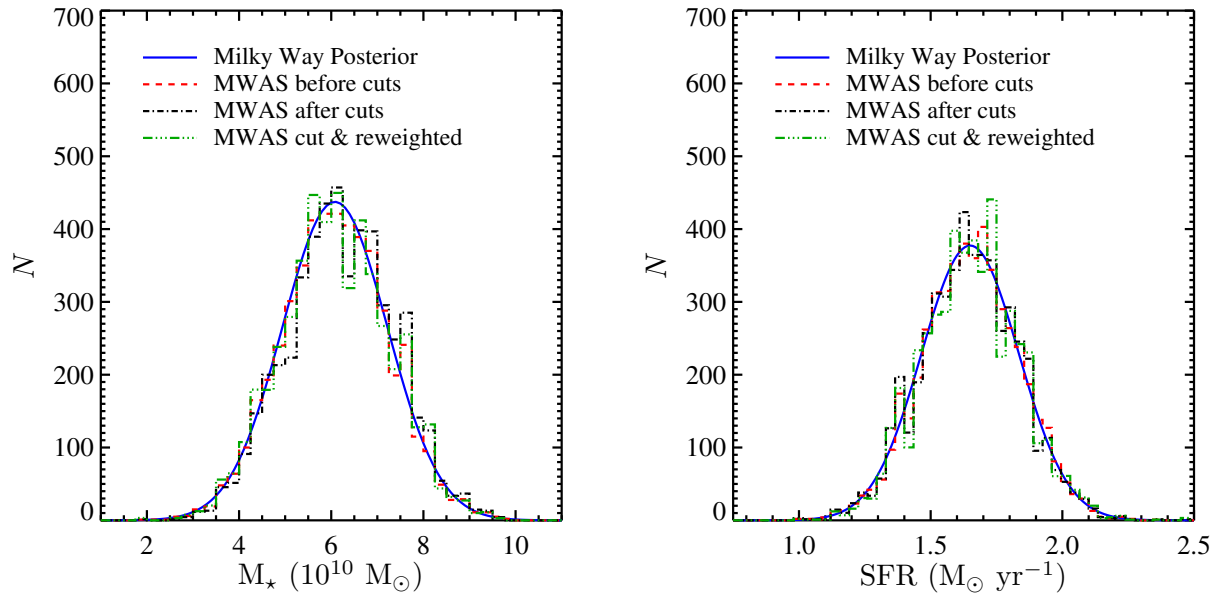


Figure 3.7: The distribution of stellar masses, M_* , (left panel) and star formation rates (SFRs), \dot{M}_* , (right panel) for our Milky Way analog sample at different stages of our analysis procedure overlaid upon the Galactic posterior probability distribution functions (blue solids curves) used for selecting them. The red dashed line shows the original sample of 5,000 analogs drawn before any cuts are applied. The black dash-dotted curve shows the remainder of the original sample after removing those that appear to be edge-on disk-dominated systems, whose inclusion would otherwise systematically redden our results for photometric properties, and then renormalized to reflect the original sample size of 5,000. The green dash-triple-dotted curve shows those objects that make up the black dash-dotted curve, but reweighted to correct for any morphological bias (i.e., the oversampling of bulge-dominated vs. disk-dominated objects; see Fig. 3.6) that our cuts introduce; see Equation (3.1).

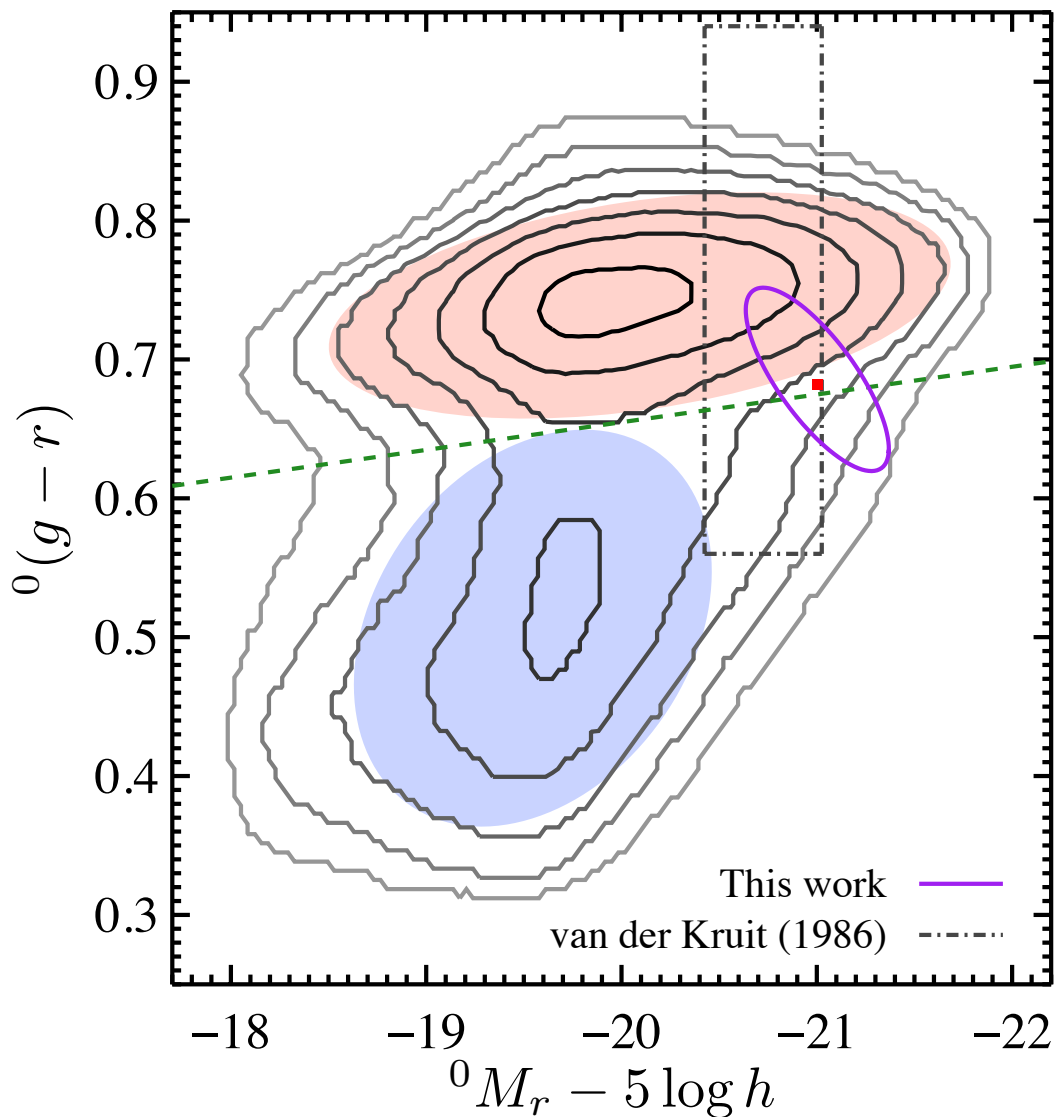


Figure 3.8: The Eddington-bias-corrected position of the Milky Way in SDSS ${}^0(g-r)$ vs. 0M_r color-magnitude space (red point and purple 1σ ellipse). For comparison, we show in grey dash-dotted lines the previously-best 1σ constraint directly measured by van der Kruit (1986, vdK86), converted to the SDSS AB magnitude system via transformation equations from Cook et al. (2014). In order to place this measurement in this plot we subtract $5 \log(h/0.7)$, allowing it to be directly compared to the SDSS sample. Log-spaced contours show the density of galaxies in our volume-limited sample; we shade the core of the red sequence and blue cloud regions in red and blue, respectively, and show the same green dashed color-division line as in Fig. 3.4. Until now, the Milky Way’s position has remained highly uncertain in this parameter space. Our new measurement dramatically improves our knowledge of how the Galaxy compares to others in the local Universe; we likely straddle the division between the blue-cloud and red-sequence populations, or the so-called “green-valley” region of this diagram. This ranks the Milky Way amongst the brightest and reddest spiral galaxies still producing new stars today. It may well be in a transitional evolutionary phase where star formation is dying out.

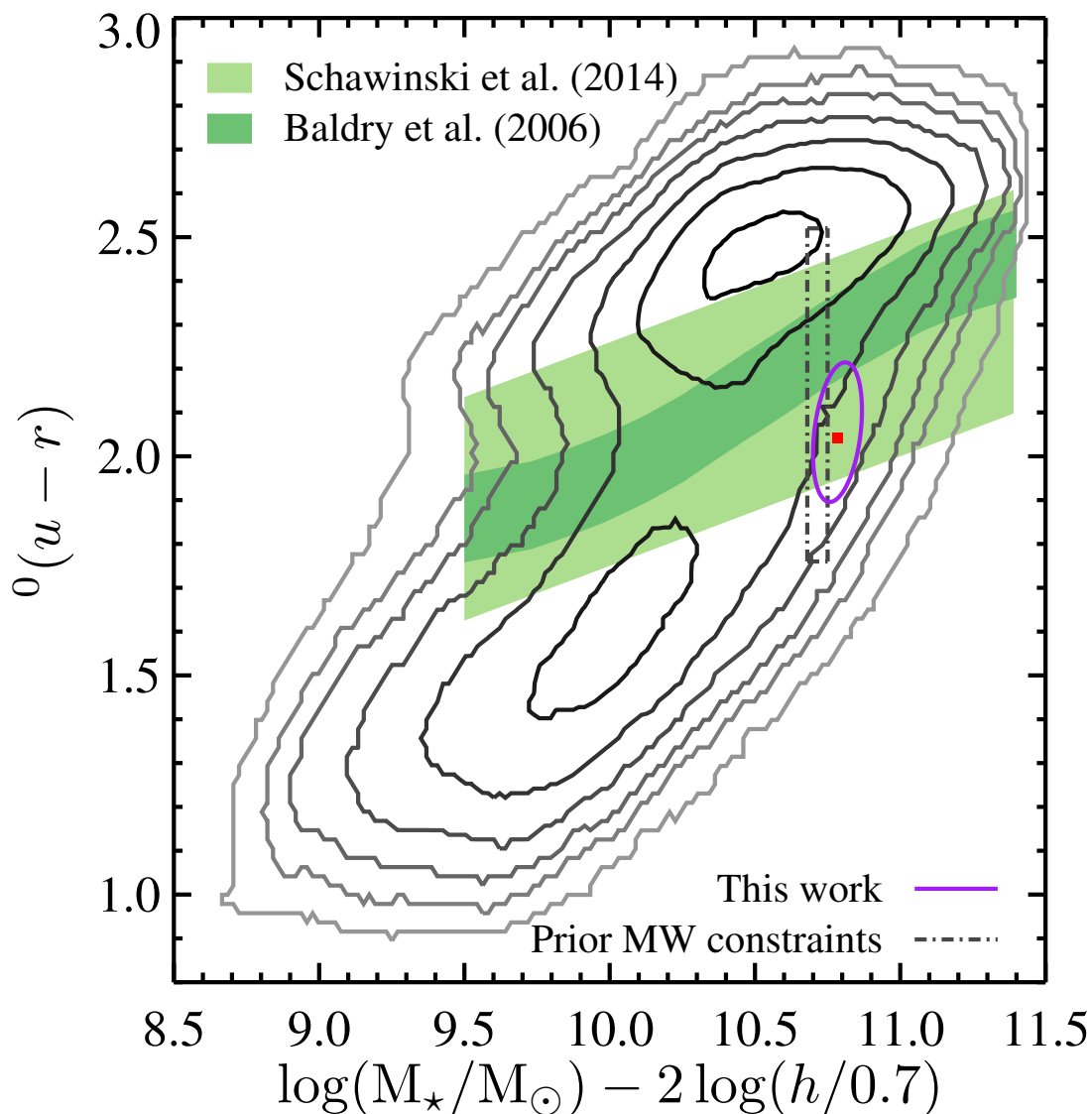


Figure 3.9: An updated version of Figure 1 from Mutch et al. (2011, M11) showing the Milky Way’s corrected position (red point and purple 1σ ellipse) in ${}^0(u-r)$ vs. M_* space, where again our new constraints are a dramatic improvement upon and consistent with the prior measurements (dash-dotted grey lines) utilized by M11 (updated here to the color transformations for galaxies from Cook et al. 2014). Comparing with Fig. 3.8, the green valley becomes much stretched out in ${}^0(u-r)$ color space. The dark shaded green region follows the same prescription as M11, using the empirically-derived Baldry et al. (2006) color division line with a ± 0.1 ${}^0(u-r)$ offset. Second, the light shaded green region is the green valley as defined by Schawinski et al. (2014, S14) for SDSS galaxies after the effects of dust are removed; this provides a suitable comparison for our dust-corrected Milky Way results, whereas the greyscale contours do not reflect this correction. A similar story emerges as from Figure 3.8: our Galaxy likely resides in the saddle of the bimodal color distribution of galaxies in the local universe. Measured externally, it would appear redder than majority of spiral galaxies, yet bluer than most ellipticals. This makes the Milky Way one of the most massive, brightest, and reddest of spiral galaxies with appreciable star formation today.

Table 3.1.
Photometric Properties for the Milky Way:
Rest-frame $z=0$ SDSS Passbands

Property	Corrected Value (mag)	Bias Removed (mag)	$\partial/\partial M_\star$ (10^{-10} mag M_\odot^{-1})	$\partial/\partial \dot{M}_\star$ (mag M_\odot^{-1} yr)
${}^0M_u - 5 \log h$	$-19.16^{+0.57}_{-0.47}$	0.240 ± 0.014	-0.05	-0.32
${}^0M_g - 5 \log h$	$-20.36^{+0.47}_{-0.41}$	0.142 ± 0.011	-0.11	-0.40
${}^0M_r - 5 \log h$	$-21.00^{+0.38}_{-0.37}$	0.134 ± 0.009	-0.11	-0.48
${}^0M_i - 5 \log h$	$-21.27^{+0.38}_{-0.36}$	0.120 ± 0.009	-0.14	-0.49
${}^0M_z - 5 \log h$	$-21.56^{+0.36}_{-0.37}$	0.126 ± 0.009	-0.15	-0.39
${}^0(u - r)$	$2.043^{+0.166}_{-0.157}$	0.090 ± 0.0060	0.07	-0.02
${}^0(u - g)$	$1.358^{+0.105}_{-0.093}$	0.077 ± 0.0047	0.06	0.02
${}^0(g - r)$	$0.682^{+0.066}_{-0.056}$	0.015 ± 0.0017	0.03	0.00
${}^0(r - i)$	$0.296^{+0.051}_{-0.046}$	0.012 ± 0.0012	0.01	0.00
${}^0(i - z)$	$0.291^{+0.043}_{-0.041}$	-0.001 ± 0.0009	0.01	-0.04

Note. — The Eddington bias estimated for each band, as described in §3.4.1, is listed in Column 3. This is subtracted from the mean property measured from the MWAS, as discussed in §3.4.2 (see Equation 3.1), in order to produce the corrected value listed in Column 2.

Table 3.2.
Photometric Properties for the Milky Way:
Rest-frame $z=0.1$ SDSS Passbands

Property	Corrected Value (mag)	Bias Removed (mag)	$\partial/\partial M_\star$ (10^{-10} mag M_\odot^{-1})	$\partial/\partial \dot{M}_\star$ (mag M_\odot^{-1} yr)
$^{0.1}M_u - 5 \log h$	$-18.85_{-0.51}^{+0.63}$	0.271 ± 0.012	0.02	-0.38
$^{0.1}M_g - 5 \log h$	$-20.07_{-0.44}^{+0.48}$	0.168 ± 0.011	-0.10	-0.45
$^{0.1}M_r - 5 \log h$	$-20.78_{-0.39}^{+0.37}$	0.130 ± 0.009	-0.10	-0.42
$^{0.1}M_i - 5 \log h$	$-21.16_{-0.37}^{+0.38}$	0.134 ± 0.009	-0.13	-0.59
$^{0.1}M_z - 5 \log h$	$-21.41_{-0.38}^{+0.39}$	0.124 ± 0.009	-0.14	-0.35
$^{0.1}(u - r)$	$2.201_{-0.172}^{+0.201}$	0.105 ± 0.0072	0.10	0.08
$^{0.1}(u - g)$	$1.419_{-0.112}^{+0.124}$	0.074 ± 0.0052	0.07	0.04
$^{0.1}(g - r)$	$0.782_{-0.063}^{+0.081}$	0.031 ± 0.0027	0.02	-0.03
$^{0.1}(r - i)$	$0.390_{-0.042}^{+0.046}$	0.001 ± 0.0010	0.01	-0.01
$^{0.1}(i - z)$	$0.275_{-0.046}^{+0.047}$	0.010 ± 0.0011	0.01	-0.05

Note. — The Eddington bias estimated for each band, as described in §3.4.1, is listed in Column 3. This is subtracted from the mean property measured from the MWAS, as discussed in §3.4.2 (see Equation 3.1), in order to produce the corrected value listed in Column 2.

Table 3.3.
Photometric Properties for the Milky Way:
Rest-frame $z=0$ Johnson-Cousins Passbands

Property	Corrected Value (mag)	Bias Removed (mag)	$\partial/\partial M_\star$ (10^{-10} mag M_\odot^{-1})	$\partial/\partial \dot{M}_\star$ (mag M_\odot^{-1} yr)
${}^0M_U - 5 \log h$	$-20.02^{+0.50}_{-0.47}$	0.232 ± 0.011	-0.10	-0.61
${}^0M_B - 5 \log h$	$-20.07^{+0.40}_{-0.44}$	0.173 ± 0.009	-0.12	-0.49
${}^0M_V - 5 \log h$	$-20.74^{+0.37}_{-0.39}$	0.132 ± 0.008	-0.12	-0.37
${}^0M_R - 5 \log h$	$-21.26^{+0.40}_{-0.36}$	0.131 ± 0.007	-0.11	-0.16
${}^0M_I - 5 \log h$	$-21.84^{+0.36}_{-0.39}$	0.125 ± 0.008	-0.12	-0.34
${}^0(U - V)$	$0.890^{+0.148}_{-0.123}$	0.094 ± 0.0055	0.02	-0.14
${}^0(U - B)$	$0.149^{+0.078}_{-0.070}$	0.063 ± 0.0038	0.01	-0.04
${}^0(B - V)$	$0.744^{+0.068}_{-0.054}$	0.028 ± 0.0022	0.01	-0.05
${}^0(V - R)$	$0.541^{+0.046}_{-0.042}$	0.005 ± 0.0008	0.00	-0.02
${}^0(R - I)$	$0.598^{+0.047}_{-0.049}$	0.007 ± 0.0009	0.01	0.01

Note. — Values in this table are determined from analyzing the distributions of properties for Milky Way analogs, but after transforming SDSS *ugriz* measurements to Johnson-Cousins *UBVRI*-equivalent values on an object-by-object basis using the `kcorrect` software. As a reminder, *UBVRI* magnitudes are on the Vega system, whereas *ugriz* magnitudes are on the AB system.

Table 3.4.
Photometric Properties for the Milky Way:
Rest-frame $z=0.1$ Johnson-Cousins Passbands

Property	Corrected Value (mag)	Bias Removed (mag)	$\partial/\partial M_\star$ (10^{-10} mag M_\odot^{-1})	$\partial/\partial \dot{M}_\star$ (mag M_\odot^{-1} yr)
$^{0.1}M_U - 5 \log h$	$-20.10_{-0.51}^{+0.60}$	0.252 ± 0.011	-0.11	-0.64
$^{0.1}M_B - 5 \log h$	$-19.96_{-0.45}^{+0.49}$	0.196 ± 0.010	-0.12	-0.56
$^{0.1}M_V - 5 \log h$	$-20.47_{-0.40}^{+0.41}$	0.136 ± 0.009	-0.12	-0.33
$^{0.1}M_R - 5 \log h$	$-20.98_{-0.35}^{+0.46}$	0.143 ± 0.008	-0.12	-0.25
$^{0.1}M_I - 5 \log h$	$-21.60_{-0.37}^{+0.41}$	0.139 ± 0.008	-0.13	-0.36
$^{0.1}(U - V)$	$0.604_{-0.135}^{+0.159}$	0.099 ± 0.0059	0.02	-0.10
$^{0.1}(U - B)$	$-0.014_{-0.090}^{+0.096}$	0.055 ± 0.0034	0.01	-0.01
$^{0.1}(B - V)$	$0.626_{-0.062}^{+0.073}$	0.037 ± 0.0031	0.01	-0.09
$^{0.1}(V - R)$	$0.518_{-0.043}^{+0.049}$	0.010 ± 0.0010	0.00	-0.04
$^{0.1}(R - I)$	$0.637_{-0.047}^{+0.048}$	0.006 ± 0.0009	0.01	0.01

Note. — Values in this table are determined from analyzing the distributions of properties for Milky Way analogs, but after transforming SDSS *ugriz* measurements to *UBVRI*-equivalent values on an object-by-object basis using the `kcorrect` software. As a reminder, *UBVRI* magnitudes are on the Vega system, whereas *ugriz* magnitudes are on the AB system.

Table 3.5.
Photometric Properties for the Milky Way:
Global Stellar Mass-to-Light Ratios

Rest-frame	Υ_u^*	Υ_g^*	Υ_r^*	Υ_i^*	Υ_z^*
$z=0$	$1.90^{+1.18}_{-0.80}$	$1.96^{+0.69}_{-0.64}$	$1.66^{+0.63}_{-0.49}$	$1.43^{+0.48}_{-0.41}$	$1.11^{+0.32}_{-0.32}$
$z=0.1$	$1.77^{+1.61}_{-0.83}$	$1.93^{+0.81}_{-0.68}$	$1.84^{+0.64}_{-0.57}$	$1.54^{+0.61}_{-0.44}$	$1.26^{+0.38}_{-0.37}$
Rest-frame	Υ_U^*	Υ_B^*	Υ_V^*	Υ_R^*	Υ_I^*
$z=0$	$1.86^{+1.05}_{-0.80}$	$1.89^{+0.78}_{-0.65}$	$1.86^{+0.69}_{-0.58}$	$1.61^{+0.59}_{-0.48}$	$1.29^{+0.43}_{-0.37}$
$z=0.1$	$1.81^{+1.39}_{-0.84}$	$1.85^{+0.97}_{-0.68}$	$1.94^{+0.82}_{-0.62}$	$1.74^{+0.59}_{-0.53}$	$1.43^{+0.47}_{-0.42}$

Note. — See the end of §3.5 for details on the calculation of these values.

4.0 SIZING UP THE MILKY WAY: A HIERARCHICAL BAYESIAN META-ANALYSIS OF PHOTOMETRIC SCALE LENGTH MEASUREMENTS

4.1 INTRODUCTION

Since the invention of the first telescopes, astronomers have been trying to explain the distribution of stars that make up the Milky Way (MW). The earliest maps of our Galaxy were developed by keeping a simple tally of the number of stars one could see as a function of their apparent brightness and position on the sky and then interpreting these star counts with a few basic assumptions (Herschel, 1785; Kapteyn & van Rhijn, 1920; Kapteyn, 1922; Seares et al., 1925; Bok, 1937; Oort, 1938). Remarkably, while the accessibility and quality of data has been drastically transformed by advancing technology, this same basic methodology has underlain most present-day photometric models of the MW (Bahcall, 1986), with only a small subset of recent studies that utilized more sophisticated techniques. Today, a wealth of high-quality, well-calibrated observational data for stars has been accumulated from a wide array of multi-band photometric surveys that have been carried out over the past three decades, using both visible and infrared (IR) light. As a result, the literature is rich with studies on the geometrical structure of the Galaxy.

The current picture of the MW has been radically transformed since the first pioneering papers, which followed the advent of detailed studies of extragalactic spiral galaxies (de Vaucouleurs, 1959; Freeman, 1970; Kormendy, 1977). Today, it is well understood that the major stellar components of the MW include a bar with a bulge or pseudobulge at its center and a flattened disk that is much more visibly extended (see, e.g., Chapter 2 and references therein). Generally, current models assume that the distribution of stars comprising the disk

to *first order* is axisymmetric and follows an exponentially declining density profile, both radially and vertically, such that the volume density may be written as

$$\rho_{\star}(R, \phi, Z) = \frac{\Sigma_{\star}(0)}{2H_d} \exp\left(-\frac{R}{L_d} - \frac{Z}{H_d}\right), \quad (4.1)$$

where R , ϕ , and Z are the Galactocentric cylindrical coordinates, $\Sigma_{\star}(0)$ is the central stellar surface density, H_d is the (vertical) disk scale height, and L_d is the (radial) disk scale length. In some cases, authors alternatively employ an isothermal-sheet model for the vertical structure that replaces the $\exp(Z)$ dependence with a $\text{sech}^2(Z)$ dependence in Equation (4.1) with the appropriate renormalization factors (cf. [Spitzer, 1942](#); [van der Kruit & Searle, 1981](#); [Freeman, 1978](#)); however, the details of this are not of interest here. More importantly, L_d represents the radius containing the first e -folding of starlight within the disk in projection, or in other words where the surface density declines to $\sim 37\%$ of $\Sigma_{\star}(0)$, and hence provides a standard measure of the absolute physical size of the Galactic disk.

Dozens of attempts have been made to determine L_d over the past few decades, making it one of the most investigated characteristics of our Galaxy. Here, we focus exclusively on those estimates from photometric models of the MW in order to enable direct comparisons to measurements of extragalactic objects. We have collected a total of 29 different measurements from the literature since 1990, 15 of them are based on optical data and 14 on IR data. Altogether, these values lie in the range of ~ 2 – 6 kpc, and upon close inspection reveal little consensus on the true size of the Galactic disk. At least some of this disparity is likely due to variations in the assumptions that go into each MW model, which typically include between one and five stellar components that are fit by up to a dozen free parameters. Other possible issues are that unidentified substructures present in the data are biasing models fit to particular lines of sight, or that there are a multitude of very different models that are roughly equally successful in fitting the data ([Jurić et al., 2008](#)). To account for these complications many authors have incorporated substructure features into their models (e.g., spiral arms and rings), while others test a variety of functional forms for the assumed density law.

In this chapter, we address the question: given the measurements available in the literature, what is the best photometric estimate of the MW’s disk scale length? In Chapter 5,

we have found that scale lengths measured from optical photometry of other massive spiral galaxies (Hall et al., 2012), which employed the same exponential density model as Equation (4.1), span a range of $\sim 1\text{--}10$ kpc. This is rather comparable to the range of values for the MW described above. To determine more precisely where the MW falls within this range, we can perform a hierarchical Bayesian (HB) meta-analysis (Chapter 2) of Galactic disk scale length estimates. This method will enable us to investigate and remedy any sources of tension amongst disk scale length measurements. Simultaneously, it will provide a single aggregate result that is built upon the rich assortment of photometric survey data that is available, but that also accounts for the possibility that any of the included estimates are offset due to systematics or bear an underestimated error bar, and then incorporate that information into the overall uncertainties in the combined result. An HB analysis will yield improved constraints on the Galactic L_d , which in turn will help us to better understand how our Galaxy measures up to its extragalactic peers.

The structure of this chapter is as follows. In §4.2, we begin by describing the sample of Galactic L_d estimates we have obtained, emphasizing the variety of observational data, MW models, and analysis techniques that they involve. In §4.3, we explain the first-order corrections we make in order to place these estimates on an equal footing, and the HB analysis we subsequently perform on the resulting dataset. Here, we also introduce a Bayesian model averaging technique that we use to produce our final posterior distributions and explain why it is appropriate to use in this work. In §4.4 we present the aggregate results for L_d , including those from both segregating and combining the IR and visible data. Here, we also present the results for the hierarchical parameters, which characterize the overall consistency of the estimates in our dataset, as well as the different ways we have tested for robustness. In §4.5, we provide comparisons to L_d estimates that have been determined from dynamical modeling, as well as to visible-to-IR scale length ratios measured for external galaxies. In this section we also construct an updated model of the stellar disk using the results found here in order to revise our previous estimate of the total stellar mass from Chapter 2. Lastly, in §4.6 we summarize this study and highlight our conclusions.

4.2 THE MILKY WAY SCALE LENGTH DATASET

We have collected 29 different measurements of the exponential scale length, L_d , of the MW’s disk published since 1990. Generally speaking, each L_d estimate is produced by fitting a model of the stellar components comprising the MW to observations of either resolved stars or unresolved starlight; 15 of these measurements were made in the visible and 14 in the infrared (IR). We have restricted this study to include only measurements made based on visible and IR starlight to match as closely as possible what is done for external galaxies. Hence, we have excluded dynamical estimates of the Galactic L_d that are constrained by fitting MW *mass* models to stellar kinematic data, as well those that critically rely on segregating stars into subpopulations based upon their spectroscopically-determined elemental abundances, as such measurements are infeasible for other galaxies.

In Figure 4.1 we display the values and time evolution of the L_d estimates that we have collected, illustrating that as an ensemble they span $\sim 2\text{--}6$ kpc, though many cluster in the 2–3 kpc range. Taking these estimates at face value, we find that they display an interquartile range of 1.2 kpc and that their simple median value is 2.5 ± 0.2 kpc, which at first glance indicates fairly good overall agreement amongst them. However, such metrics neglect the estimated errors in these measurements, not to mention the fact that several lack any error estimate at all (these are marked by dashed error bars in Figure 4.1, which depict 25% of the central value); hence, such a summary discards considerable amounts of information. Furthermore, Figure 4.1 illustrates that many of the individual estimates are incompatible with one another at the $\geq 1\sigma$ level, which indicates the possibility of systematic errors.

The presence of systematics would not be surprising; models of the MW are complex and require many assumptions about its various components. Variations in these model choices amongst authors represents a major potential source of systematic uncertainty in the L_d estimates we have collected. As we will discuss in §4.3, utilizing a hierarchical Bayesian meta-analysis technique, as opposed to more simple methods, to combine these estimates into a single aggregate result is useful on several fronts. Most importantly, it allows us to produce posterior results that incorporate the possibility that any one measurement may be faulty, such as being systematically offset or having an overly-optimistic error estimate, due

to not exploring the effects of varying model assumptions. It also provides more flexibility, e.g., in dealing with those measurements with no formal error estimates, which likely deserve less credence, but still may contain valuable information about the true L_d and hence should not be discarded entirely. In cases where there are disagreements between measurements, the hierarchical Bayesian analysis technique used here will also degrade the uncertainties in derived parameters appropriately.

The studies that we have collected employ a rich assortment of MW structural models, observational datasets, and analysis techniques. In the following subsections, we detail the diversity in each of these three ingredients that go into producing each L_d estimate that we have included in our analyses. We have also summarized these details in Table 4.1 for ease of comparison. As noted in the Table 4.1 footnote, hereafter in this chapter we will use the following reference abbreviations. BSD78: [Bohlin et al. \(1978\)](#); H81: [Hayakawa et al. \(1981\)](#); B&H82: [Burstein & Heiles \(1982\)](#); R&K85: [Rieke & Lebofsky \(1985\)](#); K91: [Kent et al. \(1991\)](#); RM91: [Ruelas-Mayorga \(1991\)](#); Y&Y92: [Yamagata & Yoshii \(1992\)](#); R92: [Robin et al. \(1992\)](#); O&L93: [Ortiz & Lépine \(1993\)](#); N95: [Ng et al. \(1995\)](#); O96: [Ojha et al. \(1996\)](#); P98: [Porcel et al. \(1998\)](#); F98: [Freudenreich \(1998\)](#); B98: [Buser et al. \(1998\)](#); M&vA98: [Mendez & van Altena \(1998\)](#); SFD98: [Schlegel et al. \(1998\)](#); C99: [Chen et al. \(1999\)](#); S99: [Schultheis et al. \(1999\)](#); L&L00: [Lépine & Leroy \(2000\)](#); D&S01: [Drimmel & Spergel \(2001\)](#); O01: [Ojha \(2001\)](#); S02: [Siegel et al. \(2002\)](#); LC02: [López-Corredoira et al. \(2002\)](#); L&H03: [Larsen & Humphreys \(2003\)](#); P&R04: [Picaud & Robin \(2004\)](#); G05: [Girardi et al. \(2005\)](#); A&L05: [Amôres & Lépine \(2005\)](#); B05: [Benjamin et al. \(2005\)](#); I05: [Indebetouw et al. \(2005\)](#); B06: [Bilir et al. \(2006\)](#); M06: [Marshall et al. \(2006\)](#); K07: [Karaali et al. \(2007\)](#); J08: [Jurić et al. \(2008\)](#); C11: [Chang et al. \(2011\)](#); R12: [Robin et al. \(2012\)](#); P13: [Polido et al. \(2013\)](#); LC&M14: [López-Corredoira & Molgó \(2014\)](#); M15: [Mao et al. \(2015\)](#).

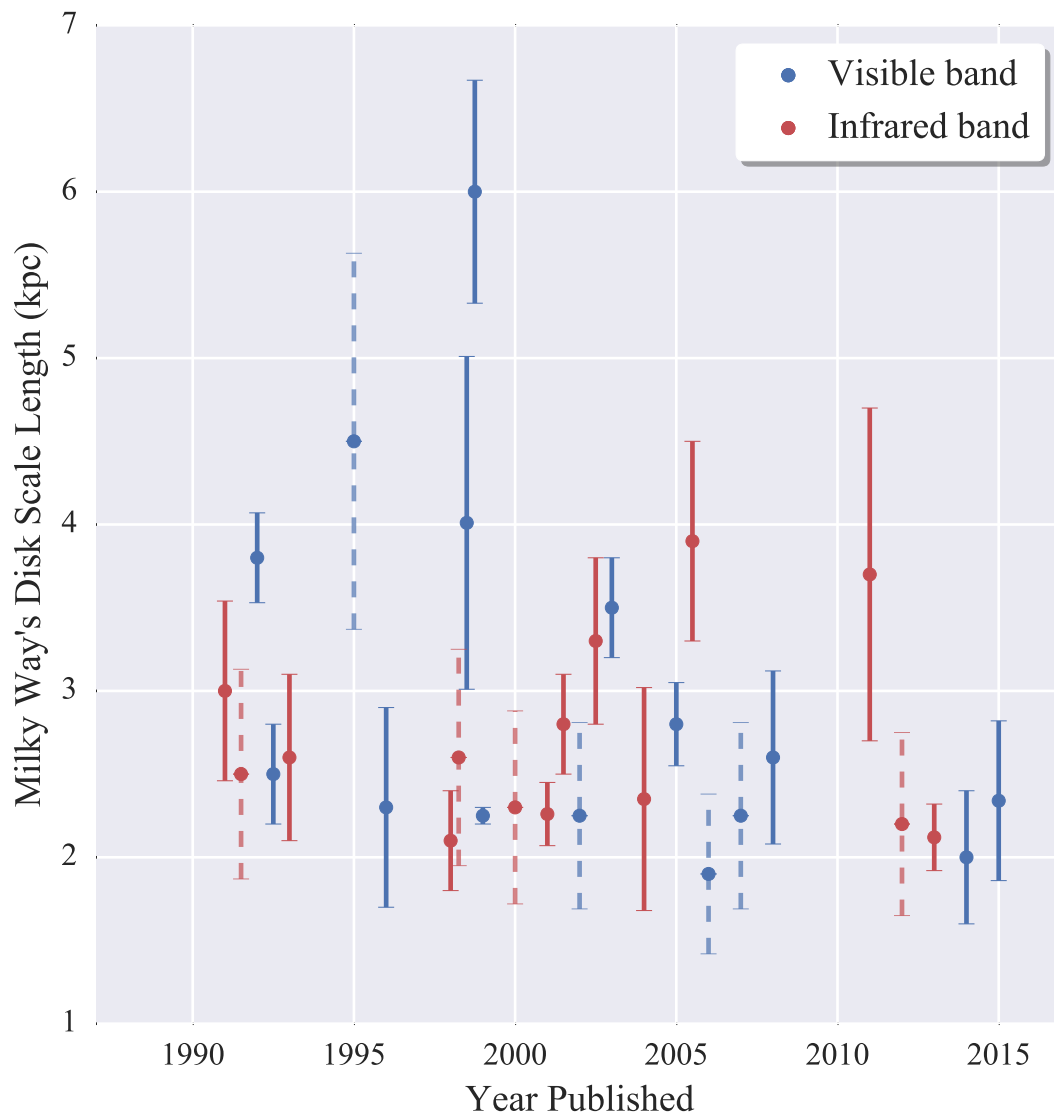


Figure 4.1: The evolution of Milky Way’s L_d estimates in the literature since 1990, which span $\sim 2\text{--}6$ kpc. There are 29 measurements in total; 15 are determined from visible starlight (shown in blue) and 14 from infrared starlight (shown in red). For those measurements that lack any error estimate, we display dashed error bars that correspond to 25% of the central value, which will be the standard treatment for our analyses (see §4.3.1.3). A detailed list of the studies that produced these estimates is provided in Table 4.1.

Table 4.1: Milky Way Scale Length Measurements:
Observational Data, Galactic Models, Analysis Techniques

Reference	$L_d \pm 1\sigma$ (kpc)	Survey/ Telescope ^a	Passbands/ Sample Description	Field(s) of View/ Sky Area	Approximate # of Stars	Dust Model	Stellar Model ^b	Analysis Technique
K91	3.00 ± 0.54	Spacelab IR Telescope	[2.4 μ m] map $f \gtrsim 0.15$ mJy/sr	$ l \lesssim 120^\circ$, $ b \lesssim 10^\circ$, $\Omega \sim 104 \text{ deg}^2$	—	BSD78	B+D1+D2(ring) 8 free parameters	integrated flux
RM91	2.50	H81 IR balloon experiments	[2.4 μ m] map, $f \gtrsim 0.02$ mJy/sr	$-70^\circ < l < 60^\circ$, $ b \lesssim 10^\circ$, $\Omega \sim 113 \text{ deg}^2$	—	double-exponential disk profile	B+D1+R	integrated flux
Y&Y92	3.80 ± 0.27	KST (pp)	UBV , $10 < V < 18$	$(l, b) = (200^\circ, 59^\circ)$, $(37^\circ, -51^\circ)$ $\Omega = 33 \text{ deg}^2$	35,600	Not specified	B+D1+D2 6 free parameters	star counts
R92	2.50 ± 0.30	CFHT (CCD) KST (pp)	UBV , $V < 25$; UBV , $V < 17.5$	$(l, b) = (179^\circ, 2.5^\circ)$, $\Omega = 2 \text{ deg}^2$	25,000	Einasto profile fit to CCDs	D1(cutoff) 2 free parameters (Besançon)	star counts
O&L93	2.60 ± 0.50	SAAO Sutherland, Teide Observatory	$K < 10$	7 fields uniform over $0^\circ < l < 60^\circ$, $b \sim 0^\circ$, $\Omega = 0.3 \text{ deg}^2$	1,100	BSD78-based Gaussian disk profile	B+D1+D2+SA	star counts
N95	4.50	Palomar-Groningen Survey (pp)	BR , $B < 18$	$(l, b) = (0^\circ, -10^\circ)$, $\Omega = 2.8 \text{ deg}^2$	481,500	$A_v \propto R$ along line of sight	B+D1+D2+SA+R	star counts
O96	2.30 ± 0.60	5 surveys (pp+CCD)	$UBVR$, $V < 18.5$	$(l, b) = (167^\circ, 47^\circ)$, $(3^\circ, 47^\circ)$, $(278^\circ, 47^\circ)$ $\Omega = 43.5 \text{ deg}^2$	48,000	Not specified	D1 1 free parameter	photometric parallax
P98	2.10 ± 0.30	TMGS	$9 < K < 10$	$30^\circ < l < 70^\circ$, $b = 5^\circ$	Not specified	Not specified	D1 1 free parameter	star counts
F98	2.60	COBE/DIRBE	JKL maps	all sky excluding $ l < 20^\circ$, $ b < 12^\circ$	—	exponential disk profile	Bar+D1(hole,warp,cutoff) 31 free parameters	integrated flux
B98	4.01 ± 1.00	Basel survey (pp)	RCU , $G \lesssim 16-20$	7 fields over $32^\circ < b < 85^\circ$, $\Omega = 15.4 \text{ deg}^2$	9,107	$E(G-R) = 0$ for fields used	D1(young+old) +D2+H 12 free parameters	star counts
M&vA98	6.00 ± 0.67	Guide Star Catalogue (pp)	BV , $8 < V < 13.7$	6 fields at $b < 10^\circ$, $\Omega = 18 \text{ deg}^2$	12,727	BH82-based exp. disk profile	D1 2 free parameters	star counts
C99	2.25 ± 0.05	4 surveys	BVR_I	4 fields over	1.7×10^7	SFD98-based	D1+D2+H	star

Table 4.1 – Continued

Reference	$L_d \pm 1\sigma$ (kpc)	Survey/ Telescope ^a	Passbands/ Sample Description	Field(s) of View/ Sky Area	Approximate # of Stars	Dust Model	Stellar Model ^b	Analysis Technique
L&L00	2.30	(pp+CCD) COBE/DIRBE, Spacelab IR Tele.	$V < 25$ [2.4 μ m] map, $f \gtrsim 0.15$ mJy/sr	$0^\circ < l < 290^\circ, b < 17^\circ,$ $\Omega \sim 7 \text{ deg}^2$ all sky; $-20^\circ < l < 120^\circ, b < 30^\circ$	—	exp. disk profile same as O&L93	2 free parameters B+Bar+D1+D2+SA	counts integrated flux
D&S01	2.26 ± 0.19	COBE/DIRBE	JK maps	all sky excluding $ l < 20^\circ, b < 30^\circ$	—	SFD98-based multi- component model	D1(warp,flare,cutoff)+SA 19 free parameters	integrated flux
O01	2.80 ± 0.30	2MASS-DR1	$JHK_s,$ $J < 16,$ $K_s < 15$	7 fields at $ b > 12^\circ,$ $\Omega = 68 \text{ deg}^2$	10^6	$A_V \propto R_{LOS}$	B+D1(cutoff)+D2+H (Einasto radial profile) (Besançon)	star counts
S02	2.25	Swope Telescope Las Campanas Obs.	$BVR_I,$ $B < 21.1,$ $V < 21.4$	7 fields at $-90^\circ < l < 120^\circ,$ $30^\circ < b < 86^\circ,$ $\Omega = 14.9 \text{ deg}^2$	70,000	SFD98	B(fixed)+D1+D2+H 7 free parameters	photometric parallax
LC02	3.30 ± 0.50	2MASS-DR2	$JK,$ $8.5 < K < 14$	12 fields over $45^\circ < l < 315^\circ, b < 12^\circ,$ $\Omega \sim 52 \text{ deg}^2$	53,000	R&L85-based CMD calibration	D1(flare,warp) 3 free parameters	star counts
L&H03	3.50 ± 0.30	APS POSS I	$OE,$ $O < 20$	88 fields uniform over $ b > 20^\circ, \Omega = 1,408 \text{ deg}^2$	2.5×10^6	B&H82	D1+D2+H 7 free parameters	star counts
P&R04	2.35 ± 0.67	DENIS	$JK_s,$ $J < 15$	94 windows of low A_V over $-8^\circ < l < 12^\circ, b < 4^\circ,$ $\Omega \sim 6 \text{ deg}^2$	Not specified	S99	B+D1(hole) 11 free parameters	star counts
G05	2.80 ± 0.25	DMS	$UBVR,$ $B < 23.8$	6 fields at high $b,$ $\Omega = 0.83 \text{ deg}^2$	19,500	SFD98	D1+H 4 free parameters	star counts
B05	3.90 ± 0.60	GLIMPSE/Spitzer	$[3.6\mu\text{m}] < 14.2,$ $[4.5\mu\text{m}] < 14.1,$ $[5.8\mu\text{m}] < 11.9,$ $[8.0\mu\text{m}] < 9.5$	$10^\circ < l < 65^\circ,$ $ b < 1^\circ,$ $\Omega \sim 220 \text{ deg}^2$	3×10^7	I05	D1 2 free parameters	star counts
B06	1.90	SDSS-DR3	$ugriz,$ $16 < g < 21$	6 fields over $4^\circ < l < 84^\circ, 41^\circ < b < 52^\circ,$ $\Omega = 70 \text{ deg}^2$	14,940	SFD98	D1 3 free parameters	photometric parallax
K07	2.25	SDSS-DR5	$ugriz,$ $g < 22.5$	$(l, b) = (90^\circ, 50^\circ),$ $(180^\circ, 50^\circ), (60^\circ, 45^\circ);$ $\Omega = 60 \text{ deg}^2$	187,000	SFD98	D1+D2+H 7 free parameters	photometric parallax
J08	2.60 ± 0.52	SDSS-DR5	$ugriz,$ $r < 22$	full SDSS footprint, mostly $ b > 25^\circ,$ $\Omega = 6,500 \text{ deg}^2$	4.8×10^7	SFD98	D1+D2+H 9 free parameters	photometric parallax

Table 4.1 – Continued

Reference	$L_d \pm 1\sigma$ (kpc)	Survey/ Telescope ^a	Passbands/ Sample Description	Field(s) of View/ Sky Area	Approximate # of Stars	Dust Model	Stellar Model ^b	Analysis Technique
C11	3.70 ± 1.00	2MASS	$5 < K_s < 14.3$	8,192 lines of sight all-sky except $ b < 30^\circ$	Not specified	SFD98	D1+D2+H 10 free parameters	star counts
R12	2.20	2MASS	JK_s , depth field dependent	200 windows over $ l < 20^\circ$, $ b < 10^\circ$	Not specified	M06	B1(bar)+B2+D1(hole)+D2 10 free parameters (Besançon)	star counts
P13	2.12 ± 0.20	2MASS	JK_s , 90% brightest objects	3,072 lines of sight over all-sky, $\Omega \sim 3,702 \text{ deg}^2$	Not specified	A&L05	B+Bar+D1(hole)+D2(hole)+SA 11 free parameters	star counts
LC14	2.00 ± 0.40	SDSS/SEGUE F/G-dwarfs	$ugriz$, $g < 21.5$	$ l > 50^\circ$, $ b < 23^\circ$, $\Omega = 1,400 \text{ deg}^2$	Not specified	SFD98	D1(hole,flare)+D2+H(fixed) 9 free parameters	star counts
M15	2.34 ± 0.48	SDSS/SEGUE G-dwarfs	$ugriz$, $15 \lesssim g \lesssim 17.5$	152 pencil beams uniform over SDSS footprint $\Omega \sim 1,000 \text{ deg}^2$	18,067	SFD98	D1+D2 5 free parameters	3D spatial 2pt correlation function

Note. — References are abbreviated as follows. BSD78: [Bohlin et al. \(1978\)](#); H81: [Hayakawa et al. \(1981\)](#); B&H82: [Burstein & Heiles \(1982\)](#); R&K85: [Rieke & Lebofsky \(1985\)](#); K91: [Kent et al. \(1991\)](#); RM91: [Ruelas-Mayorga \(1991\)](#); Y&Y92: [Yamagata & Yoshii \(1992\)](#); R92: [Robin et al. \(1992\)](#); O&L93: [Ortiz & Lépine \(1993\)](#); N95: [Ng et al. \(1995\)](#); O96: [Ojha et al. \(1996\)](#); P98: [Porcel et al. \(1998\)](#); F98: [Freudenreich \(1998\)](#); B98: [Buser et al. \(1998\)](#); M&vA98: [Mendez & van Altena \(1998\)](#); SFD98: [Schlegel et al. \(1998\)](#); C99: [Chen et al. \(1999\)](#); S99: [Schultheis et al. \(1999\)](#); L&L00: [Lépine & Leroy \(2000\)](#); D&S01: [Drimmel & Spergel \(2001\)](#); O01: [Ojha \(2001\)](#); S02: [Siegel et al. \(2002\)](#); LC02: [López-Corredoira et al. \(2002\)](#); L&H03: [Larsen & Humphreys \(2003\)](#); P&R04: [Picaud & Robin \(2004\)](#); G05: [Girardi et al. \(2005\)](#); B05: [A&L05: Amôres & Lépine \(2005\)](#); Benjamin et al. (2005); I05: [Indebetouw et al. \(2005\)](#); B06: [Bilir et al. \(2006\)](#); M06: [Marshall et al. \(2006\)](#); K07: [Karaali et al. \(2007\)](#); J08: [Jurić et al. \(2008\)](#); C11: [Chang et al. \(2011\)](#); R12: [Robin et al. \(2012\)](#); P13: [Polido et al. \(2013\)](#); LC14: [López-Corredoira & Molgó \(2014\)](#); M15: [Mao et al. \(2015\)](#).

^a Items marked with (pp) indicate that photographic plate data is included.

^b For brevity we abbreviate component types as follows: B: Bulge; D: Disk; H: Halo; R: Ring; SA: Spiral Arms. When multiple versions of the same type of component are included, each is further distinguished by a numerical value (e.g., when a model includes both a thin and thick disk component these will be marked as D1+D2). If any added substructure is included within a component or if any component is fixed (has no free parameters in the fit) this is marked in parenthesis. In cases where multiple disks are fit to the data, we include the L_d estimate corresponding to the *dominant* component (i.e., the one with largest mass), regardless of whether the author labels it “thin”, “thick”, “old”, “young”, etc. (see, e.g., O&L93 and L&L00).

4.2.1 Observational Data

In this study we are interested only in photometric measurements of the MW's scale length, which we wish to match *as closely as possible* the methods used in measurements for other disk galaxies. Therefore, the observational data employed by our set of studies is strictly limited to measurements of starlight at either visible or IR wavelengths. Despite this limitation, there are many Galactic surveys that fit this requirement; notable examples are the Two Micron All-Sky Survey (2MASS) in the IR and the Sloan Digital Sky Survey (SDSS) in the visible. While these large-scale surveys covered a large fraction of the night sky, many more smaller-scale projects were carried out to yield pencil-beam surveys of stars in the Galaxy, encompassing many different fields of view with varying sizes.

Earlier studies using measurements made in the visible were generally limited to high Galactic latitude, b , in order to minimize reddening and extinction due to dust (e.g., Yamagata & Yoshii, 1992; Ojha et al., 1996; Buser et al., 1998), or to narrow windows of low absorption (e.g., Robin et al., 1992). This limitation was mitigated, however, by the all-sky map of Galactic dust provided by Schlegel et al. (1998, hereafter SFD98), allowing for measurements based on optical data to push toward lower b (e.g., Chen et al., 1999; Siegel et al., 2002; Jurić et al., 2008). In some cases, authors use the full extinction correction out to infinity as a boundary condition for their dust model (see, e.g., Girardi et al., 2005, which employs an exponential dust distribution). We note here that many of the more recent studies that utilize the SFD98 dust maps, particularly those based on SDSS data, generally apply the full extinction correction out to infinity for each star in their sample. This clearly is an overcorrection and will bias distance or magnitude estimates; however, Jurić et al. (2008) explore the effects of this and find that it is only worrisome for stars within 100 pc of the Galactic plane when fitting structure models. For their case, this corresponds to only 0.05% of their stellar sample (which they exclude) given the magnitude limits of the SDSS instrument, concluding that overestimated interstellar extinction corrections will have negligible impact on results. IR measurements, on the other hand, are far more immune to the effects of interstellar dust, allowing studies to probe the Galactic structure over a wide range in b (e.g., Kent et al., 1991; Drimmel & Spergel, 2001; Benjamin et al., 2005).

The pertinent details of each observational dataset are listed in Table 4.1. There one can see that fields of view can range from $\sim 1 \text{ deg}^2$ to covering the full sky, corresponding to stellar sample sizes that vary from $\sim 10^3$ to $\sim 10^7$. We note that the cutoff date of 1990 is used to limit ourselves primarily to observational data yielded from CCD technology, though a few of our L_d estimates are derived from observations using photographic plates (as is noted in Table 4.1), as well as to ensure the use of modern Galactic assumptions. We note that in some cases the IR data employed did not contain a sample of photometrically resolved stars, but instead provided a map of integrated flux from Galactic light.

4.2.2 Models of the Milky Way

Almost all of the studies we have collected model the radial structure of the Galactic disk according to Equation (4.1). The exceptions to this are Robin et al. (1992) and Ojha (2001) who use an Einasto (1965) law, which yields a radial density distribution that is equivalent to an exponential profile and hence yields comparable estimates of L_d .

Depending on the field of view and depth of the survey, other components of the Galaxy may be included as well. For example, a particular model may include a bulge, a second disk, or a halo, each with their own density profile. However, with this added level of model complexity comes additional free parameters that need to be fitted for simultaneously. As a result, strong inter-parameter degeneracies can often hamper the ability to isolate a single “correct” description of the data, which is likely the main culprit for the disparate values of L_d that can be found in Table 4.1.

Lastly, there are various added features and/or substructure that are often included in the disk models employed. Jurić et al. (2008) pointed out that the presence of unidentified substructures in the true distribution of stars can bias the results from models attempting to fit the smooth, underlying profile. To handle this, many studies include substructure components in their Galactic model, such as rings and/or spiral arms (e.g., Ortiz & Lépine, 1993; Ng et al., 1995; Drimmel & Spergel, 2001; Polido et al., 2013). Others also allow for the possibility of an asymmetry or “warp” in the shape of the disk (e.g., López-Corredoira & Molgó, 2014). Alternatively, some of the included studies may allow or even force their

model to deviate from a pure exponential profile. This can take the form of truncations or holes at the center of the Galactic disk, which systematically ascribe more stellar material to the bulge component in this region (e.g., [Freudenreich, 1998](#); [Picaud & Robin, 2004](#); [López-Corredoira & Molgó, 2014](#)). Others include a cutoff radius beyond which they assume stars cease to exist, instead of extrapolating to $R = \infty$ (e.g., [Freudenreich, 1998](#)). All of these assumptions are plausible; other spiral galaxies are observed both with and without central holes and rings, their profiles can appear either flocculent or smooth, as well as warped or flat ([Buta, 2014](#); [Buta et al., 2015](#)).

4.2.3 Analysis Techniques Used for Scale Length Measurements

As seen in [Table 4.1](#), even when similar sorts of observational data are used, a wide variety of analysis techniques have been employed to measure scale lengths. We provide a summary of these methods here.

4.2.3.1 Integrated Light The first case to consider is where the observational data take the form of a smooth map of the integrated flux from Galactic light, typically produced by IR instruments with lower angular resolution. This provides the intensity of emission at some effective frequency ν , I_ν , as a function of Galactic longitude and latitude, (l, b) . To model I_ν , one first needs to adopt a model for the distribution of stars in the MW, $\rho_\star(R, \phi, Z)$, where the disk component typically follows the form of [Equation \(4.1\)](#). By assuming values for the Galactocentric radius and planar offset of the Sun, R_0 and Z_0 , respectively, one can then recast ρ_\star into heliocentric spherical coordinates (r, l, b) by

$$R = (R_0^2 + r^2 \cos^2 b - 2R_0 r \cos b \cos l)^{1/2},$$

$$Z = r \sin b + Z_0, \tag{4.2}$$

where r is the line-of-sight distance toward (l, b) . Next, one assumes a characteristic specific emissivity, ϵ_ν , for the stellar population (equivalent to assuming a luminosity function), which is multiplied by ρ_\star to obtain the stellar flux density. The observed integrated flux will be

modulated by dust absorption, however, and so one must adopt a model for the distribution of dust in order to obtain the optical depth along the line of sight, $\tau_\nu(r)$. Finally, all of these ingredients are combined into a model of the light intensity across the sky by

$$I_\nu(l, b) = \sum_c \epsilon_{\nu,c} \int_0^\infty \rho_{\star,c}(r, l, b) e^{-\tau_\nu(r)} dr, \quad (4.3)$$

where the summation over c signifies the different stellar components and populations that need to be included (see §3 of [Drimmel & Spergel, 2001](#) for more details). One then optimizes the free parameters included in the model to best fit the observational data, which yields an estimate of L_d .

4.2.3.2 Star Counts While star count analyses using photometric data began nearly a century ago (as described in [Bahcall, 1986](#); [Binney & Merrifield, 1998](#)), the practicality and hence the popularity of this technique for studying the geometric structure and size of the MW has exploded over the past few decades (see the final column of [Table 4.1](#)). This is not only due to the accuracy and depth of photometric surveys improving with technology, but also because imaging of extragalactic objects has resulted in better-informed models of stellar structure (e.g., [de Vaucouleurs & Pence, 1978](#); [Bahcall & Soneira, 1980, 1984](#)). Star count analyses have been the most prevalent method for constraining photometric models of the MW.

Here, one attempts to reproduce the observed number of stars in a field of view subtending solid angle Ω toward the direction (l, b) whose apparent magnitudes are between some lower and upper limit, denoted by m_1 and m_2 , respectively. In order to do so, one must integrate the assumed stellar density law, $\rho_\star(R, \phi, Z)$, weighted by an assumed luminosity function, $\Phi(M)$, over the volume of the survey and the range of magnitudes. After converting ρ_\star to heliocentric spherical coordinates via [Equation \(4.2\)](#), one obtains the “fundamental equation of stellar statistics” ([Bahcall, 1986](#)):

$$N(m_1, m_2, l, b, \Omega) = \sum_c \Omega \int_{m_1}^{m_2} \int_0^\infty \rho_{\star,c}(r, l, b) \Phi_c(M) r^2 dr dm, \quad (4.4)$$

where again the summation over c implies that the individual stellar components are combined to yield the total. Here, one also substitutes the absolute magnitude as $M = m -$

$5 \log r - A(r) + 5$, where $A(r)$ is the total extinction out to distance r in the passband that the magnitudes are measured using, making the above integrand a function purely of r and m . Therefore, one must also include a model of Galactic dust and its attenuation to inform the choice of $A(r)$. Using Equation (4.4), authors optimize the free parameters included in ρ_\star to achieve the best fit to the observed star counts, yielding an estimate of L_d .

The star counts method is often considered superior for making determinations of the 3D structural parameters of our Galaxy compared to the integrated-light technique described above. As [Picaud & Robin \(2004\)](#) pointed out, integrated flux profiles are dominated by the brightest and closest stars, whereas star count studies incorporate a wider range of intrinsic luminosities and distances. Furthermore, a common simplification strategy is to restrict to a narrow bin in color, allowing one to assume that all stars in the sample have approximately the same color and hence absolute magnitude via a Hertzsprung-Russell-diagram (HRD) relation, and essentially rendering Φ into a Dirac delta function (see, e.g., [López-Corredoira & Molgó, 2014](#)). As [Polido et al. \(2013\)](#) pointed out, studies using the star counts method can also be separated into two classes: those that adopt an empirical luminosity function (e.g., [Ortiz & Lépine, 1993](#); [Buser et al., 1998](#)) and those that adopt a theoretical luminosity function based on models of stellar evolution (e.g., [Picaud & Robin, 2004](#); [Girardi et al., 2005](#)).

4.2.3.3 Photometric Parallax Taking the star counts method one step further, authors have been able to make explicit distance measurements for each star in their dataset using a so-called “photometric parallax” relation (see, e.g., [Gilmore & Reid, 1983](#); [Ojha et al., 1996](#); [Jurić et al., 2008](#)). Here, one uses an appropriately-calibrated HRD to map each star’s color to its intrinsic luminosity and combine that with its apparent magnitude in order to infer its distance, r . Such a technique yields the full 3D position information (r, l, b) for each star in a sample. Authors then simply need to optimize the free parameters in their Galactic model ρ_\star to best reproduce to volume density structure displayed by the sample, yielding an estimate for L_d .

4.2.3.4 Two-Point Correlation Function Recently, [Mao et al. \(2015\)](#) have pioneered the application of the two-point correlation function, $\xi(r)$, in fitting the stellar density distribution. Traditionally, this technique has been used to study the large-scale structure of the Universe, where $\xi(r)$ quantifies the strength of galaxy clustering as a function of separation ([Peebles, 1980](#)). This is calculated as

$$\xi(r) = \frac{DD(r)}{RR(r)} - 1, \quad (4.5)$$

where $DD(r)$ is the observed number of pairs of galaxies at separations between r and $r + dr$, and $RR(r)$ is the number of pairs measured in a mock catalog of galaxies randomly distributed over the same volume. In order to constrain Galactic structure, [Mao et al. \(2015\)](#) have replaced the idea of a *random* catalog with a *model* catalog, where the positions of stars are generated from their Galactic stellar density model, which will have counts of pairs $MM(r)$ as a function of separation. Here, $DD(r)$ becomes the number of pairs of stars as a function of separation, and $MM(r)$ replaces $RR(r)$ in Equation (4.5). The free parameters of the model are then optimized to yield $\xi(r) \sim 0$, producing an estimate of L_d .

We point the reader to Table 4.1, where we have provided a detailed synopsis for each of the published works that produced an L_d estimate that we utilize in this study. Here one can find a breakdown of the observational data and methodologies that go into each. Where provided, this includes: the reference, the scale length estimate value, the survey/telescope utilized, the passbands that measurements were made using and any associated sample-defining criteria, the field(s) of view and/or sky area covered, the approximate number of stars in the sample, details of the authors' choice of dust and stellar models for the Galaxy, including both the major and substructure components incorporated and the corresponding number of free parameters, and lastly the analysis technique. The footnote of Table 4.1 explains the reference abbreviations that are used throughout this chapter, including other tables and figures.

4.3 METHODS

4.3.1 Hierarchical Bayesian Technique

Our goal is to perform a meta-analysis of the L_d estimates we have collected in order to determine a single aggregate result, encapsulating our overall knowledge from the various observational data and MW models available. As discussed above, these estimates often are in tension with each other; this is likely due at least in part to differences in assumptions and methodologies amongst them. We therefore rely on the power of a hierarchical Bayesian (HB) statistical technique (Press, 1997; Hogg et al., 2010; Dahlen et al., 2013; Chapter 2) to perform a meta-analysis of the set of literature results. This is the appropriate tool to use for a variety of reasons. Most importantly, it has been vetted as a powerful technique for extracting the consistent underlying signal from a sample of potentially flawed measurements (see, e.g., Lang & Hogg, 2012). It also yields error estimates that expand appropriately when the individual estimates are statistically inconsistent. This is a distinct advantage over the inverse variance-weighted mean (IVWM), which has more limitations than the HB framework; e.g., calculating the IVWM requires that the individual measurements are well-described by Gaussian probability distributions and that they are statistically compatible with one another. However, one helpful feature of the HB technique is that it becomes equivalent to calculating the IVWM in the limit that the data that are all found to be highly consistent with one another.

In this study, we will produce our results using the same formalism and by employing the same problematic-measurement models that are laid out in Chapter 2, though with an added level of analysis that will be introduced in §4.3.1.1; we refer the reader to this work for the full details, where one can also find a pedagogical introduction. We note, again, that while we have labeled this a “hierarchical Bayesian technique,” this is *not* to be confused with methods that recently have been labeled as “Bayesian hierarchical modeling” or “Hierarchical Bayes” (e.g., Loredo, 2012b; Gelman et al., 2013; Martinez, 2015), which are defined by having several layers of parameters, typically such that priors on model parameters are themselves dependent on additional free parameters (i.e., hyperparameters), and hence require their

own priors (i.e., hyperpriors). Here, we use the terminology “hierarchical” in the sense that our method relies on fitting for free parameters that characterize only a subset of the data that we analyze simultaneous to the physical parameter of interest (e.g., L_d). One could alternatively refer to our method as a “Bayesian mixture model” approach to meta-analysis (Hogg et al., 2010). We will now briefly summarize the details of this method, which will be important for interpreting our tables and figures below.

In short, we take a mixture-model approach by assuming that our L_d dataset can be divided into two subgroups: one where measurements are constraining the same parameter of interest with properly-estimated uncertainties (“good”), and one where measurements are inaccurate in some way, e.g., suffering from unrealistic error estimates or neglecting a potentially significant source of bias (“bad”). The probability distribution for the true value of L_d given any single measurement then looks like $P(L_d) = f_{\text{good}}P(L_d \mid \text{measurement is “good”}) + (1 - f_{\text{good}})P(L_d \mid \text{measurement is “bad”})$, where $P(A \mid B)$ generically indicates the probability distribution function (PDF) for A conditional upon B being true and f_{good} denotes the probability that the measurement is “good”. This provides a template for the likelihood function within our HB analysis. If the measurement is represented by a Gaussian distribution with mean μ and standard deviation σ , then we can straightforwardly write that

$$P(L_d \mid \text{measurement is “good”}) = \frac{1}{\sqrt{2\pi\sigma^2}} \exp\left(-\frac{(L_d - \mu)^2}{2\sigma^2}\right). \quad (4.6)$$

As mentioned above, there are a variety of ways that measurements can be problematic. We have developed a number of bad-measurement models to account for this; specifically, these are:

free- n : we assume that bad measurements have overly-optimistic error bars by a factor of n . Here $P(L_d \mid \text{measurement is “bad”})$ would be constructed by replacing σ with $n\sigma$ in Equation (4.6);

free- Q : we assume that bad measurements have neglected a significant source of uncertainty, whose overall magnitude should be added in quadrature to the nominal error bars. We quantify this as some fraction Q of the median estimate from the set of measurements, which we will denote as μ^{MED} , and construct $P(L_d \mid \text{measurement is “bad”})$ by replacing

σ^2 with $\sigma^2 + (Q\mu^{\text{MED}})^2$ in Equation (4.6);

free- F : we assume that all measurements are truly capable of reaching only a certain level of accuracy, and bad measurements are those that fall below this level. We quantify this by setting a floor value on error bars for all measurements uniformly equal to some fraction F of μ^{MED} , and hence we construct $P(L_d \mid \text{measurement is “bad”})$ by replacing σ with $F\mu^{\text{MED}}$ in Equation (4.6) in all cases where σ is below that limit;

P_{bad} -flat: we assume that bad measurements are critically flawed and should contribute zero weight to our study. We achieve this by modeling $P(L_d \mid \text{measurement is “bad”})$ as a flat PDF over all parameter space.

Equations (2.2)–(2.5) in Chapter 2 show the full form of the likelihood function for each case. We note here that making first-order corrections to our dataset, which will be discussed in following subsections, can cause μ^{MED} to shift in value. To circumvent any difficulties in interpreting our results due to this, throughout this work we invariably set $\mu^{\text{MED}} = 2.5$ kpc, as this very nearly if not equal to the median estimate value among the cases of considering the visible or IR measurements separately and when combining them.

Hereafter, we generically denote each model by \mathcal{M}_k and its set of free parameters (separate from L_d) by Θ_k ; in most cases, those free parameters are f_{good} and one of n , Q , or F . Amongst all of these scenarios, Θ_k represents free parameters that characterize the data itself, which are fit for simultaneously with the true value of L_d — the existence of these extra parameters beyond the quantity of interest is what makes our analysis hierarchical. We also explore the effect of setting $f_{\text{good}} = 0$ within each of the models described above (except for the P_{bad} -flat model, as that would mean nullifying all of our data), which corresponds to assuming that not just *some*, but all L_d measurements are flawed to some extent; these cases are denoted by appending “all-bad” to the model name. Lastly, we explore the possibility that all L_d estimates are accurate by setting $f_{\text{good}} = 1$ within any model that we have described above, which we denote as the “all-good” model. As mentioned above, this reduces our formalism to calculating the (non-hierarchical) IVWM, and serves as our null hypothesis. Overall, this constitutes eight different ways of modeling the L_d dataset; we will refer to this dataset as an ensemble with the label \mathcal{D} .

Assuming that all of the data are statistically independent, one can write the overall

likelihood function as the product of the likelihood functions for each measurement,

$$P(\mathcal{D} | L_d, \Theta_k, \mathcal{M}_k) = \prod_i P(\mu_i, \sigma_i | L_d, \Theta_k, \mathcal{M}_k), \quad (4.7)$$

where μ_i and σ_i are the mean and error estimate for the i th estimate. At this point, f_{good} (which is buried in Θ_k) may be interpreted as the fraction (or frequency) of accurate estimates in \mathcal{D} . Finally, the joint posterior for the parameters of the hierarchical model given the set of measurements used can be calculated by

$$P(L_d, \Theta_k | \mathcal{D}, \mathcal{M}_k) = \frac{P(\mathcal{D} | L_d, \Theta_k, \mathcal{M}_k)P(L_d)P(\Theta_k | \mathcal{M}_k)}{P(\mathcal{D} | \mathcal{M}_k)}. \quad (4.8)$$

4.3.1.1 Posterior Results From Bayesian Model Averaging In Chapter 2, we compared the Bayesian evidence for each model to select the one that best fits the data. For model \mathcal{M}_k with free parameters contained in the vector Θ_k , the evidence represents the probability of measuring the data \mathcal{D} given that \mathcal{M}_k is the correct model and is calculated by

$$P(\mathcal{D} | \mathcal{M}_k) = \int \int P(\mathcal{D} | L_d, \Theta_k, \mathcal{M}_k)P(L_d)P(\Theta_k | \mathcal{M}_k) dL_d d\Theta_k. \quad (4.9)$$

This is the integral of the likelihood weighted by the priors over all parameter space. Such a metric provides a natural, Bayesian method of applying the principles of Occam’s Razor to model selection by weighing the goodness-of-fit against the size of the parameter space required to achieve it. In that study, we found that the all-good model came out well ahead in this comparison, such that the other models were not comparable to it.

Unlike the results in Chapter 2, we find here that in some cases more than one bad-measurement model can be competitive in maximizing the Bayesian evidence *while also* yielding measurably different $P(L_d | \mathcal{D}, \mathcal{M}_k)$. While these differences are well below the $\sim 1\sigma$ threshold, there still remains the question of how to select the correct model. In cases where the evidence strongly favors a particular model compared to the others, or where each model yields very similar posterior results, the choice is less difficult or of little consequence.

To handle this issue, we employ a Bayesian model averaging (BMA; [Hoeting et al., 1999](#)) technique to obtain $P(L_d | \mathcal{D})$, effectively marginalizing over all models that we consider. To calculate this, we must first assume that one of the models considered is correct (but that

we do not know which one is), and then choose a prior probability $P(\mathcal{M}_k)$ for each being the true model. If there are K models to consider, then the marginalized posterior is given by

$$P(L_d | \mathcal{D}) = \sum_{k=1}^K P(L_d, \mathcal{M}_k | \mathcal{D}), \quad (4.10)$$

where $P(L_d, \mathcal{M}_k | \mathcal{D})$ is the joint posterior distribution describing the true value of L_d and whether \mathcal{M}_k is the correct model. By the definition of joint probability we can rewrite this as

$$P(L_d | \mathcal{D}) = \sum_{k=1}^K P(L_d | \mathcal{D}, \mathcal{M}_k) P(\mathcal{M}_k | \mathcal{D}), \quad (4.11)$$

where $P(\mathcal{M}_k | \mathcal{D})$ is the marginalized posterior probability for \mathcal{M}_k being the true model, which is given by

$$P(\mathcal{M}_k | \mathcal{D}) = \frac{P(\mathcal{D} | \mathcal{M}_k) P(\mathcal{M}_k)}{\sum_{j=1}^K P(\mathcal{D} | \mathcal{M}_j) P(\mathcal{M}_j)}. \quad (4.12)$$

Here, $P(\mathcal{D} | \mathcal{M}_k)$ is the Bayesian evidence for model \mathcal{M}_k given by Equation (4.9).

To apply BMA, we assume that all eight of our bad-measurement models have equal prior probability of being the correct one and hence choose $P(\mathcal{M}_k) = 1/K = 1/8$. This assumption causes a number of cancellations in Equation (4.12), and hence by plugging this into Equation (4.11) the marginalized posterior for L_d effectively becomes the evidence-weighted model average:

$$P(L_d | \mathcal{D}) = \frac{\sum_{k=1}^8 P(L_d | \mathcal{D}, \mathcal{M}_k) P(\mathcal{D} | \mathcal{M}_k)}{\sum_{j=1}^8 P(\mathcal{D} | \mathcal{M}_j)}. \quad (4.13)$$

Consequently, models with low Bayesian evidence for them will have little impact on our net posterior results, while models with comparable Bayesian evidence with each other will provide similar contributions to our net posterior results.

4.3.1.2 Choosing Priors for L_d and Θ_k The Bayesian priors for the parameters included in our bad-measurement models (i.e., those contained in Θ_k) are the same flat PDFs chosen in §2.2.3.2 of Chapter 2. As mentioned above, the dynamical range of scale lengths measured for massive spiral galaxies falls in the range of $1 \lesssim L_d \lesssim 10$ kpc. Therefore, we have chosen a flat Bayesian prior where $P(L_d) = 1/9$ where $1 \leq L_d \leq 10$ kpc, and zero otherwise. This effectively allows our posterior results to be determined purely from the data. For convenience, we tabulate the range that these flat priors span below in Table 2.

Table 2. Ranges for Flat Priors

L_d (kpc)	f_{good}	n	Q	F
[0, 9]	[0, 1]	[1, 4]	[0, 1]	$[\sigma_i^{\text{MIN}}/\mu^{\text{MED}}, 1]$

Note. — The prior on F is designed so that the free- F model explores enforcing a floor value on error estimates ($= F \times \mu^{\text{MED}}$) ranging from the smallest value in the dataset (σ_i^{MIN}) up to the median central value (μ^{MED}). As reminder, we use a value of 2.5 kpc for μ^{MED} throughout this study; this is relevant for the free- Q model as well, which explores adding extra uncertainty in quadrature to the nominal error estimates ($= Q \times \mu^{\text{MED}}$).

4.3.1.3 Corrections Toward a Uniform Dataset As described in §4.2.2, the details and assumptions that go into models of the MW can vary considerably from study to study, which could be to blame for any inconsistencies amongst the L_d estimates that we have collected. While it is not possible to correct for all differences, it is important to attempt to place each of these estimates on equal footings, as much as possible, by normalizing them to a common set of assumptions. This should optimize our meta-analysis by placing each measurement on a level playing field, and hence our posterior results should best reflect our true knowledge of L_d given all of the observational data that measurements have utilized.

Unfortunately, the complexity of MW models and the correspondingly large number of free parameters that they generally include make this a difficult job. For example, disk models that include a central truncation or “hole”, which itself is parameterized by a scale radius, L_{hole} , tend to produce a strong anti-correlation between L_d and L_{hole} , which can bias results (Picaud & Robin, 2004). Similarly, including a cutoff radius, as opposed to extrapolating to $R = \infty$, may systematically reduce L_d . Another dichotomy in Galactic models is that some incorporate substructure components (e.g., spiral arms and rings) and some do not. These types of variations are practically impossible to correct for without redoing each analysis. We note that the HB meta-analysis should yield robust results so long as the plurality of measurements are constraining the same fundamental parameter. If other models are sufficiently different in nature that they yield L_d values that are systematically offset from the consensus, they will neither cause significant offsets in the posterior probability distribution nor decrease the breadth of that distribution in an unwarranted way (in contrast to the IVWM).

One assumption that can be corrected for is the authors’ choice of R_0 . While variations in the adopted value of R_0 appear to have negligible impact on the L_d results from star count studies (see, e.g., Ng et al., 1995; Mendez & van Altena, 1998), and hence the majority of our dataset, it does have a measurable effect on measurements based on integrated flux profiles. For example, Kent et al. (1991) explicitly state that their distance measurements will scale proportionately to R_0 , while Freudenreich (1998) published his results as a function of R_0 showing L_d variations to be consistent with a linear scaling law, and Drimmel & Spergel (2001) quote their L_d estimate in units of R_0 . Therefore, we assume that integrated flux

measurements scale linearly when changing the choice of R_0 (cf. [Sackett, 1997](#) and [Hammer et al., 2007](#), who assume L_d estimates from all measurement techniques scale proportionately with R_0).

Consistent with the previous chapters, we have adopted $R_0 = 8.33 \pm 0.35$ kpc from the work of [Gillessen et al. \(2009\)](#), both because it is based upon a geometric technique robust to the systematic uncertainties in the distance ladder, and because it provides a thorough analysis of both statistical and systematic uncertainties. This is a conservative choice as the error estimate is broad enough to be consistent with estimates from a variety of other measurement techniques, and hence describes well the current knowledge of this parameter. We renormalize each L_d estimate from integrated light measurements to reflect this choice of prior. We do this using the “strict-prior” approach described in [Chapter 2](#), where we force our posterior results to reflect our choice of prior by assuming that $P(R_0 | \mathcal{D}) = P(R_0)$. Hence, we assume that the observed variations amongst L_d measurements contain no useful information about the true value of R_0 . This can be achieved through Monte Carlo simulations, which we describe in [§4.3.1.4](#) below.

Other assumptions that we make or alterations to particular estimates in [Table 4.1](#) are as follows:

- In cases where an L_d result is presented without a formal error estimate, we ascribe a 25% error bar.
- In almost all cases the scale length estimate describes the thin disk of the MW. However, a few cases exist where a thick disk is also included and appears as the dominant component of the Galaxy. Therefore, avoiding confusion due to nomenclature (e.g. “thin”, “thick”, “old”, “young”, etc.), we include the L_d estimate associated with the most massive disk component included in the model. This pertains primarily to the Galactic models in [Ortiz & Lépine \(1993\)](#) and [Lépine & Leroy \(2000\)](#). However, any studies that solely measure the scale length of stars which unambiguously belong to the thick disk are excluded (e.g. [Robin et al., 1996](#); [Zheng et al., 2001](#))
- The estimate made by [Porcel et al. \(1998\)](#) relies on assuming that all stars observed to fall into the apparent magnitude bin of $9 < K < 10$ are of type K2–K5 III. To account for the possibility that this assumption may be in error (especially given the minimal detail

presented in this study and the lack of systematics checks) we conservatively augment the error estimate to 25% of the central value.

- The estimate made by [Mendez & van Altena \(1998\)](#) relies on applying a rather outdated model of extinction to photographic plate data taken from the mid-plane of the Galaxy. Given this combination we conservatively augment the error estimate to 25% of the central value.
- The estimate made by [Chen et al. \(1999\)](#) appears to correspond to the mean and approximate standard error of the L_d values produced by fitting their model to four different fields of view. Given that this neglects the contribution of uncertainties in their model assumptions as well as in the formal fitting of the data, we augment the error estimate to 25% of the central value.
- The estimate from [Drimmel & Spergel \(2001\)](#) comes from the mean and standard deviation of values presented in their Table 4 to incorporate uncertainties in the fixed parameters of the model. We have calculated the standard deviation in the L_d values from Table 5 and 6 in this paper to account for the uncertainty due to alternative stellar and spiral models, respectively. Each of these values have been added in quadrature to the nominal error estimate to produce the error bar that we use in our analysis.

We note here that there are several estimates in the literature that we have assumed are superseded by an estimate we have included in our set, due to strong overlap in observational data, Galactic models employed, contributing authors (and hence assumptions), etc., and therefore have been excluded from this study. These include [Ruphy et al. \(1996\)](#) superseded by [Picaud & Robin \(2004, P&R04\)](#), [Spergel et al. \(1996\)](#) superseded by [Drimmel & Spergel \(2001, D&S01\)](#), [Larsen \(1996\)](#) superseded by [Larsen & Humphreys \(2003, L&H03\)](#), and [Robin et al. \(2003\)](#) superseded by P&R04. We also exclude the estimates from [Bovy et al. \(2012b\)](#) and [Cheng et al. \(2012\)](#) from our analyses as these rely critically on segregating stars into subpopulations based on their α -element abundance ratios, a technique that is not viable for measuring extragalactic scale lengths, which we ultimately want to compare our results to.

With all of these assumptions in place, we present our renormalized dataset in Table 4.2. Here we have identified them as either visible or IR measurements, and show the error

estimates updated to the assumptions listed above. We also list the value of R_0 assumed by the author, and indicate the appropriate scaling relation by α , where $L_d \propto R_0^\alpha$. Error bars are scaled similarly to central values with R_0 , such that logarithmic error bars remain constant.

Table 4.2: Milky Way Radial Scale Length Measurements Renormalized For HB Analysis

Reference	$L_d \pm 1\sigma$ (kpc)	R_0 (kpc)	α	Spectral Regime
K91	3.00 ± 0.54	8.00	1	Infrared
RM91	2.50 ± 0.63	8.75	1	Infrared
Y&Y92	3.80 ± 0.27	8.00	0	Visible
R92	2.50 ± 0.30	8.50	0	Visible
O&L93	2.60 ± 0.50	7.90	0	Infrared
N95	4.50 ± 1.13	8.06	0	Visible
O96	2.30 ± 0.60	8.09	0	Visible
P98	2.10 ± 0.53	8.50	0	Infrared
F98	2.60 ± 0.65	8.50	1	Infrared
B98	4.01 ± 1.00	8.60	0	Visible
M&vA98	6.00 ± 1.50	8.50	0	Visible
C99	2.25 ± 0.56	8.50	0	Visible
L&L00	2.30 ± 0.58	8.50	1	Infrared
D&S01	2.26 ± 0.22	8.00	1	Infrared
O01	2.80 ± 0.30	8.00	0	Infrared
S02	2.25 ± 0.56	8.00	0	Visible
LC02	3.30 ± 0.50	7.90	0	Infrared
L&H03	3.50 ± 0.30	8.00	0	Visible
P&R04	2.35 ± 0.67	8.50	0	Infrared
G05	2.80 ± 0.25	8.50	0	Visible
B05	3.90 ± 0.60	8.50	0	Infrared
B06	1.90 ± 0.48	8.60	0	Visible
K07	2.25 ± 0.56	8.00	0	Visible
J08	2.60 ± 0.52	8.00	0	Visible
C11	3.70 ± 1.00	8.00	0	Infrared
R12	2.20 ± 0.55	8.00	0	Infrared

Table 4.2 – Continued

Reference	$L_d \pm 1\sigma$ (kpc)	R_0 (kpc)	α	Spectral Regime
P13	2.12 ± 0.20	8.00	0	Infrared
LC14	2.00 ± 0.40	8.00	0	Visible
M15	2.34 ± 0.48	8.00	0	Visible

Note. — See the Table 4.1 footnotes for reference abbreviations. In cases where the authors do not specify the R_0 assumed, we assume they have used the IAU standard value of 8.5 kpc (Kerr & Lynden-Bell, 1986). In column 4, α reflects the assumed scaling law, $L_d \propto R_0^\alpha$, based on the measurement technique.

4.3.1.4 Monte Carlo Techniques Combining all of the assumptions and techniques described above requires us to perform a set of Monte Carlo simulations. For convenience, we now summarize the full process of obtaining our results. We begin by drawing 10^3 realizations of $R_{0,i}$ from $P(R_0) = 8.33 \pm 0.35$ kpc, which is the result from Gillessen et al. (2009) discussed in the previous section. For each $R_{0,i}$ we first renormalize each independent estimate of L_d in Table 4.2 from the R_0 assumed by the author to $R_{0,i}$ according to the appropriate scaling law, yielding \mathcal{D} . Next, for each bad-measurement model \mathcal{M}_k , we calculate the likelihood, $P(\mathcal{D} | L_d, \Theta_k, \mathcal{M}_k, R_{0,i})$, from Equations (2.2)–(2.5) in Chapter 2 and determine the Bayesian evidence using Equation (4.9) above.

Following the strict-prior methodology from Chapter 2 (i.e., assuming $P(R_0 | \mathcal{D}) = P(R_0)$), we next calculate the marginalized posterior for the MW’s disk scale length by

$$P(L_d | \mathcal{D}, \mathcal{M}_k) = \frac{1}{1000} \sum_{i=1}^{1000} \int \frac{P(\mathcal{D} | L_d, \Theta_k, \mathcal{M}_k, R_{0,i}) P(L_d) P(\Theta_k)}{P(\mathcal{D} | \mathcal{M}_k, R_{0,i})} d\Theta_k. \quad (4.14)$$

Lastly, we implement Bayesian model averaging (BMA) by calculating the average posterior of the models weighted by the *mean* evidence by averaging the results from the 10^3 realizations of $R_{0,i}$:

$$P(L_d | \mathcal{D}) = \frac{\sum_{k=1}^8 P(L_d | \mathcal{D}, \mathcal{M}_k) \sum_{i=1}^{1000} P(\mathcal{D} | \mathcal{M}_k, R_{0,i})}{\sum_{j=1}^8 \sum_{i=1}^{1000} P(\mathcal{D} | \mathcal{M}_j, R_{0,i})}. \quad (4.15)$$

We find that all of our results are entirely unchanged if we use the median evidence values instead of the mean.

For ease of comparison amongst our models, we will recast our presentation of the Bayesian evidence in terms of the *Bayes Factor*, which in our framework is calculated by

$$\mathcal{B}_k = \frac{P(\mathcal{D} | \mathcal{M}_k)}{P(\mathcal{D} | \mathcal{M}_{\text{all-good}})} = \frac{\sum_{i=1}^{1000} P(\mathcal{D} | \mathcal{M}_k, R_{0,i})}{\sum_{j=1}^{1000} P(\mathcal{D} | \mathcal{M}_{\text{all-good}}, R_{0,j})}. \quad (4.16)$$

This represents the ratio of the posterior odds to the prior odds in favor of model \mathcal{M}_k over the all-good model, our null hypothesis model. The standard rule-of-thumb (Kass & Raftery, 1995, and references therein) applied in the context of this study means that finding $\log \mathcal{B}_k > \sim 2$ indicates a statistically significant favorability for model \mathcal{M}_k over the all-good model. Values of $\log \mathcal{B}_k$ in the range of ~ 0.5 – 1 and ~ 1 – 2 are considered as “substantial” and “strong” favorability, respectively, but are not necessarily large enough to decisively deem \mathcal{M}_k as the superior model, and negative values of course favor the all-good model over \mathcal{M}_k on the same scale. One can also conveniently reframe this type of comparison between any two models \mathcal{M}_k and \mathcal{M}_j by simply calculating $\log \mathcal{B}_k - \log \mathcal{B}_j$.

We note here that we have also tested for the effect of treating R_0 as a free parameter in our modeling of the data and adopting the same prior $P(R_0)$. This breaks our assumption that L_d estimates contain no useful information about R_0 , and eliminates the need for marginalization through the Monte Carlo framework laid out above. We find that the marginal posterior results for L_d are nearly identical to those of our standard treatment, which is likely due to only a small subset of the L_d dataset being dependent on R_0 . Nevertheless, we believe that implementing the strict-prior methodology is well motivated and worth the added complexity for our purposes.

4.4 RESULTS

In Table 4.3 we present the results for each of the eight bad-measurement models. This includes the number of free parameters, N_{free} , the median and 68% credible interval measured from the marginalized posterior $P(L_d | \mathcal{D}, \mathcal{M}_k)$, and the corresponding $\log \mathcal{B}_k$ value. We

have broken our results down into three scenarios: analyzing the entire dataset provided in Table 4.2, analyzing only those measurements made in the visible, and analyzing only those measurements made in the IR. Lastly, for each of these three scenarios we list the median and 68% credible interval measured from the posterior marginalized over all models, $P(L_d | \mathcal{D})$, calculated via BMA (see §4.3.1.1), which serve as our nominal results. To easily compare our results with a standard non-hierarchical combination of the data, we include in Table 4.3 the inverse variance-weighted mean (IVWM) of the L_d estimates. We note that the result from the all-good model is equivalent to the IVWM of the estimates after scaling them to reflect assuming $R_0 = 8.33$ kpc according to the appropriate relation indicated in Table 4.2.

Table 4.3: HB Results for the Milky Way Radial Scale Length

Model (\mathcal{M}_k)	N_{free}	$L_d \pm 1\sigma$ (kpc)	$\log_{10} \mathcal{B}_k$
<u>IR estimates only</u>			
free- n	3	$2.48^{+0.14}_{-0.13}$	-0.28
free- Q	3	$2.51^{+0.16}_{-0.14}$	-0.27
free- F	3	$2.53^{+0.17}_{-0.15}$	-0.24
all-bad free- n	2	2.48 ± 0.14	-0.66
all-bad free- Q	2	$2.56^{+0.17}_{-0.15}$	-0.47
all-bad free- F	2	$2.62^{+0.16}_{-0.15}$	-0.37
$P_{\text{bad}}\text{-flat}$	2	2.47 ± 0.12	-0.93
all-good	1	2.48 ± 0.11	—
BMA result		$2.51^{+0.15}_{-0.13}$	
IVWM		2.46 ± 0.11	
<u>Visible estimates only</u>			
free- n	3	$2.68^{+0.21}_{-0.19}$	1.94
free- Q	3	2.64 ± 0.19	1.97
free- F	3	$2.64^{+0.18}_{-0.17}$	1.94
all-bad free- n	2	2.85 ± 0.20	1.97
all-bad free- Q	2	2.77 ± 0.21	1.95
all-bad free- F	2	$2.70^{+0.21}_{-0.18}$	1.97
$P_{\text{bad}}\text{-flat}$	2	$2.52^{+0.17}_{-0.16}$	1.03
all-good	1	2.85 ± 0.11	—
BMA result		$2.71^{+0.22}_{-0.20}$	
IVWM		2.85 ± 0.11	

Table 4.3 – Continued

Model (\mathcal{M}_k)	N_{free}	$L_d \pm 1\sigma$ (kpc)	$\log_{10} \mathcal{B}_k \pm 1\sigma$
<u>Visible and IR estimates combined</u>			
free- n	3	2.57 ± 0.12	2.39
free- Q	3	$2.60^{+0.14}_{-0.13}$	2.69
free- F	3	2.62 ± 0.12	2.85
all-bad free- n	2	2.66 ± 0.12	1.88
all-bad free- Q	2	$2.69^{+0.13}_{-0.12}$	2.64
all-bad free- F	2	2.66 ± 0.12	3.00
$P_{\text{bad-flat}}$	2	2.50 ± 0.10	1.26
all-good	1	2.66 ± 0.08	—
BMA result		2.64 ± 0.13	
IVWM		2.65 ± 0.08	

Note. — For each dataset, \mathcal{D} , the first eight rows shows the results from each of our bad-measurement models detailed in Chapter 2. N_{free} denotes the number of free parameters that each model contains. Below this point, we show the result of applying Bayesian model averaging (BMA) to all eight models, which in this study reflects the median and 68% credible interval measured from the Bayesian evidence-weighted average of all $P(L_d | \mathcal{D}, \mathcal{M}_k)$, since we assume as a prior that each model is equally probable (see §4.3.1.1). Finally, for comparison, we also list the (non-hierarchical) inverse variance-weighted mean (IVWM) from using the nominal central values and error estimates in Table 4.2. Note that the result from the all-good model is equivalent to calculating the IVWM *after* scaling individual estimates to reflect our prior on R_0 where applicable.

4.4.1 Parameters Describing the Consistency of the Data

As indicated by the Bayes factors listed in Table 4.3, the IR data are all consistent enough that the all-good model yields a satisfactory fit with no free hierarchical parameters, causing it to be favored by the evidence calculations. This corresponds to assuming high fidelity for all estimates. However, when the visible measurements are included in the dataset, either by an-

analyzing them alone or in combination with the IR measurements, there appears to be enough tension amongst them that the all-good model becomes strongly disfavored. To illustrate this further, we show in Figure 4.2 the results for parameters describing the consistency of the data from the free- n model. Each panel shows the joint posterior, $P(f_{\text{good}}, n \mid \mathcal{D}, \mathcal{M}_{\text{free-}n})$, for the fraction of “good” (i.e., accurate) estimates in the set, f_{good} , and the correction factor needed for error estimates from bad measurements, n . The white star marks the peak of the distribution.

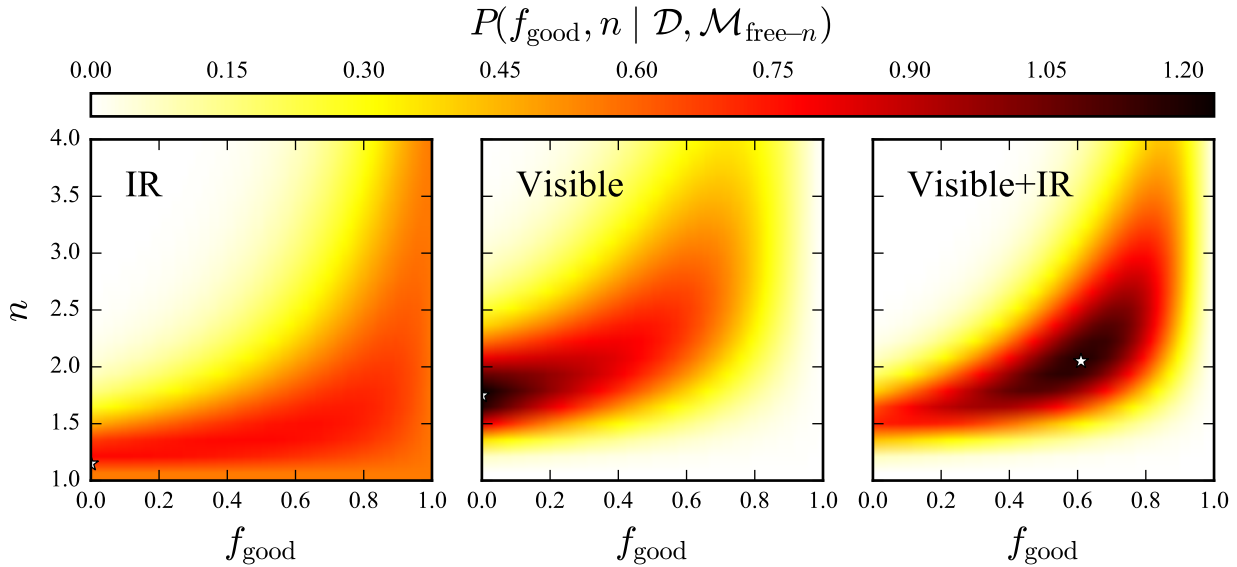


Figure 4.2: Quantifying the overall fidelity of Milky Way disk scale length measurements, \mathcal{D} , in terms of both the frequency of accurate estimates, f_{good} , and the error bar correction factor for inaccurate measurements, n . Each panel shows the joint posterior distribution, $P(f_{\text{good}}, n \mid \mathcal{D}, \mathcal{M}_{\text{free-}n})$, yielded from the free- n model, $\mathcal{M}_{\text{free-}n}$, when analyzing L_d estimates measured in the infrared (IR; left panel) or the visible (middle panel), and when analyzing both the visible and IR data together (right panel). We have marked the peak probability location in each panel by a white star. The set of IR estimates alone are in good overall consistency with one another, as the posterior peaks at $n \sim 1$, the limit where the correction for bad estimates goes away (note that values of $n = 1$ or $f_{\text{good}} = 1$ reduce to the all-good model). In contrast, the visible estimates alone, due to the strong tension amongst them, appear to contain a significant number that are biased or erroneous. Here, the posterior peaks at $f_{\text{good}} = 0$ and $n = 1.75$, corresponding to the case where all measurements are treated as having error estimates that are 75% too small. The right panel indicates that there is good consistency amongst some of the visible and IR data together, as it yields an intermediate result between analyzing the visible and IR data separately.

The left panel shows the result from analyzing the IR estimates alone. Here, we find a relatively broad posterior that peaks at $n = 1.15$ and $f_{\text{good}} = 0.03$. That is to say, the likelihood function for the free- n model is maximized under the assumption that nearly all measurements of L_d in the IR have underestimated errors by 15%. Note, however, that this

is also to say that the posterior peaks nearly along the $n = 1$ slice through this plane, where the free- n model (with 3 free parameters) becomes equivalent to the all-good model (with 1 free parameter). This explains why the latter is favored by the Bayesian evidence — it provides a similar description of the data without requiring superfluous parameter space.

The middle panel shows the result from analyzing only the visible L_d estimates, which appear to be in significant tension with one another. In this case, the posterior is more strongly peaked and is maximized at $n = 1.75$ and $f_{\text{good}} = 0$, where error estimates on all measurements are increased by 75%. Note that this is where the free- n model becomes equivalent to the all-bad free- n model, though each yields very similar $\log \mathcal{B}_k$ values. This represents an example where the added parameter space yields a large enough improvement in likelihood values that they roughly balance.

Finally, the right panel shows the joint posterior from analyzing all (visible+IR) measurements in Table 4.2, which appears to be an intermediate result compared to those from treating the visible and IR data separately. The posterior is maximized when assuming that $\sim 35\%$ of the set have overly-optimistic error estimates by a factor of ~ 2.2 . This indicates that there is a good level of consistency between many of the 14 IR and 15 visible measurements, but that there are some estimates that are in strong tension with the rest. Note the covariance between f_{good} and n in the model, which shows that there are multiple ways to account for this tension. For example, upon further inspection of Table 4.2, it seems there are a few strongly-peaked (i.e., with small estimated errors), similarly valued estimates (Y&Y92 and L&H03) that are in modest tension with a number of lower-valued, broader estimates (O96, S02, B06, K07, J08, LC14, M15); treating the former as problematic would result in larger values for both f_{good} and n , whereas considering the latter set as problematic would correspond to lower values of f_{good} and n (see Fig. 4.4 for a visual comparison, which we discuss below). Likely there are several other ways to reduce the tension amongst these measurements; each would lead to a broader posterior distribution than the IVWM by incorporating this extra uncertainty. This would typically be unaccounted for by other meta-analysis techniques. We note that despite the wide varieties of models considered, our final BMA results are consistent with all of them at $<1\sigma$; it therefore appears unlikely that entertaining more models of bad measurements would significantly change our final results.

To provide a picture of how different models compare in identifying bad measurements, Figure 4.3 displays the marginal posterior for f_{good} for all four of those that allow for the possibility that *some* of the measurements are problematic (in all others f_{good} has been either set to zero — the entries labeled as “all-bad” in Table 4.3 — or set to unity in the case of the “all-good” entries). Consistent with the story from Figure 4.2, we find that $P(f_{\text{good}} | \mathcal{D}, \mathcal{M}_k)$ peaks at $f_{\text{good}} = 1$ for all models when analyzing the IR estimates alone, but peaks well below $f_{\text{good}} = 1$ when analyzing the visible estimates alone. Interestingly, these curves show more diversity when analyzing the visible and IR estimates in combination and peak at a range of values of f_{good} .

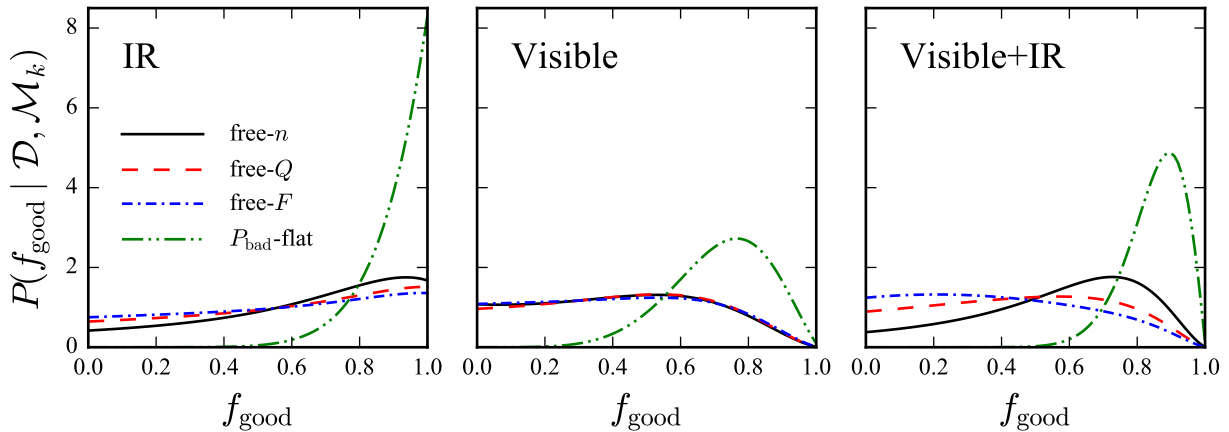


Figure 4.3: Quantifying the frequency of accurate estimates, f_{good} , amongst our L_d dataset, \mathcal{D} , using a variety of bad-measurement models, \mathcal{M}_k . Each panel shows the marginal posterior for f_{good} , $P(f_{\text{good}} | \mathcal{D}, \mathcal{M}_k)$, from the four models listed in the left panel (see §4.3.1 for a short description of these) after integrating over all other free parameters. This is divided into cases of analyzing the IR estimates alone (left panel), the visible estimates alone (middle panel), and the visible and IR estimates together (right panel). As similarly described in Fig. 4.2, the IR data alone is in good overall consistency, leading to optimal values of $f_{\text{good}} = 1$. The visible data alone, however, appear to be contaminated by erroneous measurements as the posteriors from all models peak at values of f_{good} well below unity. The results from analyzing the visible and IR data together are more divergent, with different models favoring differing values of f_{good} ; i.e., some models are able to ease inter-measurement tension by altering only a few L_d estimates, whereas others require expanding error estimates on a larger number of measurements. In all scenarios, the $P_{\text{bad-flat}}$ model favors higher values of f_{good} than the other models; this is because it effectively discards a measurement when assuming it’s inaccurate, which is a much more expeditious route to easing inter-measurement tension. As is evident in Table 4.3, the associated loss of information from this approach is more detrimental to the Bayesian evidence though, preventing the $P_{\text{bad-flat}}$ model from being the most favorable (see the discussion of Bayes Factors in §4.3.1.4). Our final results for L_d are produced by averaging over the possibility of each model being correct (see §4.3.1.1).

In all cases, the $P_{\text{bad-flat}}$ model produces a tighter posterior distribution that supports

larger values of f_{good} , as it is effectively able to discard measurements entirely when treating them as bad. However, the corresponding loss of information weakens the overall likelihood function and hence yields a smaller \mathcal{B}_k , preventing this from being the prevailing model. In contrast, the three other models, each uniquely remedying the effect of bad measurements instead of discarding them, give much more probability to lower values of f_{good} , while also yielding larger \mathcal{B}_k . In other words, the Bayesian evidence in this application more strongly supports models that attempt to correct inaccurate error estimates for measurements of the Galactic scale length, rather than assuming that outlying measurements are too problematic to contain any useful information. This is the same message in the panel corresponding to the IR data alone, except that for all models the marginalized posterior peaks at $f_{\text{good}} = 1$. As a result, each model looks quite similar to the all-good model (where f_{good} has been set to unity); it is reasonable then that the Bayesian evidence deems the all-good model superior, as it does not contain unneeded free parameters.

4.4.2 Marginalized Posterior Results for L_d

From the values in Table 4.3, one can find several instances where two models are supported by similar values of \mathcal{B}_k , but have non-negligible differences in their $P(L_d | \mathcal{D}, \mathcal{M}_k)$. This is especially common amongst our results from analyzing the visible estimates alone; here, a variety of bad-measurement models yield $\log \mathcal{B}_k$ values of ~ 2 (indicating strong favorability over the all-good model), yet central values for L_d that span from 2.64–2.85 kpc, a range that is comparable in size to the 1σ error estimate from any single model. This provides a cautionary tale: two models may be quite comparable in how well they can describe the data, but still lead to somewhat differing results (in this case, all models are consistent with each other at the $\sim 0.8\sigma$ level or better).

If we did not employ BMA, we would be left in the position of having to choose a winning model for more arbitrary reasons. In our example, one could choose the free- Q model as it maximizes the evidence (though not uniquely), or one could choose the all-bad free- Q model (where f_{good} has been set to zero, instead of treated as a free parameter) in an effort to be conservative as it yields the largest error estimate and a central value towards the center of

the pack. This illustrates a new source of uncertainty – i.e., model selection uncertainty – that needs to be accounted for. Hence, we have implemented the Bayesian model averaging (BMA) technique, detailed in §4.3.1.1, to produce the final posterior distribution for L_d ; the method effectively marginalizes over the possibility of all the models we have considered being the correct model.

In Figure 4.4 we show the finalized posterior results for the Galactic scale length from BMA for the IR, visible, and visible+IR datasets, which correspond to $2.51^{+0.15}_{-0.13}$ kpc, $2.71^{+0.22}_{-0.20}$ kpc, and 2.64 ± 0.13 kpc, respectively. So that one may visually compare the individual estimates to the aggregate result that they have been incorporated into (the thick black curves), we have overlaid the probability distribution corresponding to each estimate in colored, dashed/dotted curves. In total, each result represents our best estimate of the Galactic scale length in the IR, visible, and visible+IR regimes given the array of values available in the literature.

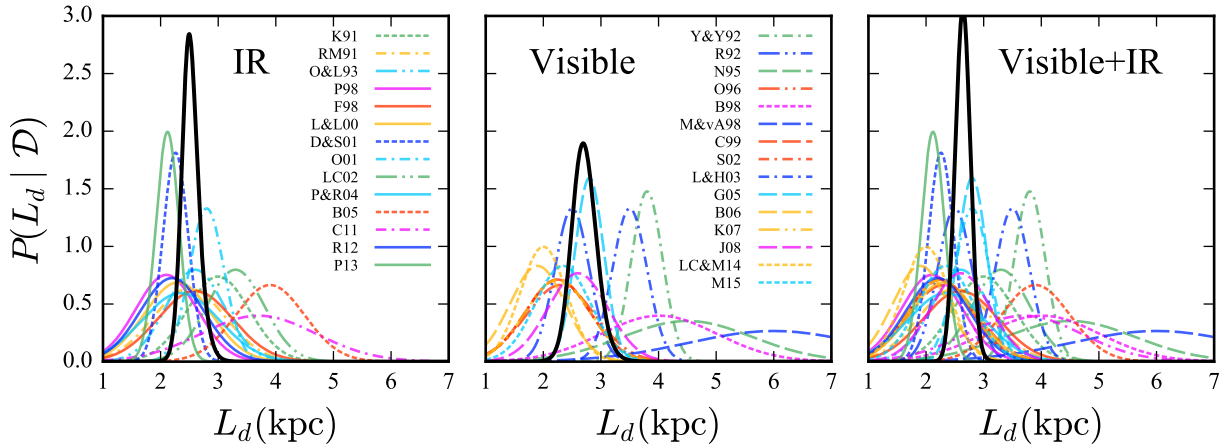


Figure 4.4: Marginal posterior results, $P(L_d | \mathcal{D})$, for the exponential scale length, L_d , of the Milky Way’s disk yielded from HB meta-analysis of IR measurements (left panel), visible measurements (middle panel), and visible and IR measurements combined (right panel), shown by a thick black curve. Each is produced via a Bayesian model averaging (BMA) technique described in §4.3.1.1, where we have effectively marginalized over the probability of each bad-measurement model we have considered as being correct, and hence incorporates all model selection uncertainties. To provide a visual comparison, we have overlaid the individual estimates of L_d that have gone into our meta-analysis as colored textured curves. The abbreviations for each study can be found in the notes for Table 4.1.

4.4.3 Impact of R_0 Prior

As discussed above, a small subset of the L_d estimates we have collected, particularly those measured from maps of integrated IR starlight, scale proportionately with the choice of R_0 (see Table 4.2). As a reminder, we have adopted a prior of $R_0 = 8.33 \pm 0.35$ kpc and have utilized Monte Carlo techniques (see §4.3.1.4) to propagate this into our posterior results for L_d . Hence, our IR and visible+IR results, too, should be dependent on the choice of R_0 to some degree. We will now discuss how our prior for R_0 affects the results we have found for L_d , which will allow one to update them as our knowledge of R_0 becomes more accurate.

We have first tested to see how much the adopted uncertainties in R_0 contribute to the overall uncertainties in L_d . To do so, in place of sampling from our R_0 prior 10^3 times, we have repeated our analysis using only a single iteration of scaling all measurements to $R_0 = 8.33$ kpc, thereby assuming 100% accuracy in our knowledge of this parameter. We find that this yields identical posterior results, indicating that R_0 uncertainties are negligible in the overall error budget for L_d .

Next, we have investigated how our results change if we adopt R_0 values anywhere in the range of 7.5–9 kpc, which is closely equal to the 2σ range from by our nominal prior. In line with our error analysis, this reveals only weak correlations between R_0 and L_d : the IR estimate is well described by $L_d = 0.12(R_0 - 8.33 \text{ kpc}) + 2.51_{-0.13}^{+0.15}$ kpc, whereas the visible+IR estimate is well described by $L_d = 0.06(R_0 - 8.33 \text{ kpc}) + 2.64 \pm 0.13$ kpc. As a reminder, none of the visible L_d estimates we have collected vary with the choice of R_0 , and hence neither does the visible L_d result found here.

4.4.4 Tests of Alternative Assumptions and Robustness

As indicated in Table 4.1, many of the visible L_d estimates we have included in our analyses pre-date the dust maps produced by Schlegel et al. (1998, SFD98), which provided a largely improved tool for modeling Galactic reddening and extinction. We have tested for the effect of deweighting visible L_d estimates that do not utilize the SFD98 dust maps by adding an extra 10% error in quadrature to their nominal error bars and repeating our entire analysis. Interestingly, in this scenario we find that when analyzing either the entire visible+IR dataset

or just the visible estimates alone, all bad-measurement models yield $\log \mathcal{B}_k$ values of ~ 0 or below; i.e., the data become much more consistent overall, and the all-good model is now the most favored. After applying BMA, we find that our aggregate visible+IR scale length estimate becomes $2.58_{-0.10}^{+0.11}$ kpc and the aggregate scale length from visible estimates becomes 2.65 ± 0.16 kpc. These values are 0.06 kpc lower than our nominal results (see Table 4.3), but consistent with them at the 0.35σ and 0.23σ levels, respectively.

Presumably IR measurements are less impacted by dust effects so we have not performed a similar deweighting test for them. However, a few of the IR estimates in Table 4.2 have relatively small error estimates (~ 0.2 kpc). To test whether our posterior results are dominated by estimates with the smallest errors, we have reanalyzed the IR data alone after replacing the P13 error estimate of 0.20 kpc with the median error estimate of 0.55 kpc. This serves to systematically decrease the overall tension among the estimates in our dataset, and, as expected, the favorability of the all-good model increases; i.e., $\log \mathcal{B}_k$ values for all other models become more negative. On the other hand, the posterior result from each model, $P(L_d | \mathcal{D}, \mathcal{M}_k)$, shifts toward higher values of L_d , and after applying BMA the posterior becomes $P(L_d | \mathcal{D}) = 2.60 \pm 0.14$ kpc. This is consistent with our nominal result at the 0.4σ level, and provides a good indication that our analysis method is robust.

Lastly, as noted above, other studies that have reviewed or analyzed Galactic L_d estimates in the literature (e.g., Sackett, 1997; Hammer et al., 2007) have assumed that each is directly proportional to the value of R_0 adopted by each author. This assumption does not appear to be clearly correct for star count analyses, which constitute the majority of our dataset. In fact, several of these studies indicated that their results for L_d are highly insensitive to the choice of R_0 , whereas studies modeling the integrated light profile of the Galaxy almost unanimously noted a linear dependence on R_0 . This is likely because star count measurements are so local that geometrical effects that depend on R_0 prove negligible. However, in case this is an error on our part, we have investigated how our results change if we assume that $L_d \propto R_0$ for all estimates uniformly. The effects on values listed in Table 4.3 are as follows.

When analyzing the visible and IR estimates together, the $\log \mathcal{B}_k$ values for each model increased by ~ 1 , indicating a substantial increase in tension amongst the data, and hence

increased favorability for bad-measurement mixture models. The 68% credible intervals measured from $P(L_d | \mathcal{D}, \mathcal{M}_k)$ increased by $\sim 30\text{--}60\%$, whereas the median values shifted by $< 2\%$. The net result from performing BMA becomes $P(L_d | \mathcal{D}) = 2.63_{-0.17}^{+0.18}$ kpc (as compared to 2.64 ± 0.13 kpc for our preferred analysis).

When analyzing the visible estimates alone, the $\log \mathcal{B}_k$ values similarly increase by ~ 1 . Changes in $P(L_d | \mathcal{D}, \mathcal{M}_k)$ were very similar to those described above for the visible+IR dataset. The net result from performing BMA becomes $P(L_d | \mathcal{D}) = 2.70_{-0.23}^{+0.27}$ kpc (as compared to $2.71_{-0.20}^{+0.22}$ kpc for our preferred analysis).

When analyzing the IR estimates only, $\log \mathcal{B}_k$ values decreased (became more negative) by < 0.2 adding slightly more favorability to the all-good (non-mixture) model. Median values and 68% credible intervals measured from $P(L_d | \mathcal{D}, \mathcal{M}_k)$ increased by $\sim 1\%$ and $\sim 10\%$, respectively, except for that the 1σ ranges for the $P_{\text{bad-flat}}$ and all-good models expanded by 25% and 35%, respectively. The result from performing BMA becomes $P(L_d | \mathcal{D}) = 2.53_{-0.16}^{+0.17}$ kpc (as compared to $2.51_{-0.13}^{+0.15}$ kpc for our preferred analysis).

By comparing to the values in Table 4.3, the overall impact on our nominal results is minimal, with shifts in the central value far below the 1σ level and error estimates increasing by $< \sim 30\%$. This may stem from the fact that the R_0 values assumed by these studies have a mean and standard deviation of 8.22 kpc and 0.27 kpc, comparable to the R_0 prior we have chosen. Regardless, our results appear robust to varying assumptions about how star count-based estimates of L_d scale with R_0 .

4.5 DISCUSSION

4.5.1 Comparisons to Dynamical Estimates

In this study we have exclusively analyzed estimates of L_d that have been produced from photometric models of the MW. We therefore have excluded many estimates that have been produced from dynamical mass models of the MW that are predominantly constrained by kinematic data. We now provide a quantitative comparison of our results to these dynamical

estimates.

We first emphasize that, just like photometric estimates, dynamical estimates of L_d too rest upon many modeling assumptions, and hence are prone to systematic errors. These predominantly rely on fitting models of both the stellar and dark matter components of the MW to measurements of stellar or gaseous kinematics. Schönrich et al. (2010) points out that those studies utilizing the asymmetric drift (AD) relation (e.g., Dehnen & Binney, 1998 and subsequent studies) are particularly vulnerable to systematics stemming from the metallicity gradient of the Galactic disk, and can violate the assumptions that underpin the AD technique when binning stars by color. Studies that aim to model the Galactic rotation curve also generally suffer from a strong disk-halo degeneracy, and hence the L_d estimates that they yield can be sensitive to choices regarding the disk mass-to-light ratio and dark matter halo parameters. Furthermore, one should keep in mind that the degree to which dynamical mass traces the distribution of starlight is not well understood, and hence to some extent these comparisons may not be apples-to-apples.

It appears that in many (but not all) cases, dynamical estimates of L_d are proportional to the adopted value of R_0 . In the following, if a particular estimate is clearly stated by the authors to depend linearly on R_0 then we have scaled this estimate to reflect the prior on R_0 chosen in this study (8.33 ± 0.35 kpc) to make a better comparison, and we have marked these values with a dagger. However, in all other cases the authors have made no indication as to the dependence of their L_d result on the choice of R_0 , have fit for both quantities simultaneously, or have stated that these quantities are independent, and so for them we compare to the nominal values they have quoted.

There are numerous dynamical estimates for L_d in the literature that compare well with our results, either being consistent at or below the $\sim 1\sigma$ level or falling into the 1σ ranges presented herein if lacking an error estimate. Such studies include Fux & Martinet (1994), who combined literature estimates of several properties of the Galactic disk with an approximated AD Jeans equation to find $L_d = 2.45 \pm 0.50^\dagger$ kpc; Durand et al. (1996), who modeled the Galactic potential using the radial velocities of 673 planetary nebulae (PNe),

[†]Denotes where the authors have stated that their L_d result scales linearly with the choice of R_0 , and so we have renormalized it to reflect our prior of $R_0 = 8.33 \pm 0.35$ kpc.

which was then used to deproject the COBE 2.2 μm map in order to find $L_d = 2.6$ kpc; [Dehnen & Binney \(1998\)](#), who optimized dynamical mass models of the MW to a variety of observational constraints available in order to find $L_d/R_0 = 0.3$, and hence $L_d = 2.5^\dagger$ kpc; and [Widrow et al. \(2008\)](#), who used both Bayesian and Markov chain Monte Carlo techniques to match an axisymmetric, equilibrium model of the MW to nine different sets of observational constraints, finding $L_d = 2.80^{+0.23}_{-0.22}$ kpc. More recently, [Reid et al. \(2014\)](#) used Bayesian methods to fit a universal rotation curve to trigonometric parallax and proper motion data for ~ 100 high-mass star forming regions, finding $L_d = 2.34 \pm 0.18^\dagger$ kpc. This compares well with our IR estimate, but is inconsistent with our visible and visible+IR estimates at the $\sim 1.4\sigma$ significance level.

There are a few studies, however, supporting a shorter radial scale length for the Galactic disk. For instance, [Bienaymé \(1999\)](#) studied AD by analyzing velocity dispersions measured for $\sim 14,000$ stars from the Hipparcos data after segregating them into 20 bins of $B - V$ color, finding $L_d = 1.8 \pm 0.2^\dagger$ kpc. This estimate is incompatible with the results presented here at the $3\text{--}3.5\sigma$ level. More recently, [Bovy & Rix \(2013\)](#) performed a sophisticated dynamical analysis of $\sim 16,000$ G-dwarfs segregated into 43 mono-abundance populations that yielded a mass-weighted average value of $L_d = 2.15 \pm 0.14$ kpc. This estimate is in tension with our results at the $1.9\text{--}2.6\sigma$ level if one were to assume that stars trace mass in the disk with a uniform mass-to-light ratio. However, we note that [Hessmann 2016 \(submitted\)](#) finds that in the DiskMass sample ([Bershady et al., 2010](#)), mass-to-light ratio varies with radius in disk galaxies, such that the mass scale length is typically 80% of the disk scale length. Testing this using our result in combination with the [Bovy & Rix \(2013\)](#) mass scale length estimate corresponds to $2.15 \pm 0.14 / 2.64 \pm 0.13 = 0.81 \pm 0.07$, in excellent agreement with that ratio.

On the other hand, there are also studies that found larger values for the Galactic disk scale length. For instance, [Feast \(2000\)](#) applied the AD relation to radial velocity data for semi-regular variables, Mira variables and PNe, yielding a weighted average for the radial density gradient of $R_0/L_d = 2.55 \pm 0.43$, which corresponds to $L_d = 3.27 \pm 0.58^\dagger$ kpc. While this compares fairly well with our visible and visible+IR result, it is inconsistent with our IR result at the 1.3σ level. [McMillan \(2011\)](#) took a Bayesian approach to fitting dynamical MW mass models (with 8 free parameters) to a variety of kinematic observational data available,

finding $L_d = 3.00 \pm 0.22$ kpc. This compares well with our visible result, but is in tension with our IR and visible+IR results at the 1.8σ and 1.4σ levels, respectively.

4.5.2 Comparisons to Multi-band Photometry for Extragalactic Disks

Due primarily to variations in their star formation histories as a function of radius (de Jong, 1996, hereafter dJ96), spiral galaxies typically become bluer with increasing radius — the exception being those of bluest integrated color, which are also bluest at their centers (cf. Verheijen, 1997, hereafter V97). For galaxies like the MW, which ranks among the reddest spirals (Chapter 3), a higher central concentration of older stars causes them to appear more compact when imaged in the IR, whereas younger stars and new star formation extending into the outskirts of the disk causes them to have a broader profile when imaged in the visible. Hence, scale lengths measured from visible light are usually larger than those measured from IR light, matching the MW results that we find here.

A number of studies have investigated the wavelength dependence of extragalactic scale lengths measured from both optical and IR photometry. For instance, Peletier et al. (1994) performed such an analysis for 37 Sb/c galaxies (closely matching the MW’s morphological type; de Vaucouleurs, 1983; Chapter 3), though with a range of inclinations, and found that extragalactic scale lengths are generally $\sim 1\text{--}2\times$ larger when measured in the visible (B -band) compared to the near-IR (K -band; see their Figure 4). Verheijen (1997) investigated the correlation of optical-to-IR scale length ratios with disk central surface brightness colors for the disk components of galaxies in the Ursa Major cluster and found similar results (see their Figure 9), with the exception of the bluest galaxies as mentioned above. While these ratios can reach to much larger values than what we find for the MW here, one must keep in mind that they stem from galaxies with a range of morphological types and, unlike our value, are not corrected for dust attenuation/reddening, which is expected to alter galaxy properties in the optical (Corradi et al., 1996; Xilouris et al., 1999; MacArthur et al., 2004; De Geyter et al., 2014).

de Jong (1996) performed multi-band photometry for 86 face-on disk-dominated galaxies, providing extragalactic data that we may straightforwardly compare to our results. We have

transcribed the data from Table 4 of that paper, which provides scale length measurements in the B , R , I , and K bands, as well as numerical morphological classifications (T ; de Vaucouleurs et al. 1991). Restricting to objects that fall into the range $2 \leq T \leq 6$, which should be similar in morphology to the MW ($T \approx 4$), yields a sample of 30 galaxies from which we have measured scale length ratios of $L_d^B/L_d^K = 1.17 \pm 0.34$, $L_d^R/L_d^K = 1.14 \pm 0.26$, and $L_d^I/L_d^K = 1.10 \pm 0.25$ (mean and standard deviation), with median values of 1.05, 1.07, and 1.06, respectively. Very similar results are found when analyzing the entire sample of galaxies that have K -band scale lengths available. Using our HB estimates of L_d presented here, we find an optical-to-IR scale length ratio of $2.71/2.51 = 1.08$ for the MW, making it appear quite typical in this respect compared to other spiral galaxies.

4.5.3 A Revised Estimate of the Milky Way’s Total Stellar Mass

In Chapter 2 we determined updated constraints on the MW’s total stellar mass by combining a HB estimate for the stellar mass in the Galactic bulge+bar with the dynamically-constrained model of the Galactic disk from Bovy & Rix (2013). As mentioned in the previous section, the scale length estimate yielded from that study is lower than values that we have found here, and is inconsistent with them at the $\sim 2\sigma$ significance level. It is likely that systematic differences in what quantity has been measured largely contribute to this tension as the methodology and assumptions used by Bovy & Rix (2013) are substantially different from those of the star count-based measurements utilized here. Furthermore, the Bovy & Rix (2013) methodology is not viable for studying external galaxies, whose scale lengths are measured from photometry. Since a key goal of our work has been comparing the properties of the MW to those of extragalactic objects, it is beneficial to produce a revised estimate of the stellar mass of the Galaxy by developing a model of the disk that utilizes the light-based scale length estimates determined in this study.

4.5.3.1 Updating the Disk Model Assumptions We begin by making several adjustments to the assumptions that went into the original disk model described in §2.4.1. From Equation (2.17), the stellar mass of the MW’s exponential disk, given its radial scale

length, L_d , the radius of the Sun from the Galactic center, R_0 , and the *mean* surface density of stellar material at R_0 , $\bar{\Sigma}_*(R_0)$, is determined by

$$M_*^D = 2\pi\bar{\Sigma}_*(R_0)L_d^2\exp(R_0/L_d). \quad (4.17)$$

Note that here we have made a slight notation change by using $\bar{\Sigma}_*(R_0)$ in place of $\Sigma_*(R_0)$; this is to remind the reader that Equation (4.17) assumes the stellar disk to be axisymmetric about the Galactic center. In our past work, just as the vast majority of previous studies have done, we assumed that the *locally* measured surface density — i.e., the column density at the location of the Sun — is representative of the mean value. However, the MW’s spiral structure certainly produces variations in the observed $\Sigma_*(R_0, \phi)$ as one varies ϕ . For reasons that will be explained in the following section, we no longer make this assumption and hence $\bar{\Sigma}_*(R_0)$ represents the stellar surface density at $R = R_0$ averaged over all ϕ . For further clarity, hereafter we denote the locally measured surface density — i.e., the observed value for the Solar neighborhood — as $\Sigma_*(R_0, \phi_0)$.

Next, since near-IR light is expected to most closely trace the distribution of stellar mass, we now adopt the HB result from analyzing IR estimates only in this chapter for the disk scale length, which corresponds to $L_d = 0.12(R_0 - 8.33 \text{ kpc}) + 2.51_{-0.13}^{+0.15} \text{ kpc}$ when including the covariance with R_0 that we have found in §4.4.3. Since this is entirely independent of the surface mass density, this nullifies the covariance between L_d and $\Sigma_*(R_0, \phi_0)$ that we needed to handle in the [Bovy & Rix \(2013\)](#) model (see Table 2.3 in Chapter 2). Consequentially, we adopt the dynamically-derived estimate of $\Sigma_*(R_0, \phi_0) = 34.8 \pm 4.3 \text{ M}_\odot \text{ pc}^{-2}$, which we arrived at before accounting for any covariance with L_d in that paper. As discussed therein, this value matches very well with estimates from photometric techniques (cf. [Flynn et al., 2006](#); [Hessman, 2015](#); [McKee et al., 2015](#)).

Furthermore, we no longer enforce a linear scaling relationship between M_*^D and values of R_0 differing from 8 kpc, as reported by [Bovy & Rix \(2013\)](#); instead, we simply allow for the exponential dependency that comes naturally with Equation (4.17). We continue to use our original prior on R_0 , corresponding to $8.33 \pm 0.35 \text{ kpc}$, as it consistent with essentially all recent measurements in the literature, and hence reasonably describes our current knowledge of this parameter.

4.5.3.2 Correcting for Local Density Variations As mentioned above, it is important to note that Equation (4.17) is obtained by integrating the surface density profile for an exponential disk under the assumption that it is axisymmetric and smooth. Most prior studies of the Galactic disk mass, including our own past work, simply took $\Sigma_{\star}(R_0, \phi_0)$ to be representative of the mean value and plugged this in for $\bar{\Sigma}_{\star}(R_0)$ in Equation (4.17). Given that the MW is known to be a spiral galaxy, a more realistic justification of this is to assume that density perturbations due to spiral structure are negligible compared to the smooth, underlying exponential distribution of stars, or that $\Sigma_{\star}(R_0, \phi_0)$ is unperturbed from $\bar{\Sigma}_{\star}(R_0)$. There is substantial evidence, however, suggesting that both of these assumptions are inaccurate.

Broadly speaking, the Sun is believed to lie in a region of rarefaction within the MW’s spiral structure, roughly midway between the Sagittarius and Perseus arms (see, e.g., [Drimmel & Spergel, 2001](#); [Quillen, 2002](#); [Xu et al., 2013](#)). Assuming that this is true in detail would indicate that the local surface density of stellar material must be rescaled to use it in a smooth model for the disk. However, it is also worth noting that the Sun lies nearby to or within a branch of star-forming regions collectively called the “Orion Spur” or “Local Arm” ([Vallee, 1995](#); [Xu et al., 2013](#), and references therein), a secondary feature in the spiral structure that is less prominent than the main arms, but also resides within a ~ 100 – 200 pc wide cavity of relatively sparse cold and neutral interstellar gas known as the “Local Bubble” ([Cox & Reynolds, 1987](#); [Lallement et al., 2014](#)). This makes it murky at best as to what the true correction factor should be, and this is likely why previous MW models have typically neglected this effect altogether ([Flynn et al. 2006](#) is one example where the authors do account for this effect by incorporating a 10% correction for spiral enhancement). Therefore, we next explore both the Galactic and extragalactic data available in order to get a handle on the size of this correction.

The effect of density perturbations is generally parameterized by the spiral arm amplitude, A , which denotes the fractional increase in the surface density (or brightness) compared to the mean. In many cases, authors report the arm-to-interarm ratio, which is related to the spiral amplitude by $\Sigma_{\text{arm}}/\Sigma_{\text{interarm}} = (1+A)/(1-A)$. For instance, [Drimmel & Spergel \(2001\)](#) produced a model of the dust, stars, and spiral arms in the MW’s disk from *COBE*/DIRBE

data, which required placing the Sun within a gap in the spiral features, consistent with the picture described above. They found arm-to-interarm ratios of 1.2 and 1.32 in the J - and K -band, respectively, corresponding to values of $A = 0.09$ and 0.14 . Liu et al. (2012) investigated the extinction and radial velocity dispersion and distribution of red clump stars in the Perseus arm, finding $\Sigma_{\text{arm}}/\Sigma_{\text{interarm}} = 1.3\text{--}1.5$, corresponding to $A = 0.13\text{--}0.20$. Most recently, Polido et al. (2013, P13) fit the Ortiz & Lépine (1993, OL93) star count model of the Galaxy, which accounts for spiral structure (see Table 4.1), to all-sky 2MASS data, yielding an estimate of $\Sigma_{\text{arm}}/\Sigma_{\text{interarm}} = 2.0_{-0.8}^{+0.6}$, corresponding to $A = 0.33_{-0.24}^{+0.11}$.

Grosbøl et al. (2004) obtained deep K -band surface photometry for 54 normal spiral galaxies and analyzed their spiral structure using Fourier techniques. This resulted in a skewed distribution of spiral amplitudes ranging from $\sim 0\text{--}0.5$ with a median value of ~ 0.2 , which we have measured from data in their Table 2. Elmegreen et al. (2011) investigated the spiral arm properties of 46 Sa–Sm galaxies with varying characteristics from their $3.6\ \mu\text{m}$ images taken in the *Spitzer* Survey of Stellar Structure in Galaxies (S^4G). The authors measured arm and interarm surface brightnesses and tabulated their ratios converted to a magnitude in their Table 2. We have converted these values back to arm-to-interarm ratios based on Equation 3 of that study and find that they span the range of $1.3\text{--}4.0$ (with one large outlier at 8.3 that we disregard), correspond to $A = 0.13\text{--}0.6$. Lastly, Kendall et al. (2015) analyzed the spiral structure of 13 galaxies from the *Spitzer* Infrared Nearby Galaxies Survey (SINGS). Column 3 of their Table 2 provides spiral amplitudes measured at $3.6\ \mu\text{m}$, which span the range of $\sim 0.1\text{--}0.4$.

In order to derive an estimate for the spiral amplitude in the MW we statistically combine these Galactic and extragalactic measurements, treating each as a Gaussian distribution with its $\pm 1\sigma$ region matching the range of values detailed above. Calculating the unweighted mean yields $A = 0.225 \pm 0.095$, whereas the inverse variance-weighted mean yields $A = 0.158 \pm 0.024$, and the median value is 0.193 . Considering these metrics, we conservatively adopt $A = 0.2 \pm 0.1$ as the spiral amplitude of the Galaxy. Assuming that the Sun lies in a density trough, the appropriate correction factor to include in our axisymmetric disk model is $\Sigma_{\text{mean}}/\Sigma_{\text{interarm}} = (1 - A)^{-1} = 1.25_{-0.14}^{+0.18}$ (median and 1σ range). However, as we mentioned above, there is considerable uncertainty about the net local density perturbation,

and it is certainly possible that the local surface density is representative of the Solar circle. We therefore adopt a correction factor, $C \equiv \bar{\Sigma}_*(R_0)/\Sigma_*(R_0, \phi_0)$, for the density variation at the Sun’s location with an additional amount of uncertainty, such that a non-correction is included well within the 2σ significance level, corresponding to $C = 1.25_{-0.20}^{+0.29}$ (this is equivalent to $(1 - A)^{-1}$ after augmenting the errors on A by 50% compared to the value derived above.) We then multiply C by $\Sigma_*(R_0, \phi_0)$ to obtain $\bar{\Sigma}_*(R_0) = 43.4_{-8.4}^{+11.5} \text{ M}_\odot \text{ pc}^{-2}$.

4.5.3.3 Revised Stellar Mass Results To summarize the above, we have developed a new model of the Galactic disk where the stellar density follows a smooth, axisymmetric exponential profile with an underlying spiral arm structure characterized by a density amplitude of $A = 0.2 \pm 0.1$. We assume that the Sun lies at a Galactocentric radius of $R_0 = 8.33 \pm 0.35$ kpc, but also in a rarefaction region of the spiral structure, roughly midway between the Sagittarius and Perseus arms, and so local measures of the stellar surface density are not representative of the mean stellar surface density along the annulus at $R = R_0$ (i.e., averaged over all ϕ). The appropriate correction factor is $\Sigma_{\text{mean}}/\Sigma_{\text{interarm}} = (1 - A)^{-1} = 1.25_{-0.14}^{+0.18}$, however, given the uncertainties about the net local density perturbation described above, we conservatively adopt a correction factor for the Sun’s position with an augmented error bar given by $C \equiv \bar{\Sigma}_*(R_0)/\Sigma_*(R_0, \phi_0) = 1.25_{-0.20}^{+0.29}$. From our previous work we adopt a dynamically-derived estimate of the local stellar surface density of $\Sigma_*(R_0, \phi_0) = 34.8 \pm 4.3 \text{ M}_\odot \text{ pc}^{-2}$, and by multiplying this with C we obtain an estimate for the mean value at R_0 given by $\bar{\Sigma}_*(R_0) = 43.4_{-8.4}^{+11.5} \text{ M}_\odot \text{ pc}^{-2}$. Given that the exponential distribution of stars should be well traced by near-IR light, we adopt the IR photometric scale length estimate derived here of $L_d = 0.12(R_0 - 8.33 \text{ kpc}) + 2.51_{-0.13}^{+0.15} \text{ kpc}$, which includes the covariance with R_0 . Lastly, the stellar mass of the Galactic disk corrected for spiral arm density variations is calculated by plugging these values into Equation (4.17).

Using this model, we have next repeated the analysis from Chapter 2 in order to produce a revised estimate of the total stellar mass, M_* . As described in §4.2 of that paper, this entails using Monte Carlo techniques to produce model-consistent realizations of the disk mass and the HB estimate of the bulge+bar mass (the stellar halo contribution is assumed smaller than the uncertainties in M_*^D and hence negligible; e.g., Bell et al., 2008b), the results of which

are summed to obtain the posterior probability distribution for M_\star . We find that while the bulge+bar mass estimate remains $0.91 \pm 0.07 \times 10^{10} M_\odot$, the posteriors for the disk and total stellar mass are described by $M_\star^D = 4.8_{-1.1}^{+1.5} \times 10^{10} M_\odot$ and $M_\star = 5.7_{-1.1}^{+1.5} \times 10^{10} M_\odot$ (median and 1σ range), or equivalently $\log(M_\star^D/M_\odot) = 10.68 \pm 0.12$ and $\log(M_\star/M_\odot) = 10.75 \pm 0.10$, which are consistent with our previous results at the 0.2σ level. Our revised model also corresponds to a bulge-to-total mass ratio of 0.16 ± 0.03 and a specific star formation rate of $\dot{M}_\star/M_\star = 2.89_{-0.67}^{+0.80} \times 10^{-11} \text{ yr}^{-1}$, or equivalently $\log(\dot{M}_\star/M_\star/\text{yr}^{-1}) = -10.54 \pm 0.11$, when combined with the star formation rate estimate of $\dot{M}_\star = 1.65 \pm 0.19 M_\odot \text{ yr}^{-1}$ from Chapter 2.

We refer the reader to Appendix B for a convenient tabulation of the properties derived in this section. There one will also find updated estimates for the photometric properties of the MW, which we have produced by entirely reperforming the analyses of Chapter 3 using the model of the Galactic disk and hence total stellar mass derived here. We note that differences between these values and the original ones are marginal compared to the uncertainties, as expected given the small change in the stellar mass estimate here compared to our original estimate in Chapter 2. Nevertheless, the values tabulated in Appendix B are all self-consistent and uniformly reflect our best-to-date model of the MW.

4.6 SUMMARY AND CONCLUSIONS

In this study, we have set out to determine a combined, robust estimate of the scale length of the Galactic disk, L_d , measured at visible and IR wavelengths, given the large array of data available in the literature. Upon thoroughly investigating the previous estimates of L_d (see Table 4.1), we find that the set of Galactic models that are employed display as much variety as the observational datasets they are optimized to match, typically containing around a dozen free parameters. Aside from the wide assortment of model assumptions involved, given that measurements of L_d are produced from fitting the smooth underlying structure of the disk, these estimates are also susceptible to systematic error due to undetected substructures present in the true distribution of stars along any particular line of sight through the Galaxy

(Jurić et al., 2008). As a result of these variations in methodology and data, the estimates we have collected fall anywhere in the range $2 \lesssim L_d \lesssim 6$ kpc. This is comparable to the dynamical range of scale lengths measured for other galaxies of similar mass to the MW in the local Universe ($1 \lesssim L_d \lesssim 10$ kpc; cf. Chapter 5), and hence an improved determination of the scale length will also improve our understanding of how the MW fits amongst the broader population of galaxies.

Foregoing less sophisticated meta-analysis techniques (e.g., the inverse variance-weighted mean; IVWM), we have opted for a robust analysis method that has proven powerful in many applications inside and outside of astronomy. More specifically, we have produced our results by statistically combining the literature estimates using a hierarchical Bayesian analysis, which allows us to account for the possibility that one or more of these estimates have not properly accounted for all statistical or systematic errors. Through Monte Carlo techniques we have ensured that all the estimates used are rescaled to reflect current knowledge of the Sun’s distance from the Galactic center, R_0 . Lastly, we have implemented a Bayesian model averaging (BMA) technique to obtain the posterior for L_d marginalized over all the bad-measurement models we have investigated, taking into account both goodness-of-fit and model complexity. Ultimately, we find the Galactic scale length to be $L_d = 2.71^{+0.22}_{-0.20}$ kpc for visible starlight, $L_d = 2.51^{+0.15}_{-0.13}$ kpc for IR starlight, and $L_d = 2.64 \pm 0.13$ kpc when integrating visible and IR starlight measurements (see §4.4.3 for discussion on how these results depend on R_0).

In Table 4.3 we have listed a full summary of results from our bad-measurement models, the result from applying BMA, as well as the non-hierarchical IVWM for comparison. We have demonstrated in §4.4.4 that our results are robust to varying many of the assumptions we have made in our analyses, and in §4.5.2 that they are consistent with passband-to-passband variations measured for external disks. We have also used our results to revise the estimate of the MW’s total stellar mass from Chapter 2 in §4.5.3. Using the IR scale length measurement found here, we find that the mass of the stellar disk is $4.8^{+1.5}_{-1.1} \times 10^{10} M_\odot$. Combining this with the HB estimate for the bulge+bar mass in a model-consistent manner using the framework of Chapter 2, we have determined the MW’s total stellar mass to be $5.7^{+1.5}_{-1.1} \times 10^{10} M_\odot$. For convenience, we have compiled in Appendix B several tables

displaying the updated constraints we have produced for the structural and mass properties of the MW, as well as updates to the results from Chapter 3 using the stellar mass derived here.

The remaining estimates of L_d in the literature we have compared our results to are generically constrained by modeling stellar kinematic observations, and hence describe the radial distribution of *total* mass in the Galaxy. Nevertheless, the majority of such estimates compare well with the values we have presented in this study based on visible/IR starlight, though there are a few that are in significant tension, favoring instead values of L_d far below or above our constraints. It is beyond the scope of this study to comment on whether a dynamically-constrained L_d is a fair comparison with those based on starlight, but this agreement adds some credence to our stellar scale length estimates. Interestingly, it appears that dynamical estimates are as prevalent *and* as disparate as photometric estimates, and astronomers in need of adopting a value from the literature would likely benefit from performing the type of HB analysis we have employed here to that set as well.

In totality, the results of this study, in combination with those of our previous works which we have updated here, provide a much improved comprehensive picture of the MW. More specifically, we have determined tight constraints on a variety of the Galaxy's global properties, including its total stellar mass, star formation rate, photometric disk scale length, and optical luminosity and color index, using methods that either circumvent or correct for many of the major systematics that have traditionally affected them. Moreover, all of these values have been produced from a single, consistent model of the MW that reflects our best-to-date knowledge its structural parameters, and which rests upon the same basic assumptions that are used for studying extragalactic objects. All of this work culminates in a newfound ability to assess accurately how the properties of our Galaxy compare to scaling relations found for external spiral galaxies. In the following chapter, we will present new comparisons of the MW to both the Tully-Fisher relation as well as 3-dimensional luminosity-velocity-size relations for other massive spiral galaxies in order to assess how our Galaxy truly fits in a variety of extragalactic contexts.

5.0 DOES THE MILKY WAY OBEY SPIRAL GALAXY SCALING RELATIONS?

5.1 INTRODUCTION

It is well established that spiral galaxies follow a set of power-law relationships amongst their global properties, generally referred to as scaling relations (Courteau & Rix, 1999; Courteau et al., 2007; Dutton et al., 2007, 2011; Hall et al., 2012, hereafter H12). The most prominent of these, known as the Tully-Fisher relation (Tully & Fisher, 1977, TFR), reflects the tight relationship between intrinsic brightness (or luminosity, L) and rotational velocity (V_{rot}). In the standard picture, spiral galaxies generically contain a luminous disk component comprised of rotationally supported stars and gas residing at the center of a much larger and more massive dark matter halo component (Fall & Efstathiou, 1980; Kauffmann et al., 1993; Cole et al., 1994; Mo et al., 1998). The TFR encodes key information about the ratio of luminous to dark matter in these systems, making it a powerful tool for studying galaxy formation and evolution (e.g., Dutton et al., 2007, 2011), though our theoretical understanding of the relation within a Λ CDM universe is still progressing (Dutton et al., 2007, 2011; H12). Correlations also are observed between disk size, or radius (R), and L or V_{rot} , but display significantly larger dispersions (Courteau et al., 2007; H12).

Determining how the properties of our Galaxy, the Milky Way (MW), fit with these scaling relations is a challenging task. A handful of studies have performed such an analysis, indicating that the MW is a 1–1.5 σ outlier from the TFR (Malhotra et al., 1996; Flynn et al., 2006; Hammer et al., 2007). This begs the question: is our Galaxy truly atypical, or have we failed to make an apples-to-apples comparison? The latter case is hard to rule out, as it is impossible for astronomers to measure the MW in the same manner as extragalactic objects,

due in large part to our uniquely inside-out perspective. Adding further complications, dust in the interstellar medium obscures most of the MW’s stars from view, especially at optical wavelengths (Green et al., 2015). Any attempt to infer global properties of our Galaxy directly typically requires extrapolating from measurements of only the most nearby stars — a tiny fraction of the total stellar population — using MW models that rest upon a large array of assumptions (e.g., Malhotra et al., 1996; Flynn et al., 2006; van der Kruit, 1986; Siegel et al., 2002; Robin et al., 2003; Girardi et al., 2005; Jurić et al., 2008; López-Corredoira & Molgó, 2014; Mao et al., 2015). As a result, estimates of MW properties have remained poorly constrained and vulnerable to systematic errors, making it difficult to assess accurately how our Galaxy fits amongst its peers.

This study aims at overcoming these challenges, which is important for a number of reasons. For instance, if the MW is truly representative of spiral galaxies, then our high-detail studies of it may be fairly used to understand the TFR, as well as other driving mechanisms of galaxy evolution. On the other hand, if our Galaxy does not fit the common mold, then identifying its unusual characteristics could offer important clues into how its formation history may have been unusual (see, e.g., Hammer et al., 2007; Liu et al., 2011; Busha et al., 2011a).

This chapter is structured as follows. In §5.2.1 we discuss the extragalactic dataset that we use to measure spiral galaxy scaling relations. In §5.2.2 we next discuss the MW measurements employed in this study and the methods used to produce them. We then focus on comparing the MW to TFRs in §5.3, with our methodologies outlined in §5.3.1 and our results discussed in §5.3.2. We next extend this type of comparison to 3-dimensional luminosity-velocity-radius (*LVR*) relations in §5.4, where likewise our methodologies are first outlined in §5.4.1 and our results are then discussed in §5.4.2. In §5.5 we provide broader discussions of our results; this includes the important differences between this study and prior ones that deemed the MW a $1\text{--}1.5\sigma$ outlier to the TFR in §5.5.1. In §5.5.2 we discuss how our results lend circumstantial evidence towards the emergent picture of a “too-small” MW Galaxy; this includes potential concerns about this conclusion in §5.5.2.1, but also how it is supported by studies of the MW’s satellite galaxy population in §5.5.2.2. Lastly, we conclude with a summary of our findings in §5.6.

Throughout this paper, we use L when generically discussing any proxy for luminosity; these include both absolute magnitudes, denoted by (italicized) M , and mass properties, denoted by (unitalicized) M . In order to compare measurements for extragalactic objects (which rely on assumptions about cosmic distance scales) directly to those for the MW (within which distances may be measured more directly), we adopt a standard Λ CDM cosmology parameterized by a mass density of dark and normal matter of $\Omega_M = 0.3$, an effective mass density of dark energy of $\Omega_\Lambda = 0.7$, and a Hubble constant of $H_0 = 70 \text{ km s}^{-1} \text{ Mpc}^{-1}$. All absolute magnitudes, on the other hand, are derived using a Hubble constant of $H_0 = 100h \text{ km s}^{-1} \text{ Mpc}^{-1}$, therefore making them truly measurements of $M - 5 \log h$. Following convention, all SDSS *ugriz* magnitudes are reported in the AB system, whereas all Johnson-Cousins *UBVRI* magnitudes are reported in the Vega system. In all cases, we use “log” to denote the base-10 logarithm. Finally, we note that in this chapter we denote disk scale length as R_d (instead of L_d , which was used in all previous chapters) to avoid any confusion with with luminosity.

5.2 DATA

In earlier chapters, we have developed improved estimates of MW properties that are robust to many sources of systematic uncertainty. Most notably, this includes new determinations of the MW’s photometric properties (i.e., its global color and luminosity at optical wavelengths), not by extrapolating from optical measurements in the Solar neighborhood, but by analyzing the integrated properties of *Milky Way analogs* — a sample of galaxies whose distributions of total stellar masses and star formation rates match the inferred posterior distributions for those same properties of the MW — observed by the Sloan Digital Sky Survey (SDSS; Chapter 3). We also have utilized a hierarchical Bayesian analysis technique to improve constraints on a variety of other Galactic properties, including the total stellar mass and star formation rate (Chapter 2), as well as the disk scale length (Chapter 4). In this paper, we use these results to explore how the MW fits with spiral galaxy scaling relations. In Table 5.2, we list the estimates for each of the MW properties that we employ in this study; these

reflect the best-to-date values available in the literature and account for all major known sources of uncertainty. All MW values in Table 5.2 have been adjusted to use the same basic assumptions as the extragalactic scaling relation data used here. Consequentially, the Galactic-to-extragalactic comparisons presented below should be robust to many potential sources of systematic offsets. We discuss these data more in the following subsections.

5.2.1 SDSS Spiral Galaxies

Our sample of spiral galaxies consists of objects that have both photometric and spectroscopic measurements from the Eighth Data Release (DR8; Aihara et al., 2011) of the SDSS (York et al., 2000), as well as 21-cm radio spectral line measurements from the SFI++ catalog (Springob et al., 2007). We have identified a sample of 422 spiral galaxies suitable for this study by cross-matching objects from the data used in Chapter 3 to those found in both the SFI++ catalog and Table 1 from H12, yielding the following measurements:

- Spectroscopic redshifts (z) with errors typically $< 0.1\%$ from SDSS-DR8;
- SDSS-DR8 *ugriz* absolute magnitudes that include K -corrections to reflect the $z = 0$ rest frame ($^0M - 5 \log h$), based on extinction-corrected `cmodel` photometry, produced in Chapter 3;
- Total stellar masses (M_*) produced in Chapter 3 by applying MPA/JHU catalog algorithms (Brinchmann et al., 2004) to DR8 photometry assuming a Kroupa initial mass function (IMF; Kroupa & Weidner, 2003);
- Neutral hydrogen (HI) gas masses (M_{HI}) determined from 21-cm line flux measurements that are corrected for beam attenuation, pointing offsets, and HI self-absorption from SFI++ (Springob et al., 2007);
- Disk rotational velocities (V_{rot}) determined from 21-cm line width measurements that are corrected for instrumental effects, redshift broadening, disk inclination, and distance from SFI++; and
- Disk inclinations corrected for projection effects and angular scale lengths (Θ_d) measured in units of arcseconds by H12 from an isophotal analysis of each galaxy’s SDSS *i*-band light profile.

Table 5.1. Global Properties of the Milky Way

Property	Mean $\pm 1\sigma$	Units	Description
V_{rot}	220 ± 22	km s^{-1}	Rotational velocity of the disk
L_d	$2.71^{+0.22}_{-0.20}$	kpc	Photometric disk scale length
M_{\star}	$5.67^{+1.53}_{-1.11} \times 10^{10}$	M_{\odot}	Total stellar mass
M_{HI}	$5.55 \pm 1.74 \times 10^9$	M_{\odot}	Neutral hydrogen gas mass
M_{bar}	$6.45^{+1.54}_{-1.14} \times 10^{10}$	M_{\odot}	Baryonic mass ($= M_{\star} + 1.4M_{\text{HI}}$)
0M_u	$-19.15^{+0.55}_{-0.47}$	mag	SDSS u -band absolute magnitude
0M_g	$-20.33^{+0.42}_{-0.43}$	mag	SDSS g -band absolute magnitude
0M_r	$-20.97^{+0.37}_{-0.40}$	mag	SDSS r -band absolute magnitude
0M_i	$-21.24^{+0.37}_{-0.38}$	mag	SDSS i -band absolute magnitude
0M_z	$-21.53^{+0.36}_{-0.39}$	mag	SDSS z -band absolute magnitude
0M_U	$-20.00^{+0.59}_{-0.47}$	mag	Johnson U -band absolute magnitude
0M_B	$-20.05^{+0.41}_{-0.45}$	mag	Johnson B -band absolute magnitude
0M_V	$-20.71^{+0.39}_{-0.40}$	mag	Johnson V -band absolute magnitude
0M_R	$-21.23^{+0.39}_{-0.39}$	mag	Cousins R -band absolute magnitude
0M_I	$-21.81^{+0.38}_{-0.38}$	mag	Cousins I -band absolute magnitude

Note. — See §5.2.2 for the details on the source of each estimate. All absolute magnitudes are derived using a cosmic distance scale with Hubble constant $H_0 = 100h \text{ km s}^{-1} \text{ Mpc}^{-1}$, and hence truly represent values of ${}^0M - 5 \log h$; the 0 superscript prefix before absolute magnitudes indicates that they include K-corrections to reflect the $z = 0$ rest-frame passbands. The rotational velocity is adopted from [Kerr & Lynden-Bell \(1986\)](#) and we have ascribed a 10% measurement error. The estimates listed for M_{HI} and M_{bar} are derived in §5.2.2. The remaining entries come from Chapter 4.

We note that H12 performed their own reduction and photometry of galaxy images and demonstrated that their methods yield much more reliable estimates of Θ_d than the SDSS imaging pipeline. Using the measurements listed above we also calculate the baryonic mass of each galaxy as $M_{\text{bar}} = M_{\star} + 1.4M_{\text{HI}}$, where the factor of 1.4 accounts for the mass present in the form of helium and metals (following H12), and its physical disk scale length as $R_d = \Theta_d d_A(z)$, where $d_A(z)$ is the angular diameter distance at redshift z from our adopted cosmology.

Identified in this way, our sample of 422 objects is analogous to “Sample C” of H12, and constitutes the subset of those objects that are found to have SDSS-DR8 imaging and spectroscopy, allowing us to use values from Chapter 3 for properties in the first three bullet points above. We next restrict to only those objects with inclinations measured to be in the range of 40 to 75 degrees. This cut eliminates galaxies whose disks are too face-on to have an accurately measured V_{rot} or are too edge-on to ensure an accurately determined Θ_d . As a result, we are left with 258 spiral galaxies, analogous to “Sample D” of H12, that should be best for determining scaling relations and which we discuss exclusively hereafter. In practice, we find that this inclination restriction reduces the observed scatter in our TFRs by $\sim 10\%$; however, the conclusions we draw are entirely insensitive to comparing the MW to scaling relations based on the sample with or without this cut applied (see Tables 5.2 and 5.4.2).

5.2.2 The Milky Way

In this section we discuss each of the MW estimates listed in Table 5.2. We note that the measurements from our previous work were derived specifically to enable comparative studies such as this one. That is, our MW estimates rest upon the same basic assumptions that were used to produce the extragalactic data. Most importantly, these include a Kroupa IMF, a single-exponential disk model, and a consistent definition of stellar mass, which includes the contributions from both main-sequence stars and remnants, but not substellar material, in accordance with the stellar evolution models of Bruzual & Charlot (2003).

In Chapter 2 we have presented a hierarchical Bayesian (HB) analysis framework for statistically combining various estimates of MW properties. In that study, we addressed

the question: given the measurements available in the literature, what is the best aggregate estimate for both the Galactic bulge+bar mass and star formation rate (SFR) of our Galaxy? The HB methodology is a vetted and powerful tool for answering these questions (see, e.g., [Press, 1997](#); [Lang & Hogg, 2012](#)), which enabled us to produce results that account for the possibility that any single measurement is potentially flawed or suffers from systematic errors, given the complexities of modeling the MW (we refer the reader to that work for more details). The same paper describes the Monte Carlo techniques we have used for determining the total stellar mass of the MW by incorporating a model for the stellar disk. Initially, we utilized the parameters of the dynamical mass model from [Bovy & Rix \(2013\)](#), but we update the model used here (q.v. below).

In [Chapter 3](#) we demonstrated that identifying a sample of MW-analog galaxies from SDSS data enabled us to convert our posterior knowledge of the Galactic M_\star and SFR from [Chapter 2](#) into tight constraints on the global photometric properties (i.e., color and luminosity) of the MW as the SDSS instrument would measure them face-on from across cosmic distances. In [Table 5.2](#), we list absolute magnitudes for the MW calibrated to the same scale as those observed for other spiral galaxies, for both *ugriz* and *UBVRI* filter passbands.

In [Chapter 4](#) we have applied the HB methodology from [Chapter 2](#) to nearly 30 different estimates of the scale length of the MW disk in the literature based on observations of either visible or infrared starlight from the Galaxy. In [Table 5.2](#), our estimate of $R_d = 2.71^{+0.22}_{-0.20}$ kpc is the result from considering visible light only, which corresponds most closely with the extragalactic scale lengths measured by H12 in the *i*-band. In comparison, we found the disk scale length to be $2.51^{+0.15}_{-0.14}$ kpc from infrared starlight, differing by only 0.8σ .

Given that infrared light is expected to trace more closely the distribution of stellar mass, in [Chapter 4](#) we next used this value to produce an updated model of the stellar disk which also accounts for local stellar density variations due to spiral structure and its associated uncertainty — a correction that typically has been ignored in MW models ([Hessman, 2015](#)). We then combine this with our bulge+bar mass estimate from [Chapter 2](#) to determine a total stellar mass for the MW of $5.67^{+1.53}_{-1.11} \times 10^{10} M_\odot$, or equivalently $\log(M_\star/M_\odot) = 10.75 \pm 0.10$. This represents only a slight change from our original estimate of 10.78 ± 0.08 from [Chapter](#)

2 when using the dynamical model of the disk from [Bovy & Rix \(2013\)](#). The absolute magnitudes listed in [Table 5.2](#) are derived using this revised M_{\star} estimate, together with the unchanged SFR value; these differ only slightly from the original values in [Chapter 3](#).

We note that all estimates of Galactic properties described so far consistently utilize a prior on the Galactocentric radius of the Sun of $R_0 = 8.33 \pm 0.35$ kpc, based on the work of [Gillessen et al. \(2009\)](#). This value stems from careful consideration of both statistical and systematic uncertainties, and represents an up-to-date, geometric estimate that is still consistent with essentially all recent R_0 measurements, which predominantly fall in the range of ~ 8 – 8.5 kpc (see, e.g., [Schönrich, 2012](#), [Do et al., 2013](#), [Reid et al., 2014](#), and [Chatzopoulos et al., 2015](#) for recent estimates that closely match our prior). Most importantly, error bars quoted for all MW quantities incorporate the uncertainties associated with our limited knowledge of R_0 . We will demonstrate in [§5.5.1](#) that prior attempts at discussing the MW in the context of the TFR were problematic due, in large part, to their treatment of R_0 .

We employ the International Astronomical Union standard value of 220 km s^{-1} for the rotation speed of the Galactic disk ([Kerr & Lynden-Bell, 1986](#)) and ascribe a conservative 10% error estimate (in line with preceding studies). We find that this agrees well with the current set of estimates available in the literature (note that these typically scale proportionately with R_0 due to the conversion from angular speed to tangential speed; see the description of estimates in [Majewski, 2008](#); [Reid et al., 2014](#), as well as those of [Bovy & Rix, 2013](#); [Sirko et al., 2004](#); [Piffl et al., 2014](#)). Several of the more recent measurements have yielded values closer to ~ 240 – 250 km s^{-1} . We note here that if we were to increase our adopted value of V_{rot} by 1σ (i.e., $+0.04$ dex in $\log V_{\text{rot}}$) to better match these, tension between the MW and the TFR increases moderately, but we still find the MW to be consistent with the relation, given its scatter. Furthermore, tension with the *LVR* relation also increases, and our overall conclusions would be unchanged.

Estimates of the neutral hydrogen gas mass (M_{HI}) of the MW are sparse in the literature. Following what [Flynn et al. \(2006\)](#) have done (but omitting molecular hydrogen to match our extragalactic data), we can scale the HI estimates tabulated by [Dame \(1993b\)](#) to our choice of $R_0 = 8.33$ kpc in order to find estimates of $M_{\text{HI}} = 3.3 \times 10^9 M_{\odot}$ based on the work of [Henderson et al. \(1982\)](#), or $M_{\text{HI}} = 6.7 \times 10^9 M_{\odot}$ by combining values for inside

and outside the solar circle from Liszt (1992) and Wouterloot et al. (1990). More recently, Kalberla et al. (2007) have made use of much more sensitive Galactic HI line surveys with improved coverage, both spatially and kinematically, in order to produce a model of the interstellar medium (ISM) that yields a total HI mass of $8 \times 10^9 M_{\odot}$ (Kalberla & Kerp, 2009). When scaled to our choice of R_0 this becomes $M_{\text{HI}} = 7.7 \times 10^9 M_{\odot}$. Lastly, the Bovy & Rix (2013) model of the Galactic disk assumes a smaller total mass for the ISM of $7 \times 10^9 M_{\odot}$ (insensitive to the choice of R_0). If we apply here the HI-to-ISM mass ratio ($= 0.65$) from the Kalberla & Kerp (2009) model, this yields an estimate of $M_{\text{HI}} = 4.5 \times 10^9 M_{\odot}$. Therefore, we take the mean and standard deviation of these four values in order to produce an aggregate estimate of $M_{\text{HI}} = 5.55 \pm 1.74 \times 10^9 M_{\odot}$, which we adopt for this study. Finally, we calculate the baryonic mass of the MW as $M_{\text{bar}} = M_{\star} + 1.4M_{\text{HI}} = 6.45_{-1.14}^{+1.54} \times 10^{10} M_{\odot}$, or equivalently $\log(M_{\text{bar}}/M_{\odot}) = 10.81 \pm 0.09$.

5.3 INVESTIGATING TULLY-FISHER RELATIONS

We begin by first investigating how the MW fits with the TFR. We explore seven versions of the TFR by examining the relationship between rotation speed and a variety of quantities related to luminosity: rest-frame absolute magnitudes (0M) in all five SDSS *ugriz* passbands, \log total stellar masses ($\log M_{\star}$), and \log baryonic masses ($\log M_{\text{bar}}$). As mentioned above, we measure each relation from our sample of 258 spiral galaxies observed by the SDSS that display moderate inclinations, allowing all quantities of interest for this study to be measured cleanly (cf. §5.2.1).

5.3.1 Methods

In each case, we perform a least-squares optimization to fit the inverse relation, where we treat $\log V_{\text{rot}}$ as the dependent variable; this is common practice to avoid any sample-selection biases in modeling the data that would be tied to errors in measurements of L (Schechter, 1980; Tully, 1988). Generically, we fit for $\log V_{\text{rot}} = a + b \log L$, where a is the zero point,

b is the slope, and $\log L$ can be any of the seven proxies listed above. We utilize the `scipy.optimize.curve_fit` package to perform a non-linear least-squares fit of each model to the data, providing the a and b values of the optimal relation. We then determine the scatter (σ_{TF}) about the relation by measuring the standard deviation of the $\log V_{\text{rot}}$ values about the best-fit line (typically ~ 0.08 dex in $\log V_{\text{rot}}$). Lastly, we measure the offset of the MW data point from the line along the $\log V_{\text{rot}}$ direction using the combination in quadrature of both σ_{TF} and MW errors.

In Table 5.2 we tabulate values pertinent to each TFR comparison, including a , b , σ_{TF} , and the level of consistency of the MW data point. Here, we also show analogous comparisons to TFRs found using the spiral galaxy sample with no inclination cuts applied, as well as to TFRs found by other authors.

We have performed several tests on the robustness of our results. For example, we have conducted a “forward” fitting of each TFR to our extragalactic data, i.e., where we model $\log L = a' + b' \log V_{\text{rot}}$, equivalent to assuming that Malmquist bias (Teerikorpi, 1997) is of minimal consequence. As is typically observed, the forward TFRs are shallower than their corresponding inverse relations, but with larger zero points (or intercepts), and have similar scatters (cf. Pizagno et al., 2007). Nonetheless, in all cases we find that the intersection of the forward and inverse relations occurs very near the MW’s L and V_{rot} ; our results would remain the same regardless of how we fit for the relation. We have also tested for any bias in our fits due to large outliers in the extragalactic data. Here, in place of our standard least-square optimization, we employ the `Statsmodels` Python module to perform robust linear modeling using M-estimators (Maronna et al., 2006). In particular, we have used both Huber’s and Tukey’s estimator functions (with tuning constants of $1.345\sigma_{\text{MAD}}$ and $4.685\sigma_{\text{MAD}}$, respectively, where σ_{MAD} is the median absolute deviation measured for the entire sample) to deweight objects with large residuals in the forward or inverse fits of the TFR. In all cases, this yields negligible changes in the best-fit line, and, again, our conclusions are negligibly affected.

5.3.2 Results

Based on our results listed in Table 5.2, we find that, in all cases, the properties of the MW are in excellent agreement with the TFR. For those relations measured in this study, where Galactic and extragalactic measurements are ensured to be on equal footings, when using SDSS magnitudes, the MW is consistent with all TFRs with deviations of less than 0.20σ . When using total stellar mass or baryonic mass, we find the MW data point to be consistent with the relation at the 0.33σ and 0.50σ levels, respectively. Figure 5.1 illustrates the analyses for i -band absolute magnitude (0M_i), total stellar mass (M_\star), and baryonic mass (M_{bar}). Table 5.2 illustrates that these results are robust to using our spiral galaxy sample with or without the inclination cut applied.

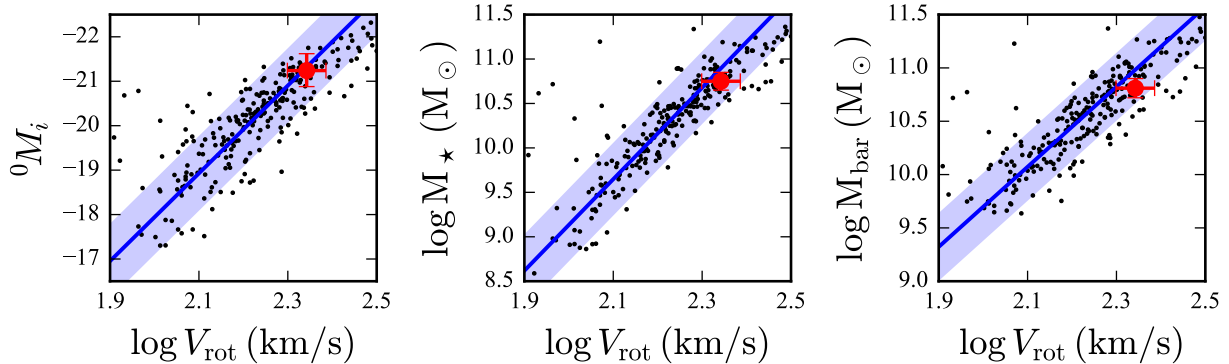


Figure 5.1: Tully-Fisher relations (TFRs) defined by rest-frame absolute i -band magnitude (0M_i ; top), total stellar mass (M_\star ; middle), and baryonic mass (M_{bar} ; bottom) of our sample of spiral galaxies. In each panel, the properties are plotted as a function of the disk rotational velocity (V_{rot}). Black dots depict the objects in Sample C and light gray dots depict galaxies with less securely measured distances. The blue line and shaded blue region shows our best-fit (inverse) TFR and 1σ range, respectively, using the black dots (see §5.3.1). Lastly, in each panel we overlay the Milky Way’s properties with error bars in red, taken from Table 5.2. In all cases, the properties of the Milky Way are in excellent agreement with the best-fit TFR (see Table 5.2).

Table 5.2: Consistency of the Milky Way with Tully-Fisher Relations

Properties ($\log L, \log V$)	Zero Point a	Slope b	Scatter σ_{TF}	MW level of consistency ^a
This study: Spiral galaxies with inclinations between 40° and 75° — Sample size: 285				
$({}^0M_u, \log V_{\text{rot}})$	0.635 ± 0.108	-0.088 ± 0.006	0.106	-0.16σ
$({}^0M_g, \log V_{\text{rot}})$	0.160 ± 0.100	-0.107 ± 0.005	0.089	-0.07σ
$({}^0M_r, \log V_{\text{rot}})$	0.168 ± 0.091	-0.103 ± 0.005	0.083	-0.05σ
$({}^0M_i, \log V_{\text{rot}})$	0.183 ± 0.086	-0.101 ± 0.004	0.081	-0.09σ
$({}^0M_z, \log V_{\text{rot}})$	0.366 ± 0.078	-0.091 ± 0.004	0.080	-0.12σ
$(\log M_\star, \log V_{\text{rot}})$	0.226 ± 0.076	0.194 ± 0.007	0.075	-0.33σ
$(\log M_{\text{bar}}, \log V_{\text{rot}})$	-0.583 ± 0.117	0.266 ± 0.011	0.080	-0.50σ
This study: Spiral galaxies with no inclination cut applied — Sample size: 422				
$({}^0M_u, \log V_{\text{rot}})$	0.752 ± 0.087	-0.082 ± 0.005	0.116	-0.14σ
$({}^0M_g, \log V_{\text{rot}})$	0.381 ± 0.083	-0.096 ± 0.004	0.102	-0.07σ
$({}^0M_r, \log V_{\text{rot}})$	0.353 ± 0.077	-0.095 ± 0.004	0.097	-0.05σ
$({}^0M_i, \log V_{\text{rot}})$	0.354 ± 0.073	-0.093 ± 0.004	0.094	-0.08σ
$({}^0M_z, \log V_{\text{rot}})$	0.449 ± 0.066	-0.087 ± 0.003	0.091	-0.10σ
$(\log M_\star, \log V_{\text{rot}})$	0.278 ± 0.065	0.189 ± 0.006	0.085	-0.34σ
$(\log M_{\text{bar}}, \log V_{\text{rot}})$	-0.526 ± 0.097	0.261 ± 0.009	0.088	-0.52σ
Dale et al. (1999) — Sample size: 522				
$(M_I, \log V_{\text{rot}})$	-0.524	-0.130	0.049	-0.38σ
Bell & de Jong (2001) ^b — Sample size: 28				
(M_B, V_{flat})	-0.191	-0.122	0.153	$(-0.62\sigma, -0.51\sigma)$
	-0.665	-0.145	0.181	$(-0.67\sigma, -0.54\sigma)$
(M_R, V_{flat})	-0.124	-0.113	0.141	$(-0.56\sigma, -0.46\sigma)$
	-0.393	-0.126	0.157	$(-0.49\sigma, -0.40\sigma)$
(M_I, V_{flat})	-0.034	-0.106	0.133	$(-0.54\sigma, -0.44\sigma)$
	-0.233	-0.116	0.145	$(-0.44\sigma, -0.36\sigma)$
$(\log M_\star, V_{\text{flat}})$	$(-0.157, -0.071)$	$(0.222, 0.230)$	$(0.029, 0.030)$	$(-0.57\sigma, -0.42\sigma)$
	$(-0.132, 0.004)$	$(0.216, 0.231)$	$(0.028, 0.030)$	$(-0.22\sigma, +0.16\sigma)$
$(\log M_{\text{bar}}, V_{\text{flat}})$	$(-0.794, -0.713)$	$(0.282, 0.290)$	$(0.028, 0.029)$	$(-0.19\sigma, -0.06\sigma)$
Geha et al. (2006) — Sample size: ~ 300				
$(M_I, \log V_{\text{rot}})$	0.339	-0.090	0.110	-0.35σ
$(\log M_{\text{bar}}, \log V_{\text{rot}})$	-0.651	0.270	0.100	-0.69σ
Pizagno et al. (2007) — Sample size: 162				
$(M_g, \log V_{80})$	-0.488	-0.136	0.073	-0.77σ
$(M_r, \log V_{80})$	-0.535	-0.135	0.063	-0.61σ
$(M_i, \log V_{80})$	-0.460	-0.130	0.061	-0.55σ
$(M_z, \log V_{80})$	-0.403	-0.127	0.058	-0.16σ

Table 5.2 – Continued

Properties ($\log L, \log V$)	Zero Point a	Slope b	Scatter σ_{TF}	MW level of consistency ^a
Courteau et al. (2007) — Sample size: 1303				
$(M_I, \log V_{\text{rot}})$	-0.257	-0.116	0.057	-0.85 σ
Noordermeer & Verheijen (2007)^c — Sample size: 48				
$(\log M_{\text{bar}}, \log V_{\text{rot}})$	-1.198	0.329	0.042	+0.31 σ
$(\log M_{\text{bar}}, \log V_{\text{max}})$	-1.183	0.328	0.052	+0.31 σ
$(\log M_{\text{bar}}, \log V_{\text{asympt}})$	-0.894	0.298	0.043	-0.39 σ
De Rijcke et al. (2007)^d — Sample size: ~300				
$(M_B, \log V_{\text{rot}})$	-0.298	-0.129	(0.05, 0.10) [†]	(-0.59 σ , -0.39 σ)
$(\log M_{\star}, \log V_{\text{rot}})$	-0.942	0.306	(0.05, 0.10) [†]	(+0.03 σ , +0.05 σ)
$(\log M_{\star+\text{HI}}, \log V_{\text{rot}})$	-1.032	0.317	0.063	+0.74 σ
Kassin et al. (2007)^e — Sample size: 544				
$(\log M_{\star}, \log S_{0.5})$	-1.070	0.300	0.140	-0.29 σ
Avila-Reese et al. (2008)^f — Sample size: 76				
$(M_B, \log V_{\text{max}})$	-0.143	-0.124	0.064	+0.01 σ
$(\log M_{\text{star}}, \log V_{\text{max}})$	-0.639	0.274	0.058	-0.50 σ
$(\log M_{\text{bar}}, \log V_{\text{max}})$	-0.979	0.303	0.058	-0.21 σ
Stark et al. (2009)^g — Sample size: 23				
$(\log M_{\text{bar}}, \log V_{\text{flat}})$	-0.552	0.265	(0.05, 0.10) [†]	-0.25 σ
Gurovich et al. (2010) — Sample size: 41				
$(\log M_{\star}, \log V_{\text{rot}})$	-0.459	0.263	(0.05, 0.10) [†]	(+0.25 σ , +0.42 σ)
$(\log M_{\star}, \log V_{\text{rot}})$	-1.082	0.312	(0.05, 0.10) [†]	(-0.70 σ , -0.43 σ)
McGaugh (2012)^h — Sample size: 47				
$(\log M_{\text{bar}}, \log V_{\text{flat}})$	-0.526	0.262	0.063	-0.51 σ
Hall et al. (2012) — Sample size: 668 (578 Mbar)				
$(M_g, \log V_{\text{rot}})$	-0.259	-0.124	0.082	-0.78 σ
$(M_r, \log V_{\text{rot}})$	-0.166	-0.117	0.077	-0.57 σ
$(M_i, \log V_{\text{rot}})$	-0.143	-0.115	0.074	-0.55 σ
$(\log M_{\star}, \log V_{\text{rot}})$	-0.558	0.264	0.075	-0.72 σ
$(\log M_{\text{bar}}, \log V_{\text{rot}})$	-0.903	0.293	0.078	-0.87 σ
Cortese et al. (2014) — Sample size: 235				
$(\log M_{\star}, \log S_{0.5})$	-1.410	0.330	0.100	-0.55 σ

Table 5.2 – Continued

Properties ($\log L, \log V$)	Zero Point a	Slope b	Scatter σ_{TFR}	MW level of consistency ^a
Bradford et al. (2016) — Sample size: 930				
($M_i, \log V_{\text{rot}}$)	−0.105	−0.118	0.095	+0.49 σ
($\log M_{\star}, \log V_{\text{rot}}$)	−0.197	0.240	0.077	+0.55 σ
($\log M_{\text{bar}}, \log V_{\text{flat}}$)	−0.991	0.309	0.077	+0.04 σ

Note. — The zero point a and slope b correspond to the inverse TFR, i.e., $\log V_{\text{rot}} = a + b \log L$, and errors denote the uncertainty in the formal fits for these parameters. The scatter, σ_{TFR} , denotes the standard deviation of the extragalactic data about each relation along the velocity axis in units of dex (i.e., units of $\log V$). The final column lists the consistency level between the Milky Way and each TFR in units of $\sigma = (\sigma_{\text{MW}} + \sigma_{\text{TFR}})^{-1/2}$, where σ_{MW} is the uncertainty in the Milky Way property along the independent-variable axis (which can be found in Table 5.2). For some of the relations we have explored a range of values for one or more parameters yielding a range of consistency levels for the MW; these are indicated by parentheses. In cases where the authors have only provided parameters from fitting the forward relation to their data, we have listed the MW’s consistency assessed along the luminosity/mass axis here, but have tabulated the inverse relation-equivalent values in all other columns for ease of comparison. Where necessary, luminous TFR parameters have been adjusted to reflect using absolute magnitudes calculated as $^0M - 5 \log h$. Comparisons to relations defined by other authors can differ either because they rely on quantities calculated differently from those used here or because they employ systematically different samples (see Bradford et al., 2016 for a thorough investigation of these effects). Despite these variations, the MW is broadly consistent with the relation, and can fall above or below it depending on the study.

[†] The authors did not provide a measurement of the scatter; so here we explore a range of plausible values based upon the work of McGaugh (2012).

^a A negative sign indicates that, given its rotational velocity, the Milky Way is sub-luminous/massive compared to the TFR, whereas a plus sign indicates that it is super-luminous/massive.

^b We have included a -0.15 dex correction to adjust mass-to-light ratios to the Kroupa IMF based upon Geha et al. (2006). The authors indicate a scatter of ~ 0.4 – 0.5 mag, 0.13 dex, and 0.1 dex for their luminous, stellar mass, and baryonic mass relations, respectively, yielding the range of scatters shown. They also determine galaxy stellar masses using four different passbands, yielding the range of parameters displayed for mass-based TFRs. In each row, the upper values correspond to using mass-dependent dust corrections, whereas lower values correspond to using mass-independent corrections (see Table 2 of Bell & de Jong, 2001).

^c We have included a -0.15 dex correction to adjust mass-to-light ratios to the Kroupa IMF based upon Geha et al. (2006).

^d $M_{\star+\text{HI}}$ denotes the sum of the stellar and neutral hydrogen gas masses, and we have used values from Table 5.2 to calculate the Milky Way value for this comparison.

^e The internal velocity, $S_{0.5}$, is calculated by $(0.5V_{\text{rot}}^2 + \sigma_V^2)^{-1/2}$, and combines the contribution of both rotational velocity and velocity dispersion, σ_V , to the dynamical support of a galaxy. To make this comparison, we have assumed that the Milky Way’s σ_V is 24 km s^{-1} based on the work of Kalberla & Kerp (2009).

^f Here, M_{bar} includes the contribution of molecular gas. To make this comparison, we have assumed a morphological type of $T = 4$ for the Milky Way (cf. Chapter 2) and calculated its baryonic mass according to Equation (3) of that paper and the subsequent discussion within it.

^g Results are quoted for the “Portinari-Kroupa” subsample.

^h Results are quoted for the full sample from their Table 1, which includes a strong overlap with the data from Stark et al. (2009).

MW properties appear to be in good overall agreement with TFRs measured in other studies as well, with consistencies that generically fall well below the 1σ threshold. It is important to note that comparisons to relations defined by other authors are relatively less guarded from systematic offsets, as they can differ either because they rely on quantities calculated differently from those used here or because they employ systematically different samples (see Bradford et al., 2016 for a thorough investigation of these effects). Despite these variations, the MW is broadly consistent with the relation, and can fall above or below it depending on the study (denoted by the $+/-$ in the final column of Table 5.2).

5.4 INVESTIGATING 3-DIMENSIONAL LVR RELATIONS

As mentioned above, measures of galaxy size, or radius (R), also obey scaling relations with L and V_{rot} . The distribution of starlight from a spiral galaxy’s disk component can be fit well to first order by an exponentially declining profile (cf. Chapter 4). We denote the radius where light has dimmed by a factor of $1/e$ (or $\sim 37\%$) compared to the brightness at the center of the disk as the radial scale length (R_d), which serves as a standardized measure of size for spiral galaxies. We next compare the MW’s properties to scaling relations found in 3-dimensional luminosity-velocity-radius (LVR) parameter spaces.

5.4.1 Methods

To investigate scaling relations that include galaxy size, we now add a third axis, corresponding to disk scale length measurements, to each of the seven TFR diagrams investigated above. In each 3D parameter space, we perform principal component analysis (PCA; Jolliffe, 2002) on the extragalactic data to determine the best-fit LVR relation using the `numpy.linalg.svd` Python routine. We use this function to factor the LVR data in matrix form via singular value decomposition in order to determine three orthonormal eigenvectors, or principal components. The first principal component (PC1) indicates the direction in LVR space for which the data displays maximal variance. The second principal component (PC2) indicates the direction of next largest variance that is perpendicular to PC1, and the third principal component (PC3) is the direction orthogonal to both the PC1 and PC2. We define each best-fit LVR relation as the line parallel to PC1 that passes through the mean position of the data. Next, in the PC2-PC3 plane (i.e., the plane orthogonal to the PC1), we determine the 68% and 95% scatter about the relation by finding the most compact elliptical contours that envelope those percentages of the data. Figure 5.2 shows this analysis for the particular case of using 0M_i for luminosity, where we show each principal component in LVR space and also show the data projected onto each of the coordinate planes in PCA space. We subtract off the mean and renormalize the data into units of the standard deviation along each of the LVR axes in order to produce the PCA-plane projections.

To quantitatively assess the MW’s consistency with each LVR relation, we perform a series of Monte Carlo simulations where we randomly generate MW data points by drawing values from the probability distribution functions (PDFs) for Galactic properties listed in Table 5.2; simultaneously we bootstrap resample from our spiral galaxy data. For each realization, this involves the following:

1. Generate a MW data point by randomly drawing values for $\log L$, $\log V_{\text{rot}}$, and $\log R_{\text{d}}$ independently of each other from the PDFs described in Table 5.2;
2. Randomly draw galaxies from our extragalactic sample, each with equal probability and with repeats allowed, until the original sample size is achieved;
3. Perform a new PCA on this bootstrapped sample;
4. Measure the distance of all data points from the PC1 by calculating their elliptical radii from the origin in the PC2-PC3 plane by $[(d_{\text{PC2}}/\sigma_{\text{PC2}})^2 + (d_{\text{PC3}}/\sigma_{\text{PC3}})^2]^{1/2}$; and,
5. Finally, calculate the fraction of objects that lie inside of the ellipse passing through the MW data point, which we denote as $f_{<\text{MW}}$.

We perform this analysis 10^4 times, resulting in a distribution of $f_{<\text{MW}}$ values that incorporates all uncertainties in MW properties and all underlying uncertainties in fitting the LVR relation. For each relation that we investigate, we list in Table 5.4.2 the mean location ($\bar{\mu}$) of the data, the standard deviation ($\bar{\sigma}$) along each LVR axis, the PC1 eigenvector, and $f_{<\text{MW}}$.

Lastly, independent of the PCA described above, we also investigate the disk scale length that the LVR data would predict for a galaxy of the MW’s luminosity and rotational velocity. Here, we perform multivariate linear regression on the extragalactic data, modeling $\log R_{\text{d}}$ as a function of the predictor variables $\log L$ and $\log V_{\text{rot}}$. More explicitly, we can write

$$\log R_{\text{d}} = \alpha \log L + \beta \log V_{\text{rot}} + \gamma + \epsilon, \quad (5.1)$$

where α , β , and γ are the fitted coefficients and ϵ reflects the residual between a given $\log R_{\text{d}}$ value and the prediction from that galaxy’s $\log L$ and $\log V_{\text{rot}}$. By inspecting a normal probability plot for ϵ using the `scipy.stats.probplot` Python routine, we find that the residual in all cases is well approximated by a Gaussian distribution. We then perform Monte

Carlo simulations where we randomly draw values independently from the MW probability distributions for $\log L$ and $\log V_{\text{rot}}$ listed in Table 5.2 and from the distribution of ϵ values; each set of values $(\log L, \log V_{\text{rot}}, \epsilon)$ is then combined with the best-fit coefficients in Equation (1) in order to build up a distribution of $\log R_{\text{d}}$ values. The median value and 68% confidence interval for R_{d} measured from each distribution is listed in the final column of Table 5.4.2. These correspond to the range of disk scale lengths that one would expect to obtain from an externally measured SDSS i -band image of a galaxy with the MW's L and V_{rot} .

One might be concerned that these predictions could be affected by attenuation bias; i.e., the reduction of the amplitude of measured regression coefficients from their underlying values due to errors in the predictor variables. We test for this by adding random Gaussian noise to the predictors, drawn from a normal distribution of mean 0 and standard deviation σ^* , where σ^* reflects the typical measurement error (see §4.1 of H12). We find that this produces a $<0.1\%$ shift in the predicted $\log R_{\text{d}}$, indicating that our results are robust to attenuation bias.

5.4.2 Results

Including all known sources of uncertainty, we find that the fraction of objects lying closer to the LVR relation than the MW datapoint is ~ 0.90 (with minor variations depending on the proxy used for L). Hence, our Galaxy lies just inside of the 95% confidence region boundary for the LVR relation, but well outside of the 68% confidence region. We illustrate the LVR analysis using i -band absolute magnitude in Figure 5.2. In all cases, we find that the offset of the MW data point is consistent with being entirely along the direction of the scale length axis. Considering only measurement errors, this constitutes $\sim 9.5\sigma$ evidence that the MW is unusually compact compared to typical spiral galaxies of its L and V_{rot} . However, $\sim 10\%$ of galaxies lie even further from the LVR relation; so the MW is clearly undersized, but not extraordinarily so.

From our exercise of turning this analysis around and performing a multivariate regression on our extragalactic sample, and in particular to predict R_{d} values from a galaxy's 0M_i and V_{rot} , we find that the expected scale length of the MW disk, as measured externally

from photometric techniques (such as in H12), would be $4.92_{-1.53}^{+1.82}$ kpc. This is nearly double the observed value that we have adopted here of $2.71_{-0.20}^{+0.22}$, and these estimates are inconsistent with each other at the $\sim 1.4\sigma$ confidence level (incorporating both MW errors and the observed scatter about the regression relation).

5.5 DISCUSSION

5.5.1 Comparison to Prior Investigations of the Milky Way’s Consistency with the TFR

Our finding that the MW’s properties are highly consistent with the TFR contrasts with prior investigations that labeled our Galaxy a $1\text{--}1.5\sigma$ outlier to the relation. It is important to note that all of these studies, including this one, adopted the same value of 220 km s^{-1} with a $\sim 10\%$ uncertainty for the MW’s V_{rot} . We conclude instead that the difference is a result of systematic differences in Galactic luminosity estimates arising primarily, if not entirely, from varying choices of Galactic parameters. Specifically, these prior studies adopted luminosity estimates derived from MW models that depend strongly on the assumed values of R_0 and R_d . It is a common practice in Galactic astronomy to adopt a fixed, consensus value for R_0 — typically 8 or 8.5 kpc with no uncertainties included — so that one can straightforwardly compare results between various MW models. This becomes less sensible, however, once one becomes interested in Galactic-to-extragalactic comparisons (as in this study), as any error in the assumed value of R_0 will become a source of systematic uncertainty.

For example, [Flynn et al. \(2006\)](#) analyzed data from the Hipparcos and Tycho stellar surveys, determining the local surface luminosity in the I -band to be $29.54 L_{\odot} \text{ pc}^{-2}$. They then extrapolated this to a global luminosity estimate using an exponential model of the disk by assuming $R_0 = 8 \text{ kpc}$ (with no uncertainty) and exploring values of R_d in the range of $2.5\text{--}5.0 \text{ kpc}$. After including a 10% correction for spiral arms and adopting a near-infrared bulge luminosity of $\sim 10^{10} L_{\odot}$ (ignoring any uncertainty), they find a global value of $M_I = -22.3 \pm 0.2$. Using the same value of V_{rot} for the MW that we have adopted

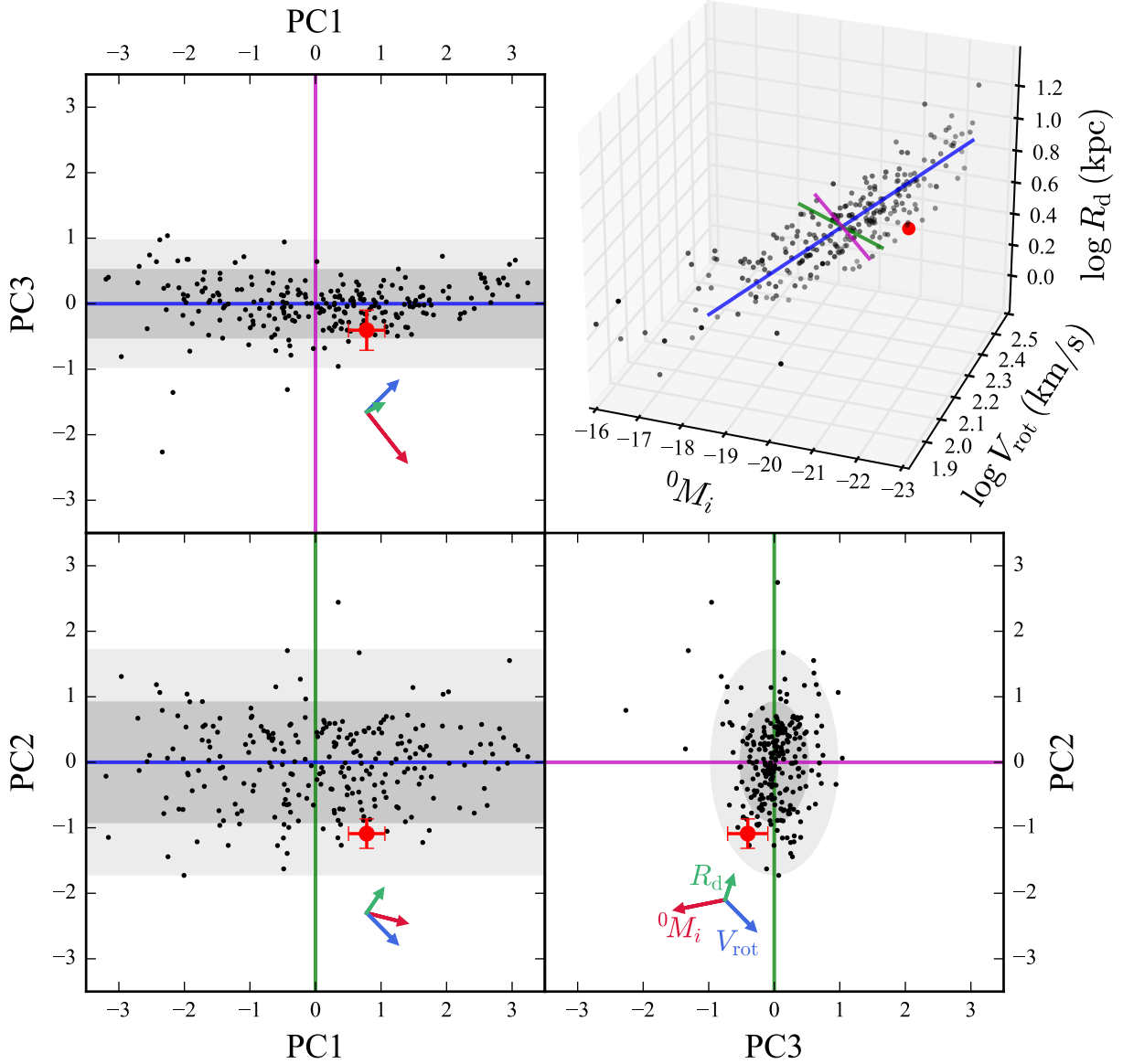


Figure 5.2: The distribution of our spiral galaxies from SDSS in luminosity-velocity-size (LVR) space (top right) and PCA space (all other panels). In the top right panel, we show the 3D distribution using rest-frame absolute i -band magnitude, 0M_i , log of the disk rotational velocity, $\log V_{\text{rot}}$, and log of the disk scale length, $\log L_d$. The first, second, and third principal components (PC1, PC2, and PC3; see §5.4.1) describing the (black) data are shown as blue, green, and magenta lines, respectively. We show the Milky Way datapoint as a red dot. The other three panels show the data projected onto each of the 2D planes in PCA space. Here, we plot the distance d measured from the mean position of the data, marked by the intersection of the orthogonal green, blue and magenta lines. The 68% and 95% confidence regions are shaded in dark and light gray, respectively. In red we overlay the Milky Way datapoint with error bars. The bottom right panel shows the projection of the data onto the plane that is perpendicular to the PC1; in this space we have determined that the Milky Way lies just inside of the 95% confidence region for our best-fit 3D scaling relation for spiral galaxies. See §5.4.1 for a more detailed analysis. Lastly, we illustrate that this discrepancy is predominantly due to the small size of the Galactic disk by showing the effect on the Milky Way datapoint due to a 3σ shift in 0M_i (red arrow), V_{rot} (blue arrow), and L_d (green arrow). Large changes in *both* 0M_i and V_{rot} would be required to reduce this tension, whereas increasing values of L_d would push it directly toward the LVR relation, and in fact landing on it when reaching ~ 5.25 kpc.

Table 5.3. Consistency of the Milky Way with LVR Relations

$\log L$ proxy (1)	Sample $\vec{\mu}$ (2)	Sample σ (3)	PC1 eigenvector (4)	$f_{<MW}$ (5)	Predicted MW R_d (6)
Spiral galaxies with $40^\circ < i < 75^\circ$ – Sample size: 285					
0M_u	(−17.963, 2.219, 0.547)	(1.106, 0.144, 0.205)	(−0.592, 0.583, 0.556)	$0.88^{+0.07}_{-0.13}$	$4.75^{+1.98}_{-1.51}$
0M_g	(−19.242, 2.219, 0.547)	(1.064, 0.144, 0.205)	(−0.610, 0.572, 0.548)	$0.90^{+0.06}_{-0.13}$	$4.97^{+1.92}_{-1.54}$
0M_r	(−19.825, 2.219, 0.547)	(1.139, 0.144, 0.205)	(−0.612, 0.575, 0.543)	$0.90^{+0.06}_{-0.11}$	$4.99^{+1.90}_{-1.53}$
0M_i	(−20.106, 2.219, 0.547)	(1.179, 0.144, 0.205)	(−0.613, 0.577, 0.540)	$0.89^{+0.07}_{-0.12}$	$4.92^{+1.82}_{-1.53}$
0M_z	(−20.299, 2.219, 0.547)	(1.314, 0.144, 0.205)	(−0.610, 0.586, 0.533)	$0.84^{+0.08}_{-0.12}$	$4.62^{+1.81}_{-1.49}$
$\log M_\star$	(10.262, 2.219, 0.547)	(0.634, 0.144, 0.205)	(0.612, 0.589, 0.528)	$0.82^{+0.07}_{-0.11}$	$4.53^{+1.67}_{-1.47}$
$\log M_{\text{bar}}$	(10.520, 2.219, 0.547)	(0.450, 0.144, 0.205)	(0.615, 0.570, 0.545)	$0.84^{+0.08}_{-0.13}$	$4.42^{+1.39}_{-1.25}$
Spiral galaxies with no inclination cut – Sample size: 422					
0M_u	(−17.732, 2.209, 0.565)	(1.154, 0.150, 0.214)	(−0.583, 0.584, 0.565)	$0.91^{+0.05}_{-0.10}$	$5.09^{+2.50}_{-1.65}$
0M_g	(−19.015, 2.209, 0.565)	(1.139, 0.150, 0.214)	(−0.599, 0.577, 0.555)	$0.91^{+0.06}_{-0.08}$	$5.24^{+2.37}_{-1.61}$
0M_r	(−19.611, 2.209, 0.565)	(1.210, 0.150, 0.214)	(−0.603, 0.578, 0.550)	$0.92^{+0.05}_{-0.09}$	$5.27^{+2.43}_{-1.59}$
0M_i	(−19.896, 2.209, 0.565)	(1.253, 0.150, 0.214)	(−0.604, 0.579, 0.547)	$0.91^{+0.05}_{-0.09}$	$5.23^{+2.27}_{-1.66}$
0M_z	(−20.120, 2.209, 0.565)	(1.357, 0.150, 0.214)	(−0.604, 0.583, 0.543)	$0.89^{+0.05}_{-0.09}$	$4.92^{+2.11}_{-1.49}$
$\log M_\star$	(10.212, 2.209, 0.565)	(0.654, 0.150, 0.214)	(0.607, 0.585, 0.537)	$0.86^{+0.06}_{-0.09}$	$4.85^{+1.97}_{-1.53}$
$\log M_{\text{bar}}$	(10.493, 2.209, 0.565)	(0.465, 0.150, 0.214)	(0.611, 0.567, 0.552)	$0.89^{+0.06}_{-0.09}$	$4.68^{+1.61}_{-1.25}$

Note. — Column (1) shows the proxy used for $\log L$ that is combined with $\log V_{\text{rot}}$ and $\log R_d$ to construct each LVR relation. Values in Columns (2)(4) are measured from our nominal spiral galaxy sample. Values in Column (5) are produced from PCA using the Monte Carlo techniques described in §5.4.1. These values reflect the 16th, 50th, and 84th percentiles of the resulting distribution of $f_{<MW}$; i.e., the fraction of the bootstrapped sample closer to its first principal component than the current realization of the Milky Way datapoint. Values in Column (6) represent the $\log R_d$ predicted for the Milky Way in units of kpc based on its L and V_{rot} , as described in §5.4.1.

for this study, they then found that our Galaxy is under-luminous by $\sim 1\sigma$ with respect to the I -band TFR defined by external spirals from Dale et al. (1999, though see Bovy & Rix, 2013 for an update). We find that if the Flynn et al. (2006) estimates were to instead utilize the same values of R_0 and R_d as we have employed for this study, they would yield $M_I = -22.73 \pm 0.25$, which is in excellent agreement with our slightly dimmer estimate of ${}^0M_I - 5 \log(h/0.7) = -22.61_{-0.39}^{+0.36}$ from Chapter 3. Consequentially, the MW would appear only ~ 0.05 mag dimmer than the I -band TFR from Dale et al. (1999) and would be consistent with it at the 0.1σ level.

Similarly, Hammer et al. (2007) used a K -band absolute magnitude estimate of -22.15 (converted to the AB system) for the MW from Drimmel & Spergel (2001), based on an exponential disk model with $R_0 = 8$ kpc (with no uncertainty) and $R_d = 2.26 \pm 0.08$ kpc, as well as the same value of Galactic V_{rot} adopted here, to find that our Galaxy is again $\sim 1\sigma$ under-luminous with respect to the K -band TFR defined by combining three different local galaxy samples. Unfortunately, the MW model of Drimmel & Spergel (2001) is complex, with 19 free parameters in total, making it difficult to straightforwardly scale to different choices of Galactic parameters. However, if we use the standard exponential model in order to approximate a first-order correction, we find that translating to the values of R_0 and R_d that we have adopted corresponds to an increase of approximately -0.3 mag for M_K , which would leave the MW 0.3 ± 0.5 mag dimmer than the TFR, and hence consistent with it at the 0.6σ level.

On the other hand, Malhotra et al. (1996) adopted $R_0 = 8.5$ kpc and the same V_{rot} employed here to derive $M_K = -24.06$ for the MW using a model similar to that of Drimmel & Spergel (2001). This indicated our Galaxy to be $\sim 1\sigma$ *over*-luminous with respect to the K -band TFR relation that they find for five nearby well-measured galaxies with Cepheid-based distances. Again corrections are difficult to make and the sample size for this TFR is small, but reducing the value of R_0 to match current data and incorporating the associated uncertainties would yield a dimmer M_K value and eliminate much of this tension, just as in the other cases.

A related analysis with broadly similar conclusions was recently published in McGaugh (2016). These authors utilized a novel approach to determining Galactic properties: they

iteratively adapted mass models of the MW by hand until they produce a terminal velocity curve that by-eye matches HI and CO observations taken in the first and fourth quadrant of the Galaxy, with a particular focus on reproducing the “bumps and wiggles” in that data. The authors suggest that this should account for substructure (e.g., spiral arm) features in the stellar surface density that would be unaccounted for by assuming a smooth exponential profile (cf. [Sancisi, 2004](#)). They explore six MW models in total, corresponding to a range of parameter values, specifically: $M_{\star} = 5\text{--}6 \times 10^{10} M_{\odot}$, $V_{\text{rot}} = 222\text{--}233 \text{ km s}^{-1}$, and $R_{\text{d}} = 2.0\text{--}2.9 \text{ kpc}$; all of these values assume $R_0 = 8 \text{ kpc}$ (with no uncertainty) and the authors claim that varying this assumption would affect their results, particularly V_{rot} and M_{\star} estimates, in a non-straightforward way. Nevertheless, these values are all in excellent agreement with the ones we have used in this study. They also adopt a total gas mass (atomic + molecular, corrected for He and metals) of $1.18 \times 10^{10} M_{\odot}$ (with no uncertainty ascribed to this value) which they add to M_{\star} to yield $M_{\text{bar}} = 6.18\text{--}7.18 \times 10^{10} M_{\odot}$. Finally, they compare their MW results to extragalactic data (a subset of which is used in this study), assessing qualitatively that the MW appears normal with respect to the baryonic TFR, but is somewhat compact for its mass. While there are significant differences between the assumptions and methodologies underlying the Galactic versus extragalactic data that are compared within [McGaugh \(2016\)](#) — differences that we have sought to minimize in this work — the results from [McGaugh \(2016\)](#) nevertheless broadly agree with the conclusions presented here.

5.5.2 The Emergent Picture of a “Too-Small” Milky Way Galaxy

As we have detailed in this paper, comparing measurements of the MW’s luminosity/mass, rotational velocity, and disk scale length to both Tully-Fisher and LVR relations for other spiral galaxies indicates that our Galaxy is approximately two times smaller (more compact) than is typical for its L and V_{rot} . This is potentially valuable knowledge for determining what evolutionary histories are possible for our Galaxy, especially as simulations of disk galaxies with an assortment of merger histories are growing in both number and mass resolution (see, e.g., [Martig et al., 2014](#); [Taylor et al., 2015a](#)). Therefore, it is important to know what potential concerns and additional support can be associated with our results, and we discuss

these here.

5.5.2.1 Potential Concerns The greatest potential area of concern is that we may not be making an apples-to-apples comparison of galaxy sizes. In general, one measures R_d for extragalactic objects by fitting an exponential model to the disk component of projected surface brightness profiles from imaging. A variety of ingredients may go into these measurements, such as sky subtraction and inclination correction (see, e.g., H12). Given that it is impossible to measure the integrated light profile of the MW as would be observed externally, photometric estimates of our Galaxy’s R_d have primarily come from analyzing star counts along various lines-of-sight through the disk (see Chapter 4 for a review of recent measurements). This requires optimizing a model of the stellar density profile to match observations, requiring assumptions about both stars initial mass or luminosity function and the effects of dust extinction. While we have ensured that the same basic assumptions about stellar disk structure have been used in both the Galactic and extragalactic estimates of R_d utilized in this study, there remain distinct differences in both the nature of the observational data and the analysis techniques used for each. These serve as potential sources of systematic error in our comparisons.

However, as described in Chapter 4 there are a number of reasons to have confidence in the robustness of the Galactic R_d value used here. First and foremost, a wide array of mass models for the MW have been developed based upon dynamical (velocity) measurements, which yield estimates of R_d that are independent of star count data. These dynamical estimates all fall in the range of $\sim 2\text{--}3$ kpc, matching well with our estimates of $2.71_{-0.20}^{+0.22}$ kpc and $2.51_{-0.14}^{+0.15}$ kpc based upon visible or IR light, respectively. Furthermore, the observed difference between the visible and IR scale length of the MW is similar to that observed for extragalactic objects. Based on these facts, it seems unlikely that the MW scale length is different from that measured for typical spirals of the same L and V_{rot} due to a catastrophic error in the Galactic R_d measurements.

We could instead consider the possibility that our estimate of the MW scale length is correct and instead the value for the Galactic luminosity/mass or rotational velocity is in error. To address this, we have investigated the magnitude of shifts in both L and V_{rot} that

are required to push the MW data point on a trajectory toward the LVR relation in PCA space. We find that a $\sim 6\sigma$ increase in 0M_i in combination with a $\sim 6\sigma$ decrease in V_{rot} could achieve this for the i -band luminosity relation, whereas a $\sim 9\sigma$ decrease in M_{\star} in combination with a $\sim 6\sigma$ decrease in V_{rot} accomplishes this for the stellar mass relation. Note that since the MW falls below the LVR relation almost entirely along the R_d axis, these shifts also correspond to moving the MW data point roughly along the TFR (and hence the MW would remain highly consistent with that relation). Therefore, it is possible that our Galaxy is truly typical in size for its mass, but this would imply that the current estimates of L and V_{rot} are both biased extraordinarily high in a conspiring way so as to offset each other in the TFR. Given that these estimates are made independently of each other and stem from differing methodologies, this scenario seems highly unlikely.

5.5.2.2 External Support We have found that our Galaxy’s intrinsic brightness and internal dynamical motions appear to be linked together just as the extragalactic TFR would predict, suggesting that the relationship between luminous and dark matter in the MW is similar to that in spiral galaxies in general. In contrast, the MW appears to be unusually compact (and therefore dense) compared to its peers. This may indicate that the MW has followed a distinct and perhaps rare evolutionary path. Interestingly, a variety of recent studies have come to strikingly similar conclusions by studying the properties of the MW’s coterie of satellite dwarf galaxies, which should also be strongly linked to its dark matter halo and formation history.

The most well-known example of this has been coined “the missing satellites problem”, which signifies the stark contrast between the number of dwarf galaxies (DGs) observationally found in orbit about the MW and the number of dark matter subhaloes (which are expected to host such DGs) that simulations of the Universe with a Λ CDM cosmology predict for MW-mass galaxies. This problem has persisted since the early 1990s and has been confirmed by many authors (see, e.g., [Kauffmann et al., 1993](#); [Klypin et al., 1999](#); [Moore et al., 1999](#); [Kravtsov, 2010](#)), and despite a recent influx of ultra-faint DGs discoveries from studying survey data (e.g., [Willman, 2010](#); [Laevens et al., 2015](#); [Drlica-Wagner et al., 2015](#)), the fact remains that DGs with $L > 10^6 L_{\odot}$ are ~ 10 times rarer than expected ([Bullock, 2010](#)).

It also appears that DGs are more compactly distributed around the MW than expected. For example, [Yniguez et al. \(2014\)](#) compared spherically averaged radial number counts for $> 10^5 L_{\odot}$ DGs within 400 kpc of the MW and its comparably massive neighbor, Andromeda (or M31). They found that MW satellites are much more centrally concentrated than M31’s, while also finding that the radial distribution of M31 satellites matches well with predictions from Λ CDM cosmological simulations of Local Group-like (i.e., MW+M31) pairs.

Finally, the MW also seems to be unusual in that it has two $\sim 10^9 L_{\odot}$ DGs located within ~ 60 kpc of it, namely the Small and Large Magellanic Clouds. [Liu et al. \(2011\)](#) found that only 3.5% of MW-mass galaxies in the local Universe fulfill this criterion (see also [Busha et al., 2011b](#)). Additionally, [Busha et al. \(2011a\)](#) investigated the properties of both “mass analogs” and “satellite analogs” of the MW found in the Bolshoi cosmological simulation data. This analysis revealed that having not only a MW-like mass but also two Magellanic Cloud-like subhalos associated with them corresponded to host halos having a $\sim 1\sigma$ higher concentration parameter (i.e., the ratio of the virial radius to the scale radius) and a 60% larger density of DM within 8 kpc ($\approx R_0$). Unfortunately, the Bolshoi simulations do not incorporate any luminous matter, so we cannot directly connect this to the distribution of stars. State-of-the-art simulations are now becoming available, however, that model both stars and gas within their parent dark matter halos, and with improving mass resolution (e.g., [Kuhlen et al., 2009](#); [Vogelsberger et al., 2014](#); [Schaye et al., 2015](#); [Wetzel et al., 2016](#)). With more and more realistic simulations of MW-like galaxies it should be feasible to investigate whether the anomalies in the MW’s scale length and satellite population might be linked, which in turn may improve our understanding of the formation history of our Galaxy.

5.6 SUMMARY AND CONCLUSIONS

Overall, our results provide a significant improvement in our understanding of how the MW fits in extragalactic contexts. First and foremost, with consistently normalized Galactic and extragalactic data, we find excellent agreement of MW properties with TFRs measured for other spiral galaxies, in contrast to prior investigations, which deemed our Galaxy a $1\text{--}1.5\sigma$

outlier to the relation. These tensions can be almost entirely explained by systematic errors in past work, particularly the values assumed for the distance of the Sun from the Galactic center (R_0) and for the R_d of the MW, which both affect luminosity estimates. The Galactic luminosity estimates used here are based upon updated knowledge of these structural parameters and incorporate all associated uncertainties. This overall conclusion holds up when comparing our MW estimates to TFRs found by other authors, where systematic differences between Galactic and extragalactic measurements are relatively more worrisome; nonetheless, the MW falls sometimes above or below these relations, and is generically consistent with them at below with 1σ threshold. We can confidently deem the MW a typical galaxy in the context of the TFR, and hence it is a suitable laboratory for studying the driving mechanisms of the relation.

By extending this type of comparison to 3-dimensional LVR relations, we have also established strong evidence that our Galaxy appears overtly compact for its mass. The MW disk would need to be nearly twice as large as the measured value to be of typical size given our Galaxy’s L and V_{rot} . Furthermore, we find that $\sim 90\%$ of spiral galaxies lie closer to the LVR relation in 3D parameter space than does our Galaxy, characterizing it as a rather significant outlier in this context, though not extraordinarily so. Many simulations of galaxy formation have been tuned to yield MW-like scale lengths on average for galaxies that resemble the MW in other respects (e.g., [Governato et al., 2008](#); [Bonoli et al., 2015](#)); however, the implicit assumption made that the MW is typical in its disk properties clearly fails. This broadly matches suggestions that the MW may be “too small” based upon its satellite population. As cosmological simulations and theoretical machinery continue to improve, the results from this study may ultimately provide strong constraints on how our Galaxy came to be.

6.0 DISSERTATION CONCLUSION

In this dissertation I have focused on applying modern statistical tools to better understand many global characteristics the Milky Way, and hence develop a more comprehensive picture of the Galaxy that we live in. In turn, this enabled me to accurately examine how our Galaxy fits in to a variety of extragalactic contexts, which until now has remained rather confused. This is an important step not only for Galactic astronomy, but also for bridging the gap between Galactic and extragalactic science. The Milky Way provides a unique laboratory for studying galaxies: it is the only place where we can study gas and dust, as well as large samples of individual stars in exquisite detail; however, the trade-off is that it is practically impossible to make measurements of our Galaxy in the same way that we would for any other. Overcoming this challenge is crucial for extending our knowledge of the Milky Way to galaxies in general, which is a necessary step toward ultimately deciphering how such systems have formed and evolved through cosmic history. Readers who are interested in a tabulation the finalized results produced in this dissertation should refer to Appendix B below. In the following I will give a short summary of each of the preceding chapters and then conclude with ideas on how to further this work.

6.1 SUMMARY OF PREVIOUS CHAPTERS

In Chapter 2 I introduced a hierarchical Bayesian (HB) framework for statistical combining a set of estimates for a given Milky Way property into one aggregate result. This is advantageous because in several cases the literature is rich with such estimates, which employ a wide variety of independent observational datasets, but, as discussed in that chapter, are

typically prone to systematic errors. The HB framework is designed to account for this and has, in fact, been vetted in other scientific contexts as a powerful tool for extracting the consistent underlying signal from a sample of potentially flawed measurements. By incorporating parameters that characterize the consistency of the data, and then marginalizing over these parameters, the HB analysis provides robust estimates for Milky Way quantities with error estimates that we can have high confidence in. In this chapter, we first applied this machinery straightforwardly to estimates of the Galactic star formation rate (SFR, \dot{M}_\star). Next, we took on the more complex case of performing a HB meta-analysis of bulge+bar mass measurements while simultaneously combining this with a model of the disk in a self-consistent manner using Monte Carlo techniques in order to constrain the total stellar mass (M_\star) of the Galaxy. Ultimately, this study yielded updated and improved constraints on a wide array of Milky Way mass properties, incorporating many key sources of uncertainty that often have been neglected by prior studies, but also normalized to the same assumptions that are used for studying other galaxies to facilitate our comparisons to extragalactic objects in later chapters.

In Chapter 3 I demonstrated a new statistical method of determining the global photometric properties of the Milky Way — i.e., its integrated absolute magnitude and color index at visible wavelengths — to an unprecedented degree of accuracy, allowing our Galaxy to be compared directly to objects measured in extragalactic surveys. Capitalizing on the high-quality imaging and spectroscopy dataset from the Sloan Digital Sky Survey (SDSS), I exploited the inherent dependence of galaxies luminosities and colors on their total stellar mass and SFR by selecting a sample of *Milky Way analog galaxies* designed to reproduce the best Galactic M_\star and \dot{M}_\star measurements derived in Chapter 2. Making the Copernican assumption that the Milky Way is not extraordinary among galaxies of similar stellar mass and SFR, I then analyzed the photometric properties of this matched sample, constraining the characteristics of our Galaxy without suffering interference from interstellar dust. I explored a variety of potential systematic errors that could affect this method, and showed that they are subdominant to random uncertainties. This work yielded new determinations of absolute magnitudes, color indexes, and stellar mass-to-light ratios in both SDSS *ugriz* and Johnson-Cousins *UBVRI* passbands at both $z=0$ and $z=0.1$ rest frames; these are in

agreement with previous estimates but can have up $3\times$ lower errors. From comparison to SDSS galaxies, I showed that the Milky Way most likely resides in the green-valley region of the color-magnitude diagram and ranks as one of the brightest and reddest spiral galaxies in the local Universe. In terms of the observed luminosity function, the Milky Way appears consistent with being a L_* in all of the *ugriz* passbands.

In Chapter 4 I applied the HB meta-analysis technique to nearly 30 estimates of the exponential scale length (L_d) of the Galactic disk. This is a critical parameter for describing the global physical size of our Galaxy, important both for interpreting other Galactic measurements and helping us to understand how our Galaxy fits into extragalactic contexts. While L_d is among one of the most studied characteristics of our Galaxy, current estimates span a wide range of values ($\sim 1\text{--}6$ kpc) and often are statistically incompatible with one another — a strong indication that some must be contaminated by systematic or underestimated errors. Interestingly, in this application it appeared that different ways of modeling the inclusion of erroneous measurements in our dataset were equally favored by the Bayesian evidence, yet yielded appreciably different marginalized posteriors for L_d . To hand this situation we introduced a Bayesian model averaging technique to determine an overall posterior result that incorporated any model-selection uncertainty. By analyzing different subsets of the data, I determined photometric scale lengths for visible, IR, and visible+IR starlight. These matched well not only with dynamically-determined estimates of L_d for the Milky Way, but also with ratios between visible and IR scale lengths measured for other spiral galaxies. Lastly, to match as closely as possible what is done for extragalactic objects, we used the IR photometric L_d estimate to produce an updated new model of the stellar disk, which also newly accounts for variations in the local stellar surface density due to the Milky Way’s spiral arm structure. We then used this model to repeat the analyses and update the results for Milky Way mass properties in Chapter 2 and photometric properties in Chapter 3; these are the values listed in the tables provided in Appendix B.

Finally, in Chapter 5 I used several of the updated Milky Way estimates from Chapters 2–4 to investigate how our Galaxy measures up to spiral galaxy scaling relations. A key aspect of this comparison is that the possibility of any systematic offsets has been minimized by ensuring that all Milky Way estimates rest upon the same basic assumptions that are used to

determine extragalactic properties. I showed that, contrary to prior claims in the literature, our Galaxy unequivocally follows the same Tully-Fisher relations as other spiral galaxies, adopting any of a wide variety of proxies for luminosity. Next, I focused on comparing the Milky Way to 3-dimensional scaling relations in luminosity-velocity-size (LVR) space determined from principle component analysis. Here, I showed that $\sim 90\%$ of other spiral galaxies lie closer to the LVR relation than does the Milky Way, which in fact appears to be unusually compact by a factor of ~ 2 compared to other galaxies of similar luminosity and rotational velocity. Lastly, I discussed the potential concerns about this result, but also how it may correspond to peculiarities found when comparing Milky Way satellite galaxies to predictions from Λ CDM cosmological simulations.

6.2 FUTURE WORK

There are a number of ways that the work described in this dissertation may be expanded upon, particularly relating to the method of studying Milky Way analog galaxies. I have focused on selecting such a sample of objects based on their star formation rates and total stellar masses, given that these two properties correlate strongest with integrated optical luminosities and colors; however, incorporating other well constrained parameters of the Milky Way into this selection process could potentially lead to constraints tighter than those presented herein. For example, the results from Chapter 5 indicate that the Milky Way's disk scale length is atypical for its mass. Therefore, an interesting follow-up to this work would be to select Milky Way analogs based on their L_d in lieu of or in addition to their \dot{M}_* in combination with their M_* to match the best estimates of those properties for our Galaxy. Another option would be to investigate the effect of incorporating bulge-to-total ratio — a property that was tightly constrained in Chapter 2 — or morphological type into the analog galaxy selection. By imposing these extra criteria one may be able to select galaxies more representative of our own, but possibly at the cost of attaining a much smaller sample. In principle, as the sample of Milky Way analogs selected becomes fine-tuned to an increasingly number of Galactic properties one should be able to constrain other photometric

properties that cannot be directly measured, such as central surface brightness and global global Sérsic index, but are commonly measured for other galaxies. This would open the doors to examining our Galaxy in variety of new extragalactic contexts.

Another important extension of this work would be to investigate the multi-wavelength properties of our Galaxy by studying Milky Way analogs with UV-wavelength data from GALEX — enabling one to more accurately assess whether the Milky Way belongs in the green valley (cf. [Wyder et al., 2007](#)) — as well as utilize WISE near-IR data. In addition, employing the analog analysis method for our nearest Milky Way-like neighbor, M31, the Andromeda Galaxy, whose proximity and thus brightness can cause saturation effects in survey data, would also likely lead to improved estimates of its multi-wavelength properties.

One could also study Milky Way analog galaxies to determine the “duty cycle” of our Galaxy — i.e., the fraction of time that the Milky Way’s supermassive black hole is accreting material and visible. Here the idea would be to make a determination of the fraction of analog galaxies that display an active galactic nucleus (AGN) and relate this to the fraction of time that our Galaxy displays one. This should be feasible with existing publicly-available X-ray data or using SDSS emission line catalogs. Additionally, one could perform a similar type of analysis to assess the typicality of the Milky Way’s satellite population. Here one could answer the question: how often are Milky Way analogs accompanied by two or more satellites as large as the Small and Large Magellanic Clouds? Do these galaxies show different properties than those without large satellites? This also would be an extension of the work by [Liu et al. \(2011\)](#) which identified Milky Way analogs based on their luminosities, but other properties of those galaxies may be appreciable different from the Milky Way.

The sample of Milky Way analogs we have obtained for this work could also be used to explore other properties with new observations. For example, performing 21-cm spectral line follow-up measurements of the galaxies in our Milky Way analog sample would enable one to determine their neutral hydrogen (HI) masses. This would allow for a determination of the HI mass in the Galaxy, as it should be directly tied to measurements of M_{\star} and \dot{M}_{\star} . At the same time, this would enable one to estimate the Milky Way’s star formation efficiency (i.e., how efficiently Milky Way analogs are converting their neutral hydrogen into new stars). This may already be feasible using data from the GALEX-Arecibo-SDSS-Survey (GASS).

GASS is designed to study the evolution of galaxies through the \dot{M}_*/M_* vs. M_* plane by measuring the neutral hydrogen content of 10^3 massive galaxies, which uniformly sample the SDSS spectroscopic and GALEX imaging surveys.

Finally, an ancillary target program is now underway to provide integral-field unit observations for a subset of the Milky Way analog sample studied herein as a part of the SDSS-IV MaNGA survey (Bundy et al., 2015). This will provide spatial-resolved spectroscopy for each galaxy at visible wavelengths, and will ultimately yield two-dimensional maps of a myriad of their properties. This includes stellar velocity and velocity dispersion, mean stellar age and star formation history, stellar metallicity, element abundance ratio, stellar mass surface density, ionized gas velocity, ionized gas metallicity, star formation rate and dust extinction. Such an extensive dataset could be used to perform a broad range of science. For example, the metallicity, ionization state, and kinematics of ionized gas as well as the stellar metallicity gradient in the Milky Way analogs may be studied over their full extent, whereas in the Milky Way, such studies are generally limited by dust extinction to only the nearest portions of the disk. Kinematics of both stars and gas may be measured and compared without the distance ambiguities that affect Milky Way gas velocity measurements. Asymmetric drift velocities for the analogs may be compared to the measurements for the Milky Way, enabling consistency tests and checks on methodology. Spectral bulge/disk decompositions and resolved stellar population diagnostics will, amongst other things, enable assessment of how common pseudobulges vs. classical bulges are amongst Milky Way analogs; there are claims that the Galaxy lacks a classical bulge (e.g., Kormendy & Kennicutt, 2004), and we can assess how common that is in galaxies of similar star formation history using this sample. This sample in particular will be especially important for building upon the efforts describing in this work, and hence will provide a major advancement in understanding the characteristics of the Milky Way, how it came to be, and how it truly fits into the world of galaxies.

APPENDIX A

ALTERNATIVE MODELS OF THE GALACTIC DISK

If the exponential disk model used by [Bovy & Rix \(2013\)](#) is far from reality, the total mass estimates in Chapter 2 will, of course, be incorrect. The true global structure of the Galactic disk remains an active area of research, and the direct measurements available in the literature that probe the (luminosity and mass) distribution of its stars have generally been limited to the range of $3 \lesssim R \lesssim 9$ kpc (e.g., [Jurić et al., 2008](#); [Bovy & Rix, 2013](#)). Limiting the range of radii in this way mitigates the problem of needing to distinguish bulge/bar stars from disk stars where they overlap. These components may be separated with kinematical information, but that is available for few stars and is of course impossible for studies based on aggregate light (e.g., [Freudenreich, 1998](#); [Drimmel & Spergel, 2001](#)). Similarly, studies that investigate the inner stellar mass at $R \lesssim 3$ kpc, such as all of those in our Table 2.4, must account for the bulge+bar and disk components either by fitting for them simultaneously or subtracting off the contribution from stars in the inner disk based on the model that is assumed. We remind the reader that, as described in §2.4.3, we have attempted to renormalize all of the bulge+bar mass measurements in Table 2.4 to reflect uniform assumptions about the disk. Ultimately, all of this data is consistent with an exponential mass density profile, such as the one we have used for this study; in general, structural decompositions and model magnitude measurements for external galaxies also assume such a profile for disks.

In order to assess the impact which a non-exponential mass profile would have on the inferred total disk mass, we investigate the impact of allowing the mass profile to be described

by a Sérsic model (Sérsic, 1968) in the radial direction, rather than a pure exponential, which in the radial (but not azimuthal) direction is equivalent to a Sérsic profile with an index of $n = 1$. Sérsic indices from global fits to the light from star-forming galaxies in the Sloan Digital Sky Survey cluster around a value just above 1, with a tail to larger values whose strength increases to redder colors (Blanton et al., 2003a). This is consistent with a picture where disks are indeed exponential and larger Sérsic indices are obtained in earlier-type spirals with greater bulge contributions (a de Vaucouleurs-profile bulge would have a Sérsic index of $n = 4$).

To investigate this further, we have employed the NYU Valued-Added Galaxy Catalog (VAGC; Blanton et al., 2005), which includes Sérsic radial profile fits to the r -band 2D images of a sample of galaxies from the Seventh Data Release (DR7; Abazajian et al., 2009) from the Sloan Digital Sky Survey (York et al., 2000). These fits provide the Sérsic index (n), scale radius (r_0), and the covariance matrix between n and r_0 . From Data Release 8 (DR8; Aihara et al., 2011) we have also obtained the spectroscopically measured redshift (z), the fraction of light from a de Vaucouleurs (bulge-like) profile when combined with a pure exponential ($n = 1$) profile that best fits the 2D image (`fracDeV`), the axis ratio (b/a) from the best-fit exponential profile to the 2D image, and the $g - r$ color from `model` magnitudes that are extinction- and K -corrected to $z = 0$ (which we denote ${}^0(g - r)$; Blanton & Roweis, 2007). We restrict to only those galaxies found in both the NYU-VAGC and DR7/8 datasets that are also part of the cleanly-measured volume-limited sample described in Chapter 3. Overall, this ensures that all galaxies lie in the range $0.03 < z < 0.09$ and have cleanly measured images. From this sample we then reduce to only those that meet the following criteria: ${}^0(g - r) < 0.5$, $\sigma(n) < 0.25$, $\sigma(r_0) < 0.25$, `fracDeV` < 0.1 , and $b/a > 0.7$. This yields a set of 5,533 star-forming galaxies with minimal bulge-like components that appear \sim face-on and that have well-measured radial Sérsic profile fits. We expect that the Sérsic indices for this sample can be used to broadly constrain the plausible values for the Galactic disk.

We find the median of this distribution to be 1.08 and the 1σ range to be $[0.9, 1.3]$. Given that this sample still includes objects with a nonzero bulge mass (even a small de Vaucouleurs bulge would increase the combined Sérsic index), values of n near but larger

than 1 can be easily explained by bulge contributions to the light. Apparent values of n below 1 are predicted to be observed for intrinsically pure exponential disks due to projection effects and dust absorption (see [Pastrav et al., 2013a,b](#), and references therein). Furthermore, one expects substantial scatter when fitting Sérsic models to objects with visible substructure (e.g., spiral arms). As a result, the Sérsic index distributions of disk-dominated galaxies in SDSS appear to be highly consistent with a scenario where the effective Sérsic index for disks, if measured with no bulge contribution, would in fact be $n = 1$ (i.e., exponential). We therefore do not find any compelling evidence that would cause us to discard the assumption that the Milky Way disk is exponential so that a more complicated model is needed.

Although we have not found any compelling evidence that the exponential disk assumption should be discarded, in order to assess what the impact of non-exponential profiles could be on our results, we have explored the effect that varying the Sérsic index has on the distribution of stellar mass in the Milky Way compared to a pure exponential ($n = 1$) profile, while keeping fixed the mean values of the disk parameters listed in [Table 2.3](#). For fixed disk parameters, decreasing values of n increasingly add more stellar mass towards the center of the Galaxy, while increasing values of n remove it. For instance, decreasing from $n = 1$ to 0.9 effectively \sim doubles Σ_* at the the Galactic center as well as the total disk mass at $R < 3$ kpc (from $1.97 \times 10^{10} M_\odot$ to $3.74 \times 10^{10} M_\odot$), which would imply that the disk is the dominant component over the bulge at all radii. The possibility that the disk may be described by a radial Sérsic index that is non-negligibly below 1 can therefore be discarded, as such models would be in strong tension with direct measurements of the Galactic rotation curve at these inner radii, as well as the mass measurements of the bulge we use in this study.

In contrast, we find that the mass of the disk between $R = 3$ kpc (roughly where the bulge truncates) and $R = 25$ kpc (well beyond the likely truncation radius of a Sérsic-model disk) is rather stable for $n \geq 1$; increasing n anywhere from 1 up to 1.5 yields changes that are always $\lesssim 5 \times 10^9 M_\odot$, which is modest compared to the overall uncertainties in the disk mass estimate we present in [§2.4.5](#). For changes at $R < 3$ kpc, disk mass and bulge/bar mass are traded off against each other (due to our definition of the central mass), so total masses are minimally affected. Of course, given that we have renormalized all of the bulge+bar

mass measurements in Table 2.4 to reflect an exponential ($n = 1$) disk, it would not be consistent to combine our HB bulge+bar mass result with a generalized Sérsic model of the disk. Hence, the effects we have explored here only constitute a first-order correction; doing better would require determining how a wide variety of historical bulge mass measurements would change if a very different disk model were used in fitting, which goes far beyond the scope or purpose of this study. We note that, since our definition of the bulge/bar mass is the additional mass in excess of an extrapolated exponential disk, even if the disk equivalent n were in fact less than 1, we would have included that mass in our bulge component, so our total mass would be minimally affected (with only the fraction of that mass assigned to the bulge and disk changing).

We note that the ultimate goal of this study is to produce measurements of the mass of the Milky Way that may be directly compared to those for other galaxies, particularly the mass determinations from the MPA-JHU SDSS catalog. The photometry in that catalog is based on model fits to galaxies that assume de Vaucouleurs bulges and pure exponential disks; if a very different model were used for determining the Milky Way mass, it is unlikely the results would be directly comparable. We also note that studies of the Galactic disk find that its vertical structure is well described by an exponential distribution with roughly constant scale height (e.g., Jurić et al., 2008; Bovy & Rix, 2013), inconsistent with a Sérsic model. Given all this, we consider an exponential mass profile, rather than a generalized Sérsic profile, the best option for modeling the Galactic disk. Should this assumption prove incorrect in the future (e.g., based on additional tests that will be provided by *Gaia* (Gilmore et al., 2012) or APOGEE-2 (Sobeck et al., 2014) measurements), nonetheless we have found that changing the disk model within reasonable bounds should have negligible impact on our total stellar mass estimates.

APPENDIX B

UPDATED ESTIMATES OF MILKY WAY PROPERTIES

The following tables provide a comprehensive summary of the Milky Way properties derived in Chapter 4, as well as those derived in Chapters 2 and 3 after updating them to the model of the stellar disk from §4.5.3, which utilizes our estimate for the IR photometric disk scale length and accounts for local density variations due to spiral structure.

Table B1. Updated Structural Properties of the Milky Way

Parameter	Optimal Value $\pm 1\sigma$	Units	Source
A	0.20 ± 0.10		Chapter 4
R_0	8.33 ± 0.35	kpc	Gillessen et al. (2009)
L_d	$0.12(R_0 - 8.33 \text{ kpc}) + 2.51^{+0.15}_{-0.13}$	kpc	Chapter 4
$\Sigma_\star(R_0, \phi_0)$	34.75 ± 4.30	$M_\odot \text{ pc}^{-2}$	Chapter 2
C	$1.25^{+0.29}_{-0.20}$		Chapter 4
$\bar{\Sigma}_\star(R_0)$	$43.44^{+11.54}_{-8.43}$	$M_\odot \text{ pc}^{-2}$	Chapter 4

Note. — A description of each parameter is as follows: A is the spiral amplitude of the Milky Way disk, R_0 is the radius of the Sun from the Galactic center, L_d is the photometric disk scale length measured from IR starlight, $\Sigma_\star(R_0, \phi_0)$ is the surface density of stellar material (main sequence stars plus stellar remnants, but not brown dwarfs) at the Sun’s location, and C is the ratio between the *mean* surface density at $R = R_0$, denoted by $\bar{\Sigma}_\star(R_0)$, and $\Sigma_\star(R_0, \phi_0)$. See §4.5.3 for discussion of these estimates.

Table B2. Updated Mass Properties of the Milky Way

Parameter	Optimal Value $\pm 1\sigma$	Units	Source
M_\star^B	$0.91 \pm 0.07 \times 10^{10}$	M_\odot	Chapter 2
M_\star^D	$4.76^{+1.51}_{-1.09} \times 10^{10}$	M_\odot	Chapter 4
M_\star	$5.67^{+1.53}_{-1.11} \times 10^{10}$	M_\odot	Chapter 4
B/T	0.16 ± 0.03		Chapter 4
\dot{M}_\star	1.65 ± 0.19	$M_\odot \text{ yr}^{-1}$	Chapter 2
\dot{M}_\star/M_\star	$2.89^{+0.80}_{-0.67} \times 10^{-11}$	yr^{-1}	Chapter 4

Note. — A description of each parameter is as follows: M_\star^B is the stellar mass of the bulge+bar, M_\star^D is the stellar mass of the disk, M_\star is the total stellar mass, B/T is the mass bulge-to-total ratio, \dot{M}_\star is the global star formation rate, and \dot{M}_\star/M_\star is the specific star formation rate. Note that the mass of the stellar halo is assumed negligible (it is much smaller than the uncertainties in M_\star^D ; e.g., Bell et al., 2008b) in this model, such that $M_\star \equiv M_\star^B + M_\star^D$. These values are found by reperforming the Monte Carlo HB analyses of Chapter 2 using the updated model of the Galactic disk from Chapter 4. The parameters of the updated disk model are listed in Table B1. See §4.5.3.3 for discussion of these estimates.

Table B3. Updated Photometric Properties for the Milky Way: Rest-frame $z=0$

Passbands

Absolute Magnitude	Optimal Value $\pm 1\sigma$ (mag)	Color Index	Optimal Value $\pm 1\sigma$ (mag)
${}^0M_u - 5 \log h$	$-19.15^{+0.55}_{-0.47}$	${}^0(u-r)$	$2.029^{+0.153}_{-0.150}$
${}^0M_g - 5 \log h$	$-20.33^{+0.42}_{-0.43}$	${}^0(u-g)$	$1.349^{+0.107}_{-0.092}$
${}^0M_r - 5 \log h$	$-20.97^{+0.37}_{-0.40}$	${}^0(g-r)$	$0.678^{+0.069}_{-0.057}$
${}^0M_i - 5 \log h$	$-21.24^{+0.37}_{-0.38}$	${}^0(r-i)$	$0.294^{+0.052}_{-0.046}$
${}^0M_z - 5 \log h$	$-21.53^{+0.36}_{-0.39}$	${}^0(i-z)$	$0.288^{+0.042}_{-0.041}$
${}^0M_U - 5 \log h$	$-20.00^{+0.59}_{-0.47}$	${}^0(U-V)$	$0.879^{+0.150}_{-0.125}$
${}^0M_B - 5 \log h$	$-20.05^{+0.41}_{-0.45}$	${}^0(U-B)$	$0.143^{+0.082}_{-0.071}$
${}^0M_V - 5 \log h$	$-20.71^{+0.39}_{-0.40}$	${}^0(B-V)$	$0.740^{+0.065}_{-0.056}$
${}^0M_R - 5 \log h$	$-21.23^{+0.39}_{-0.39}$	${}^0(V-R)$	$0.540^{+0.044}_{-0.041}$
${}^0M_I - 5 \log h$	$-21.81^{+0.38}_{-0.38}$	${}^0(R-I)$	$0.594^{+0.050}_{-0.049}$

Note. — These values are found by reperforming the analysis of Chapter 3 using the updated model the Galactic disk and hence total stellar mass derived in Chapter 4, which are tabulated in Tables B1 and B2. The changes are marginal compared to the uncertainties.

Table B4. Updated Photometric Properties for the Milky Way: Rest-frame $z=0.1$

Passbands

Absolute Magnitude	Optimal Value $\pm 1\sigma$ (mag)	Color Index	Optimal Value $\pm 1\sigma$ (mag)
${}^{0.1}M_u - 5 \log h$	$-18.84^{+0.56}_{-0.50}$	${}^{0.1}(u-r)$	$2.187^{+0.193}_{-0.164}$
${}^{0.1}M_g - 5 \log h$	$-20.05^{+0.46}_{-0.46}$	${}^{0.1}(u-g)$	$1.411^{+0.121}_{-0.113}$
${}^{0.1}M_r - 5 \log h$	$-20.75^{+0.38}_{-0.40}$	${}^{0.1}(g-r)$	$0.777^{+0.078}_{-0.065}$
${}^{0.1}M_i - 5 \log h$	$-21.13^{+0.36}_{-0.40}$	${}^{0.1}(r-i)$	$0.389^{+0.047}_{-0.042}$
${}^{0.1}M_z - 5 \log h$	$-21.38^{+0.35}_{-0.39}$	${}^{0.1}(i-z)$	$0.272^{+0.047}_{-0.048}$
${}^{0.1}M_U - 5 \log h$	$-20.08^{+0.54}_{-0.50}$	${}^{0.1}(U-V)$	$0.592^{+0.161}_{-0.136}$
${}^{0.1}M_B - 5 \log h$	$-19.93^{+0.46}_{-0.46}$	${}^{0.1}(U-B)$	$-0.021^{+0.097}_{-0.092}$
${}^{0.1}M_V - 5 \log h$	$-20.44^{+0.42}_{-0.41}$	${}^{0.1}(B-V)$	$0.620^{+0.073}_{-0.063}$
${}^{0.1}M_R - 5 \log h$	$-20.95^{+0.38}_{-0.39}$	${}^{0.1}(V-R)$	$0.516^{+0.047}_{-0.042}$
${}^{0.1}M_I - 5 \log h$	$-21.57^{+0.38}_{-0.38}$	${}^{0.1}(R-I)$	$0.634^{+0.050}_{-0.045}$

Note. — These values are found by reperforming the analysis of Chapter 3 using the updated model the Galactic disk and hence total stellar mass derived in Chapter 4. The changes are marginal compared to the uncertainties.

Table B5. Updated Global Stellar Mass-to-light Ratios for the Milky Way

Rest-frame	Υ_u^*	Υ_g^*	Υ_r^*	Υ_i^*	Υ_z^*
$z=0$	$1.84_{-0.76}^{+1.20}$	$1.93_{-0.64}^{+0.72}$	$1.64_{-0.51}^{+0.52}$	$1.41_{-0.42}^{+0.41}$	$1.10_{-0.32}^{+0.32}$
$z=0.1$	$1.71_{-0.79}^{+1.29}$	$1.87_{-0.63}^{+0.86}$	$1.82_{-0.57}^{+0.67}$	$1.51_{-0.44}^{+0.53}$	$1.26_{-0.37}^{+0.38}$
Rest-frame	Υ_U^*	Υ_B^*	Υ_V^*	Υ_R^*	Υ_I^*
$z=0$	$1.81_{-0.75}^{+1.12}$	$1.85_{-0.63}^{+0.80}$	$1.84_{-0.59}^{+0.66}$	$1.59_{-0.47}^{+0.56}$	$1.28_{-0.37}^{+0.44}$
$z=0.1$	$1.76_{-0.81}^{+1.26}$	$1.81_{-0.65}^{+0.84}$	$1.92_{-0.60}^{+0.84}$	$1.72_{-0.53}^{+0.60}$	$1.41_{-0.41}^{+0.45}$

Note. — All values are expressed in units of M_\odot/L_\odot and are found by reperforming the analysis of Chapter 3 using the updated model the Galactic disk and hence total stellar mass derived in Chapter 4. The changes are marginal compared to the uncertainties.

BIBLIOGRAPHY

- Abazajian, K. N., Adelman-McCarthy, J. K., Agüeros, M. A., et al. 2009, *ApJS*, 182, 543
- Aihara, H., Allende Prieto, C., An, D., et al. 2011, *ApJS*, 193, 29
- Akaike, H. 1974, *IEEE Transactions on Automatic Control*, 19, 716
- Allende Prieto, C., Majewski, S. R., Schiavon, R., et al. 2008, *Astronomische Nachrichten*, 329, 1018
- Amôres, E. B., & Lépine, J. R. D. 2005, *AJ*, 130, 659
- Anders, F., Chiappini, C., Santiago, B. X., et al. 2014, *A&A*, 564, A115
- Avila-Reese, V., Zavala, J., Firmani, C., & Hernández-Toledo, H. M. 2008, *AJ*, 136, 1340
- Bahcall, J. N. 1986, *ARA&A*, 24, 577
- Bahcall, J. N., & Soneira, R. M. 1980, *ApJS*, 44, 73
- . 1984, *ApJS*, 55, 67
- Baldry, I. K., Balogh, M. L., Bower, R. G., et al. 2006, *MNRAS*, 373, 469
- Bell, E. F., & de Jong, R. S. 2001, *ApJ*, 550, 212
- Bell, E. F., Zucker, D. B., Belokurov, V., et al. 2008a, *ApJ*, 680, 295
- . 2008b, *ApJ*, 680, 295
- Benjamin, R. A., Churchwell, E., Babler, B. L., et al. 2005, *ApJ*, 630, L149
- Bershady, M. A., Verheijen, M. A. W., Swaters, R. A., et al. 2010, *ApJ*, 716, 198
- Bienaymé, O. 1999, *A&A*, 341, 86
- Bilir, S., Karaali, S., Ak, S., Yaz, E., & Hamzaoglu, E. 2006, *New Astronomy*, 12, 234
- Binney, J., & Merrifield, M. 1998, *Galactic Astronomy* (Princeton, NJ: Princeton Univ. Press)

- Bissantz, N., Englmaier, P., Binney, J., & Gerhard, O. 1997, MNRAS, 289, 651
- Bissantz, N., & Gerhard, O. 2002, MNRAS, 330, 591
- Blanton, M. R., Eisenstein, D., Hogg, D. W., Schlegel, D. J., & Brinkmann, J. 2005, ApJ, 629, 143
- Blanton, M. R., & Roweis, S. 2007, AJ, 133, 734
- Blanton, M. R., Hogg, D. W., Bahcall, N. A., et al. 2003a, ApJ, 594, 186
- . 2003b, ApJ, 592, 819
- Blum, R. D. 1995, ApJ, 444, L89
- Bohlin, R. C., Savage, B. D., & Drake, J. F. 1978, ApJ, 224, 132
- Bok, B. J. 1937, The distribution of the stars in space (Chicago, IL: Univ. Chicago Press)
- Bonoli, S., Mayer, L., Kazantzidis, S., et al. 2015, ArXiv e-prints, arXiv:1508.07328
- Bottinelli, L., Gouguenheim, L., Paturel, G., & de Vaucouleurs, G. 1985, ApJS, 59, 293
- Bovy, J. 2013, private communication
- Bovy, J., & Rix, H.-W. 2013, ApJ, 779, 115
- Bovy, J., Rix, H.-W., & Hogg, D. W. 2012a, ApJ, 751, 131
- Bovy, J., Rix, H.-W., Liu, C., et al. 2012b, ApJ, 753, 148
- Bradford, J. D., Geha, M. C., & van den Bosch, F. C. 2016, ArXiv e-prints, arXiv:1602.02757
- Brinchmann, J., Charlot, S., White, S. D. M., et al. 2004, MNRAS, 351, 1151
- Bruzual, G., & Charlot, S. 2003, MNRAS, 344, 1000
- Bullock, J. S. 2010, ArXiv e-prints, arXiv:1009.4505
- Bullock, J. S., & Johnston, K. V. 2005, ApJ, 635, 931
- Bundy, K., Bershadsky, M. A., Law, D. R., et al. 2015, ApJ, 798, 7
- Burnham, K. P., & Anderson, D. R. 2002, Model selection and multimodel inference: a practical information-theoretic approach (Springer)
- Burningham, B., Cardoso, C. V., Smith, L., et al. 2013, MNRAS, 433, 457
- Burstein, D., & Heiles, C. 1982, AJ, 87, 1165
- Buser, R., Rong, J., & Karaali, S. 1998, A&A, 331, 934

Busha, M. T., Marshall, P. J., Wechsler, R. H., Klypin, A., & Primack, J. 2011a, *ApJ*, 743, 40

Busha, M. T., Wechsler, R. H., Behroozi, P. S., et al. 2011b, *ApJ*, 743, 117

Buta, R. J. 2011, ArXiv e-prints, arXiv:1102.0550

Buta, R. J. 2014, in *Astronomical Society of the Pacific Conference Series*, Vol. 480, *Structure and Dynamics of Disk Galaxies*, ed. M. S. Seigar & P. Treuthardt, 53

Buta, R. J., Sheth, K., Athanassoula, E., et al. 2015, *ApJS*, 217, 32

Calchi Novati, S., de Luca, F., Jetzer, P., Mancini, L., & Scarpetta, G. 2008, *A&A*, 480, 723

Cappellari, M., Scott, N., Alatalo, K., et al. 2013, *MNRAS*, 432, 1709

Cardelli, J. A., Clayton, G. C., & Mathis, J. S. 1989, *ApJ*, 345, 245

Chang, C.-K., Ko, C.-M., & Peng, T.-H. 2011, *ApJ*, 740, 34

Charlot, S., & Longhetti, M. 2001, *MNRAS*, 323, 887

Chatzopoulos, S., Fritz, T. K., Gerhard, O., et al. 2015, *MNRAS*, 447, 948

Chen, B., Figueras, F., Torra, J., et al. 1999, *A&A*, 352, 459

Cheng, J. Y., Rockosi, C. M., Morrison, H. L., et al. 2012, *ApJ*, 752, 51

Chomiuk, L., & Povich, M. S. 2011, *AJ*, 142, 197

Cole, S., Aragon-Salamanca, A., Frenk, C. S., Navarro, J. F., & Zepf, S. E. 1994, *MNRAS*, 271, 781

Cook, D. O., Dale, D. A., Johnson, B. D., et al. 2014, *MNRAS*, 445, 890

Corradi, R. L. M., Beckman, J. E., & Simonneau, E. 1996, *MNRAS*, 282, 1005

Cortese, L. 2012, *A&A*, 543, A132

Cortese, L., Fogarty, L. M. R., Ho, I.-T., et al. 2014, *ApJ*, 795, L37

Courteau, S., Dutton, A. A., van den Bosch, F. C., et al. 2007, *ApJ*, 671, 203

Courteau, S., & Rix, H.-W. 1999, *ApJ*, 513, 561

Cox, D. P., & Reynolds, R. J. 1987, *ARA&A*, 25, 303

Cruz, K. L., Reid, I. N., Kirkpatrick, J. D., et al. 2007, *AJ*, 133, 439

Dahlen, T., Mobasher, B., Faber, S. M., et al. 2013, *ApJ*, 775, 93

- Dale, D. A., Giovanelli, R., Haynes, M. P., Campusano, L. E., & Hardy, E. 1999, *AJ*, 118, 1489
- Dame, T. M. 1993a, in *American Institute of Physics Conference Series*, Vol. 278, *Back to the Galaxy*, ed. S. S. Holt & F. Verter, 267–278
- Dame, T. M. 1993b, in *Back to the Galaxy*, ed. S. S. Holt & F. Verter, Vol. 278 (New York: AIP), 267–278
- D’Antona, F., & Mazzitelli, I. 1997, *Mem. Soc. Astron. Italiana*, 68, 807
- Dawson, K. S., Schlegel, D. J., Ahn, C. P., et al. 2013, *AJ*, 145, 10
- Day-Jones, A. C., Marocco, F., Pinfield, D. J., et al. 2013, *MNRAS*, 430, 1171
- De Geyter, G., Baes, M., Camps, P., et al. 2014, *MNRAS*, 441, 869
- de Jong, R. S. 1996, *A&A*, 313, 377
- De Rijcke, S., Zeilinger, W. W., Hau, G. K. T., Prugniel, P., & Dejonghe, H. 2007, *ApJ*, 659, 1172
- de Vaucouleurs, G. 1959, *Handbuch der Physik*, 53, 311
- . 1970, *ApJ*, 159, 435
- de Vaucouleurs, G. 1977, in *Evolution of Galaxies and Stellar Populations*, ed. B. M. Tinsley & R. B. G. Larson, D. Campbell, 43
- . 1983, *ApJ*, 268, 451
- de Vaucouleurs, G., & Corwin, Jr., H. G. 1986, *ApJ*, 308, 487
- de Vaucouleurs, G., de Vaucouleurs, A., & Corwin, Jr., H. G. 1976, *Second Reference Catalogue of Bright Galaxies* (Austin, TX: Univ. Texas Press)
- de Vaucouleurs, G., de Vaucouleurs, A., Corwin, Jr., H. G., et al. 1991, *Third Reference Catalogue of Bright Galaxies* (Berlin: Springer)
- de Vaucouleurs, G., & Pence, W. D. 1978, *AJ*, 83, 1163 (dV&P)
- Dehnen, W., & Binney, J. 1998, *MNRAS*, 294, 429
- Djorgovski, S., & Davis, M. 1987, *ApJ*, 313, 59
- Do, T., Martinez, G. D., Yelda, S., et al. 2013, *ApJ*, 779, L6
- Dressler, A., Lynden-Bell, D., Burstein, D., et al. 1987, *ApJ*, 313, 42
- Drimmel, R., & Spergel, D. N. 2001, *ApJ*, 556, 181

- Drlica-Wagner, A., Bechtol, K., Rykoff, E. S., et al. 2015, *ApJ*, 813, 109
- Durand, S., Dejonghe, H., & Acker, A. 1996, *A&A*, 310, 97
- Dutton, A. A., van den Bosch, F. C., Dekel, A., & Courteau, S. 2007, *ApJ*, 654, 27
- Dutton, A. A., Conroy, C., van den Bosch, F. C., et al. 2011, *MNRAS*, 416, 322
- Dwek, E., Arendt, R. G., Hauser, M. G., et al. 1995, *ApJ*, 445, 716
- Efron, B. 1979, *The annals of Statistics*, 1
- Einasto, J. 1965, *Trudy Astrofizicheskogo Instituta Alma-Ata*, 5, 87
- Elmegreen, D. M., Elmegreen, B. G., Yau, A., et al. 2011, *ApJ*, 737, 32
- Faber, S. M., & Jackson, R. E. 1976, *ApJ*, 204, 668
- Faber, S. M., Willmer, C. N. A., Wolf, C., et al. 2007, *ApJ*, 665, 265
- Falcon, R. E., Winget, D. E., Montgomery, M. H., & Williams, K. A. 2010, *ApJ*, 712, 585
- Fall, S. M., & Efstathiou, G. 1980, *MNRAS*, 193, 189
- Fang, J. J., Faber, S. M., Salim, S., Graves, G. J., & Rich, R. M. 2012, *ApJ*, 761, 23
- Feast, M. 2000, *MNRAS*, 313, 596
- Fernández Lorenzo, M., Sulentic, J., Verdes-Montenegro, L., et al. 2012, *A&A*, 540, A47
- Flynn, C., Holmberg, J., Portinari, L., Fuchs, B., & Jahreiß, H. 2006, *MNRAS*, 372, 1149
- Freeman, K. C. 1970, *ApJ*, 160, 811
- Freeman, K. C. 1978, in *IAU Symposium, Vol. 77, Structure and Properties of Nearby Galaxies*, ed. E. M. Berkhuisen & R. Wielebinski (Dordrecht: Reidel), 3–10
- Freudenreich, H. T. 1998, *ApJ*, 492, 495
- Fuchs, B., Jahreiss, H., & Flynn, C. 1998, *A&A*, 339, 405
- Fukugita, M., Hogan, C. J., & Peebles, P. J. E. 1998, *ApJ*, 503, 518
- Fukugita, M., Shimasaku, K., & Ichikawa, T. 1995, *PASP*, 107, 945
- Fux, R., & Martinet, L. 1994, *A&A*, 287, L21
- Gadotti, D. A. 2009, *MNRAS*, 393, 1531
- Gallazzi, A., Charlot, S., Brinchmann, J., White, S. D. M., & Tremonti, C. A. 2005, *MNRAS*, 362, 41

- Geha, M., Blanton, M. R., Masjedi, M., & West, A. A. 2006, *ApJ*, 653, 240
- Gelman, A., Carlin, J., Stern, H., et al. 2013, *Bayesian Data Analysis*, Third Edition, Chapman & Hall/CRC Texts in Statistical Science (Taylor & Francis)
- Genzel, R., Eisenhauer, F., & Gillessen, S. 2010, *Reviews of Modern Physics*, 82, 3121
- Ghez, A. M., Salim, S., Weinberg, N. N., et al. 2008, *ApJ*, 689, 1044
- Gillessen, S., Eisenhauer, F., Trippe, S., et al. 2009, *ApJ*, 692, 1075
- Gilmore, G., & Reid, N. 1983, *MNRAS*, 202, 1025
- Gilmore, G., Randich, S., Asplund, M., et al. 2012, *The Messenger*, 147, 25
- Girardi, L., Groenewegen, M. A. T., Hatziminaoglou, E., & da Costa, L. 2005, *A&A*, 436, 895
- Gonçalves, T. S., Martin, D. C., Menéndez-Delmestre, K., Wyder, T. K., & Koekemoer, A. 2012, *ApJ*, 759, 67
- Governato, F., Mayer, L., & Brook, C. 2008, in *Astronomical Society of the Pacific Conference Series*, Vol. 396, *Formation and Evolution of Galaxy Disks*, ed. J. G. Funes & E. M. Corsini, 453
- Graham, A. W. 2013, *Elliptical and Disk Galaxy Structure and Modern Scaling Laws*, ed. T. D. Oswalt & W. C. Keel (Springer: Dordrecht), 91
- Graham, A. W., & Worley, C. C. 2008, *MNRAS*, 388, 1708
- Graves, G. 2012, private communication
- Green, G. M., Schlafly, E. F., Finkbeiner, D. P., et al. 2015, *ApJ*, 810, 25
- Grosbøl, P., Patsis, P. A., & Pompei, E. 2004, *A&A*, 423, 849
- Gurovich, S., Freeman, K., Jerjen, H., Staveley-Smith, L., & Puerari, I. 2010, *AJ*, 140, 663
- Hall, M., Courteau, S., Dutton, A. A., McDonald, M., & Zhu, Y. 2012, *MNRAS*, 425, 2741
- Hamadache, C., Le Guillou, L., Tisserand, P., et al. 2006, *A&A*, 454, 185
- Hammer, F., Puech, M., Chemin, L., Flores, H., & Lehnert, M. D. 2007, *ApJ*, 662, 322
- Han, C., & Gould, A. 1995, *ApJ*, 447, 53
- . 2003, *ApJ*, 592, 172
- Hayakawa, S., Matsumoto, T., Murakami, H., et al. 1981, *A&A*, 100, 116

- Henderson, A. P., Jackson, P. D., & Kerr, F. J. 1982, *ApJ*, 263, 116
- Herschel, S. W. 1785, *Philosophical Transactions of the Royal Society of London*, 75, 213
- Hessman, F. V. 2015, *A&A*, 579, A123
- Hodges, Jr., J. L., & Lehmann, E. L. 1963, *Ann. Math. Statist.*, 34, 598
- Hoeting, J. A., Madigan, D., Raftery, A. E., & Volinsky, C. T. 1999, *Statist. Sci.*, 14, 382
- Hogg, D. W., Baldry, I. K., Blanton, M. R., & Eisenstein, D. J. 2002, *ArXiv Astrophysics e-prints*, astro-ph/0210394
- Hogg, D. W., Bovy, J., & Lang, D. 2010, *ArXiv e-prints*, arXiv:1008.4686
- Holberg, J. B., Sion, E. M., Oswalt, T., et al. 2008, *AJ*, 135, 1225
- Hubble, E. 1929, *Proceedings of the National Academy of Science*, 15, 168
- Ilbert, O., Salvato, M., Le Floch, E., et al. 2010, *ApJ*, 709, 644
- Indebetouw, R., Mathis, J. S., Babler, B. L., et al. 2005, *ApJ*, 619, 931
- Jahreiß, H., & Wielen, R. 1997, in *ESA Special Publication, Vol. 402, Hipparcos - Venice '97*, ed. R. M. Bonnet, E. Høg, P. L. Bernacca, L. Emiliani, A. Blaauw, C. Turon, J. Kovalevsky, L. Lindegren, H. Hassan, M. Bouffard, B. Strim, D. Heger, M. A. C. Perryman, & L. Woltjer, 675–680
- Jin, S.-W., Gu, Q., Huang, S., Shi, Y., & Feng, L.-L. 2014, *ApJ*, 787, 63
- Jolliffe, I. 2002, *Principal component analysis* (New York: Springer Verlag)
- Jurić, M., Ivezić, Ž., Brooks, A., et al. 2008, *ApJ*, 673, 864
- Kalberla, P. M. W., Dedes, L., Kerp, J., & Haud, U. 2007, *A&A*, 469, 511
- Kalberla, P. M. W., & Kerp, J. 2009, *Annual Review of Astronomy & Astrophysics*, 47, 27
- Kapteyn, J. C. 1922, *ApJ*, 55, 302
- Kapteyn, J. C., & van Rhijn, P. J. 1920, *ApJ*, 52, 23
- Karaali, S., Bilir, S., Yaz, E., Hamzaoglu, E., & Buser, R. 2007, *Publications of the Astronomical Society of Australia*, 24, 208
- Kass, R. E., & Raftery, A. E. 1995, *Journal of the American Statistical Association*, 90, 773
- Kassin, S. A., Weiner, B. J., Faber, S. M., et al. 2007, *ApJ*, 660, L35
- Kauffmann, G., White, S. D. M., & Guiderdoni, B. 1993, *MNRAS*, 264, 201

Kauffmann, G., Heckman, T. M., White, S. D. M., et al. 2003, MNRAS, 341, 33

Kendall, S., Clarke, C., & Kennicutt, R. C. 2015, MNRAS, 446, 4155

Kennicutt, Jr., R. C. 1998a, ARA&A, 36, 189

—. 1998b, ApJ, 498, 541

Kent, S. M. 1992, ApJ, 387, 181

Kent, S. M., Dame, T. M., & Fazio, G. 1991, ApJ, 378, 131

Kerr, F. J., & Lynden-Bell, D. 1986, MNRAS, 221, 1023

Kirkpatrick, J. D., Gelino, C. R., Cushing, M. C., et al. 2012, ApJ, 753, 156

Klypin, A., Kravtsov, A. V., Valenzuela, O., & Prada, F. 1999, ApJ, 522, 82

Klypin, A., Zhao, H., & Somerville, R. S. 2002, ApJ, 573, 597

Knox, R. A., Hawkins, M. R. S., & Hambly, N. C. 1999, MNRAS, 306, 736

Kormendy, J. 1977, ApJ, 217, 406

Kormendy, J., & Kennicutt, Jr., R. C. 2004, ARA&A, 42, 603

Kravtsov, A. 2010, Advances in Astronomy, 2010, 8

Kreiken, E. A. 1950, Some Remarks on the Surface Brightness of the Stellar System, O.S.R. Publikation (The Organisation)

Kroupa, P., & Weidner, C. 2003, ApJ, 598, 1076

Kuhlen, M., Madau, P., & Silk, J. 2009, Science, 325, 970

Laevens, B. P. M., Martin, N. F., Bernard, E. J., et al. 2015, ApJ, 813, 44

Lallement, R., Vergely, J.-L., Valette, B., et al. 2014, A&A, 561, A91

Lang, D., & Hogg, D. W. 2012, AJ, 144, 46

Larsen, J. A. 1996, PhD thesis, Univ. of Minnesota

Larsen, J. A., & Humphreys, R. M. 2003, AJ, 125, 1958

Leauthaud, A., Tinker, J., Bundy, K., et al. 2012, ApJ, 744, 159

Leggett, S. K., Ruiz, M. T., & Bergeron, P. 1998, ApJ, 497, 294

Lépine, J. R. D., & Leroy, P. 2000, MNRAS, 313, 263

- Liszt, H. S. 1992, in *Astrophysics and Space Science Library*, Vol. 180, The Center, Bulge, and Disk of the Milky Way, ed. L. Blitz, 111–130
- Liu, C., Xue, X., Fang, M., et al. 2012, *ApJ*, 753, L24
- Liu, L., Gerke, B. F., Wechsler, R. H., Behroozi, P. S., & Busha, M. T. 2011, *ApJ*, 733, 62
- Loebman, S. R. 2013, PhD thesis, University of Washington
- López-Corredoira, M., Cabrera-Lavers, A., Garzón, F., & Hammersley, P. L. 2002, *A&A*, 394, 883
- López-Corredoira, M., Cabrera-Lavers, A., Mahoney, T. J., et al. 2007, *AJ*, 133, 154
- López-Corredoira, M., & Molgó, J. 2014, *A&A*, 567, A106
- Loredo, T. J. 2012a, ArXiv e-prints, arXiv:1208.3036
- . 2012b, ArXiv e-prints, arXiv:1208.3036
- MacArthur, L. A., Courteau, S., Bell, E., & Holtzman, J. A. 2004, *ApJS*, 152, 175
- Majewski, S. R. 2008, in *IAU Symposium*, Vol. 248, IAU Symposium, ed. W. J. Jin, I. Platais, & M. A. C. Perryman, 450–457
- Malhotra, S., Spergel, D. N., Rhoads, J. E., & Li, J. 1996, *ApJ*, 473, 687
- Maller, A. H., Berlind, A. A., Blanton, M. R., & Hogg, D. W. 2009, *ApJ*, 691, 394
- Mandel, K. S., Foley, R. J., & Kirshner, R. P. 2014, *ApJ*, 797, 75
- Mao, Q., Berlind, A. A., Holley-Bockelmann, K., et al. 2015, ArXiv e-prints, arXiv:1507.01593
- March, M. C., Karpenka, N. V., Feroz, F., & Hobson, M. P. 2014, *MNRAS*, 437, 3298
- Maronna, R., Martin, D., & Yohai, V. 2006, *Robust Statistics: Theory and Methods*, Wiley Series in Probability and Statistics (Wiley)
- Marshall, D. J., Robin, A. C., Reylé, C., Schultheis, M., & Picaud, S. 2006, *A&A*, 453, 635
- Martig, M., Minchev, I., & Flynn, C. 2014, *MNRAS*, 442, 2474
- Martinez, G. D. 2015, *MNRAS*, 451, 2524
- McGaugh, S. S. 2012, *AJ*, 143, 40
- . 2016, *ApJ*, 816, 42
- McKee, C. F., Parravano, A., & Hollenbach, D. J. 2015, ArXiv e-prints, arXiv:1509.05334

- McMillan, P. J. 2011, MNRAS, 414, 2446
- Mendez, A. J., Coil, A. L., Lotz, J., et al. 2011, ApJ, 736, 110
- Mendez, R. A., & van Altena, W. F. 1998, A&A, 330, 910
- Miyamoto, M., & Nagai, R. 1975, PASJ, 27, 533
- Mo, H. J., Mao, S., & White, S. D. M. 1998, MNRAS, 295, 319
- Montero-Dorta, A. D., & Prada, F. 2009, MNRAS, 399, 1106
- Moore, B., Ghigna, S., Governato, F., et al. 1999, ApJ, 524, L19
- Mutch, S. J., Croton, D. J., & Poole, G. B. 2011, ApJ, 736, 84 (M11)
- Newman, J. A., Zepf, S. E., Davis, M., et al. 1999, ApJ, 523, 506
- Ng, Y. K., Bertelli, G., Bressan, A., Chiosi, C., & Lub, J. 1995, A&A, 295, 655
- Noordermeer, E., & Verheijen, M. A. W. 2007, MNRAS, 381, 1463
- Ojha, D. K. 2001, MNRAS, 322, 426
- Ojha, D. K., Bienayme, O., Robin, A. C., Creze, M., & Mohan, V. 1996, A&A, 311, 456
- Oohama, N., Okamura, S., Fukugita, M., Yasuda, N., & Nakamura, O. 2009, ApJ, 705, 245
- Oort, J. H. 1938, Bull. Astron. Inst. Netherlands, 8, 233
- Ortiz, R., & Lépine, J. R. D. 1993, A&A, 279, 90
- Ostriker, J. P., Peebles, P. J. E., & Yahil, A. 1974, ApJ, 193, L1
- Oswalt, T. D., Smith, J. A., Wood, M. A., & Hintzen, P. 1996, Nature, 382, 692
- Pastrav, B. A., Popescu, C. C., Tuffs, R. J., & Sansom, A. E. 2013a, A&A, 553, A80
- . 2013b, A&A, 557, A137
- Peebles, P. J. E. 1980, The Large-Scale Structure of the Universe (Princeton, NJ: Princeton Univ. Press)
- . 1993, Principles of Physical Cosmology (Princeton, NJ: Princeton University Press)
- Peletier, R. F., Valentijn, E. A., Moorwood, A. F. M., & Freudling, W. 1994, A&AS, 108, 621
- Picaud, S., & Robin, A. C. 2004, A&A, 428, 891
- Piffl, T., Scannapieco, C., Binney, J., et al. 2014, A&A, 562, A91

Pizagno, J., Prada, F., Weinberg, D. H., et al. 2007, *AJ*, 134, 945

Polido, P., Jablonski, F., & Lépine, J. R. D. 2013, *ApJ*, 778, 32

Porcel, C., Garzon, F., Jimenez-Vicente, J., & Battaner, E. 1998, *A&A*, 330, 136

Press, W. H. 1997, in *Unsolved Problems in Astrophysics*, ed. J. N. Bahcall & J. P. Ostriker (Princeton, NJ: Princeton Univ. Press), 49–60

Quillen, A. C. 2002, *AJ*, 124, 924

Reach, W. T., Abergel, A., Boulanger, F., et al. 1996, *A&A*, 315, L381

Reid, M. J., Menten, K. M., Brunthaler, A., et al. 2014, *ApJ*, 783, 130

Rieke, G. H., & Lebofsky, M. J. 1985, *ApJ*, 288, 618

Rix, H.-W., & Bovy, J. 2013, *A&A Rev.*, 21, 61

Robin, A. C., Creze, M., & Mohan, V. 1992, *A&A*, 265, 32

Robin, A. C., Haywood, M., Creze, M., Ojha, D. K., & Bienayme, O. 1996, *A&A*, 305, 125

Robin, A. C., Marshall, D. J., Schultheis, M., & Reylé, C. 2012, *A&A*, 538, A106

Robin, A. C., Reylé, C., Derrière, S., & Picaud, S. 2003, *A&A*, 409, 523

Rubin, V. C., Ford, W. K. J., & Thonnard, N. 1980, *ApJ*, 238, 471

Rubin, V. C., Thonnard, N., & Ford, Jr., W. K. 1978, *ApJ*, 225, L107

Ruelas-Mayorga, R. A. 1991, *Revista Mexicana de Astronomía y Astrofísica*, 22, 27

Ruphy, S., Robin, A. C., Epchtein, N., et al. 1996, *A&A*, 313, L21

Sackett, P. D. 1997, *ApJ*, 483, 103

Salim, S., Rich, R. M., Charlot, S., et al. 2007, *ApJS*, 173, 267

Salim, S., Dickinson, M., Michael Rich, R., et al. 2009, *ApJ*, 700, 161

Sancisi, R. 2004, in *IAU Symposium, Vol. 220, Dark Matter in Galaxies*, ed. S. Ryder, D. Pisano, M. Walker, & K. Freeman, 233

Sato, M., Reid, M. J., Brunthaler, A., & Menten, K. M. 2010, *ApJ*, 720, 1055

Schawinski, K., Urry, C. M., Simmons, B. D., et al. 2014, *MNRAS*, 440, 889

Schaye, J., Crain, R. A., Bower, R. G., et al. 2015, *MNRAS*, 446, 521

Schechter, P. L. 1980, *AJ*, 85, 801

- Schlegel, D. J., Finkbeiner, D. P., & Davis, M. 1998, *ApJ*, 500, 525
- Schmidt-Kaler, T., & Schlosser, W. 1973, *A&A*, 29, 409
- Schönrich, R. 2012, *MNRAS*, 427, 274
- Schönrich, R., Binney, J., & Dehnen, W. 2010, *MNRAS*, 403, 1829
- Schultheis, M., Ganesh, S., Simon, G., et al. 1999, *A&A*, 349, L69
- Schwarz, G. 1978, *Annals of Statistics*, 6, 461
- Seares, F. H., van Rhijn, P. J., Joyner, M. C., & Richmond, M. L. 1925, *ApJ*, 62, 320
- Sérsic, J. L. 1968, *Atlas de Galaxias Australes* (Cordoba: Obs. Astronómico) (Cordoba: Observatorio Astronomico)
- Sevenster, M., Saha, P., Valls-Gabaud, D., & Fux, R. 1999, *MNRAS*, 307, 584
- Shetty, R., Kelly, B. C., & Bigiel, F. 2013, *MNRAS*, 430, 288
- Shetty, R., Kelly, B. C., Rahman, N., et al. 2014, *MNRAS*, 437, L61
- Siegel, M. H., Majewski, S. R., Reid, I. N., & Thompson, I. B. 2002, *ApJ*, 578, 151
- Simien, F., & de Vaucouleurs, G. 1986, *ApJ*, 302, 564
- Sion, E. M., Holberg, J. B., Oswalt, T. D., McCook, G. P., & Wasatonic, R. 2009, *AJ*, 138, 1681
- Sirko, E., Goodman, J., Knapp, G. R., et al. 2004, *AJ*, 127, 914
- Sobeck, J., Majewski, S., Hearty, F., et al. 2014, in *American Astronomical Society Meeting Abstracts*, Vol. 223, *American Astronomical Society Meeting Abstracts #223*, #440.06
- Sofue, Y., & Rubin, V. 2001, *ARA&A*, 39, 137
- Spergel, D. N., Malhotra, S., & Blitz, L. 1996, in *Spiral Galaxies in the Near-IR*, ed. D. Minniti & H.-W. Rix (Garching: ESO), 128
- Spitzer, Jr., L. 1942, *ApJ*, 95, 329
- Springob, C. M., Masters, K. L., Haynes, M. P., Giovanelli, R., & Marinoni, C. 2007, *ApJS*, 172, 599
- Stark, D. V., McGaugh, S. S., & Swaters, R. A. 2009, *AJ*, 138, 392
- Strateva, I., Ivezić, Ž., Knapp, G. R., et al. 2001, *AJ*, 122, 1861
- Strauss, M. A., Weinberg, D. H., Lupton, R. H., et al. 2002, *AJ*, 124, 1810

Sumi, T., Abe, F., Bond, I. A., et al. 2003, *ApJ*, 591, 204

Tago, E., Saar, E., Tempel, E., et al. 2010, *A&A*, 514, A102

Taylor, C., Boylan-Kolchin, M., Torrey, P., Vogelsberger, M., & Hernquist, L. 2015a, *ArXiv e-prints*, arXiv:1510.06409

Taylor, E. N., Hopkins, A. M., Baldry, I. K., et al. 2015b, *MNRAS*, 446, 2144

Teerikorpi, P. 1997, *ARA&A*, 35, 101

Tempel, E., Tamm, A., Gramann, M., et al. 2014, *A&A*, 566, A1

Tully, R. B. 1988, *Nature*, 334, 209

Tully, R. B., & Fisher, J. R. 1977, *A&A*, 54, 661

Unavane, M., Wyse, R. F. G., & Gilmore, G. 1996, *MNRAS*, 278, 727

Unterborn, C. T., & Ryden, B. S. 2008, *ApJ*, 687, 976

Vallee, J. P. 1995, *ApJ*, 454, 119

van den Bergh, S. 2000, *PASP*, 112, 529

van der Kruit, P. C. 1986, *A&A*, 157, 230

van der Kruit, P. C., & Freeman, K. C. 2011, *ARA&A*, 49, 301

van der Kruit, P. C., & Searle, L. 1981, *A&A*, 95, 105

Vanhollebeke, E., Groenewegen, M. A. T., & Girardi, L. 2009, *A&A*, 498, 95

Vázquez, G. A., & Leitherer, C. 2005, *ApJ*, 621, 695

Verheijen, M. A. W. 1997, PhD thesis, Univ. of Groningen

Vogelsberger, M., Genel, S., Springel, V., et al. 2014, *MNRAS*, 444, 1518

Weinberg, S. 1972, *Gravitation and Cosmology: Principles and Applications of the General Theory of Relativity* (New York, NY: Wiley), 688

Wetzel, A. R., Hopkins, P. F., Kim, J.-h., et al. 2016, *ArXiv e-prints*, arXiv:1602.05957

Widrow, L. M., Pym, B., & Dubinski, J. 2008, *ApJ*, 679, 1239

Wilk, M. B., & Gnanadesikan, R. 1968, *Biometrika*, 55, 1

Willman, B. 2010, *Advances in Astronomy*, 2010, 285454

Willmer, C. N. A., Faber, S. M., Koo, D. C., et al. 2006, *ApJ*, 647, 853

Wong, O. I., Schawinski, K., Kaviraj, S., et al. 2012, MNRAS, 420, 1684

Wouterloot, J. G. A., Brand, J., Burton, W. B., & Kwee, K. K. 1990, A&A, 230, 21

Wyder, T. K., Martin, D. C., Schiminovich, D., et al. 2007, ApJS, 173, 293

Wyse, R. F. G. 2006, Mem. Soc. Astron. Italiana, 77, 1036

Xilouris, E. M., Byun, Y. I., Kylafis, N. D., Paleologou, E. V., & Papamastorakis, J. 1999, A&A, 344, 868

Xu, Y., Li, J. J., Reid, M. J., et al. 2013, ApJ, 769, 15

Yamagata, T., & Yoshii, Y. 1992, AJ, 103, 117

Yanny, B., Rockosi, C., Newberg, H. J., et al. 2009, AJ, 137, 4377

Yin, J., Hou, J. L., Prantzos, N., et al. 2009, A&A, 505, 497

Yniguez, B., Garrison-Kimmel, S., Boylan-Kolchin, M., & Bullock, J. S. 2014, MNRAS, 439, 73

York, D. G., Adelman, J., Anderson, Jr., J. E., et al. 2000, AJ, 120, 1579

Zhao, H. 1996, MNRAS, 283, 149

Zheng, Z., Flynn, C., Gould, A., Bahcall, J. N., & Salim, S. 2001, ApJ, 555, 393

Zwicky, F. 1933, Helvetica Physica Acta, 6, 110